Computer-Aided Detection and Classification of Microcalcifications in Digital Breast Tomosynthesis

Pui Shan (Candy) HO

Balliol College

Wolfson Medical Vision Lab

Department of Engineering Science

Supervisors:

Professor Sir Michael Brady

Dr. Julia Schnabel

A thesis submitted for the degree

Doctor of Philosophy

Trinity Term 2011

Computer-Aided Detection and Classification of Microcalcifications in Digital Breast Tomosynthesis

Pui Shan (Candy) HO
Balliol College, University of Oxford

Doctor of Philosophy, Trinity Term 2011

Abstract

Currently, mammography is the most common imaging technology used in breast screening. Low dose X-rays are passed through the breast to generate images called mammograms. One type of breast abnormality is a cluster of microcalcifications. Usually, in benign cases, microcalcifications result from the death of fat cells or are due to secretion by the lobules. However, in some cases, clusters of microcalcifications are indicative of early breast cancer, partly because of the secretions by cancer cells or the death of such cells. Due to the different attenuation characteristics of normal breast tissue and microcalcifications, the latter ideally appear as bright white spots and this allows detection and analysis for breast cancer classification. Microcalcification detection is one of the primary foci of screening and has led to the development of computer-aided detection (CAD) systems.

However, a fundamental limitation of mammography is that it gives a 2D view of the tightly compressed 3D breast. The depths of entities within the breast are lost after this imaging process, even though the breast tissue is spread out as a result of the compression force applied to the breast. The superimposition of tissues can occlude cancers and this has led to the development of digital breast tomosynthesis (DBT). DBT is a three-dimensional imaging involving an X-ray tube moving in an arc around the breast, over a limited angular range, producing multiple images, which further undergo a reconstruction step to form a three-dimensional volume of breast. However, reconstruction remains the subject of research and small microcalcifications are "smeared" in depth by current algorithms, preventing detailed analysis of the geometry of a cluster. By using the geometry of the DBT acquisition system, we derive the "epipolar" trajectory of a microcalcification. As a first application of the epipolars, we develop a clustering algorithm after using the Hough transform to find

corresponding points generated from a microcalcification. Noise points can also be isolated. In addition, we show how microcalcification projections can be detected adaptively.

Epipolar analysis has also led to a novel detection algorithm for DBT using a Bayesian method, which estimates a maximum a posterior (MAP) labelling in each individual image and subsequently for all projections iteratively. Not only does this algorithm output the binary decision of whether a pixel is a microcalcification, it can predict the approximate depth of the microcalcification in the breast if it is.

Based on the epipolar analysis, reconstruction of just a region of interest (ROI) e.g. microcalcification clusters is possible and it is more straightforward than any existing method using reconstruction slices. This potentially enables future classification of breast cancer when more clinical data becomes available.

Acknowledgements

I am very grateful to my supervisors Professor Sir Michael Brady, Dr. Julia Schnabel and a postdoctoral advisor Dr. Chris Tromans. They all have given me invaluable advice and encouragement over the course of my DPhil.

Professor Sir Michael Brady is an excellent supervisor. He is very enthusiastic and he has put tremendous effort on me during the course of my project. I am very thankful to him that he is very patient in pushing me understand the epipolar geometry and other related areas. You cannot imagine how he can manage his time in such a good way, but at the same time entertain me with my unreasonable intensive meetings during the last few months in my DPhil. Thank you very much, Mike!

I would also like to thank Julia and Chris for their assistance. They help me understand the topics more clearly. I am especially very thankful to Chris because my project is closely related to his as I need to use his implementation in generating the tomosynthesis projections. He is always very helpful and he always inspires me a lot in my research.

Special thanks to Dexela Ltd., especially Spencer Gunn, for the support in acquiring the DBT datasets, Technology Strategy Board for funding my DPhil, and SPIE, Santander and my department and college for giving me some of the financial support in attending the conferences.

Thanks to all members in the WMVL and IBME, especially Carolina who supports me a lot and all other members who discuss and work with me together. Thanks also to those I met during conferences, who have shared with me the ideas related to my project.

Last but not least, I would like to thank my family and friends, especially the friends I met in Oxford, for their encouragement and support throughout my study.

Contents

Chapter 1

Introduction

Sad to say, *"It is estimated that 207,090 women will be diagnosed with and 39,840 women will die of breast cancer in USA in 2010."* (Quoted from [1]). These huge figures, representing only one country in the world, should have sufficiently captured the reader's attention to the severity of the threat of breast cancer. In fact, every woman in the world, not necessarily those in USA, is also at risk of breast cancer. What should we do to fight against breast cancer?

1.1 Understanding Breast Cancer

1.1.1 Prevalence of Breast Cancer

Breast Cancer is one of the most common cancers in many countries, causing many deaths every year. To have a more global picture about how serious it is in different countries, statistics of incidence and mortality rates can be obtained from the relevant authorities. For example, according to the Hong Kong Cancer Statistics *2007* from Hong Kong Cancer Registry, breast cancer is the major cancer in women with an incidence rate of *74.2* per *100,000* women, causing a mortality rate of *14.5* [2], comprising the third leading cause of cancer death in Hong Kong. In the United Kingdom (UK), the situation is even worse. The incidence and the mortality rates per *100,000* women are *121.4* and *28.4* respectively, calculated as three-year averages for *2003-2005*, making breast cancer the major cancer in women and the second leading cause of cancer death in UK, figures obtained from the report issued in *2008* by the Office of National Statistics, UK [3]. The situation in the USA is similar to the UK, with a slightly lower death rate. From the statistics retrieved from the National Cancer Institute, the incidence and the mortality rates based on cases diagnosed is *124.0* (in *2004-2008*) and *24.0* (in *2003-2007*) respectively [1]. Further to this, GLOBOCAN

2008, a project on cancer incidence and mortality worldwide in 2008 by the World Health Organisation [4] has reported that an estimated *1.38* million new breast cancer cases were diagnosed in *2008*. All these figures have revealed that the prevalence of breast cancer in the world cannot be neglected and that more efforts are required to fight against breast cancer.

1.1.2 What is Breast Cancer?

We need to understand what breast cancer is. Breast cancer is the result of DNA alterations, such as mutations, damage, or abnormal changes in the genes, leading to uncontrolled cellular proliferation forming tumours [5, 6]. Benign tumours do not invade neighbouring tissues or spread to other parts of the body, while malignant tumours do. Breast cancer refers to "a malignant tumour that has developed from the cells in the breast" [6]. To understand the situation, a brief overview of breast anatomy is presented.

1.1.3 Breast Anatomy

Here, a simplified breast anatomy is shown:

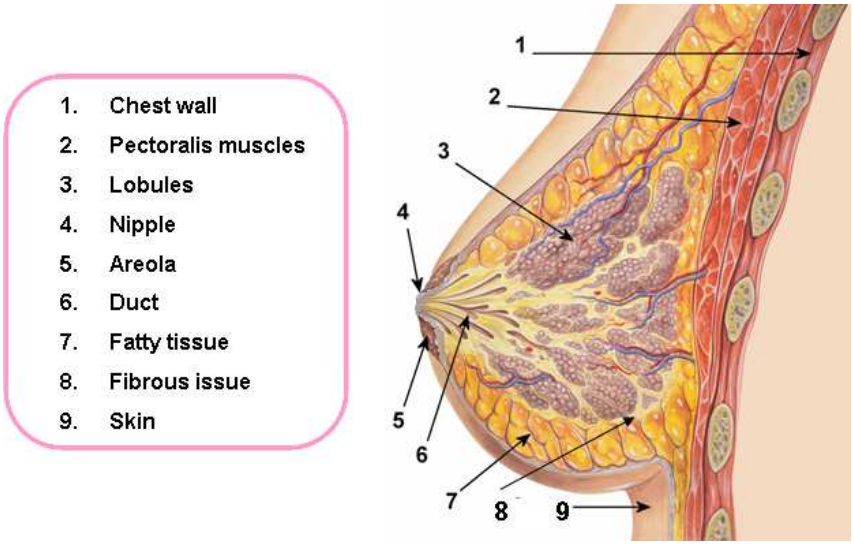

Figure 1.1: Basic Breast Anatomy (Modified from [7].)

The breasts sit over the pectoralis muscle and cover a large part of the chest wall. They are composed of three main types of tissues: fatty (adipose), fibrous (connective) and glandular (parenchyma). Fatty tissue surrounds the interior of the breast, like a cushion; fibrous tissue is the connective support for the breast and gives it its shape; glandular

tissue is functional, and includes the lobules (which contain milk glands) and the ducts (responsible for the production and transmission of the milk to nipple). The figure also shows a region called the areola, the circular area which surrounds the nipple and which contains glands for providing lubrication to the nipple during nursing [5]. Sometimes, the fatty and fibrous tissues are collectively termed the stroma, which refers to the structural tissues or connective tissues, as opposed to the parenchyma, which are the functional parts of the breast and are mainly refer to the ducts and lobules.

Figure 1.2 shows the breast in another view. It depicts the stroma, lobule, duct, lymph nodes and vessels:

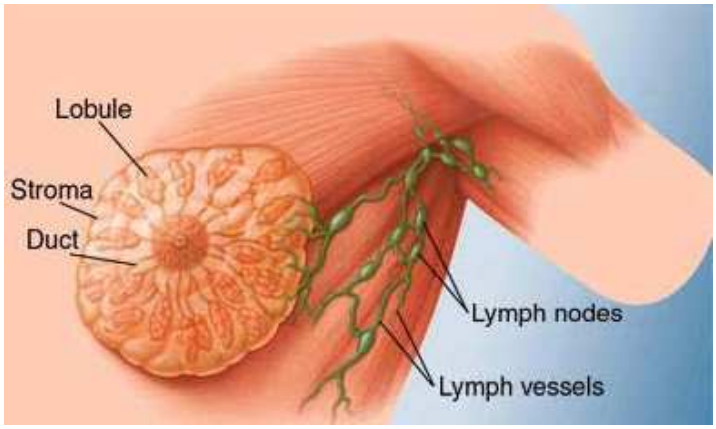

Figure 1.2: Breast showing stroma, lobule, duct, lymph nodes and vessels. (Extracted from [8].)

Usually, cancer cells originate in the cells of the lobules or the ducts. Sometimes, however, they can also be found in the stromal tissues. It is observed that there exist some lymph nodes and vessels under the arms. These are part of the immune system and help filter out foreign bodies such as bacteria and viruses. Unfortunately, if the cancer cells spread into the lymph nodes, they have a pathway to other parts of the body. Most cancer deaths result from metastases.

1.1.4 Types of Breast Cancer

In general, there are two types of breast cancer: non-invasive and invasive. The non-invasive types are the two very early types having abnormal cells inside ducts (DCIS – ductal carcinoma in situ) or lobules (LCIS – lobular carcinoma in situ) of the breast; but which have not yet started to spread into the surrounding breast tissues. It is noted that DCIS, although non-invasive, is more severe than LCIS and needs to be treated as early as possible. This is because about one-fourth of all DCIS cases will develop into invasive cancer within 10 years if there is no treatment [9]. On the other hand, LCIS

generally does not become invasive, although women with LCIS face a higher risk of developing breast cancer.

The invasive types include invasive ductal carcinoma, invasive lobular carcinoma, inflammatory breast cancer and Paget's disease, and some other very rare types such as medullary breast cancer and tubular breast cancer [10, 11]. Ductal breast cancer is the most common type of breast cancer, accounting for *70-80%* of cancer cases [10]. Invasive ductal carcinoma refers to the situation in which cancer cells are not only found in ducts, but have broken through the walls of the ducts into nearby breast tissue. Instead of ducts, invasive lobular carcinoma refers to the situation in which cancer starts in the cells that line the lobules of the breast and the cells spread to other nearby tissues. About *10%* of breast cancers are invasive lobular carcinoma [10].

The following figures depict DCIS, LCIS and invasive ductal / lobular cancer:

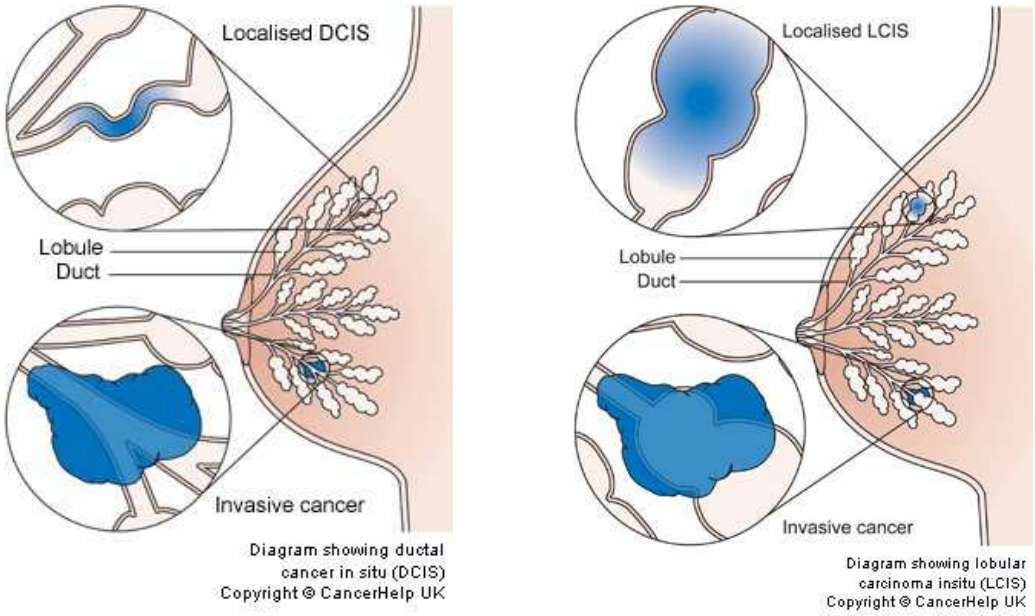

Figure 1.3: (Left) Ductal carcinoma; (Right) Lobular carcinoma. (Extracted from [10].)

One preliminary approach to classification of breast cancer into malignant and benign, currently used by the radiologists, is based on the shape of clusters of microcalcifications or the distribution of microcalcifications that appear in mammograms. This can partly be explained by the location of the cancer cells in the breast that produce calcium secretions. For example, DCIS can sometimes be identified when curvilinear shaped microcalcification clusters are observed in a mammogram.

1.2 Breast Screening

As mentioned, unusual DNA changes can cause breast cells to become cancerous. Some DNA changes are inherited. However, most of the DNA changes that lead to breast cancer occur during a woman's life instead of having been inherited. The causes of these DNA mutations are still not determined [12]. Hence, in fighting against breast cancer, two effective methods may be considered: early diagnosis and effective therapies. These constitute respectively breast screening and the availability of chemotherapies, particularly Tamoxifen and related drugs. In this thesis, breast screening is focused upon.

1.2.1 Breast Screening: A Reason of Mortality Rate Decreases?

From a paper in the BMJ [13] in August *2010*, breast cancer mortality in women in *30* European countries between *1987-1989* was compared with that between *2004-2006*. It was found that the mortality rate of the UK had fallen from *41.9* to *28.1* per *100,000* people. Of course, there are multiple factors that can account for the fall, e.g. lifestyles changes, better treatment. However, the impact of the significant change in early breast cancer detection brought about by the introduction of the breast screening programme in the UK in *1988* must not be ignored. *Figure 1.4* shows a comparison of the mortality from breast cancer in some European (EU) countries. Most of them have seen a significant fall in the rates. (Some examples of the launch year of national breast screening: Netherlands started nationwide breast screening around *1989* [14]; Ireland started in *1999* [15].) On the contrary, Bulgaria is the only country in the EU that does not have a screening program for cancer as of *25th June 2010* [16]. Its death rate from breast cancer has seen a slight increase during the same period.

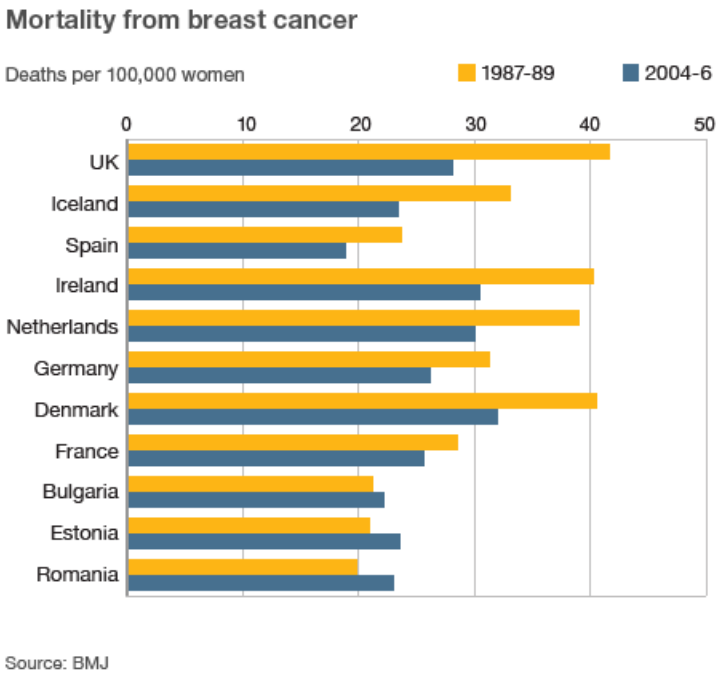

Figure 1.4: Mortality from breast cancer in some European countries in the periods of 1987-1989 and 2004-2006 (Extracted from [17].)

Some studies have also supported breast cancer screening. As early as *2002*, the International Agency for Research on Cancer (IARC) of the World Health Organisation (WHO) published a handbook of breast cancer screening, in which it states that mammography is proven for the efficacy of screening women aged *50-69* years in reducing mortality from breast cancer [18]. In *2007*, a case-control study was completed on the impact of the East Anglian breast screening programme on breast cancer mortality and it suggests that the programme had achieved a reduction in breast cancer deaths [19].

1.2.2 Current Imaging Modalities

Breast screening refers to the use of **imaging technologies** to **detect breast abnormalities** as soon as possible if they exist, so that early diagnosis can take place to prevent the cancer from proliferating. In this section, we highlight some current imaging modalities and then discuss them in more detail in Chapter 2. In the next section, we present a very short summary on the abnormalities found in the breast which will be further expanded in Chapter 3.

Thanks to advances in imaging technologies, e.g. X-ray, ultrasound, magnetic resonance imaging (MRI), researchers are using these techniques for early detection of breast cancer. Among these imaging modalities, mammography is the most common

technology used in breast screening, after consideration of the trade-offs of costs and its higher sensitivity and specificity. Among the *19* countries responding to a survey on characteristics of breast cancer screening programs in *2002*, all are based on mammography [20]. Mammography is the process of passing relatively low dose X-rays through the breast generating images called mammograms. Due to the properties of X-rays and the different characteristics of the breast tissues and the abnormalities, these 2D mammograms may show signs of cancer in the breast, so that radiologists may mobilise their knowledge and experience to determine whether or not the woman is suspected of having breast cancer.

In some cases, e.g. women with highly dense breasts (i.e. a large amount of glandular tissues in the breast), a mammogram may not be able to show the actual situation of the breast. In this case, some supplementary modalities, such as ultrasound or MRI, may be used for better diagnosis.

1.2.3 Detection of Breast Abnormalities

There are three major signs of breast cancer which can be found in mammograms: masses, microcalcifications and architectural distortion. Among these three, we focus on microcalcification detection in this thesis, as there has been a key finding that microcalcifications may be an early sign of cancer. Unlike masses, they cannot be detected by palpation (a physical examination to detect an abnormality by hand).

Microcalcifications are tiny bits of salts, primarily calcium, and may appear in clusters. Usually, in benign cases, they are the result of the death of fat cells or are due to secretion by the lobules. Sometimes clusters of microcalcifications can also indicate early breast cancer, partly because of the secretions by the cancer cells or the death of such cells. They are one of the findings, appearing as small white dots, which can be seen in the mammograms.

Examples of mammograms showing these three breast abnormalities are shown in *Figure 1.5*:

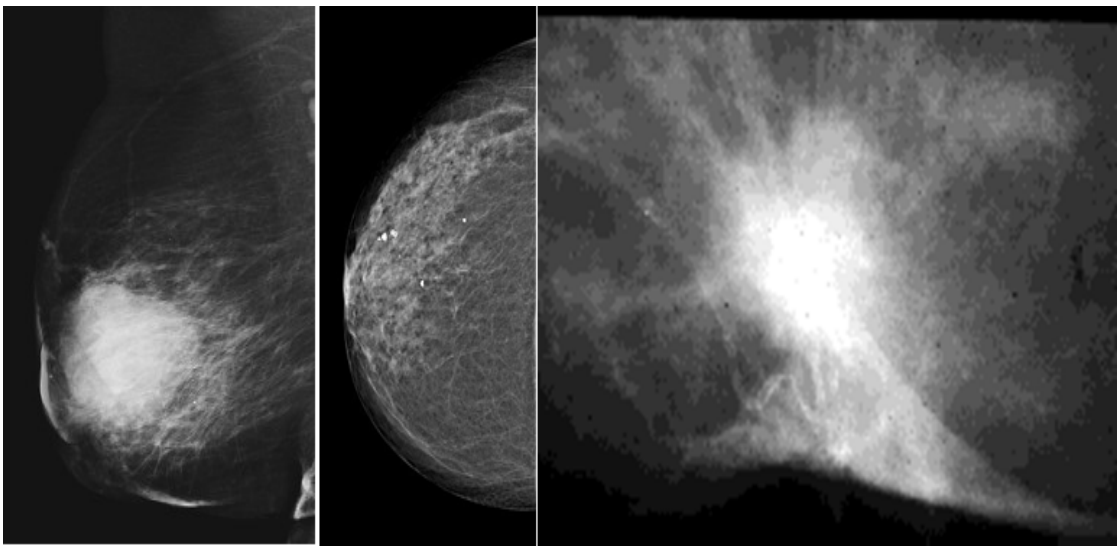

Figure 1.5: Mammograms with mass (Left), microcalcifications (Middle) and architectural distortion (Right). (Extracted from [21].)

1.2.4 Current Problems in Breast Screening and Mammography

Despite the encouraging news about breast cancer screening, there remains some opposition to it [22-24]. One argument is that many women would be wrongly diagnosed with this life-threatening disease, making them worried and causing them to undergo unnecessary treatment. Some people may therefore suggest that breast cancer screening may be doing more harm than good. While the benefits of breast screening and the effectiveness brought by mammography cannot be doubted, as can be seen from Section 1.2.1, we should nevertheless look for ways to make the detection more accurate and thus minimize the number of false positives. This is precisely what this research addresses.

A fundamental limitation of mammography is that it gives a 2D view of the tightly compressed 3D breast. As one may imagine, the depth details of the breast are lost after this imaging process, in addition to the pain experienced by the woman due to breast compression. Tissue overlap is an issue in some cases and this is why people argue that mammography wastes a lot of resources on unnecessary diagnosis. Hence, some 3D solutions should be considered for better detection accuracy.

1.2.5 Computer-Aided Detection and Classification of Microcalcifications (CAD) in Digital Breast Tomosynthesis (DBT)

In theory, computed tomography (CT), which is another X-ray imaging technique, may be considered. CT takes multiple X-ray pictures of the organ over the full 360^o angular directions and then the organ is reconstructed in 3D using a reconstruction algorithm. However, CT is currently not feasible because the radiation dose would be too great, although some scientists e.g. [25] are investigating it. On the other hand, people have developed something between mammography and CT. This something should be able to generate a 3D form of the breast similar to CT and at the same time the radiation dose should be limited to be similar to mammography. The compromise consists of taking projections over a limited angular range – Digital Breast Tomosynthesis (DBT).

DBT is similar to mammography and CT, both using an X-ray tube moving over the breast. The difference is that X-rays projections are captured in DBT over a limited angular range, instead of at most two in mammography. These multiple images are the advantages of DBT because it allows the reconstruction of the breast in 3D, while retaining the dose of mammography. Recently, a study [26] has reported that DBT is comparable or superior to digital mammography for microcalcifications in *95%* of *103* cases. The following figure shows a comparison of two X-ray images generated by digital mammography and DBT, of the same breast containing a cluster of microcalcifications:

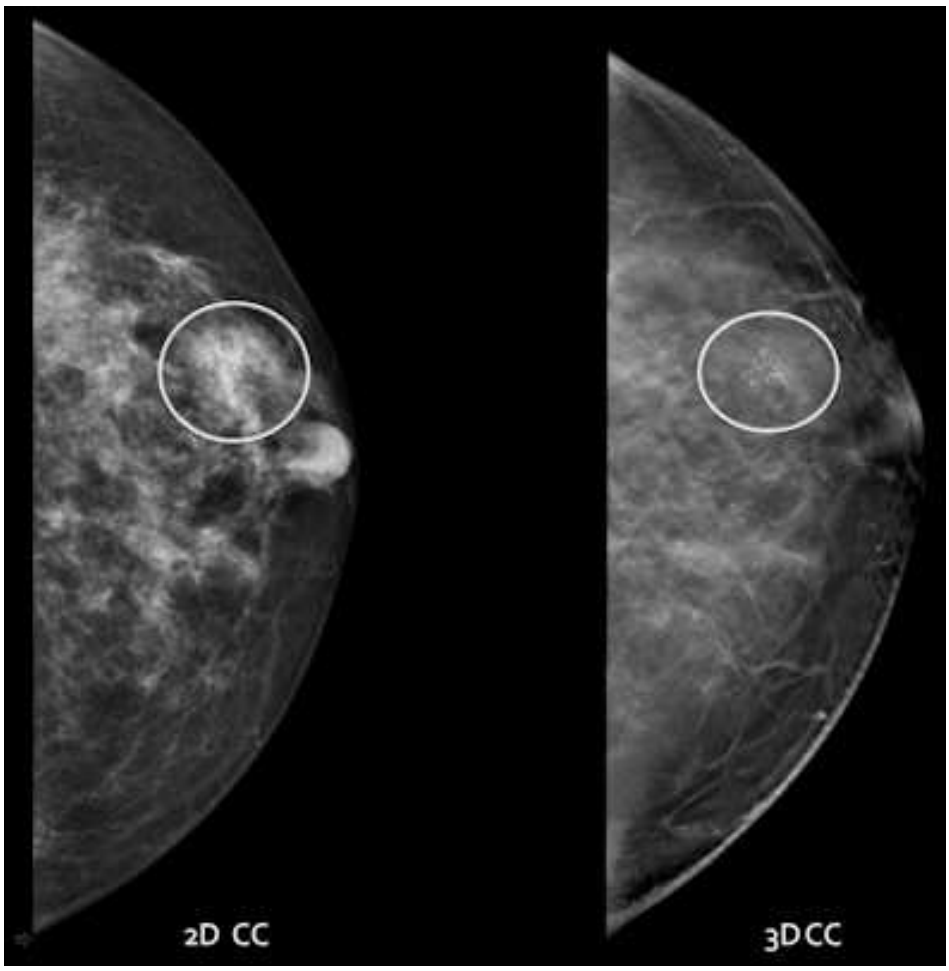

Figure 1.6: Digital mammography (Left) and DBT (Right) with microcalcifications. (Extracted from [26].)

It can be seen from the figure that the cluster is much clearer in the DBT images.

In addition to considering new 3D imaging technology, another approach to resolve the current problems in breast screening can be an automatic accurate detection technique to assist the radiologists in the diagnosis.

To date, most detection tasks rely on the knowledge and experience of radiologists. The workload of radiologists should not be underestimated. In addition, human manipulation is always subjective and manual tasks often generate unexpected errors which should never happen in computer systems if they are designed and implemented correctly. Hence, it is necessary for the development of good computer systems and algorithms to find suspicious breast tumours for further diagnosis.

There exist some good computer-aided detection systems e.g. Hologic's R2 ImageChecker CAD [27], which was the first FDA (US Food and Drug Administration) approved CAD system for mammography, and can highlight most of the suspected regions with microcalcifications accurately, alerting the radiologists for further analysis. Unfortunately, it is a commercial product for which many details have not been

published. Regarding DBT, with reference to the report in [28] by the National Health Service UK (NHS), with the possible exception of GE Healthcare, all other vendors do not yet provide CAD in DBT.

1.3 Objectives of this Project

Combining all these observations, we arrive at the main theme of this thesis: To design and develop a good algorithm for the computer-aided detection and classification of microcalcifications (CAD) in digital breast tomosynthesis (DBT).

1.4 Contribution of this Project

In this thesis, we develop a novel approach to microcalcification detection and reconstruction in DBT, **the Epipolar Curves Approach**, which subsequently facilitates the classification of breast into malignant and benign.

The core idea, epipolar curves, starts from the observation of combining all microcalcification candidates from all DBT projections into a single 2D coordinate frame, with the assumption that these microcalcification candidates are detected by some detection algorithms (See *Figure 1.7*). Some examples of these detection algorithms can simply be those already used in mammography.

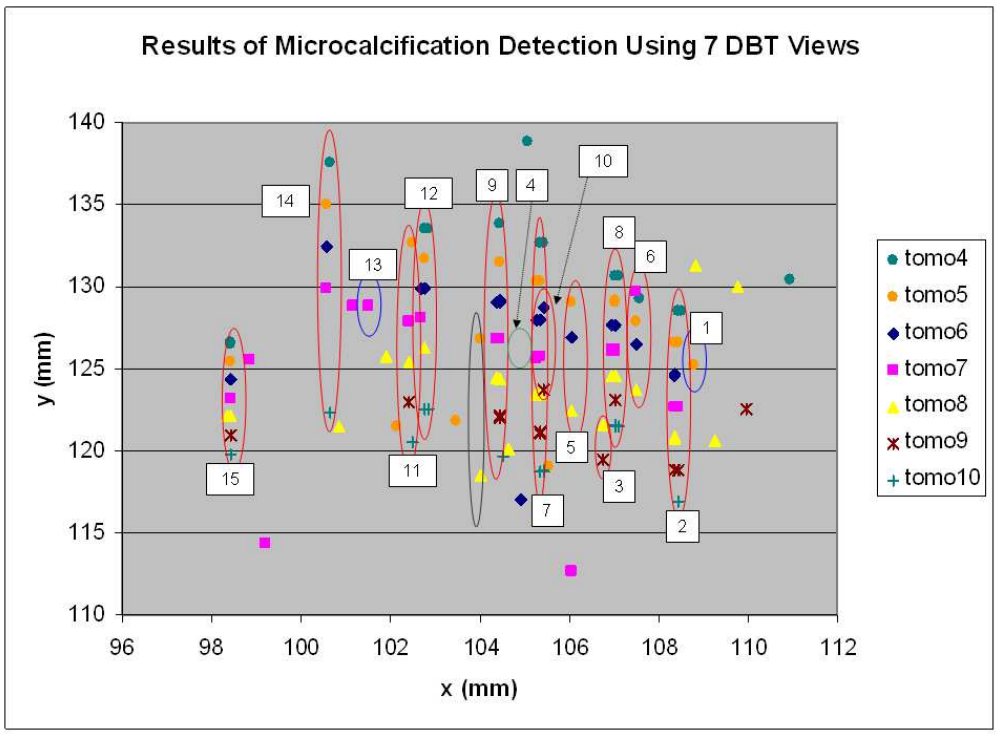

Figure 1.7: Microcalcification candidates from 7 DBT projections in a single 2D coordinate frame.

It is readily observed that the set of corresponding projection points from each microcalcification forms a cluster (red ellipses in the figure) which is a single trajectory in this 2D coordinate frame, and that isolated points may be considered to be noise. We call this trajectory, an epipolar curve. Using the geometry of the DBT acquisition system, mathematically, each epipolar curve can be derived.

With the use of the epipolar formulae, we illustrate a clustering algorithm using the Hough transform to find corresponding points generated from one microcalcification. The epipolar curves approach will be presented in more detail in Chapter 6.

Previously, we have assumed that microcalcification detection algorithms are available. This is partly true because we can apply those that have been developed for mammography. However, as one may expect, there is no free lunch: the image quality in a single X-ray image is considerably worse in DBT than in mammography, as the total radiation dose for both techniques are similar. The good news is that for DBT we have multiple projections. Extending the epipolar curves approach, we can detect microcalcifications adaptively. Those missing points in the initial detection round can be detected using other projections (See *Figure 1.8*). This adaptive approach will be introduced in Chapter 7.

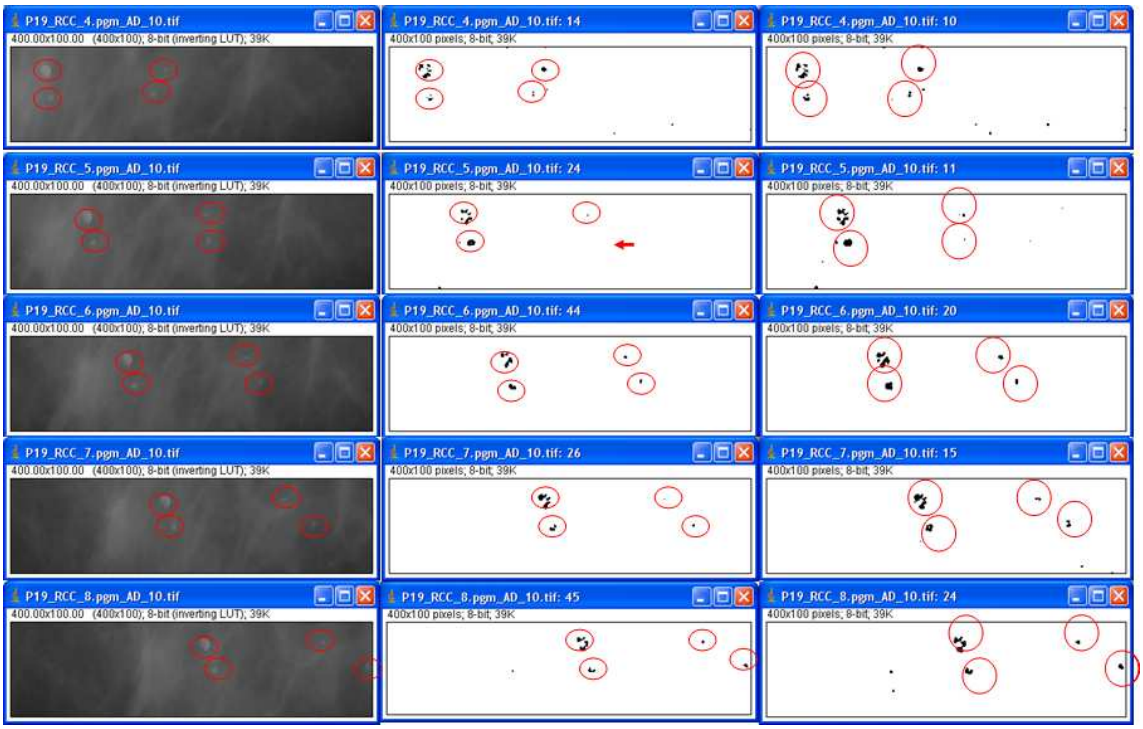

Figure 1.8: Original images (Left); Detection results initially (red arrow indicating possible missing point) (Middle); Detection results after threshold adjustment (Right) of patient 19.

We will also show a new detection algorithm for DBT using Markov random fields and belief propagation in Chapter 8. By gathering all the detection results in single projections, we can label a pixel either as a microcalcification or not, and even its depth in the breast if it is a microcalcification, such that the labelling is found with maximum posterior probability for the projection.

Now, knowing the correspondence across the DBT projections, we can easily find the 3D positions. Basic geometry tells us that with the 3D positions of the *2* sources and *2* projection points, the intersection point is the corresponding 3D position of the microcalcification. Instead of using this simple intersection method which may be sensitive to noise, we further extend our epipolar curves formulae and the 3D positions of the microcalcification (a,b,c) can be obtained in a straightforward way. This is covered in Chapter 9.

Finally, clusters of microcalcifications can be reconstructed. Analysis of the shape and distribution of microcalcifications within a cluster, which are some of the most important criteria in assessing malignancy, can be performed. In Chapter 10, we present a feasibility study by considering the ellipsoidal shape of the clusters.

1.4.1 Conference Papers

The work in this thesis has led to *3* oral presentations and *1* poster presentation in *3* conferences with the following conference papers in *2010*:

1. C. P. S. Ho, C. Tromans, J. A. Schnabel, and M. Brady, "The reconstruction of microcalcification clusters in digital breast tomosynthesis," presented (oral) at SPIE - Medical Imaging, San Diego, USA, 2010.
2. C. P. S. Ho, C. Tromans, J. A. Schnabel, and M. Brady, "Microcalcification Detection in Digital Breast Tomosynthesis Using an Epipolar Curve Approach," presented (oral) at International Workshop on Digital Mammography (IWDM), Girona, Spain, 2010.
3. C. P. S. Ho, C. Tromans, J. A. Schnabel, and M. Brady, "A Clustering Method for the Extraction of Microcalcifications Using Epipolar Curves in Digital Breast Tomosynthesis," presented (oral) at International Workshop on Digital Mammography (IWDM), Girona, Spain, 2010.
4. C. P. S. Ho, C. Tromans, J. A. Schnabel, and M. Brady, "Classification of Clusters of Microcalcifications in Digital Breast Tomosynthesis, ” presented (poster) at the Annual International Conference of IEEE Engineering in Medicine and Biology Society (EMBC 2010) at Buenos Aires, Argentina, 2010.

.

1.5 Overview of the Thesis Structure

Here is a route map through the thesis from Chapter 1 to Chapter 11:

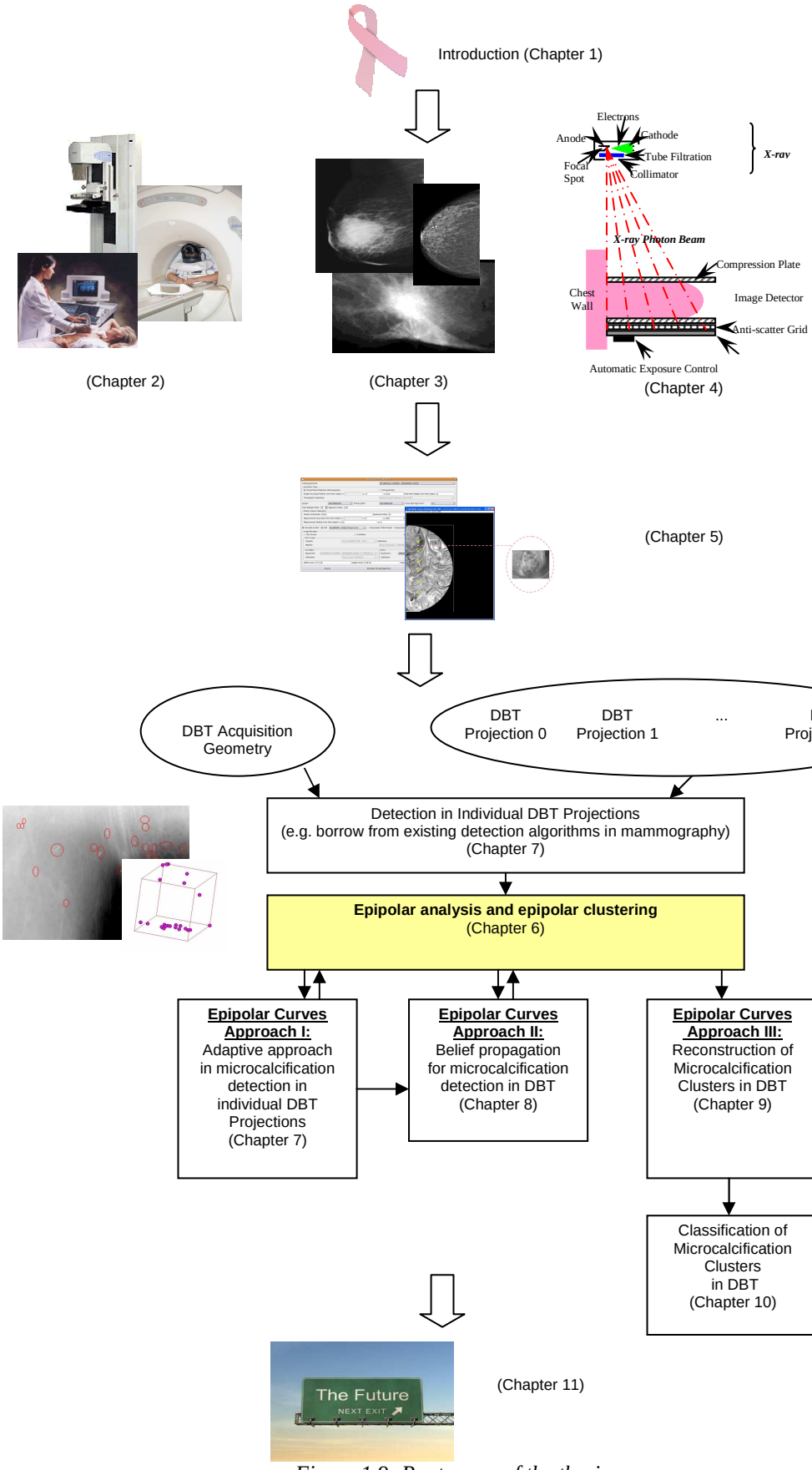

Figure 1.9: Route map of the thesis.

1.5.1 Background Information

Chapter 1-4 provides the reader with an introduction to the topic:

Chapter 1: Introduction

This introductory chapter gives readers a very brief introduction to breast cancer and the need for early detection. The objective of this thesis is also given.

Chapter 2: Breast Imaging Modalities and Digital Breast Tomosynthesis

In Chapter 2, current breast imaging modalities such as mammography, magnetic resonance imaging, ultrasound imaging and computed tomography will be summarized. DBT is discussed in more detail, including its acquisition systems, its technical features, the advantages and challenges it faces, some clinical study results and its role in future.

Chapter 3: Breast Abnormalities and Breast Calcifications

In Chapter 3, the three breast abnormalities will be introduced, particular breast calcifications.

Chapter 4: X-ray Images: Formation and Analysis

In Chapter 4, the formation of an X-ray image will be explained. This will be followed by a discussion on the analysis of the X-ray image, including its appearance, breast density, image contrast and image noise.

1.5.2 Datasets and Materials

Chapter 5: Datasets – Simulations, Phantoms, Real DBT Datasets

In Chapter 5, we review current simulation models and present our own simulation model for illustration in our approach. Then, we present other datasets that we use throughout the project, including the phantoms and also some real DBT datasets.

1.5.3 Epipolar Curves Approach and Its Extension

Chapter 6 – 10 are the main chapters which contain our core ideas and extension of our epipolar curves approach. A summary has been given in Section 1.4.

Chapter 6: Detection and Reconstruction of Microcalcifications in DBT: an Epipolar Curves Approach

Chapter 7: Epipolar Curves Approach I: An Adaptive Approach in Microcalcifications Detection in Individual DBT Projections

Chapter 8: Epipolar Curves Approach II: Belief Propagation for Microcalcification Detection in DBT.

Chapter 9: Epipolar Curves Approach III: The Reconstruction of Microcalcification Clusters in Digital Breast Tomosynthesis

Chapter 10: Feasibility Study of Classification of Clusters of Microcalcifications in DBT

1.5.4 Conclusions and Future Work

Chapter 11: Conclusions and Future Work

Finally, the thesis will end with the conclusions and future work. We will explore the possibilities of ongoing research on our epipolar curves approach on CAD in DBT.

Chapter 2

Breast Imaging Modalities and Digital Breast Tomosynthesis

A variety of imaging modalities is currently being applied to breast cancer detection. Some key factors to consider when evaluating each such modality include: the number of false positive findings that it typically gives; access by the relevant population of women to the modality; workflow considerations; and cost effectiveness [29]. An introduction to three major imaging modalities is given in Section 2.1. Of these, mammography is currently the most commonly used. As we have seen, it uses low-dose X-rays to generate an image called a mammogram and it is proven to decrease breast cancer mortality in screening populations. Unfortunately, its performance is not very good for women with dense breasts. Thus, other alternatives such as magnetic resonance imaging (MRI) and breast ultrasound imaging (breast USI) are considered as supplementary. In addition to these, we also overview breast computed tomography (breast CT), as this may be another promising technology for breast screening in the future.

In Section 2.2, we further expand on the limitations of mammography. Due to its inherently 2D nature, some cancer cases are ignored, while some normal cases are wrongly considered as cancer. This has led recently to the development of a new 3D modality – Digital Breast Tomosynthesis (DBT), which involves an X-ray tube moving in an arc around the breast over a limited angular range and producing a set of X-ray images. With the 3D nature of DBT, tissue superimposition problems found in mammography are reduced by DBT. In Section 2.3, we discuss DBT in more detail, including existing acquisition systems, their technical features, as well as the advantages and current challenges. A brief review of the performance of DBT in clinical studies will also be given. The results of DBT are promising. Having said that, since DBT is

still a very new modality, its role, either as a primary screening and diagnostic tool or as an adjunct to conventional mammography, is yet to be determined.

2.1 Current Imaging Modalities

In this section, we discuss the most common imaging modalities which can often be found in hospitals: Mammography, Magnetic Resonance Imaging (MRI) and Ultrasound Imaging. Breast CT will be briefly introduced at the end of this section.

2.1.1 Mammography

Mammography is an imaging method which uses low-dose X-rays (whose frequency ranges between $1.7 - 3.6 * 10^{18}$ Hz) to examine the breast and generate an X-ray image, called a mammogram. Conventional mammography (screen-film mammography (SFM)) uses film to record the image. Digital mammography (DM) is an advancement to SFM. This has been around for *12* years and is widely adopted in some countries. For example, *>80%* of hospitals are using DM in the USA, and *100%* in Netherlands and Ireland. DM employs the same principles and processes as screen-film mammography except that a digital detector replaces the screen-film combination and converts X-rays into digital signals. An example of a mammography system, Hologic Selenia [30], is given as shown in *Figure 2.1* (Right):

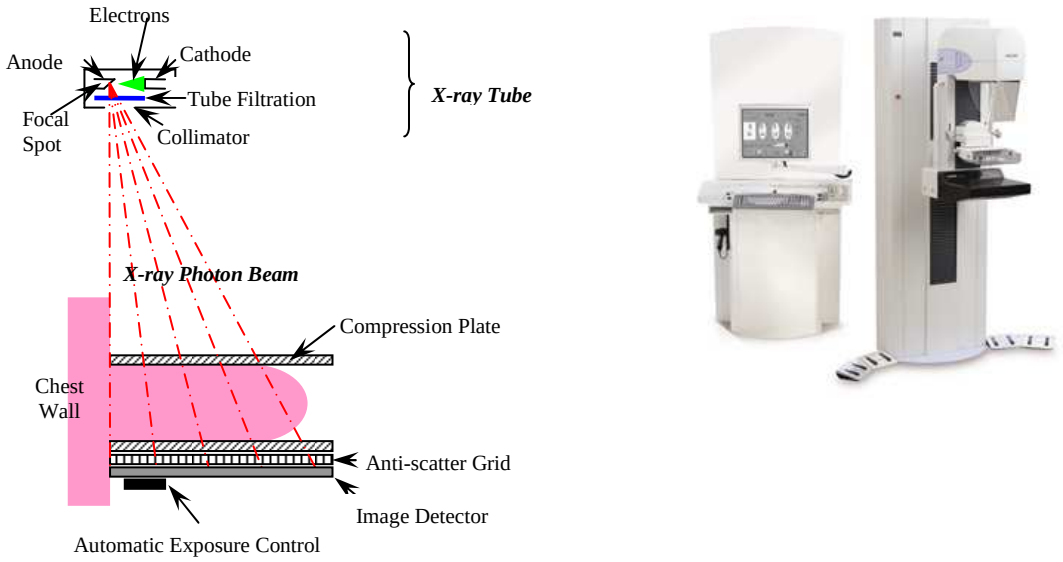

Figure 2.1: A schematic representation (Left) (Modified from [31].); a model (Hologic Selenia) (Right) [30] of a typical digital mammography system

A typical digital mammographic system consists of an X-ray tube, compression plate, anti-scatter grid, automatic exposure control and an image detector (See *Figure 2.1* (Left)). Radiologists analyze the images either from films/digitized images or through the computer display/outputs to check whether there is any sign of breast cancer, such as calcifications, that warrants follow-up. During most routine breast screening, two mammograms are generated for each breast: one in a cranio-caudal (CC) view (taken from above a horizontally-compressed breast); one in mediolateral-oblique (MLO) view (taken from the side and at an angle of a diagonally-compressed breast) [32] (*Figure 2.2*), in order to capture as much of the breast details as possible for analysis.

(a) (b)

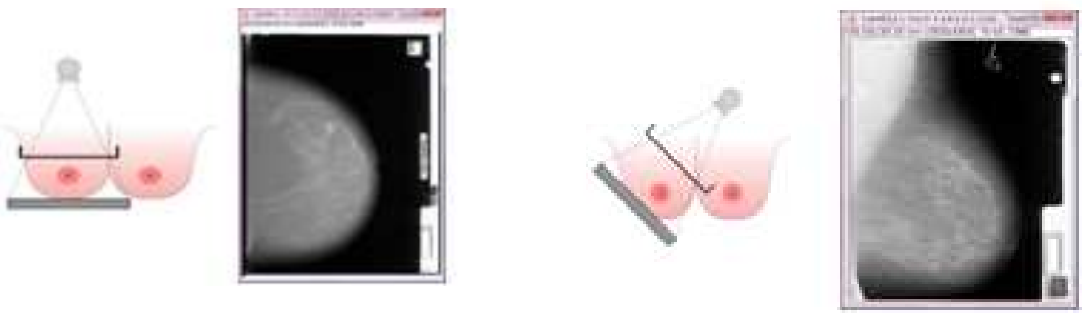

Figure 2.2 : Pictures showing how the view is taken and the mammograms generated from each view. (a) Cranio-caudal view; (b) Mediolateral-oblique view (Extracted from [33]and image data obtained from MammoGrid database [34].)

(As the basic principle of mammography, i.e. the formation of an X-ray image, is very important in our research, a more detailed discussion will be presented separately in Chapter 4.)

Currently, mammography is the most cost-effective breast imaging modality for women who are of, or approaching, screening age, that is, typically from *50-69*. It has been proven to reduce breast cancer mortality in randomized clinical trials for this age group. Hence, it is always chosen to be the first screening tool before any others are considered. However, mammography has its weaknesses. Dense breasts can make mammograms more difficult to interpret because both tumours and dense tissues appear as similarly solid white areas on the mammogram. So, a tumour can be easily missed in dense breasts [35].

To cope with this situation, additional breast imaging modalities have been considered:

2.1.2 Magnetic Resonance Imaging (MRI)

A breast MRI scan is a non-invasive imaging method using radio frequency waves at approximately *64* MHz (for *1.5*T machine) or *127* MHz (for *3*T machine) (*1* Tesla (T) is 10^4 gauss), which penetrate the tissues in the breast. Signals caused by the magnetized spins of the hydrogen protons returning to the lower energy state during free induction decay, form a stack of 2D slices of the breast. An example of a slice with breast cancer is shown in the following figure:

Figure 2.3: Breast cancer detected by MRI (arrow) (Extracted from [36].)

Basic Principles of MRI

(This section gives a brief overview of the basic principles of MRI. An excellent description can be referred to the book "MRI The Basics" by Hashemi et al. [37] and theses by Olivier Noterdaeme [38] and Lydia Nathania Tanner [39].)

A hydrogen nucleus is a single, positively charged proton. The proton spins about an axis, creating a magnetic dipole moment. In a magnetic field, it has two energy states which correspond to the spin being in the same or opposite direction of the magnetic field. The random orientation of the individual hydrogen spins means the dipoles cancel each other in each tissue. Nuclei with an odd number of protons or neutrons can be used for MRI. However, hydrogen is used because of its abundance that approximately *60%* of the body is water. Hydrogen protons (^1H) can be found in water (H_2O) and fat ($-CH_2-$).

A MRI unit consist of a large cylindrical tube which contains a powerful magnet, providing an external magnetic field B_0. Patients lie on a moveable examination table that slides into the center of the magnet. They lie face down on their stomach with their breasts hanging freely into cushioned openings, surrounding by a breast coil.

Figure 2.4: A patient lying on an examination table for a MRI breast scan (Extracted from [40].)

The spinning hydrogen protons in the breast become magnetised, aligning themselves such that approximately half of them align with the magnetic field in a "north" direction and half align with "south". About one in a million extra spins point north, equivalent to about 10^{17} excess hydrogen protons pointing north in each gram of tissue (as there are over 10^{23} molecules per gram of tissue). This makes the net magnetization point in the direction of B_0 which is pointing north.

When the protons are placed in a large magnetic field, they begin to "wobble" or precess about the axis of the external magnetic field B_0. The rate at which the proton precesses around the external magnetic field is given by the Larmor equation:

$$\omega = \gamma B_0 \qquad \textit{Eqn. 2.1}$$

where ω is the angular precssional frequency of the proton. γ is the gyromagnetic ratio which is proton specific, e.g. ^1H has a $\gamma = 42.6 MHz/T$

To create a MRI image, radio frequency (RF) pulses are transmitted into the patient. These pulses flip the longitudinal magnetization (the external magnetic field in the cylindrical tube), for example into the x-y plane, and generate a signal when the RF signal stops. The signals generated in this way do not have to encode spatial information and so it is not possible to determine the locations of tissues. Hence, we need to spatially encode the received signal by using the gradient coils corresponding to the axes x, y and z in a three-dimensional coordinate system. For an axial breast image, the three gradients are referred to as: slice-select gradient (G_z) which selects a slice position and thickness; phase-encoding gradient (G_y) and frequency-encoding gradient (G_x) which encode the spatial locations within a slice.

Recall that during the MRI imaging process, we have an external magnetic field in a longitudinal (*z*) axis M_0 and then RF pulses (*x*-*y* plane) are sent. Once the RF pulses are turned off, the protons will have to realign with the axis of the B_0 magnetic field and give up all their excess energy. This is termed relaxation, meaning that the spins are relaxing back into their lowest energy state, the equilibrium state. The net magnetization over time t is an exponential function in the form: $1-e^{-t/T1}$. T1 is tissue specific and is the longitudinal relaxation time which is the time taken for the spins to realign along the *z* axis. There is another time constant which characterizes the rate at which the magnetization component in the *x*-*y* plane (M_{xy}) (transverse component) decays. In addition to this decay, there are spin-spin interactions which are the very small magnetic fields affecting by the nearby protons and are one of the two causes of spin dephasing. The relaxation time of the decay (transverse relaxation time) together with the time of the spin-spin interactions is called T2 relaxation time. T2 is also tissue-specific. Another spin dephasing is caused by the inhomogeneities of the external magnetic field. The inhomogeneities are very small, but because of this, spins will then

be exposed to slightly different magnetic field strength, making protons in different locations precess at different frequencies. T2* is defined to denote the relaxation time by the two causes of spin dephasing and it is not fixed as it depends on the homogeneity of the external magnetic field.

There are three parameters that define the RF pulses in forming different MRI images: the flip angle α, the repetition time TR and the echo time TE. α is the angle that the RF pulses flip the net magnetization into the *x-y* plane. TR is the interval between successive RF pulses. TE is the short delay period between the application of the RF pulse and measuring the transverse component of the signal. The image signal (S) will then be related to the simultaneous delay of T2* and the recovery of T1. By considering TE and TR, we then have:

$$S \propto N(H)M_0(1-e^{-TR/T1})e^{(-TE/T2^*)} \qquad \textit{Eqn. 2.2}$$

where N(H) is the number of mobile hydrogen protons.

So, by acquiring images with short (long) TR, we enhance (reduce) the T1 effect so that tissues with very different T1 values will demonstrate greater (smaller) contrast. By using a long (short) TE, we enhance (reduce) the T2* effect. Different flip angles also cause different overall contrast in the image.

Insufficiency of Standard MRI on Breast Screening

A standard MRI of the breast can show soft tissue contrasts, cysts, enlarged ducts or lymph nodes, haematomas (a collection of blood formed when small blood vessels are damaged, causing block leakage or bleeding into the tissues), and ruptured breast implants [40].

However, it is unable in general to detect breast abnormalities or tumors. This is because the contrast between the fatty tissues, fibroglandular tissues and the breast abnormalities generated in the MRI image, governed by the tissues' intrinsic relaxation times T1 and T2, does not enable tumors to be detected.

Another main reason why breast MRI is not a primary screening tool is that with MRI, microcalcifications are difficult to be detected using standard pulse sequences [41]. Calcium deposits may appear as tiny signals and their detection in MRI is not as reliable as mammography.

Dynamic Contrast-Enhanced MRI (DCE MRI)

This section gives a brief overview of DCE MRI which is summarized from [38, 39, 42].

The basis of contrast-enhanced breast MRI is the intravenous injection of a contrast agent before the acquisition of the MRI images. In this way, the cancer surroundings are enhanced. Cancer is not just the soft tissue contrast, it is a physiological abnormality. One major sign is angiogenesis (the growth of new blood vessels from existing ones) and so cancerous tissues have a chaotic and leaky vasculature in general. On the other hand, the contrast agents are distributed in the extravascular space and tend to accumulate in tissues with rich vascularity. As a result, the use of contrast agents help "highlight" the cancer tissues.

Currently, the most widely used and only clinically approved contrast agents are Gadolinium chelates. Gadolinium is a paramagenetic substance which has seven unpaired orbital electrons. The external magnetic field B_0 of the MRI system causes these electrons to magnetized, in the same direction as this external magnetic field, leading to a reduction in the T1 and T2 relaxation times for protons in tissues near or with the contrast agents. This explains why cancerous tissues show a relatively higher and earlier uptake of Gadolinium-based contrast agent than the normal tissue. A baseline scan is then subtracted from the post-contrast image to provide information about the contrast agent take-up as a function of time, which is related to the vascular density, essentially giving information about tissue perfusion

Advantages of DCE MRI

DCE MRI screening may benefit patients with high risk or dense breast tissue which can sometimes hide a tumour on a mammogram (See *Figure 2.5*). Also, it can also be used to measure the size of tumour before treatment, during, and after neo-adjuvant chemotherapy.

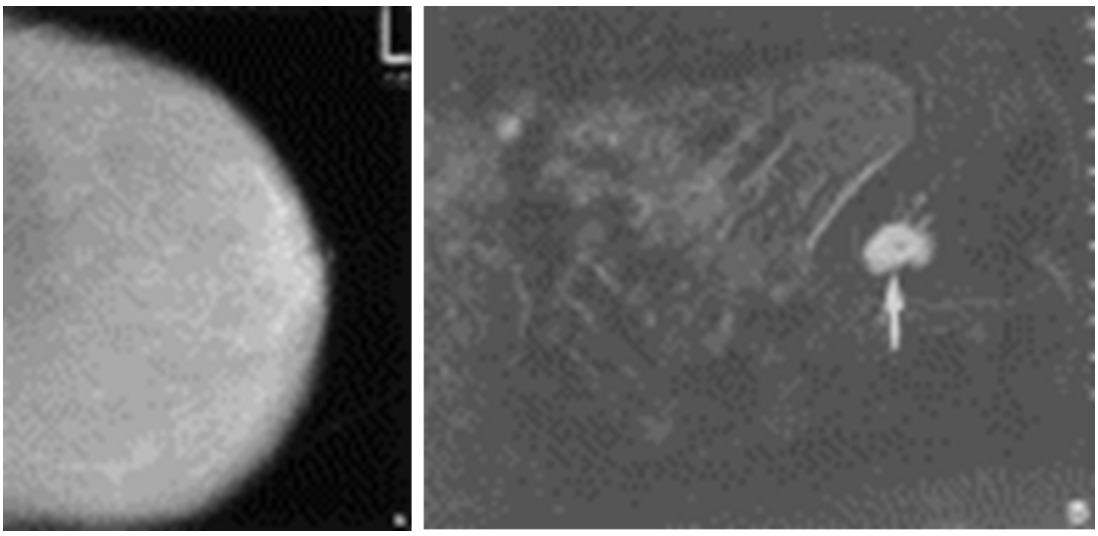

Figure 2.5: A patient with invasive ductal carcinoma. Left: Mammography did not show any evidence of malignancy; Right: Coronal MR early subtraction image displays an ill-defined 1.7 cm enhancing mass (arrow). (Extracted from [43].)

Problems of DCE MRI in Breast Screening

A concern regarding DCE MRI is the potential side effects from the use of gadolinium-based contrast agents. It is not advised for patients with a range of hepatic disorders or those with acute or chronic severe renal insufficiency. Certain patients may have an increased risk for developing a serious systemic fibrosing disease, Nephrogenic Systemic Fibrosis [44]. Despite the toxicity, it may be justified for use in women which have a high risk in developing breast cancer.

Another major drawback is the limited specificity by DCE MRI. The problem is that some benign entities e.g. fibroadenoma, sclerosing adenosis, may also enhance similar to malignant cases [43], causing false positive cases.

Other disadvantages are its high cost (*US$500*, compared with *US$100* for mammography) and its long screening time (*15* minutes, compared with possibly a few minutes for mammography). Also, some patients suffer from claustrophobia and find the confinement discomforting.

2.1.3 Ultrasound Imaging (USI)

Similar to MRI, breast ultrasound is a non-ionising imaging modality using sound waves having frequencies above the audible range, typically *7.5* MHz or higher [5],

which penetrate into and through the breast tissues. These sound waves reflect at breast tissue boundaries, creating "echoes", which are recorded by the computer, yielding an ultrasound image. An example showing a 2D ultrasound image with a simple breast cyst is shown in the following figure:

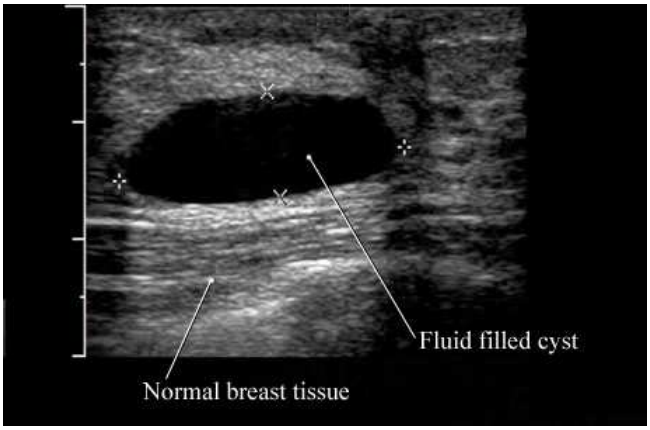

Figure 2.6: A 2D ultrasound image with a simple breast cyst (Extracted from [45].)

In recent years, 3D breast ultrasound has gradually been used in hospitals. Instead of a single 2D image, a volume consisting of a stack of 2D slices can be obtained. This allows the display of the coronal plane of the breast for improvement in breast diagnosis and biopsy procedures. (An introductory chapter on 3D and 4D breast ultrasound can be found in the book of Ultrasound in obstetrics and gynecology: Gynecology by Eberhard Merz [46].)

Basic Principles of USI

The following summary follows the discussion from [5, 47].

Typical ultrasound equipment contains a hand-held unit called transducer. The transducer is usually composed of a piece of piezoelectric material e.g. lead zirconate titanate (PZT), which can generate ultrasound pulses and receive echoes from the breast tissues.

Normally, a patient lies supine on the examination table with the hand placed under the head as shown:

Figure 2.7: A patient lying on an examination table for an ultrasound breast scan (Extracted from [48].)

This positioning makes the breast thinner and flatter, allowing adequate ultrasound pulses to penetrate to the chest wall, and minimizing the effects caused by some breast tissues which may be otherwise steeply obliquely oriented in upright or prone positions [49].

Ultrasound pulses are generated by inducing the piezoelectric material to vibrate, by applying either a sinusoidal electric field or a sharp electrical spike across the material. The ultrasound waves then enter the breast and pass through different tissue types in the breast. Depending on the tissue types which have different acoustic impedance and attenuation coefficients, the sound waves can be reflected, scattered, absorbed or attenuated. Echoes are then returned, inducing a varying voltage across the piezoelectric material. By measuring and recording the strength of the signal of each returning echo, an ultrasound image can then be computed.

Advantages of USI

The major benefit of ultrasound is its ability to determine if an abnormality is a solid malignant cancerous tumour or fluid-filled benign cyst, as the sound waves have different behaviour towards different composition. For example, a solid mass reflects the sound wave while the wave may pass through the fluid-filled cyst, hence producing a different signal or echo in these two cases. This is useful in the analysis of the composition of the tumor, which may not be possible in mammography or MRI.

Other advantages of USI include its relatively inexpensive cost, and the mobility and portability of the machine.

Microcalcification Detection Using USI – Limitation of USI in Breast Screening

Many articles e.g. [50] have suggested that microcalcifications cannot be seen in USI due to their small size and the low resolution of USI. Microcalcifications are always confused with the complex structure of breast tissue and the substantial speckle noise [51]. This is the major reason why USI is now a supplementary breast screening tool to mammography, when a mass is suspected.

2.1.4 Breast Computed Tomography (Breast CT)

As briefly mentioned in Chapter 1, X-ray computed tomography is a medical imaging method which generates a 3D image of the object from hundreds of 2D X-ray images spanning 360^o. This allows a complete picture of the breast, represented as a stack of image slices, to be reconstructed by a suitable reconstruction algorithm.

Basic Principles of CT

The following summary is extracted from a lecture and a thesis in the KTH Royal Institute of Technology [52, 53].

The basic idea is explained using the projection of a 2D object. Similar extension can be applied to 3D. The projection of a 2D object on a 1D detector array is shown in the following figure:

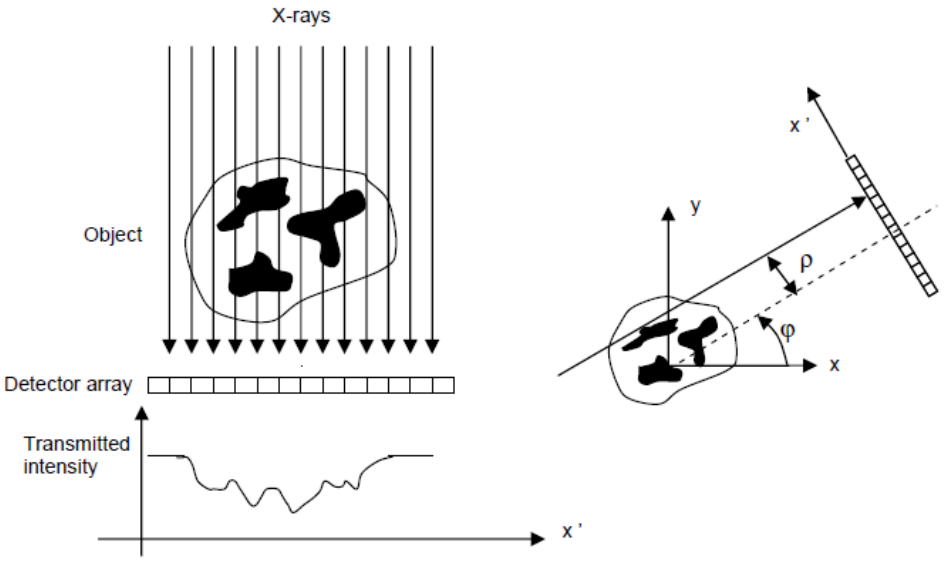

Figure 2.8: Projection of a 2D object onto a 1D detector array (Extracted from [53].)

At different angles φ and offsets ρ from the origin of a defined 2D coordinate system, a projection is formed. The intensity $\boldsymbol{I}$, in simple terms, is a measure of the attenuation of the X-ray on the tissue column along the path from the source with initial intensity $\boldsymbol{I}_0$ (More details on the formation of X-ray will be discussed in Chapter 4):

$$\boldsymbol{I} = \boldsymbol{I}_0 \boldsymbol{e}^{-\int \mu(x,y)\boldsymbol{ds}} \qquad \textit{Eqn. 2.3}$$

where $\boldsymbol{ds}$ is a line element along the path of the ray.

The projection of the ray at angle ϕ and offset ρ is defined as:

$$\boldsymbol{P}(\rho,\varphi) = -\ln \frac{\boldsymbol{I}(\rho,\varphi)}{\boldsymbol{I}_0} = \int \mu(\boldsymbol{x},\boldsymbol{y})\boldsymbol{ds} \qquad \textit{Eqn. 2.4}$$

This is the Radon transform which maps the function $\mu(\boldsymbol{x},\boldsymbol{y})$ to a function $\boldsymbol{P}(\rho,\varphi)$, where $\boldsymbol{P}(\rho,\varphi)$ is the line integral of $\mu(\boldsymbol{x},\boldsymbol{y})$ over the line defined by φ and ρ. Given an angle φ, the 1D Fourier transform along ρ equals the 2D Fourier transform of the object μ along the line in Fourier space defined by φ. The Radon transform is invertible and hence the reconstruction can be done using the inverse transform and the Fourier slice theorem. (An introduction to reconstruction algorithms is given in Chapter 9.)

Limitations of Conventional CT

The radiation dose is always a concern in conventional CT. For example, a conventional diagnostic chest CT imparts a radiation dose of *20-50 mGy* (Gray *Gy* is the SI unit of absorbed radiation dose of X-ray) to the breasts of an average-sized woman which is equivalent to taking *10-25* two view mammographic examinations [54].

Another limitation is the spatial resolution which is *150 to 400 μm*, a size too large for detecting microcalcifications.

For these reasons, breast CT has not to date been adopted for breast screening or indeed for regular breast imaging.

Dedicated Breast CT

Many researchers are still investigating different technologies on X-ray tubes and scanners, hoping to improve this imaging technique suitable for screening. An example is the dedicated breast CT system proposed by Boone et al. [25]:

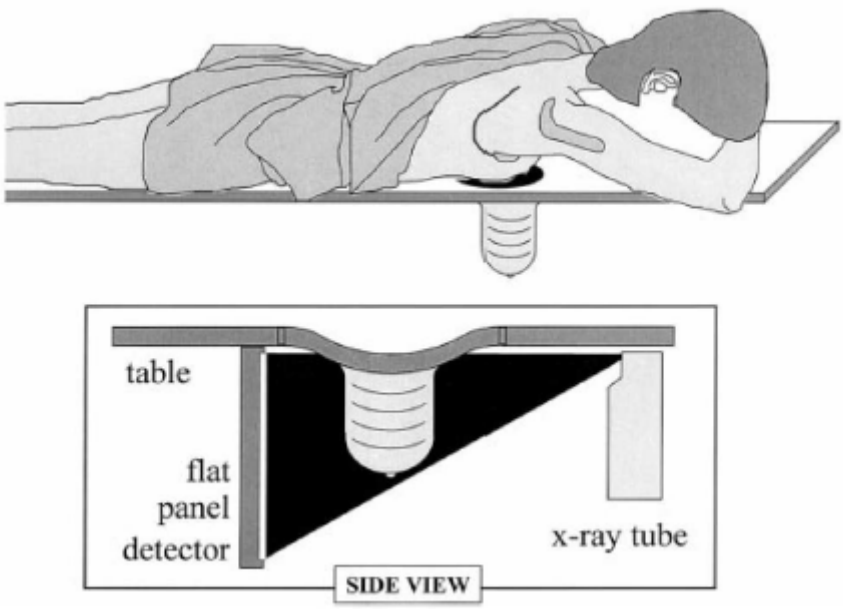

Figure 2.9: Drawings of a dedicated CT system proposed by Boone et al. (Extracted from [25].)

As reported by the authors, the design prevents the unnecessary exposure of tissues in the thoracic cavity and breast compression is not required. Also, the dose levels are claimed to be comparable to mammography. In their recent paper in IWDM *2010* [55], they performed a computer modeling of mass lesions (but not microcalcifications) synthetically added to *348* breast CT cases obtained from patient volunteers in a Phase II clinical trial. The breast image data is also projected to simulate mammographic projections. They then compared the performance using a pre-whitened matched filter model observer study. They claimed in the paper that "tomographic imaging of the breast may lead to better cancer detection rates for smaller and earlier cancers".

Dedicated breast CT may be promising. However, there remains a question about microcalcification detection, as said by Boone in *2008* [56], "We feel the breast CT was superior to traditional mammography for mass lesions, but mammography remains superior over breast CT for microcalcifications."

To conclude about dedicated breast CT, the comments by Boone are borrowed, "The role of breast CT is evolving and will depend on continuing research and how it bears out".

2.2 More on Mammography: Its Limitations

Despite the fact that mammography is the most widely used imaging methodology in today's breast screening programmes, a number of limitations exist in mammography. As discussed previously, two-dimensional mammograms cannot represent a complete picture of the three-dimensional breast. Tissue superimposition is a fundamental, intrinsic problem which will always limit the diagnostic information provided by mammography.

For example, the shape and spatial aspects of a microcalcification cluster can be greatly distorted by the angle at which it is viewed [57] so that a two dimensional projection does not exactly reflect the true picture of breast calcifications:

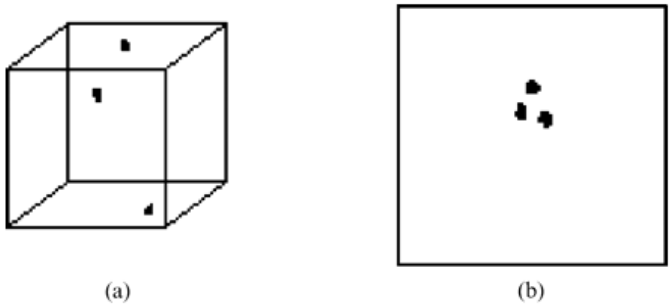

Figure 2.10: (a) 3D representation of 3 individual calcifications. (b) 2D projection of calcifications showing false clustering. (Extracted from [58].)

The morphology and distribution of breast calcifications are two of the most important clues for assessing the implications of microcalcifications for breast cancer. Such an image can easily lead to false-positives, and, more seriously, false-negatives.

In addition, women always feel uncomfortable having a mammogram. One reason is that the breast is squeezed and this generates pain. However, in order to keep the image quality for the detection of breast cancer but at the same time minimize the radiation dose, tight breast compression is necessary [59]. In terms of image quality, the tissue is spread out in a way that small abnormalities are less obscured by overlying breast tissue. In terms of radiation dose, the breast is now thinner which means less radiation dose is used.

Hence, with the advance in X-ray detectors and other technologies, a novel imaging method has been proposed: Digital Breast Tomosynthesis (DBT).

2.3 Digital Breast Tomosynthesis (DBT)

(Some of the materials covered in this section were obtained from the NHSBSP Publication No *69* on Digital Breast Tomosynthesis, September *2010* [28].)

2.3.1 Introduction

In DBT, instead of only taking CC and MLO views, the X-ray tube moves in an arc around the breast over a limited angular range e.g. in degrees, *-20* to *20*, producing multiple projections, typically *9* to *25*, with a few degrees difference between projections, while the total examination dose in DBT is similar to that in mammography. The following figure shows the principle of the acquisition of DBT projections:

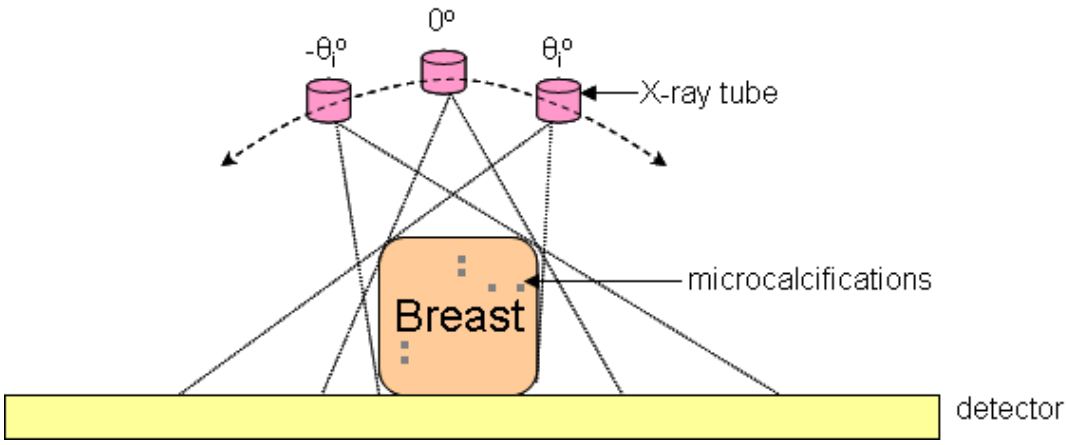

Figure 2.11: Principle of digital breast tomosynthesis acquisition.

These DBT projections are then reconstructed algorithmically to form a three-dimensional volume of the breast, for example in the form of a set of depth slices parallel to the detector plane. (Reconstruction algorithms will be reviewed in Chapter 9.) The in-plane (XY) spatial resolution is determined by the spatial resolution of the detector and the resolution in the third dimension (Z) is limited due to the limited angular range. A typical DBT reconstruction has *50-100* µm in-plane pixel size and *1* mm slice thickness. From [28], Dexela mentioned that their minimum reconstruction slice thickness is *0.5 mm*; while all Hologic, Sectra, Siemens and XCounter are *1 mm*; and GE is confidential. The optimal slice thickness is *1 mm* for Dexela, Hologic and Siemens.

2.3.2 DBT Acquisition Systems

Similar to a typical digital mammographic system, a DBT acquisition system also consists of an X-ray tube, compression plate, automatic exposure control and an image detector, except that the anti-scatter grid may not be used after the considerations of the radiation dose with a DBT projection geometry [60].

Currently, there are *4* main manufacturers researching and developing DBT acquisition systems and related technologies: GE, Hologic, IMS and Siemens. Some of the DBT systems are illustrated as follows:

Figure 2.12: Senographe Essential by GE (Top Left) [61]; Selenia Dimensions by Hologic (Top Right) [62]; Giotto by IMS (Bottom Left) [63]; MAMMOMAT Inspiration by Siemens (Bottom Right) [64].

In February, *2011*, Hologic's Selenia Dimensions was given approval by the U. S. Food and Drug Administration (FDA). This is a major step towards the possible future widespread take-up of DBT technology.

2.3.3 Technical Features of DBT Systems

(a) Geometry

To generate multiple projections, there are, in general, two different geometrical configurations of the acquisition system: (a) systems that use a completely isocentric motion; and (b) systems that use a partial isocentric motion. In the first of these, the X-ray tube and the detector rotate about the same axis. In the second case, only the X-ray tube rotates and the detector remains stationary:

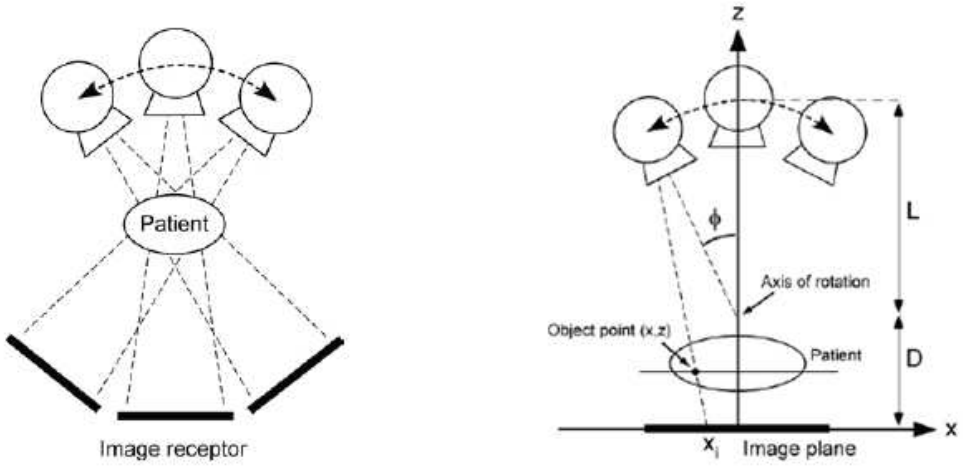

Figure 2.13: Complete isocentric motion (Left); Partial isocentric motion (Right). (Extracted from [28].)

The geometrical configuration varies considerably between manufacturers, e.g. For IMS and Hologic (as it appears from published information), their systems adopt the method of partial isocentric motion, whereas Siemens uses the complete isocentric motion.

The epipolar analysis developed later in the thesis can be applied to either configuration. Common to both is the planar motion of the projector, irrespective of whether or not the detector moves. We have chosen to illustrate our method with the partial isocentric configuration. More details will be discussed in Chapter 6.

(b) Radiation Dose

In DBT, the total radiation dose is the sum of the doses for each of the projections [65, 66]. This should be comparable to the dose used in DM. From the report by NHS [28], the mean glandular breast radiation dose ranges from *1* to *2.5* mGy which is similar to that in DM. This also fulfills the average requirements of American College of Radiology which recommends that the mean glandular dose to a breast that is *4.2* cm thick and composed of *50%* fat and *50%* glandular tissue should not exceed *3* mGy [5].

However, since there are more projections in DBT, it is to be expected that the image quality will deteriorate due to the lower dose in each projection. The challenge has been met by minimizing noise in the images by advancing the technology of X-ray detectors and X-ray tube which are to be discussed shortly.

(c) X-ray Detector

The main requirements of a suitable DBT detector are that the detector should have a large imaging area, a rapid readout rate and a high detector quantum efficiency (DQE) which is a measure of the combined effects of the signal and noise performance of an imaging system. Flat panel detectors fulfill all of these requirements. Two of the major developers are Dexela and Anrad and their detectors are shown as follows:

Figure 2.14: Detectors by Dexela (Left)[67] and Anrad (Right) [68].

The detector type varies between different manufacturers e.g. the Dexela one is based on CMOS technology while the Anrad one is amorphous Selenium-based. The detector size is approximately *24* cm * *30* cm and the detector pixel size which is the image resolution is *50-100* µm.

(d) X-ray Tube (Anode/Filter Materials)

Until recently, the target/filter materials were primarily molybdenum (Mo). In recent years, other materials giving high energy spectra such as rhodium (Rh) or tungsten (W) as target, and rhodium (Rh) or aluminium (Al) or silver (Ag) as filters have been introduced. With such a change, X-rays become more penetrating. This can lead to a lower breast dose, while at the same time a greater photon flux can reach the imaging detector which produces a better signal to noise ratio, as the relative amount of quantum noise in the image is reduced.

2.3.4 Advantages of DBT

(a) Solving the superimposition problem

The key attribute of DBT is to facilitate the visibility of malignant lesions which may be hidden in the 2D mammographic image (false negative cases) or to reduce the ambiguous but normal cases (false positive cases). As a 3D modality, DBT can reduce the tissue overlap problem encountered in 2D mammography and hopefully improve the accuracy of diagnosis of breast cancer.

Clinical examples have shown that DBT can help solve the false-positive and false-negative issues found in mammography:

(a) (b)

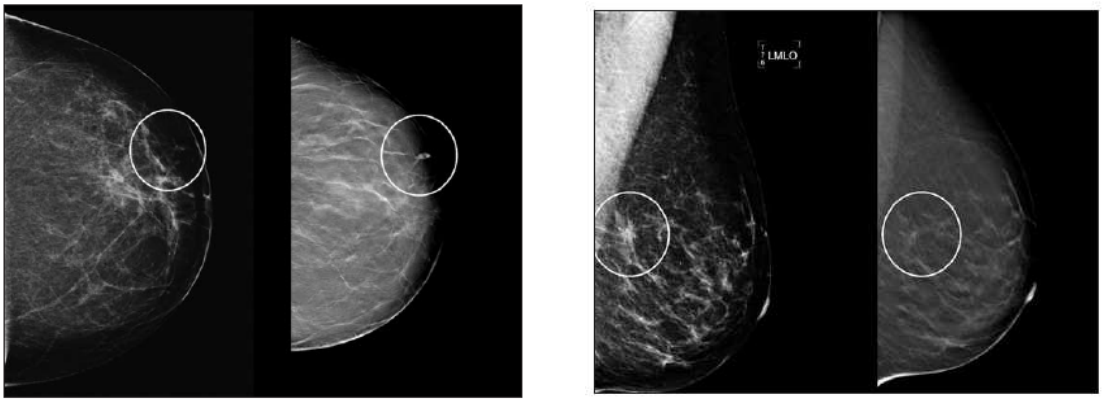

Figure 2.15: Clinical examples. (a) Tubulolobular adenocarcinoma not seen well in digital mammogram (Left) is shown much better in the DBT slice (Right); (b) Suspicious areas in DM can be resolved with DBT. (Extracted from [69].)

(b) Minimal breast compression force

In DBT, tight breast compression is not necessary because the breast can be reconstructed to 3D. Instead, breast compression is used to minimize blurring of the image caused by motion. Some researchers are working on pilot studies to assess how reduction in compression can affect dose and image quality. Having said that, it is hoped that less compression can be applied and hence less pain will be caused in future breast screening but at the same time providing a more accurate result.

(c) Similar acquisition systems as digital mammography

Most existing 2D mammographic systems can be upgraded to have DBT capability [28]. For example, Hologic's Selenia Dimensions shares the same imaging chain as Selenia digital mammographic system [70]. The selenium detector, tungsten X-ray tube with

rhodium and silver filtration are a direct conversion from the DM system. It means that hospitals can upgrade their existing DM systems to DBT easily.

2.3.5 Challenges Encountered by DBT

(a) Null-space problem in reconstruction

Unlike CT which images the breast over 360^o, DBT views are only captured over a limited angular range. It can be imagined that data is insufficient causing certain uncertainties in the reconstruction, which is called the null-space problem (the null-space problem will be discussed in Chapter 9.). Of course, there exists some work-around in the reconstruction algorithms, e.g. regularization, by adding more constraints and using Bayesian models. However, the null-space problem is intrinsic to the design of DBT. Continuing research may at most improve the reconstruction outcomes. As reported by the thesis of Dominique Van de Sompel [71] who worked intensively on DBT reconstruction algorithms, "Reconstructions in undersampled tomography are strongly influenced by the particular Bayesian model used. The problem resides in the fact that inaccuracies in the model may not or only weakly be countered by the projection data." Even for the work-around, a lot of effort is still required to investigate the robustness of constraints on the reconstruction solutions.

(b) Processing time by both computers and radiologists

In DBT, multiple projections are generated instead of two. It can be imagined that it is more demanding for the acquisition systems. For example, the read-out rate of detectors must be improved. Many detector manufacturers have put a lot of effort in to solve this problem. Also, the processing time for reconstruction and display needs to be shortened, which can be as long as *2* minutes for machines developed by Dexela Ltd. as reported in [28].

For radiologists, instead of viewing two X-ray images for each case, they will need to look at more slices which may comprise, say, *80* slices for a case. It is hoped that the additional workload can be balanced by fewer unnecessary recalls and biopsies. More research is required to improve the workflow and training is necessary for the radiologists to adapt to the new technology, when compared with the current workflow.

(c) Balance between dose and image quality

The image quality in each DBT projection is inevitably worse than in mammography. (More about the image quality and image noises will be discussed in Chapter 4.). As mentioned, the advance in technology has helped improve the situation. However, more research is required for better image quality.

(d) Availability of CAD for masses and calcifications

Reconstruction artefacts are unavoidable during reconstruction (More about DBT artefacts will be discussed in Chapter 4.). This may make tumour detection more difficult in some cases, e.g. microcalcifications. Evidently, there are new challenges in developing new computer-aided detection algorithms specifically for DBT. To date, apart from GE Healthcare, which claims to have a CAD system available, all other vendors do not yet provide CAD in DBT. In this thesis, we will address this issue, and hopefully, contribute a new approach in the development of a CAD system for DBT.

The various ongoing challenges posed by DBT explains why it has taken such a long time for manufacturers to obtain FDA approval after a research group at Massachusetts General Hospital came up with the DBT idea in mid-*1990*s, although DBT is definitely an improvement to mammography in terms of tissue overlapping issues.

2.3.6 Clinical Studies of Performance of DBT

To obtain FDA approval, one must go through a premarket approval (PMA) process, which requires clinical tests to assure safety and efficacy. For Hologic, the FDA reviewed results from two clinical studies in which board-certified radiologists were invited to review 2D and 3D images from more than *300* mammography examinations [72]. In both studies, a *7*% improvement was obtained if radiologists were reading both 2D and 3D images instead of only 2D ones.

In addition to these clinical results, there are numerous clinical studies of the performance of DBT which supports this new technology. For example, [73] considered *125* breast cases assessed by *8* experienced radiologists. It was found that combining both DM and DBT, there was a *30*% reduction in recalls for the false positive cases compared with the use of DM alone. Using DBT alone can also reduce

the recall rate by approximately *10*%. In [74], 100 single-breast cases were analyzed by 3 experienced radiologists, each of whom were given images of same breasts taken by both DBT and mammography. The results demonstrate DBT superiority for conspicuity of findings and showed potential for superior clinical performance.

2.3.7 Role of DBT: Primary Tool or Adjunct to Mammography

"The role of DBT as a primary screening and diagnostic tool or as an adjunct to conventional mammography has yet to be determined." [75]. It is unclear whether DBT will replace conventional mammography or will just be an adjunct to it, or whether some combination of these approaches will be employed. As mentioned in the last section, some literature suggests that using both DM and DBT may reduce recall rate more than DBT alone. Some studies suggest that DBT is superior to DM. As more DBT acquisition systems become commercialized and released in the market and more research and development are performed, the workflow in the real clinical environment of using DBT will be clearer in the future.

Chapter 3

Breast Abnormalities and Breast Calcifications

Early detection relies on searching for breast abnormalities such as masses, architectural distortion and microcalcifications, as they are possible signs of breast cancer. In this chapter, we first briefly present the former two abnormalities. Breast calcifications will then be given in more detail.

3.1 Masses

Masses are defined as a central space-occupying lesion with different densities. Their shapes and margins shown in mammograms help determine the benignancy and malignancy of the breast. For example, circumscribed oval and round masses are usually benign, such as cysts and fibroadenomas. Masses with irregular shapes and ill-defined or spiculated margins have a higher likelihood of malignancy. Some examples of masses in mammograms are shown in the following figures:

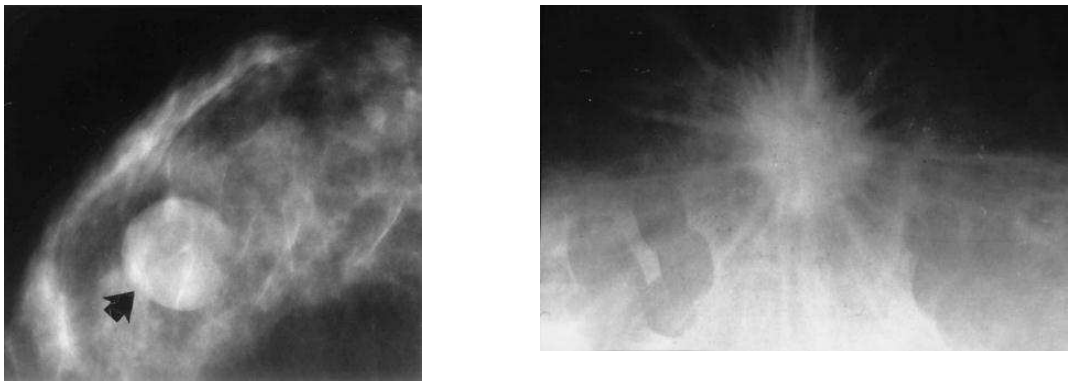

Figure 3.1: Left: Benign cyst, showing a round circumscribed mass; Right: Invasive ductal carcinoma, showing a mass with irregular shape and speculated margins. (Extracted from [76] .)

3.2 Architectural Distortion

Architectural distortion is defined as distortion of the normal breast parenchymal pattern with no definite mass visible. Spiculations are seen radiating from a point. It can be observed in benign conditions, such as radial scar and sclerosing adenosis, or in invasive breast carcinoma. An example of a subtle architectural distortion is shown as follows:

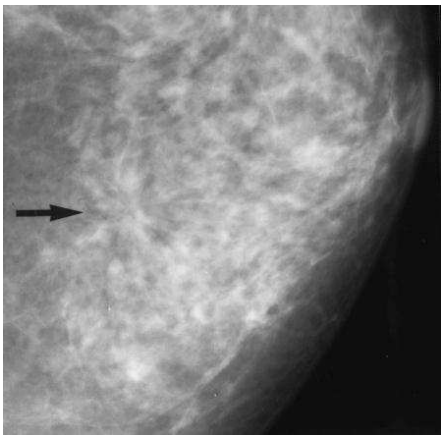

Figure 3.2: Invasive carcinoma presenting as a subtle architectural distortion. (Extracted from [76].)

3.3 Breast Calcifications

Breast calcifications are tiny calcium deposits, such as calcite, aragonite, calcium oxalate, apatite, in dried secretions and damaged cells with necrosis, within the breast [77]. Due to calcium's higher linear attenuation coefficient, the amount of X-ray radiation absorbed, in comparison to other breast tissues, such as adipose and glandular tissue, breast calcifications appear as small white regions on a mammogram (*Figure 3.3*).

Figure 3.3: Breast calcifications (Extracted from [78].)

3.3.1 Types of Breast Calcifications

There are several ways to classify breast calcifications: size in the mammogram [79, 80], type of breast disease, or chemical composition:

(a) Size in the mammogram

According to their size, we classify them either as macrocalcifications or microcalcifications.

Macrocalcifications:

These are larger and coarser calcium deposits and appear as large white regions with size > *500 μm*. In almost all cases, macrocalcifications are benign.

Microcalcifications:

These are smaller in size. Any white region which is < 500μm is called a microcalcification. Microcalcifications may appear individually or scattered in a mammogram, or they can appear as clusters. Microcalcifications can be benign, indeterminate or malignant. Since the early stages of breast cancer are often signalled by the occurrence of microcalcifications, their detection and analysis has been considered to be very important and the analysis of breast calcifications always refers to microcalcifications.

(b) Breast disease

In terms of breast disease, calcifications can generally be classified into benign and malignant. However, some calcifications are indeterminate and may be found in cancer precursor lesions. Radiologically, the morphology of individual regions and the distribution of breast calcifications are used as the fundamental assessment criteria in classification [81]. Typically, benign calcifications are coarse and round shape; while malignant ones are linear and branching. The topic on microcalcification classification will be covered in Chapter 10.

The following shows some occurrences of calcifications in breast disease:

Benign

Benign calcifications are caused by benign breast diseases (obtained from [80]):

(i) Fibrocystic changes leading to benign cysts. Calcium deposits are found within the fluid of these cysts;
(ii) Fibroadenoma (a benign lump in the breast);
(iii) Sclerosing adenosis (excessive growth of tissues in the breast's lobules).
(iv) Previous injury in the breast area forming post-traumatic fat necrosis calcification
(v) Dilated milk duct;
(vi) Inflammation due to infection or mastitis;
(vii) Dermatitis or residue from metallic particles in powders, ointments and deodorants forming skin (dermal) calcifications;
(viii) Radiation therapy for breast cancer;
(ix) Arteries containing calcium deposits called vascular calcifications;

Malignant

Calcifications found in malignant lesions, specifically DCIS and invasive cancer.

Indeterminate

Some calcifications are found in cancer precursor lesions such as LCIS.

(c) Chemical composition

In terms of chemical composition, microcalcifications often occur as one of two basic types: Type I: calcium oxalate (dihydrate) and Type II: calcium hydroxyapatite [82-84]. Two papers [82, 83] suggest that Type I appears to be found in benign lesions while Type II can be found in both malignant and benign lesions.

Type I: Calcium Oxalate (Dihydrate)

"Type I microcalcifications were found only in benign cysts and were not associated with carcinoma or epithelial hyperplasia." [82]. "The presence of oxalate-type microcalcification appears to be a reliable criterion in favor of the benign nature of the lesion or, at most, of a lobular carcinoma in situ." [83].

Type II: Calcium Hydroxyaptite

"Type II microcalcifications were associated with benign or malignant lesions." [82]. "Calcium hydroxyapatite (HA) crystals are associated with both benign and malignant breast tumors." [83].

3.3.2 Formation of Benign Breast Calcifications

Benign breast calcifications can be caused by the death of fat cells or due to secretion by the lobules [85].

Some benign calcifications develop because fat cells in the breast die after injury, for example caused by surgery, trauma or infection. Alternatively, the breast may be exposed to radiation. In other cases, a benign cyst may be formed. After the fat cells die, fatty acid will then be released and combine with calcium in the breast, forming benign calcifications.

Calcifications can also be found in the glandular tissue where milk is produced and in the milk ducts to the nipple. The lobules may secrete small amounts of calcium-containing fluid which may be crystallized, forming calcifications.

3.3.3 A Deeper Look at the Causes of Breast Calcifications in Breast Cancer

In this section, we further explore the causes of breast calcifications in breast cancer. Interested readers are suggested to refer to other references if they would like to understand it more biologically.

(a) Breast cancer cells secrete parathyroid hormone-related protein occasionally.

To start with, calcification, in general, is the accumulation of calcium salts in soft tissue. It is found that breast cancer cells sometimes secrete a parathyroid hormone-related protein (or PTHrP) [86]. From [87], PTHrP can be found in about *60%* of breast cancer tumours. Normally, PTHrP facilitates the development and maintenance of normal mammary gland [88]. In the case of breast cancer, the breast tumour secretes this hormone which circulates in the blood causing the bones to release calcium [89]. The blood calcium is then increased. Hence, when excessive calcium accumulates in the breast, it forms breast calcifications, which can be an indication of

breast cancer. (For interest, [90] suggests that "controlling PTHrP production in breast cancer may be useful therapeutically".)

(b) Death of the cancer cells

A paper by Harvard Medical School [85] presented several reasons for the connection between calcifications and breast cancer.

In DCIS, a calcified line along the duct will remain if the cancer cells die when these cells do not receive sufficient nutrients and blood. Calcifications can also be found with invasive cancer in areas where cancer cells have died or in damaged connective tissues between cancer cells.

3.3.4 Some Examples of Calcifications in Mammograms

The following figures show an example of one of each benign and malignant case:

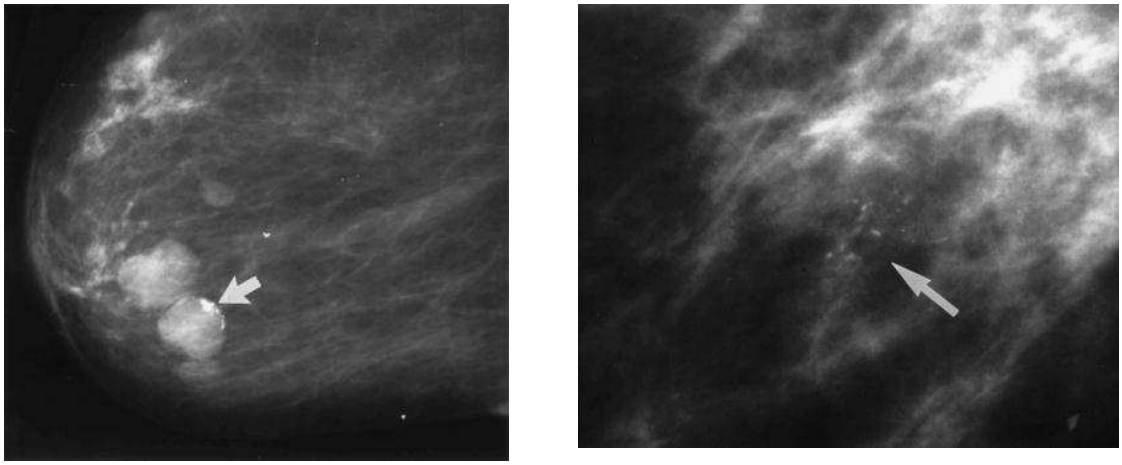

Figure 3.4: Left: Coarse calcification (arrow) on the rim of a fibrodenoma; Right: The fine, linear and branching calcifications (arrow) are highly suspicious of intraductal carcinoma. Biopsy revealed comedocarcinoma with calcification of necrotic debris in the center of tumor-filled duct. (Extracted from [76].)

3.3.5 Microcalcification Detection in Mammograms

The microcalcification detection task, no matter by radiologists or computer programs, is often difficult. In some cases, the true microcalcifications are sometimes hidden by the surrounding tissues (poor image contrast). In other cases, other white spots e.g. noise points appear in the mammogram and may be confused with microcalcifications. To better understand microcalcification detection, it is necessary to have some

knowledge of the image formation process of a mammogram and analyse the mammogram in details. The topic will be addressed in Chapter 4.

Chapter 4

X-ray Images: Formation and Analysis

In this chapter, a mathematical model of mammogram image formation [91] is first discussed. We explore the path that the X-ray photons follow. Next, we look at the outputs of mammography – the mammogram, discussing image quality and noise [92]. We will consider the situation in DBT as well.

4.1 X-ray Image Formation

4.1.1 Mammographic System: How is a digital mammogram formed?

A typical digital mammographic system consists of an X-ray tube, compression plate, anti-scatter grid, automatic exposure control and an image detector. A schematic representation of such a system can be referred to *Figure 2.1* in Chapter 2.

When a mammogram is performed, a beam of X-ray photons, which has a spectrum of energies that is characteristic of the tube voltage and anode material, is generated in the X-ray tube. This X-ray radiation is directed through a very small area called the focal spot. A filter is installed so that the low-energy photons, which contribute to patient exposure, but not to the image formation, are filtered out. The collimator is used to confine the X-rays to the area of interest. The breast is squeezed between two compression plates. The beam is directed through the compressed breast. Next, it passes through the anti-scatter grid which removes a proportion of the scattered radiation. This is important since scatter is a major degrading factor in image quality. The automatic exposure control in the system aims to control the amount of radiation reaching the image detector. Finally, the beam of photons arrives at the image detector which converts the photon energies to digital signals forming the digital mammogram.

4.1.2 Mammographic Imaging Process Model: The Path of the X-ray Photons

The subsections follow the path of the X-ray photons.

(i) From X-ray tube to breast

Incident radiation starts from the X-ray tube. As the electron beam hits the target material at the anode, X-ray photons with different energies are produced, forming a poly-energetic X-ray beam (a spectrum). Different tube voltages applied to different anode materials produce different energy spectrums.

The penetrative power of the photons depends on their energies, the material they pass through, and the thickness of the material. Lower energy photons can pass through relatively shorter distances. In order to avoid the patient being exposed to unnecessary radiation (i.e. the photons are absorbed by the tissue only, without any contribution to the image), a filter is used in the X-ray tube.

The average photon energy (in units of *keV*, kilo-electron Volts) can be controlled by adjusting the tube voltage which has units of *kVp* (peak of the waveform of the kilo-Voltages against time). In addition to the average photon energy, the number of photons is also a measure of the amount of X-radiation. Higher tube voltages produce higher photon output (per unit current and area) (in the unit of *photons/mA/mm*^{2}) and higher average photon energy. Higher tube currents (in units of *mA*, milli-Amperes) and longer exposure times produce more photons (in terms of overall radiation). With the tube voltage V_t, photon output $f(V_t)$ (photons per unit current and area) and tube current $I_t(V_t)$ (current per unit time) we can compute the photon flux $\phi(V_t, x, y)$ over the area corresponding to spatial position (x, y). The units of flux are photons per unit area per unit time:

$$\phi(V_t, x, y) = f(V_t) * I_t(V_t) \qquad \textit{Eqn. 4.1}$$

The incident radiation, i.e. the incident energy on a small area (A_p) of the compression plate (before entering the breast) at spatial position (x, y), with time of exposure (t_s), is the summation over the energy (ε) the photons possess, over the given area and the exposure time. Mathematically:

$$E_0^{plate}(x, y) = \phi(V_t, x, y) A_p t_s \int_0^{\varepsilon_{\max}} N_0^{rel}(V_t, \varepsilon) \varepsilon d\varepsilon \qquad \textit{Eqn. 4.2}$$

where we use $N_0^{rel}(V_t, \varepsilon)$ to represent the number of photons per unit energy at energy ε relative to the total number of photons in the incident spectrum and $\varepsilon_{\max}$ is the maximum energy a photon can acquire.

Then, the X-ray photons pass through the compression plate where some are absorbed. The number absorbed is related to the plate's thickness h_{plate} and its linear attenuation coefficient at each energy level $\mu_{plate}(\varepsilon)$. By Beer's law,

$$\begin{aligned} &\textit{Number of exiting photons} \\ &= \textit{Number of incident photons} * e^{-h_{plate}\,\mu_{plate}(\varepsilon)} \end{aligned} \qquad \textit{Eqn. 4.3}$$

We therefore have the total incident energy to the breast:

$$E_0^{breast}(x, y) = \phi(V_t, x, y) A_p t_s \int_0^{\varepsilon_{\max}} N_0^{rel}(V_t, \varepsilon) \varepsilon e^{-h_{plate}\mu_{plate}(\varepsilon)} d\varepsilon \qquad \textit{Eqn. 4.4}$$

(ii) Through the breast

It is of great interest how the photons travel through the breast. Recall from the Breast Anatomy section that a normal breast consists of different tissue types: fibrous, glandular and adipose (fat) tissues, and sometimes, but rarely, calcification. The penetration of the photons is different for different tissues. For photons having the same energy, they are "attenuated" much more by calcification than adipose tissue. Quantitatively, we use the linear attenuation coefficient μ to represent the attenuation of different tissues at a particular energy level. The larger the value of the linear attenuation coefficient of the tissue, the more the photons are attenuated when they pass through that tissue. An example of the linear attenuation coefficient of different tissue types at different photon energies is shown in the following table:

Tissue Type	***μ(cm^{-1}) at photon energy (keV)***		
	18	***20***	***25***
Adipose	*0.558*	*0.456*	*0.322*
Fibrous	*1.028*	*0.802*	*0.506*
Cancerous (Infiltrating duct carcinoma)	*1.085*	*0.844*	*0.529*
Calcification	*26.1*	*19.3*	*10.8*

Table 4.1: Linear attenuation coefficient of different tissue types at different photon energies (Figures obtained from [91].)

From the Table, it is evident that at higher photon energies, the linear attenuation coefficient decreases for all materials. We can also see that calcification has the highest

linear attenuation coefficient regardless of the photon energy. For *18 keV*, the linear attenuation coefficient is approximately *26* times higher than that of fibrous tissue and even much higher than that of adipose tissue. It is this behaviour of calcium that enables us to detect calcifications in mammograms. This leads to the bright spots seen in images and detection algorithms are developed from this. Detection will be discussed in more detail in later chapters.

By applying Beer's law again, we can obtain the radiation of the primary beam leaving the breast:

$$E_0^{exit(breast)}(x,y) = \phi(V_t,x,y)A_p t_s \int_0^{\varepsilon_{\max}} N_0^{rel}(V_t,\varepsilon)\varepsilon e^{-h_{plate}\mu_{plate}(\varepsilon)} e^{-h\mu(\varepsilon)} d\varepsilon \qquad \textit{Eqn. 4.5}$$

where $h\mu(\varepsilon)$ is the photons being attenuated at energy ε with linear attenuation coefficient $\mu(\varepsilon)$, by passing through the breast with thickness *h*.

Note that in *Eqn. 4.5*, we show only the primary beam. In reality, there are other components namely scattered radiation (photons which do not follow the original direction they should have) and extra-focal radiation (photons that "leak" away from the focal spot), making up the signal exiting the breast. (Readers may refer to [91] for further discussion of these components.) All these components contribute to the intensity observed in the mammogram.

(iii) Reaching the image detector

Finally, the photons arrive at the image detector, which converts the energy to a digital signal and sends this digital signal to the output device. Different detector materials have different sensitivities to different photons energies. It is pointed out in [93] that Caesium Iodide has poor absorption at higher energies and Selenium is a better choice. The different amount of absorption of photons energies at different location of the detector gives rise to the difference in the intensity in the images.

4.2 Analysis of X-ray Images

4.2.1 Appearance of a Mammogram

Now, a mammogram is formed after the journey of the X-ray photons. In a mammogram, the brighter region, on a greyscale (as opposed to the region in black

colour) shows the region of interest, i.e. the breast: adipose tissue appears to be darker while denser, fibrous and glandular tissues appear to be lighter. The pectoral muscle is shown if the mammogram is taken in the MLO view. The following figure shows a typical mammogram at MLO view:

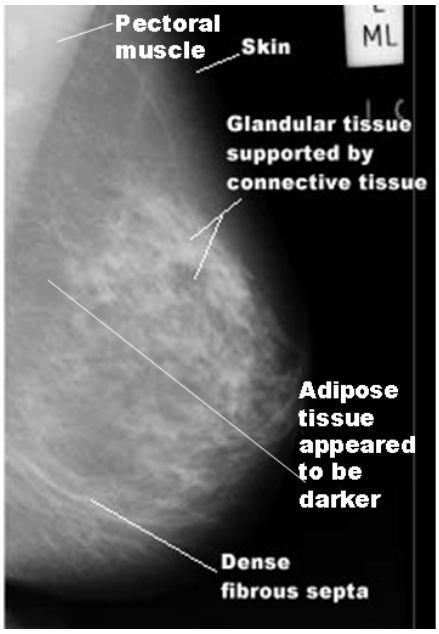

Figure 4.1: A typical mammogram in MLO view. (Extracted from [94].)

There exist individual variations in terms of radiographic appearance. This is caused by the differences in the relative amounts and X-ray attenuation characteristics of adipose and connective tissue [95] – breast density or breast composition.

4.2.2 Breast Density

Breast density is related to the features of the breast tissue as seen from a mammogram [96]. On a mammogram, due to differences in X-ray attenuation, the fibroglandular tissues of the breast appear as shades of gray to white, while adipose tissue appears much darker. The difference in visual appearance caused by these different tissue compositions in a breast has been classified both qualitatively and quantitatively as a way to describe breast density [96]. Classification schemes have been proposed for breast density. One such is the American College of Radiology (ACR) Breast Imaging Reporting and Data System (BI-RADS). Depending of the breast appearance (which is measured by the percentage of the breast that appears dense – the "amount" of glandular tissues in the breast; a review of the measurement of mammographic density can be found in [97].), the breast is classified into four types: Type *1* (*<25%*) Breast is almost

entirely fat; Type *2* (*25-50*%) There are scattered fibroglandular densities; Type *3* (*50-75*%) Breast is heterogeneously dense; Type *4* (*>75*%) Breast is extremely dense. The following figure shows an example mammogram of each of these *4* types:

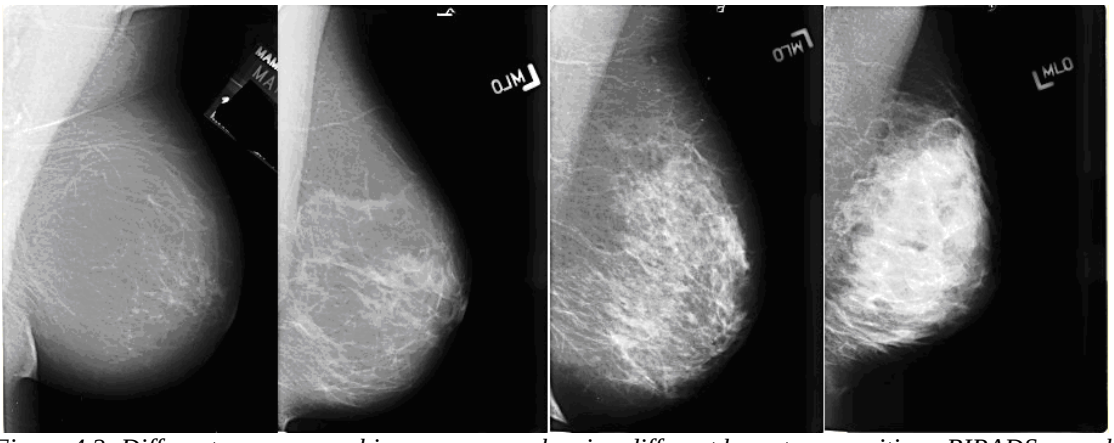

Figure 4.2: Different mammographic appearance showing different breast composition. BIRADS overall breast density categories 1-4 from left to right. (Extracted from [98].)

Breast density is an important topic in breast cancer research. Studies e.g. [99] show that breast density is strongly associated with the risk of developing breast cancer. As regards our research, the consequences of different mammographic appearance from different breast composition, forming different backgrounds, has a major impact on microcalcification detection and this will be discussed in later chapters.

4.2.3 Mammographic Image Quality Against Radiation Dose: Image Contrast and Image Noise

There are other factors that affect the appearance of a mammogram, better images making detection tasks simpler. In the following, we discuss some other factors affecting the image quality, which unfortunately is related to the radiation dose that is detrimental to the patients' health.

(i) Image Contrast [92]

The quality of a medical image often refers to how clear, how distinctive, how much detail of the object we can see. This is often reflected in the image contrast, which is represented by local differences in image intensities. An object within the body will be visible if it has sufficient contrast relative to the surrounding tissue. Contrast exists because different materials have different physical or chemical properties (e.g. physical

density and effective atomic number). The fact that different materials absorb different amounts of radiation, together with the differences in the thicknesses of the materials that the photons pass through, results in the different intensities in the image. In addition, the contrast we see in an image depends on the quality and the quantity of the image spectrum generated by the X-ray tube (which may further depend on the breast thickness being imaged), which are determined by the choice of the anode and filter materials; the tube voltage; the current supplied; and the exposure time. In [100], Dance et al. conducted a study of the influence of anode/filter material and tube potential on contrast, signal-to-noise ratio (SNR) and average absorbed dose in mammography. They found that, in digital mammography, the standard Molybdenum/Molybdenum combination is superior for *2 cm* breasts, yielding the lowest dose for a given SNR at a tube voltage of *28 kV*. For other breast thicknesses, other combinations of anode/filter and tube voltage may be more suitable.

Please refer to *Table 4.1* on the linear attenuation coefficients of different tissue types at different photon energies. It is found that the difference between the attenuation coefficients of the breast tissues rises with lower energy and thus there is a greater difference in the X-ray signal exiting the breast when a lower energy beam is used, leading to more contrast in the image. It seems that we should generate a spectrum with low photon energy. Nevertheless, we also need to consider another very important factor – dose to the patients. Dose refers to the amount of radiation absorbed by the patients. The lower the dose, the fewer detrimental effects are caused to a patient. At very low energies, the contrast is high, but the penetration ability of the photons is low, resulting in a higher dose to the patients. On the other hand, the penetration ability is higher for photons with higher energies. This reduces the dose but also the contrast. Hence, we always need to strike a balance between contrast and dose. The optimum spectrum between contrast sensitivity and radiation dose for an average size breast is one with most of the radiation with photon energies below about *20* keV [92].

(ii) Image Noise [92]

Image noise reduces image quality and this makes detection tasks more difficult. Understanding noise generated in mammography is crucial to design a good detection

algorithm. Many studies [101-103] have applied a noise model in the design of CAD algorithms in mammography and DBT. (We will discuss these algorithms in later chapters.) So, what is noise and what causes it? Noise is a random signal that can hide the signal that provides the useful information.

(a) Quantum noise

In the imaging process of generating X-ray photons, the photons are distributed in a random manner within the image. The following figure illustrates the concept:

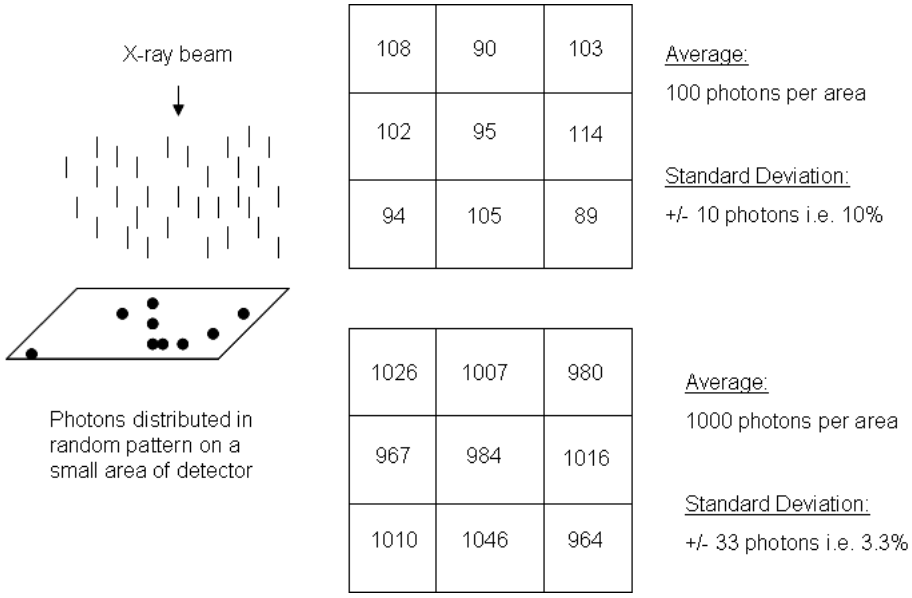

Figure 4.3: The Concept of Quantum Noise. (Redrawn from [92].)

Although the average number of photons is fixed, the actual number of photons varies randomly at different locations. These randomly distributed photons cause some unpredicted differences in image contrast and thus affect the image quality. It is also shown in the figure that the larger the average number of photons (meaning higher exposure), the smaller the standard deviation at each location. Hence, this reduces the quantum noise. However, since dose is an important factor which we need to consider, we therefore need to find an optimal trade-off between the image quality and the dose absorbed by the patients.

(b) Electronic Noise

The electronic noise is in the form of random electrical currents produced by thermal activity within the device. In digital mammography, the electronic noise may be generated when the radiation is converted to electronic signals.

(c) Structure Noise (Tissue Noise)

Structure noise refers to the tissue overlap in the mammograms. In mammography, only *2* images are obtained. This may obscure some important information in the breast. In DBT, it is expected that the structure noise will be reduced as 3D slices are generated which can reduce the tissue overlap. However, out-of-plane artifacts are still found in the slices in DBT due to reconstruction. (Further discussion on DBT related to image quality, contrast and noise will be found in the next section.) An example of structure noise in mammography and the tissue overlap being reduced in DBT is shown in the following figure:

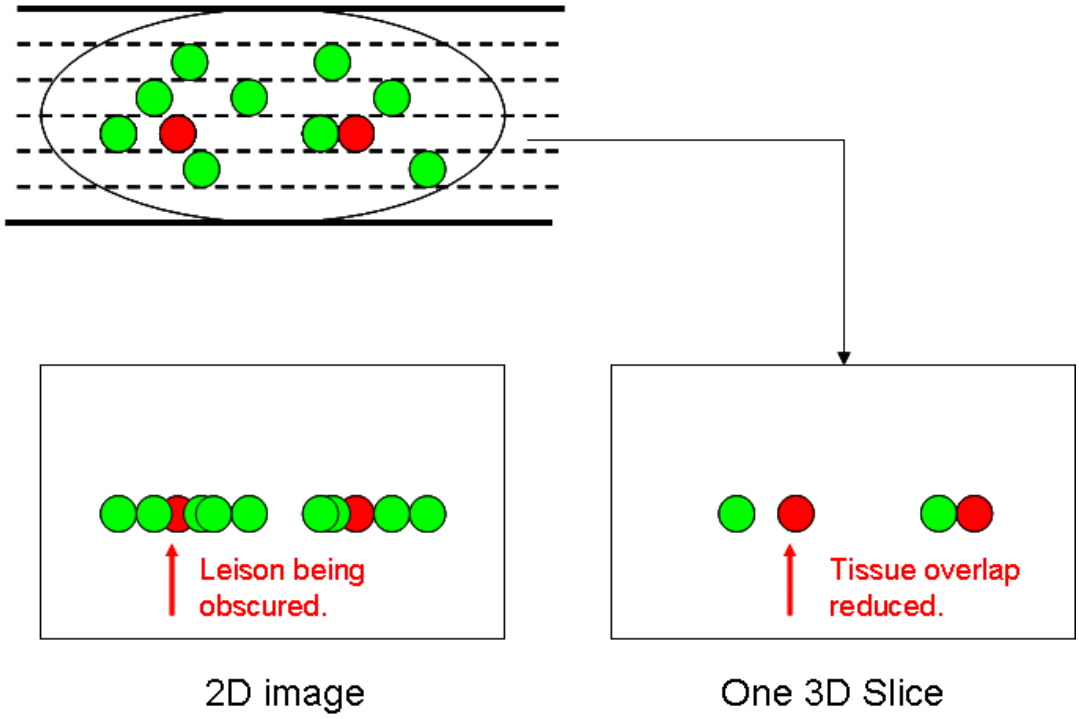

Figure 4.4: Structure Noise. (Modified from [104].)

4.2.4 Digital Breast Tomosynthesis

We now look at the situation in DBT. The fundamental principles of X-ray image formation in DBT are the same as in digital mammography. Regarding image quality, DBT can reduce tissue overlap when viewing from a corresponding slice, as pointed out previously in the context of structure noise. This improves cancer detection. Nevertheless, there are a number of noise issues which require attention in DBT. Two dimensions are taken into consideration: the projections generated during acquisition

and the slices produced after reconstruction. Now, each projection is formed using, for example, about one-sixth of the dose as that in the mammogram (consider *13* exposures for DBT and *2* for DM), so that the total examination dose used is similar in these two modalities. It is expected that the quantum noise will be greater in DBT (Refer to *Figure 4.3* that standard deviation of photons distribution is larger for smaller amount of dose). When designing a good detection algorithm for DBT based on projection images, this factor must be considered. There exist certain artifacts ("tomosynthesis noise") which are found in DBT only but not in mammography, since slices are generated in DBT but not mammography. It is found that some low-contrast shadows of a high-contrast object are seen in the planes outside the plane of interest. Out-of-plane artifacts in slices can be explained by the following simple reconstruction idea and figures extracted from A. Smith's paper [105]:

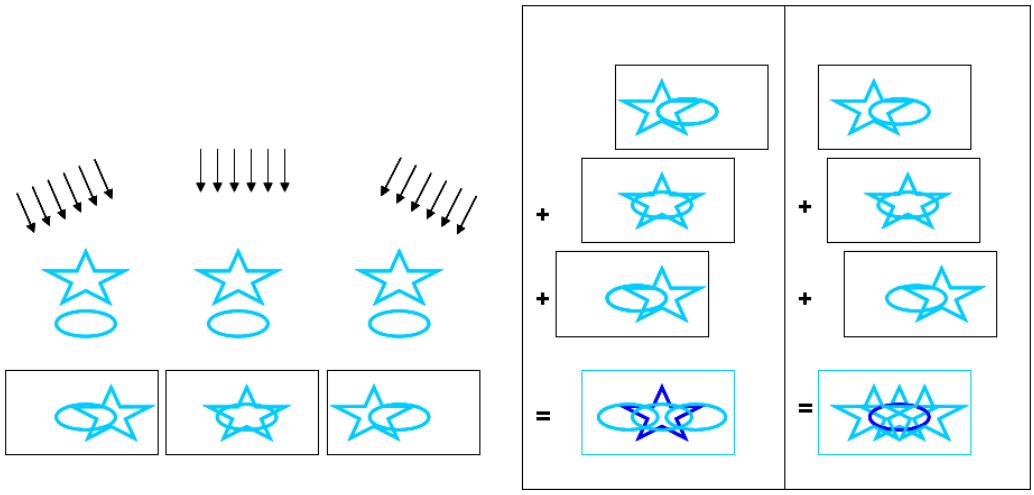

Figure 4.5: Three projections acquired from different angles (Left). Two slices are formed after reconstruction (by shifting and adding the projections). The object is more visible in the plane of interest while object at other height is blurred, causing the out-of-plane artifacts(Right). (Modified from [105].)

As seen from the figure, the circle object is blurred in the slice when the star object is clearly displayed and vice versa. The following figure shows this out-of-plane artifacts found in real reconstructed slices [33]:

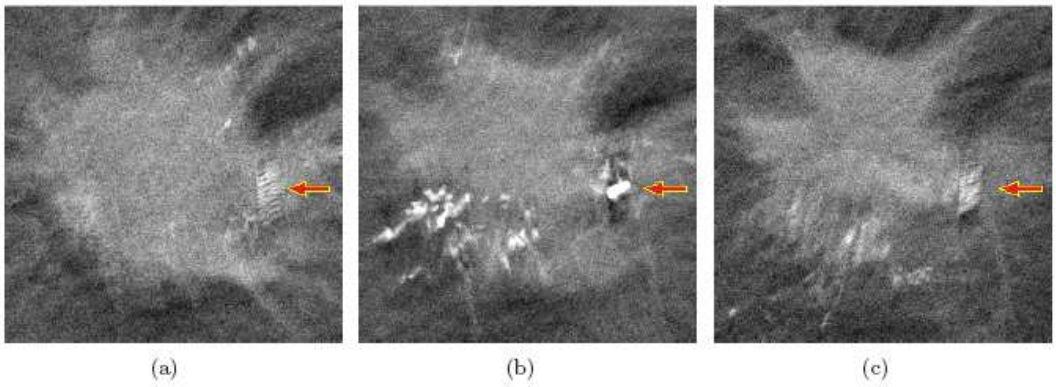

Figure 4.6: Out-of-plane artifacts. (b) Plane of interest with the object (red arrow); (a) and (c) Slices that are located 4mm below and above the plane of interest respectively. (Extracted from [33].)

From the figure, some low-contrast shadows are formed in other out-of-plane slices. Some reconstruction algorithms may result in fewer out-of-plane artifacts. Nevertheless, such noise should be catered for when designing a good detection algorithm based on reconstructed slices. We will briefly introduce a method by Badea et al. [103] for noise removal in DBT in Chapter 6 when the microcalcification detection algorithms in DBT is presented.

Chapter 5

Datasets: Simulations, Phantoms, Real DBT Datasets

In this thesis, we have experimented with a range of datasets to develop and test our ideas.

We begin with software-generated X-ray projections generated by a simulation model. It is common in the medical imaging research community to develop simulation models. One reason is that the availability of real datasets with confirmed lesions is always limited e.g. because only a small percentage (*0.8*% -- *14,166* cases of cancer diagnosed when *1.8* million women aged *45* and over were screened in *2008-2009*) of cancer cases in the mammography screening population [106], or due to privacy issues. Another reason is that the methods and algorithms developed can be evaluated more accurately using simulation models. In Section 5.1, a review of different simulation models with breast microcalcifications is first discussed. Some models generate microcalcification clusters on the basis of real statistics from mammograms and superimpose the clustered microcalcifications on a mammographic background [107, 108]. The mammograms generated by these models look very similar to real ones, but we cannot adopt such models, partly because there is not yet sufficient data for reasonable statistical analysis. Other models [109, 110] use algorithmic and software approaches to simulate a 3D breast with microcalcifications and produce synthetic mammograms. One 3D model [109] is very comprehensive and nearly fulfilled our requirements. Unfortunately, it is too complex and may not be flexible enough in some cases which, e.g. we may simply want a very simple background; and the microcalcification locations are randomly sampled in the current software version; but what we need is a more flexible way in setting the 3D positions of microcalcifications. The second model [110] has its own merits but is unfortunately not applicable in our

case, because the simulation is simply placed on a real mammographic background, but we need the accurate 2D positions of microcalcifications on the projections taken at different angles. There are two other models [111, 112] which are more tailor-made to simulate DBT projections at different angles, but one [111] is too primitive while the other [112] generates images from a biopsy specimen in which we cannot have an accurate ground truth of 3D positions for our mathematical derivation and verification. We therefore developed our own simulation model to generate DBT projections containing clustered microcalcifications and this model will be presented in detail in Section 5.2. Our model helps ensure that the mathematics of the methods to be presented in Chapters 6, 9 and 10 is correct, and that the subsequent algorithms are correctly implemented. Certainly, the projections are far simpler than real mammograms; nevertheless, they enable the basic ideas to be communicated.

In Section 5.3, a phantom procured from CIRS [113] will be adopted. Our model can only simulate a breast containing equal amounts of adipose and fibroglandular tissues, which is sufficient for our derivation and development of the epipolar curves approach (Chapter 6), with the analysis of geometric accuracy of 3D positions of microcalcifications after reconstruction (Chapter 9), and for our feasibility study of the classification of microcalcification clusters (Chapter 10), but is not adequate to simulate a real breast. This phantom can be used to assess the detectability of various sized lesions within a tissue equivalent, complex and heterogeneous background. This helps our analysis in the microcalcification detection in individual projection to be discussed in Chapter 7.

Finally, a few real datasets, by courtesy of Dexela Limited, a partner in the TSB project which funded this research, will be introduced in Section 5.4, although, of course, the ground truth is not (in general) available. As a first taste, these real datasets have been applied to demonstrate our concepts developed throughout Chapters 6-10, and provide some promising initial results of applying our proposed detection and reconstruction algorithms in reality.

5.1 Literature Review

In this section, several simulation models for clustered calcifications will be reviewed. Most of the models discussed are designed for mammography, so some are limited to

two-dimensions [107, 108] (Section 5.1.1), though there are some three-dimensional models [109, 110] (Section 5.1.2). Then, we review a prototype which generates simulated DBT projections without the use of X-rays directly for DBT analysis, with the use of a phantom of clustered microcalcifications [111] (Section 5.1.3). Finally, a recently developed simulation model of microcalcifications in breast tomosynthesis by Shaheen et al. [112] (Section 5.1.4) is presented.

5.1.1 Two-dimensional Simulation Models

(a) A simulation model of clustered breast microcalcifications

The simulation model developed by Lefebvre et al. [107] is a mathematical model in which all the parameters are randomly sampled using distribution laws determined from a statistical analysis of *408* real clusters containing a total of *8,611* microcalcifications. *10* parameters are required, relating to: (a) the global features of the cluster; (b) the features of individual microcalcifications; and (c) the gray level values of the individual microcalcification. Some of the parameters include: n, the number of microcalcifications within the cluster (a global feature parameter); m_a, the mean area of the microcalcifications within the cluster (a size parameter for an individual microcalcification); σ_c, the standard deviation of the contrast of the microcalcifications within the cluster (a contrast parameter for the assignment of the gray level values to the individual microcalcification). Statistical analysis is performed on the raw data (*408* clusters, *8,611* microclcifications). They computed the mean, standard deviation, skewness, kurtosis, and minimum and maximum values of each parameter. For example, the mean and the standard deviation of the mean area of the microcalcifications within the cluster, i.e. the parameter m_a, is *17.5* and *5.7* respectively. Then, statistical methods are used for the simulation. A graphical display of the distributions of the observations led them to use three statistical distributions, namely, Gaussian, logarithm of a Gaussian, and a gamma distribution. For example, for the parameter m_a, they assumed a logarithm of Gaussian probability distribution. For each generation of a cluster, the *10* parameters are sampled using the distribution laws previously observed. Finally, the clusters are then superimposed on a normal mammographic background. The model was evaluated on a test set of *100*

mammograms with the help of two radiologists. The results did not reveal any statistically significant differences between the simulated and the real clusters.

The model enables the generation of simulated mammograms with microcalcification clusters that appear similar to those in real mammograms. This can be used as an initial evaluation of the detection accuracy of computerized methods. It is also useful in cases in which a large number of mammograms is required e.g. large scale testing in microcalcification detection algorithms. However, the appearance of the simulated mammograms generated is strongly dependent on the statistics of the real datasets. The distribution law applied to each parameter may not necessarily hold.

The simulation model is not applicable in our case. It requires a huge dataset to derive the statistics for the sampling. As DBT is a new technology, the number of datasets is limited and does not have accurate statistics. Even if we try to use mammographic data as an alternative, there are a number of issues which need to be resolved. Mammographic data can be used to generate some parameters such as number of microcalcifications in a cluster, but not parameters such as mean contrast of the microcalcifications within the cluster, because there are significant intensity differences between a mammogram and a DBT projection. Moreover, we want a simulation model to generate series of DBT projections, and to have the true 3D positions of the clusters of microcalcifications for verification after the reconstruction process.

(b) Comparison of real and computer-simulated clustered microcalcifications on digital mammograms. ROC study.

The approach used by Lado et al. is similar to Lefebvre et al.'s in the way that the parameters are determined on the corresponding values extracted from real mammograms [108]. The number of datasets they used is far fewer than Lefebvre et al.: *58* mammograms with *74* real clusters of microcalcifications. The simulation model involves the detection of real microcalcifications using wavelet transform techniques, feature analysis, creation of a binary image, assignment of gray level values to the pixels of the binary microclacification, and background correction. Similar to Lefebvre, their model also consists of global parameters e.g. the number of microcalcifications, the mean area of the cluster, and individual parameters of each microcalcification e.g.

the size and location within the clusters and the average gray level value. Instead of statistical laws employed in generating the parameters for the simulation model, the global features are extracted from the real cluster using wavelet transform techniques. The individual parameters are randomly sampled from a wide set of values centered on the corresponding values extracted from the mammogram. The average gray level value is calculated from the contrast value of the microcalcification and the background, and from the gray level value of the surrounding pixels. Finally, instead of superimposing simulated clustered microcalcifications on a normal mammographic background, the microcalcifications were superimposed on mammograms containing real clusters of microcalcifications.

The simulation model described in this paper is less representative than Lefebvre's, because the size of the dataset they used is much smaller and they did not explain clearly how they sample the parameters. The model suffers from similar problems as in Lefebvre's and is not suitable in our case.

5.1.2 Three-dimensional Simulation Models

(a) A three-dimensional breast software phantom for mammography simulation

Bliznakova et al. [109] present a three-dimensional computer model of the breast. The complete software breast phantom represents a complex aggregate of a breast external shape, duct system, abnormalities, mammographic texture, Cooper's ligaments and pectoralis muscles. After all these elements are modelled, breast abnormalities including microcalcifications are inserted to complete the breast phantom.

They consider three basic shapes in simulating microcalcifications: round or ovoid, elongated and irregular shape. The round shape is modelled as spheres and ellipsoids with different radii and semi-axes values being assigned. The elongated shaped microcalcifications are simulated using an algorithm similar to the duct tree generation. The irregular shape ones are represented by 3D voxel matrices and are generated using a 3-D random walk algorithm. The microcalcification cluster is defined by the cluster centre and the randomly sampled among all tree branches and lobules. The number of microcalcifications within a cluster is assigned by the user. The position of each microcalcification is represented by a spherical coordinate with reference to the cluster center. A Gaussian distribution is assumed in determining the distance between

the microcalcification and the cluster centre, and the polar and azimuthal angles for each microcalcification are chosen randomly.

After the software breast phantom is built, it is subjected to simulation of the radiographic imaging process. In this simulation, the 3D imaging mode allows angular projections by rotating the source by the corresponding angle. Synthetic mammograms of the modelled breast can then be produced after the image acquisition parameters have been assigned.

The comprehensive model enables 3D phantom modelling and visualization, as well as generation of simulated X-ray projection images from different angle views. However, the current version may not be flexible enough and may be too complex in some situations e.g. we may simply want a very simple background. Also, the positions of microcalcifications are currently randomly sampled and the implementation does not allow input of the 3D positions of microcalcifications which we require for the development and testing in our approach.

(b) Algorithmic 3D simulation of breast calcifications for digital mammography

Nappi et al. [110] presented a model which includes the following parts: (1) simulation of the X-ray image acquisition; (2) algorithmic 3-D simulation of the calcification particles of a specified type; (3) 3-D simulation of the breast structures associated with the calcifications; (4) placing of the calcifications onto a real or simulated mammographic background.

Firstly, the X-ray image acquisition model is based on the principles of the actual physical process. It consists of three components: an X-ray field, a simulated breast volume and a film plane. The simulated breast volume will later on contain the microcalcification clusters. Next, specifically for microcalcifications, they have developed three principal methods for modelling calcification particles: irregular, ovoid and elongated. Since the growth pattern of most calcification clusters relates to the location and shape of the breast structures, e.g. the duct network and the terminal ductal lobular units, within which the calcification particles appear, they have also performed the modelling for breast structures and mammographic background. The purpose of this is simply to get a detailed simulation of 3D calcification clusters in a more realistic shape as in the breast. It is therefore not necessary to place the simulated duct network

into the breast volume for imaging. Finally, they combined the 3D simulated calcifications with mammographic background, by analysis of the intensities and contrast of calcifications and the surrounding background.

The model provides a way to put algorithmically 3D simulated calcifications to real mammographic data. This model is less detailed than the previous model e.g. modelling the composition of the breast and the imaging acquisition geometry. The consideration they have in building 3D clusters is good as a reference, but this is not applicable in our case.

5.1.3 Prototype for DBT Analysis

The prototype proposed by Fernandez et al. [111] is a very simple one which involves the use of a slide projector and a commercial available scanner. The phantom contains semi-transparent elements and is placed between the projector and the scanner. A semi-transparent paper is put on top of the scanner as image plane. The set up is shown in the following figure:

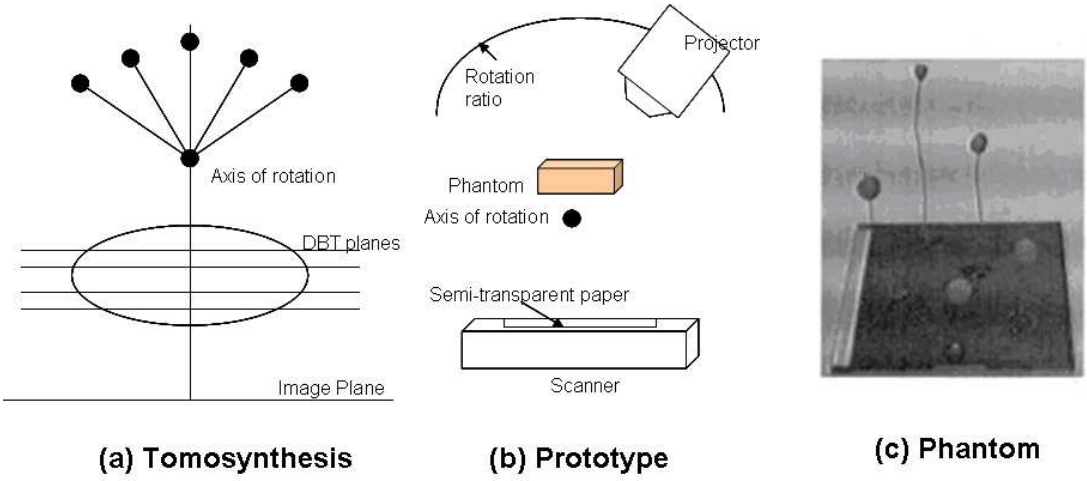

Figure 5.1: The proposed prototype and the phantom of microcalcifications. (Modified from [111].)

They take different "projections" as the projector rotates, similar to DBT. Afterwards, they perform a shift-and-add algorithm to reconstruct a 3D volume, as shown in the following diagram:

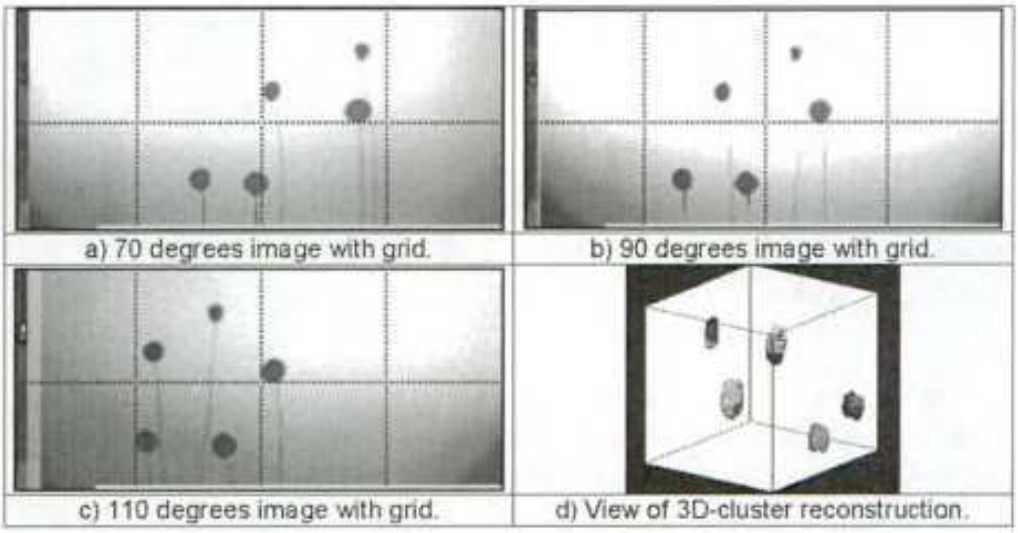

Figure 5.2: The simulated DBT projections and the reconstruction volume. (Extracted from [111].)

The prototype is good in the sense that it provides an alternative to the generation of DBT-like projections and is useful for some three dimensional analysis. However, the model is very primitive in the sense that it does not consider biological aspects such as the tissue constituents of the breast, or the impacts of the X-ray properties on different tissues and calcifications. The image properties of the projections produced cannot be compared with those generated by DBT e.g. the image intensity and contrasts, as the images are only generated using a projector and a scanner. We cannot apply it in investigating calcification detection algorithms. Also, the discussion of the generation of the clustered microcalcifications phantom in the paper is very brief. The size and the 3D positions of the microcalcifications in the phantom seem not to be very accurate. It makes this not suitable for our work.

5.1.4 Realistic Simulation of Microcalcifications in Breast Tomosynthesis [112]

One of the emphases in this approach is simulation of the morphologic characteristics of microcalcifications according to Le Gal's classification [114], as the shape of individual microcalcifications is one of the features which can be used for breast classification into malignant and benign.

There are *3* steps in this simulation process. Firstly, a 3D model of microcalcifications is built using biopsy specimens containing clusters of microcalcifications with different Le Gal types and a micro-CT scanner. The 3D model is obtained after segmentation of the reconstructed micro-CT images. Secondly, using

this 3D model, a template is obtained after ray-tracing and modification according to the corresponding DBT detector characteristics. Finally, this template containing microcalcification clusters of different Le Gal types is inserted into real raw DBT projection images of the biopsy specimen using a DBT system, Siemens Inspiration TOMO.

The following figure shows some results of the simulated clusters against the real ones of different Le Gal types:

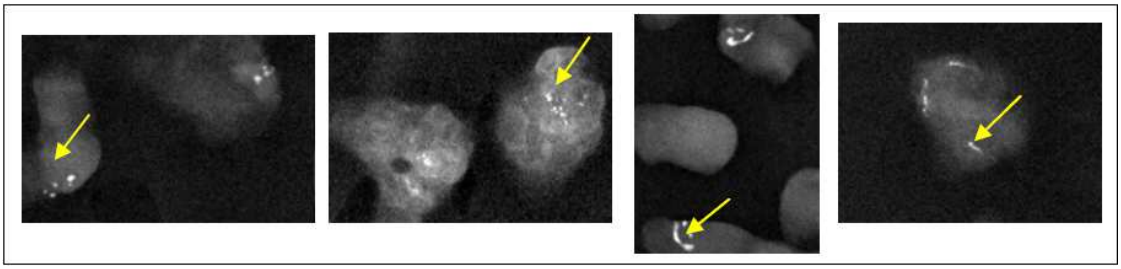

Figure 5.3: Simulated vs Real clusters of microcalcifications of different Le Gal types (Left to Right: Type 2 to 5). The simulated cluster is indicated by arrows. (Extracted from [112].)

The simulation here is encouraging because it is based on the real shapes and distributions of microcalcifications. As pointed out by the authors, their verification of the simulation procedure is performed in a simple homogeneous background. To consider whether the simulation is really successful, further work is required in different aspects such as insertion of the microcalcifications under different anatomical background, different breast glandularity, or in different positions into a breast.

The major characteristics of the model are that the microcalcifications are modelled according to the Le Gal types, which is one of the most common classifications adopted in the research community, and the use of real DBT projections. However, the simulation is limited by the biopsy specimens and the ground truth of the 3D positions of microcalcifications generated in this way is not very exact, if not unknown. It is also not flexible for us to generate microcalcifications at designated positions.

5.2 Simulation of DBT Projections with Clustered Microcalcifications

In this section, we introduce a software-based simulation model which generates DBT projections containing clustered microcalcifications. Our objective is to develop a simulation model which allows X-ray projections generated at different angles and

containing clusters of microcalcifications of different shapes at designated 3D positions. For a study of mathematical derivation and analysis, the tissue background needs to be not too complex, a homogeneous background, a *50/50* adipose to glandular tissue composition is sufficient for our analysis of the epipolar curves approach. This can easily be changed, if required.

The model consists of three parts: (1) generation of a three-dimensional calcification cluster matrix; (2) generation of DBT projections by incorporating the calcification matrix into a breast model in a homogeneous background; (3) addition of noise in the simulated DBT projections.

5.2.1 Generation of a three-dimensional calcification cluster matrix

The calcification cluster matrix is a three-dimensional binary matrix, where *1* indicates the presence of a calcification. One matrix represents one calcification cluster containing *n* individual calcifications. An individual calcification, depending on its size, may consist of a few neighbouring matrix elements. The features we have considered to date include: (a) shapes and size of individual calcifications; (b) distribution and location of individual calcifications within the clusters.

(a) Shapes and size of individual calcifications

Our model follows the calcification types defined in the Le Gal classification, as the types indicate the degree of malignancy of the breast diseases:

Type 1: Annular

The calcification of this type looks like a ring. The shape is formed by a thin hollow cylinder (or torus).

Type 2: Regularly punctiform

The calcification of this type looks like a point or sphere given by $x^2 + y^2 + z^2 \leq r^2$.

Type 3: Dusty

The calcification of this type is similar to Type 2, except that $r = 1$.

Type 4: Irregular punctiform

The shape is irregular. Given the size of the calcification, we start from the first matrix element. For each element, there are *26* neighbour elements (except the

boundary elements). The neighbours are then selected randomly until the number of matrix element equals the size of the calcification.

Type 5: Vermicular

Calcifications of this type resemble a worm. For simplicity, we form *4* types of rectangular block of size *n*: vertical, horizontal, tilted at *45* degrees, tilted at *135* degrees.

Different types of calcification shapes are generated and shown as follows:

Type 1: Annular	Type 2: Regularly Punctiform	Type 3: Dusty	Type 4: Irregular Punctiform	Type 5: Vermicular
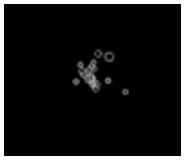	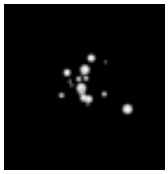		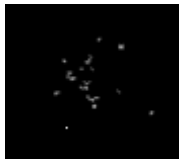	

Figure 5.4: Calcification shapes according to Le Gal's classification

(b) Distribution and location of individual calcifications

We can assign the locations of individual calcifications by deliberately choosing some designated positions and set a value of *1* in those positions in the matrix for a microcalcification. Otherwise, we can simulate them according to two breast conditions. Benign breast conditions typically correspond to diffuse clusters, while malignant breast conditions tend to have curvilinear configurations. Therefore, clusters of the two types of distribution are simulated: diffuse and linear.

Each calcification is represented by a spherical coordinate (r, θ, φ), where r is the distance between the microcalcification and the cluster center (the middle element of the matrix), θ and φ is the polar angle and azimuthal angle with respect to the cluster center respectively.

For a diffuse distribution, we simply place the individual calcification randomly in the cluster. For a linear distribution, we build a linear equation forming the path of possible locations of the calcification and the individual calcification is then randomly sampled along the path. (Note that the path is not indicated in the matrix. We simply

use it for choosing the location of the calcification.) Clusters of microcalcifications with different distribution configurations are shown as follows:

Diffuse	Linear
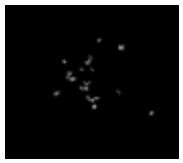	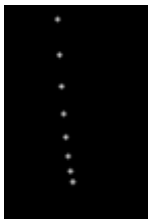

Figure 5.5: Calcification Distribution

The output of this step is a matrix of the size of a bounding box of the cluster divided by the resolution. For example, a bounding box of size *25 mm * 25 mm * 15 mm* and a resolution of *0.1* mm means a matrix of *250 * 250 * 150* elements. Each element is either *1* (microcalcification) or *0* (non-microcalcification).

5.2.2 Generation of DBT projections

Tromans has developed a comprehensive model of X-ray image formation [31]. This model simulates the X-ray tube, ray tracing, the image receptor, scattered radiation and anti-scatter grid. It generates X-ray projections after providing the acquisition parameters. An interface of the model is shown in the following figure:

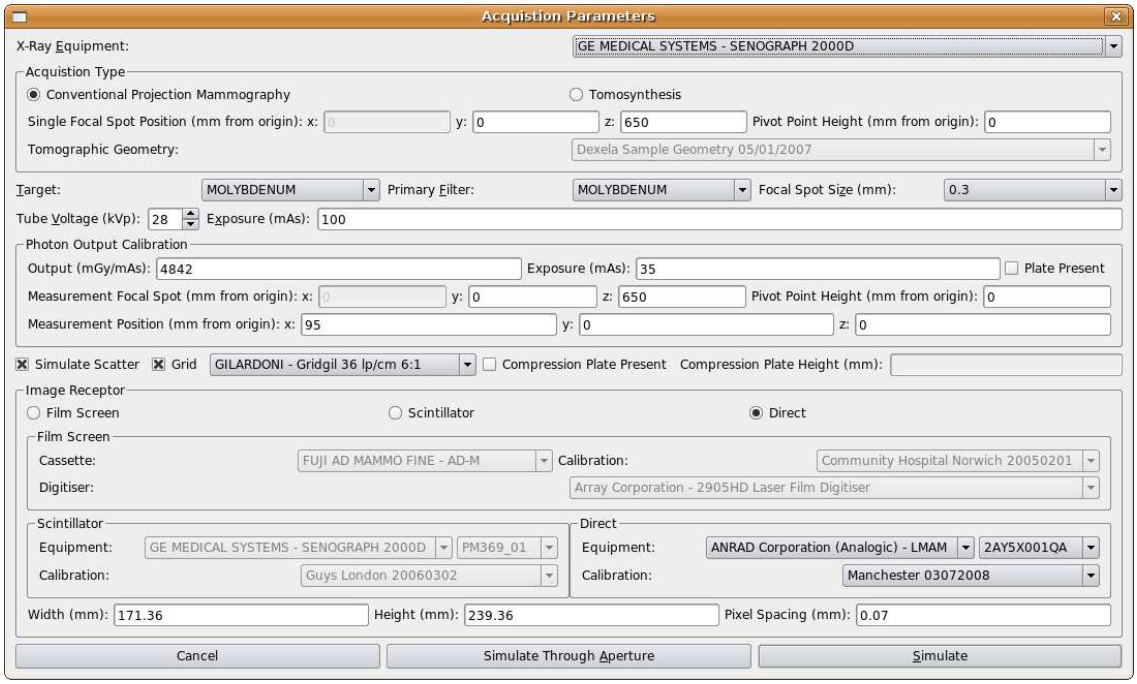

Figure 5.6:A screenshot of the X-ray Simulation Software developed by Tromans [31].

The acquisition parameters can be retrieved from the system by default according to the X-ray equipment chosen or adjusted manually through the interface.

Users have a choice of either generating a single mammogram or multiple projections as in DBT. For the latter case, a tomographic geometry is necessary. The interface allows users to specify the parameters for the X-ray tube, e.g. the anode/filter materials, the focal spot size, the tube voltage, the exposure etc. They also have the option to simulate scatter with or without an anti-scatter grid. The X-ray projections can then be simulated as film-screen, or generated with a digital detector, after the image size and the pixel spacing are given.

The model assumes a breast of box size *100* mm * *100* mm * *60* mm and accepts the calcification cluster matrix, the location and the size of the matrix in order to generate the DBT projections with microcalcifications. One projection for each calcification type has been extracted and is illustrated as follows:

Type 1: Annular	Type 2: Regularly Punctiform	Type 3: Dusty	Type 4: Irregular Punctiform	Type 5: Vermicular
				

(Note: Window/Level is performed for visualization purpose.)

Figure 5.7: DBT projection of calcifications with different shapes

Using this simulation model, we have generated a set of *15* DBT projections with a calcification cluster matrix of eight Type *2* microcalcifications in a linear configuration. The dimensions of the bounding box of the calcification cluster is *25* mm * *25* mm * *15* mm with resolution = *0.1* mm. In other words, the matrix contains *250* * *250* * *150* elements. The radius of each microcalcification is *1.5* matrix units and the microcalcification location is calculated arbitrarily using a simple parametric function *f(t)*:

$$f(t) = \begin{cases} x = t; \\ y = t^2 + 2t + 1; \\ z = t; \end{cases}$$

and choosing $1 \le t \le 8$.

For visualization, *3* DBT projections are extracted as shown:

	Projection 0	Projection 7	Projection 14
DBT Projection	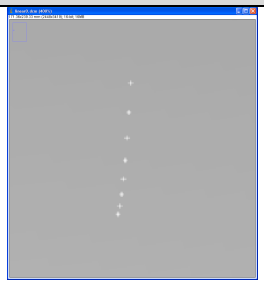	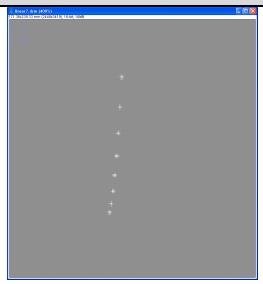	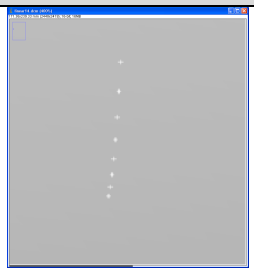
Focal Spot Position	*y: -208.49* *z: 623.89*	*y: 1.73* *z: 660*	*y: 211.85* *z: 622.68*

(Note: The focal spot arrangement follows Dexela's setting on 05/01/2007.)
Figure 5.8: Tomosynthesis projections of simulated calcification cluster with linear configuration

5.2.3 Addition of noise in the simulated DBT projections

A major objective of microcalcification detection algorithms is to differentiate between noise and microcalcifications, and to detect faint microcalcifications. In order to maximize the realism of the simulation so that the DBT projections contain noise, we conducted a range of experiments to record the noise distribution using a Hologic mammography machine with a Lorad detector. A block of polymethyl methacrylate (PMMA) was used and enclosed in lead, leaving a *2* mm diameter aligned pair of apertures at the top and bottom, such that a narrow primary ray would pass through and would be incident upon a prescribed position on the image receptor. Different tube current values ranging from *12* mA to *325* mA at tube voltage *28* kVp were used and a plot of standard deviation against he mean pixel value obtained from pixels in a *2* mm-diameter circular region is shown:

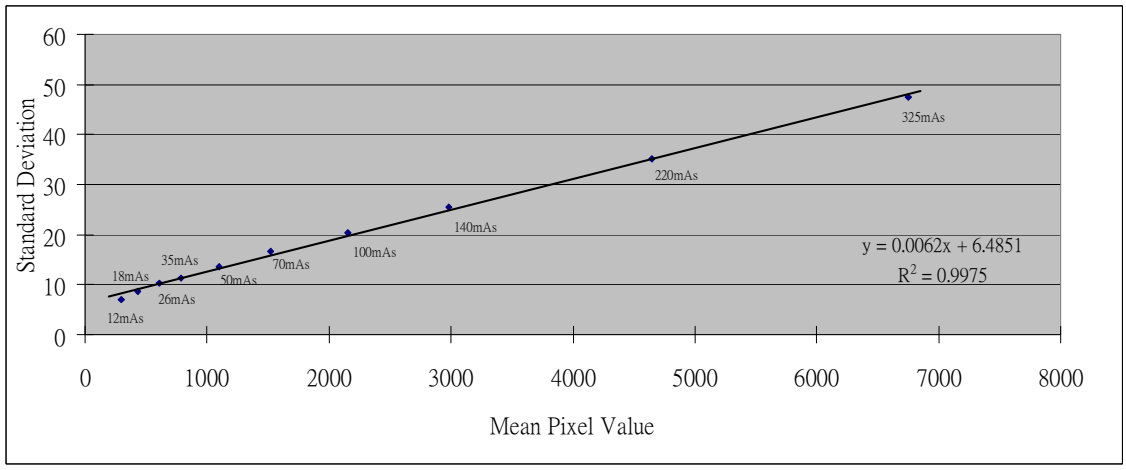

Figure 5.9: A plot of standard deviation against mean pixel value, showing results of noise distribution at different values of tube current.

After the noise distribution was obtained, we added zero-mean additive Gaussian noise using the standard deviation from the plot on our simulated images. One projection of a linear cluster, simulating a malignant one, before and after adding noise, is shown:

Figure 5.10: Left: A noiseless projection showing the linear malignant cluster; Right: The same projection after adding noise.

5.2.4 Merits of our simulation model

In Section 5.1, we discussed several recent simulation models. A very recent model (Section 5.1.4) simulates DBT projections containing clusters of microcalcifications based on biopsy specimens. Their DBT projections generated are very realistic. This is a very good model to facilitate analysis of realistic shapes and distribution of microcalcifications. However, the simulation is limited to those clusters in the biopsy specimens and is not sufficiently flexible for us to create microcalcifications at designated positions. On the other hand, our model is totally software-based. In theory, infinite different shapes and distribution of microcalcifications can be generated using our model to fulfil any possible form in reality. More importantly, our model is based on a mathematical and physical model of X-ray generation. This means that the ground

truth information can be obtained, leading to correct and accurate derivations and calculations in terms of geometry, shape and distribution analysis.

5.3 Mammography BR3D Phantom

The DBT projections of our simulation model discussed in Section 5.2 are in a homogeneous background, which simplifies our geometrical analysis. However, real DBT projections are formed from breasts of heterogeneous breast tissues and different breast glandularity. In order to facilitate our analysis in the detection task, projections in a complex and heterogeneous background are required. For this reason, our laboratory acquired the CIRS Model 020 BR3D Mammography Phantom [113].

From the specification, the phantom consists of a set of *6* slabs, each of which has a unique swirl pattern, providing varying background when arranged in multiple combinations and thicknesses. One of the *6* slabs contains *36* $CaCO_3$ specks of various sizes ranged from *0.13* to *0.40* mm, simulating microcalcifications. They are arranged in circles according to their size in *6* groups. The following figure shows an X-ray projection of this phantom and the magnified view of one of the groups of *6* $CaCO_3$ specks:

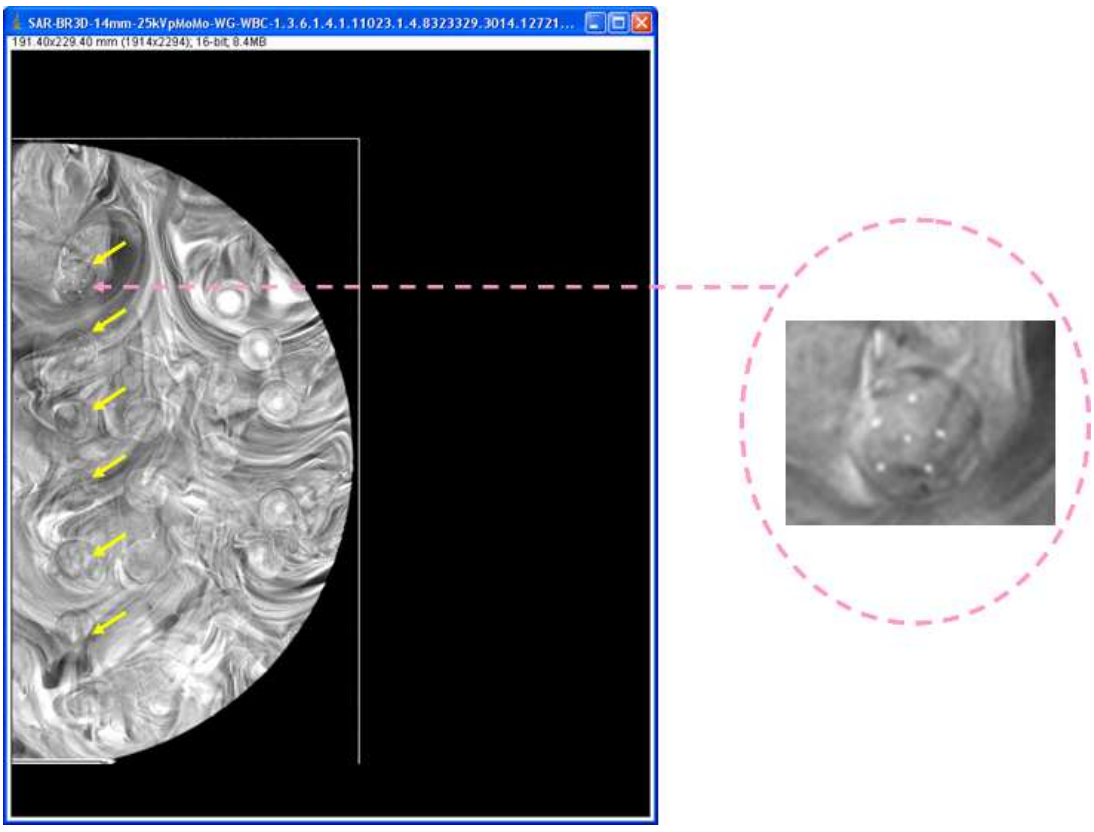

Figure 5.11: Left: An X-ray projection of the Mammography BR3D Phantom; Right: A magnified view of

a group of 6 $CaCO_3$ specks.

Using the projections of this phantom, we can demonstrate and evaluate the microcalcification detection algorithms on a more realistic background. More on detection algorithms will be discussed in Chapter 7.

5.4 Real DBT Datasets

To finally test the ideas presented in the following chapters, eight real DBT datasets were obtained, from IMS by courtesy of Dexela Limited:

No	Patient ID	Histological Results
1	P7	IDC + DCIS
2	P12	ILC + LCIS + DCIS
3	P13	IDC
4	P16	IDC
5	P17	IDC
6	P19	IDC+DCIS
7	P20	IDC
8	P24	IDC

(where IDC: Invasive/Infiltrating Ductal Carcinomas; ILC: Invasive/Infiltrating Lobular Carcinomas; DCIS: Ductal Carcinoma in Situ; LCIS: Lobular Carcinoma in Situ.)

Table 5.1: Real DBT datasets.

For each case, *13* DBT projections using an IMS DBT prototype machine were generated in a CC mode. The geometry of the machine will be discussed in Chapter 6 when the epipolar curves approach is introduced.

The following is one of the examples from *Patient 7*. In this dataset, it is obvious to see a number of calcifications under the armpit. One of the DBT projections taken at angle 0.04^o and the magnified region around the armpit are shown in the following figure:

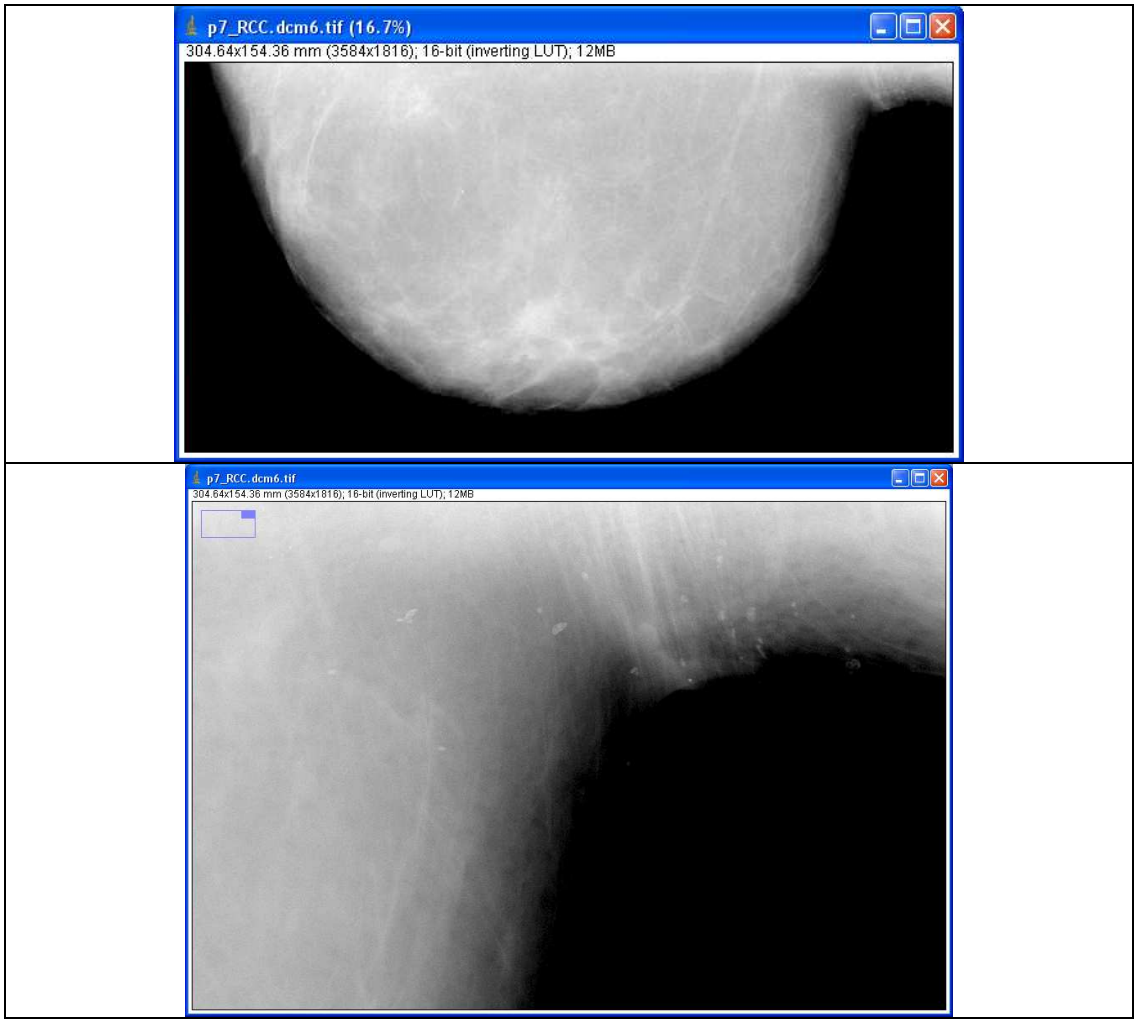

Figure 5.12: Top: A real DBT projection; Bottom: A magnified view under the armpit region showing a number of bright white specks as microcalcifications.

The advantage of DBT is its 3D nature. By simply looking at the 2D projection in the figures, it is impossible to imagine the real distribution of the microcalcifications. Here, we give the reader a glimpse and present our reconstruction outcomes of the positions of the microcalcifications in this woman's right breast, before we explain our idea in later chapters, in the following figure at the right (Left figure is used for comparison.):

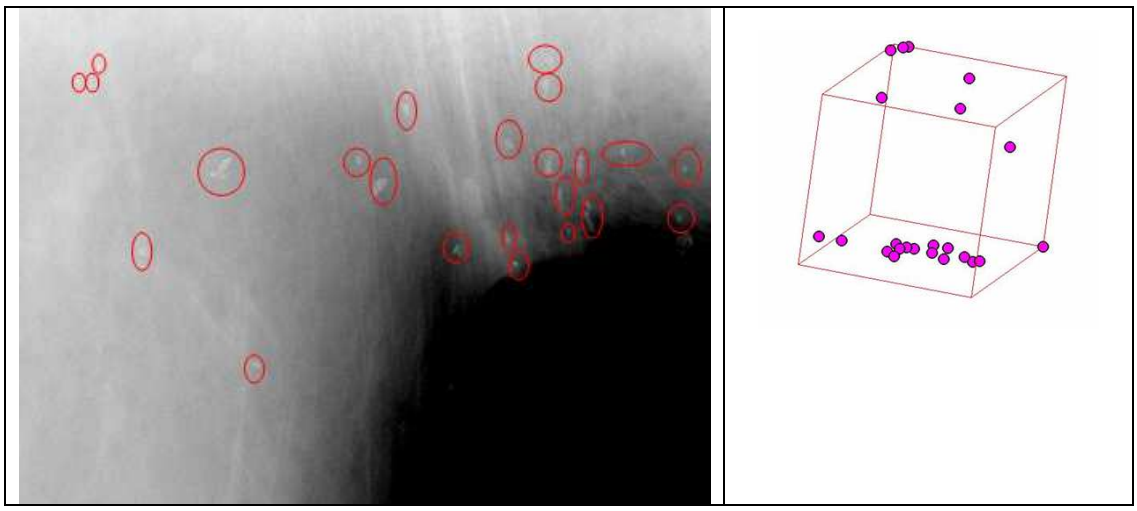

Figure 5.13: Left: A region from one of the real DBT projections showing a number of bright white spots; Right: The reconstructed 3D positions after the epipolar curves approach.

It can be seen that the spots are distributed into *2* groups at different depths. This shows that the reconstruction of microcalcification clusters is feasible, making a more accurate analysis on microcalcifications for the early detection of breast cancer.

Chapter 6

Detection and Reconstruction of Microcalcifications in DBT: an Epipolar Curves Approach

Over the past two decades, many research groups have developed microcalfication detection algorithms, others have studied the reconstruction of microcalcification clusters. Due to the physical nature of the breast and the limitations of mammography, the detection results need further improvement and the reconstruction outcomes are far from satisfactory. By utilizing the multiple projections generated in DBT, in this chapter we propose a new approach, called the Epipolar Curves Approach, to detect microcalfications and reconstruct clusters, and subsequently their classification.

Nearly all research groups working on DBT investigate the algorithms to reconstruct the 3D breast in the form of DBT slices. A new approach in microcalcification detection using DBT slices can therefore be proposed, in addition to enhancing existing detection algorithms on X-ray projections. We start this chapter with a literature review on microcalcification detection in DBT. Our approach shares some of the benefits of using projection views as research groups that use this approach. We explain the reasons why our approach uses projections instead of slices and give an overview of our approach in Section 6.2.

Epipolar geometry is an important topic in 3D computer vision or stereo-based imaging [115-120]. 3D computer vision analyses how 3D information can be recovered with two (or more) views of the same scene, inferring depth information geometrically. There are geometric relations between the 3D point and the corresponding projection points onto the 2D images, leading to constraints between the projection points. This is called epipolar geometry. Given the image x in the first view projected from a point X in 3-space, an epipolar line associated with the point x can be drawn in the second view.

This epipolar line determines where the image point *x'* in the second view projected from the same point X is. In our case, DBT generates multiple 2D microcalcification projection points in each view from a cluster of microcalcification in the 3D breast and one key task is to recover the cluster for subsequent breast cancer detection. DBT has similarities to 3D computer vision. For this reason, we give a brief introduction to 3D computer vision and epipolar geometry in Section 6.3.

Next in Section 6.4, we discuss the geometry of DBT. Our approach uses *2* coordinate systems: a world coordinate frame, and a sensor coordinate frame. With the geometry and the coordinate frames defined, together with the assumption that microcalcification points are detected in each projection, the epipolar geometry will then be applied to yield constraints in solving the correspondence problem of microcalcifications in each projection of DBT. Now, the solution space of our correspondence matching problem is reduced from 2D (the whole image) to 1D (the epipolar line). Furthermore, in DBT, there is usually a compression plate on top of the breast. This limits the possible 3D positions of the microcalcification. With this, the solution space in DBT can be further reduced, as will be shown in Setion 6.5.

Nevertheless, the search space is still too large, especially in situations where there are too many projection points, either noise points or true microcalcification points, in each DBT view. Also, there is no obvious way to distinguish between the false and the true ones. We will show that, given the DBT geometry, the projection points from all DBT views lie nearly on the same straight line with nearly constant spacing. We have derived a curve of all the corresponding 2D positions in each DBT view from the same 3D position. We call this an epipolar curve, by analogy with stereovision. The derivation will be given in detail in Section 6.6.

Now, given that each epipolar curve represents a unique microcalcification in the breast, we demonstrate how our epipolar curves approach helps in typical situations of breast containing n microcalcifications. By analyzing all the projection images simultaneously and putting them in the same 2D coordinate frame, we show in Section 6.7 that our approach finds all the correspondences of each microcalcification and identifies noise points and missing points.

Ideally, if there are *m* DBT views, there will be *m* projection points lying on the corresponding epipolar curve. These *m* points represent the same microcalcification in

the breast. So, if there are *n* microcalcifications, then there will be *n***m* points in the same 2D coordinate system. Our next task therefore is to cluster the *n***m* points into *n* groups, with each group containing *m* points. We develop in Section 6.8 a clustering method to perform this clustering task.

In Sections 6.3 to 6.8, we primarily use simulated datasets and the corresponding DBT geometry to present our concepts. The chapter is completed in Section 6.9 by showing our approach applied to a real DBT dataset generated on a prototype DBT machine that has recently been announced commercially, and which has a geometry that is slightly different to that discussed in Section 6.3. In Section 6.8, we introduce one clustering method to extract microcalcifications. In this section, we also present another method, based on the Hough transform, a feature extraction technique which can help identify lines in an image. We demonstrate how the Hough transform can be applied to our clustering task. The chapter ends with a conclusion and discussion section.

6.1 Literature Review

In this section, the literature on two different approaches (using slices or projections) is reviewed.

6.1.1 Detection using DBT Slices

(a) Noise removal in tomosynthetic mammographic imaging

Badea et al. proposed a noise removal method using noise mask subtraction [103, 121] which is performed on the slices after reconstruction. The method generates a noise-mask on the plane of interest from the noisy, out-of-focus planes. The selected out-of-focus plane is projected for every tomographic angle used onto the image formation plane. Then, these projections are reconstructed and synthesize a blurred image on the plane of interest. Now, the blur that originates from the selected noisy plane appears on the plane of interest. This forms the noise-mask. After subtraction, the noise in the out-of-focus plane is removed. Detection can then take place on the slices after the noise structures are removed.

(b) Noise model for microcalficiation detection in reconstsructed tomosynthesis slices

Similar to the noise model in mammography, Karssemeijer's group has also investigated a noise model for microcalcification detection in reconstructed DBT slices using the techniques of local contrast normalization [101]. The method, like that developed for mammography, first involves calculation of the local contrast at each pixel, which is obtained by subtracting a smoothed image from the original one, where the smoothed image is generated by convolving the original image with a Gaussian kernel. Then, the pixel values are divided into bins of fixed length. In each bin, the mean and standard deviations of the local contrast values are computed. Karssemeijer's group considers this local contrast as noise and the standard deviation of this local contrast to be equivalent to the standard deviation of the noise. For the detection of microcalcifications, Karssemeijer's group uses different local contrast values, m_i, calculated from the smoothed image using another Gaussian kernel and values in the neighbourhood. This local contrast feature m_i is considered to be a feature for detection without the noise model. To compare the results of detection with noise model implemented, the group normalizes the local contrast feature m_i by the standard deviation of noise i.e. $m_i^{'} = m_i / \sigma(y_i)$ where $\sigma(y_i)$ is the standard deviation of the noise in pixel value y_i. The preliminary results suggest that image noise depends on the signal and can be modelled. Detection performance can be improved with the use of the estimated noise model.

6.1.2 Detection using DBT Projections

(a) Microcalfication detection in digital tomosynthesis mammography

Instead of considering the noise in the slices, Wheeler et al. have developed another noise model based on the projection images [122]. They generate calcification residual images for each of the projection images by computing the quantum noise, electronic noise and the tissue noise variance at each pixel. The noisy estimate of the calcification residual $\hat{c}_n(i, j)$ is modelled as:

$$\hat{c}_n(i, j) = \hat{y}_n(i, j) - \hat{b}_n(i, j) \qquad \textit{Eqn. 6.1}$$

where in simple terms, $\hat{y}_n(i, j)$ is the projection and $\hat{b}_n(i, j)$ is the low-pass filtered projection obtained using a 2D Gaussian smoothing kernel of $\hat{y}_n(i, j)$, and the noisy estimate of calcification residual $\hat{c}_n(i, j)$ is the difference between the two.

Then, the noisy estimate of the calcification residual is divided by the variance of all the noise including quantum, electronic and tissue noise: $\hat{c}_n(i, j) / \sigma^2_{c,n}(i, j)$ where $\sigma^2_{c,n}(i, j)$ is the variance of the noise of the *n*th projection which is estimated from the projection data. (Readers may refer to [122] for details of how the estimation is performed.) Next, they calculate the value $\hat{D}$ by making use of the calcification residual of all *N* projections and the minimum variance estimator:

$$\hat{D} = \left[\sum_{n=1}^{N} \hat{c}_n(i, j) / \sigma^2_{c,n}(i, j) \right] / \sum_{n=1}^{N} 1 / \sigma^2_{c,n}(i, j) \qquad \textit{Eqn. 6.2}$$

Finally, the value $\hat{D}$ is thresholded for the detection of calcification.

(b) Automated detection of microcalfication clusters for digital breast tomosynthesis using projection data only: A preliminary study

Reiser et al. have proposed a comprehensive detection algorithm [123] which is independent of the particular reconstruction algorithm, and uses the projection views only. Within this detection scheme, each projection image is treated as a separate mammogram and analyzed separately. A binary image is created for each projection with sites corresponding to microcalcification candidates set to one. All binary images are backprojected into the breast volume. In this volume, high intensity regions indicate an increased likelihood for the presence of a microcalcification. Calcification candidates are identified in this feature volume by analyzing the maximum-intensity projection (MIP), which is formed by selecting the maximum intensity value along the ray for each pixel. The *(x, y, z)* coordinates of each microcalcification candidate in the feature volume are identified by finding the slice with a pixel value equal to that in the MIP image.

6.1.3 Discussion between the Two Approaches

To date, there is little clinical DBT data available and almost all DBT machines have been prototypes. As a result, the performance of all the studies on microcalcification detection in DBT remains to be proven.

In the previous sections, we have reviewed a few literatures using either approach. Regarding detection approach using DBT slices, as DBT reconstruction algorithms are still being developed and optimized, it is unavoidable that many artefacts

cannot be removed, affecting the detection results. This approach definitely requires more research effort for more satisfactory outcomes.

For the detection approaches using projection images, it is expected (as Reiser et al. [123] admit in their paper) that the signal-to-noise ratio in the projection images may be too low for the detection of subtle microcalcifications. It seems as if this approach is not any better than the other approach. However, and crucially, as we will show, the microcalcification does not need to be detected in every projection image in order to be detected in the point backprojection. In their experience, a microcalcification that was detected in eight projection images (amounting to about *75*%) becomes conspicuous in the point-backprojected image. This means that it is not necessary to have a perfect detection algorithm which can detect microcalcifications in every single projection, but only a good detection algorithm which can detect microcalcifications in the majority of projections. The weakness of the detection approach using projections i.e. poor signal-to-noise ratio in each projection, can therefore be compensated by utilizing detection information from other projections.

Furthermore, judged from the aspect of computational efficiency, approaches using projection views should be computationally more efficient, because about *15* projections need to be analyzed for each breast rather than, for example, *40-90* slices.

6.2 Our Proposed Approach

6.2.1 Reasons for Using Projection Views

We propose a novel approach based on Epipolar Curves, and which is based on projection images. There are many benefits to using projection data over DBT slices:

Firstly, refer to the previous discussion, our approach shares the advantages of computational efficiency in processing projection data instead of slices, and Reiser et al. [123]'s experience that not a full set of projection images may be required in discovering some microcalcifications (but at the same time, our approach hopefully improves, if not resolves, the issues encountered by Reiser et al. about the detection on subtle microcalcifications).

In addition, the generation mechanism of projection images in DBT is similar to that in mammography. Detection algorithms in DBT need not be re-invented, rather the algorithms can be similar to those used in mammography which have been studied extensively and thoroughly by many research groups over many years.

Furthermore, detection using slices is complicated since the artefacts are serious in slices which are out-of-plane. This makes it difficult to design suitable algorithms to identify the microcalcifications which are only small white spots without having too many false positives due to artefacts and noise (i.e. detection task) and determine the correct slice (i.e. depth) of the microcalcifications (i.e reconstruction task). The following figure shows the same region of a microcalcification in a number of projections and a few slices above or below the slice that the microcalcifications are in-plane:

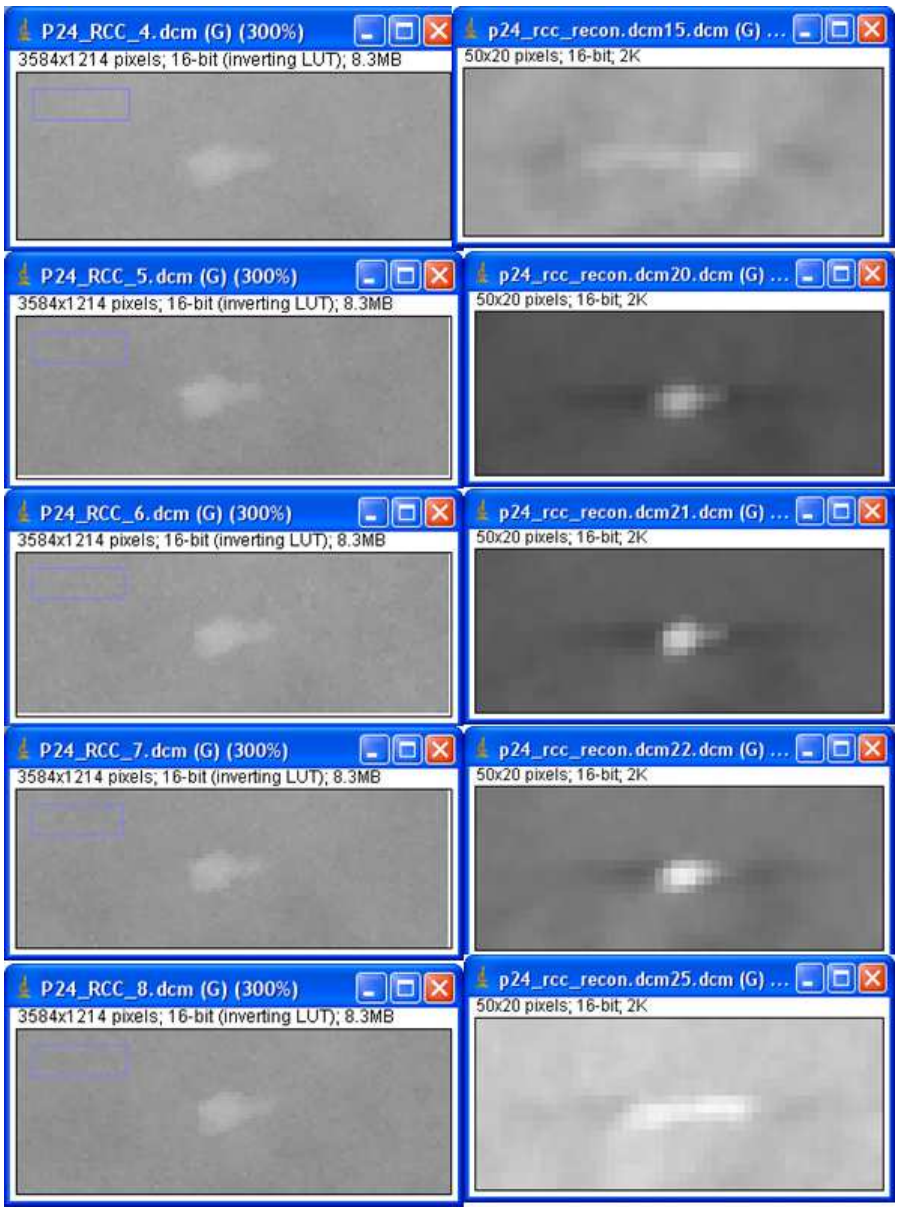

Figure 6.1: Left: Projections 4,5,6,7 and 8 of a microcalcification; Right: Slices 15,20,21,22 and 25 of the same microcalcification

From the figure, we can see that microcalcification detection using slices seems more complicated and requires more intelligence than doing the same task with projection images. For example, in slices *15* and *25*, the white blocks are the artefacts of the microcalcification caused by reconstruction. Detection algorithms that use slices are required to overcome these issues. Also, we cannot determine the depth of microcalcification (e.g. whether the center of microcalcification is at *20, 21, 22 or 19, 23* which are not shown here) as well.

Hence, with all these benefits from projection data and foreseeable simpler detection algorithms, we have adopted an approach using projection data.

6.2.2 Overview of Our Proposed Approach

The flow chart of our proposed approach of CAD in DBT is shown as follows, and is developed over this and the following chapters:

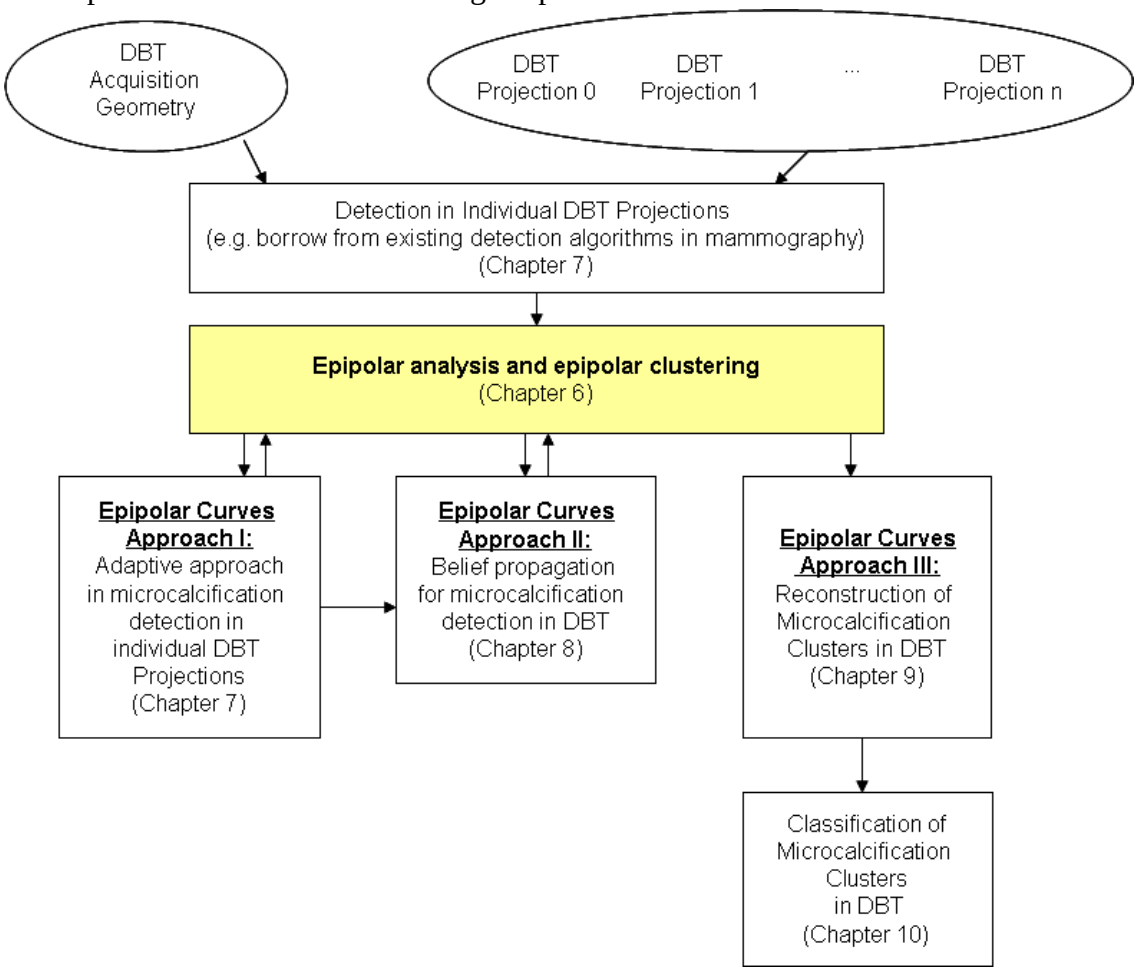

Figure 6.2: Flow Chart of the proposed approach of CAD in DBT

Our approach utilizes both the DBT acquisition geometry and the individual DBT projections. Using both inputs, we start with the detection in individual DBT projections. As DBT projections are generated in a very similar way as in mammography and many readily available algorithms have been developed for mammography e.g. corner detectors, image filters etc, one natural approach is to adopt such algorithms (albeit with minor modifications e.g. thresholds setting) in DBT. (Since the detection algorithms in single X-ray projections have been studied for a long time, we postpone discussion of such algorithms in the next chapter.)

For the moment, assume that we have detected microcalcification candidates in each projection; we now develop epipolar analysis and epipolar clustering. By

combining results from each projection, and with the use of the acquisition geometry, we derive the trajectory of projection points corresponding to the same microcalcification in the breast. This helps us find the corresponding projection points, isolate noise points, identify missing points and provide a more accurate means of 3D reconstruction of microcalcification clusters. We introduce the core idea in the following sections. Also, one clustering algorithm, using the Hough transform, will also be presented to illustrate one way in finding clusters of 2D projection points representing one same microcalcification in the breast.

With this in hand, a number of extensions are described, which further improve the detection and reconstruction results. There may be certain subtle microcalcification points missing during detection individually in some projections. We show that we can adaptively change e.g. the thresholds, in the detection algorithm, which is applied to the predicted positions in those failed projections. This can improve our confidence in believing some points belong to true microcalcifications. This adaptive approach will be presented together with the review of existing detection algorithms in the next chapter.

Another extension of our approach is a novel detection algorithm combining all individual projections detection results in DBT (after adaptive detection for better performance optionally), with Markov random fields and belief propagation. Not only does the algorithm detect microcalcification candidates in individual projections, it can also estimate the depths of the suspected microcalcifications in the breast. This algorithm will be introduced in more detail in Chapter 8.

Having at least two corresponding points, we can then reconstruct the 3D positions of the microcalcification in the breast. Using our epipolar curve approach, we can immediately compute the 3D positions of the microcalcifications. Some real reconstruction results will also be shown in Chapter 9.

Now, with the 3D positions available, we can further analyze the shape and distribution of microcalcification clusters to attain our ultimate goal of classification of the breast into malignant and benign. In Chapter 10, we will present a feasibility study in classification in DBT. This illustrates its feasibility and completes our CAD in DBT study at present. As soon as more clinical data becomes available, further analysis will be possible. This will then improve the accuracy of classification results.

6.3 3D Computer Vision and Epipolar Geometry

Epipolar geometry plays a fundamental role in the correspondence problem in stereo vision, in the way that the epipolar constraint reduces the search space of corresponding points from two-dimensions to one-dimension in stereo matching between two views.

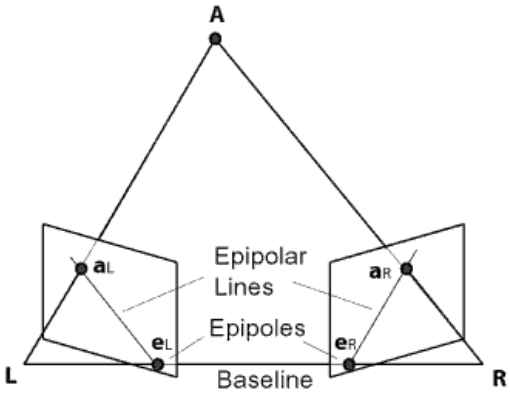

Figure 6.3:Epipolar Geometry (Extracted from [120] .)

Figure 6.3 demonstrates the concept of epipolar geometry [120]. In this figure, it shows two cameras indicated by two centers L and R and the image planes. The object A produces the projections a_L and a_R in the two views. The correspondence problem is that given the point a_L, we need to find a_R from the right image. At first sight, the answer lies within a 2D search space. Fortunately, the point a_R can only lie on a line passing through e_R and a_R. We call this line the epipolar line of a_L. It is sufficient to search just this 1D epipolar line for a_R. Similarly, if a_R is given, the correspondence of a_R can be found in the epipolar line $e_L a_L$. In the figure, the plane ALR is called the epipolar plane and the epipolar lines $e_L a_L$ and $e_R a_R$ are the intersections of the epipolar plane with the left and right image planes respectively. The epipolar constraint reduces searches from 2D to 1D. Hence, the correspondence matching process can be faster and fewer incorrect correspondences will be found as the search space is now smaller.

6.4 Geometry of DBT: An Initial Example

As an initial example, we have assumed the DBT acquisition system has a partial iso-centric motion, in which the detector is stationary and the X-ray tube rotates about some point of rotation. (Note, however, that the geometry used here is for illustrative purpose only. The concept presented in this chapter can be adapted to any DBT geometry.)

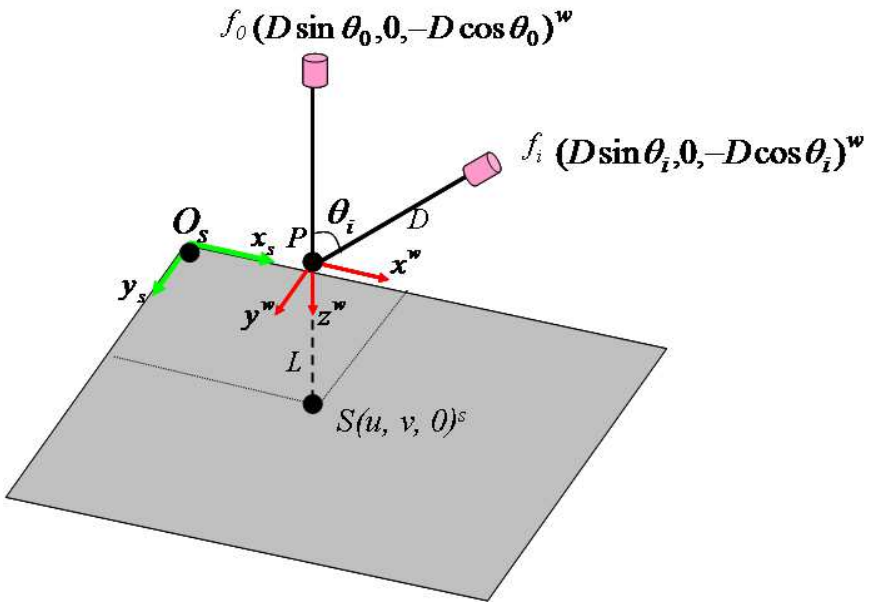

Figure 6.4:An example of the geometry of DBT.

Figure 6.4 shows the geometry: the image detector plane *S*, the pivot point *P* about which the X-ray tube lever arm rotates, the focal spot f_0 (central projection, i.e. $\theta_0 = 0^o$) and another focal spot f_i when the X-ray tube lever arm rotates by θ_i. Note that the length of rotation arm is of length *D* mm and that *P* is located *L* mm above the image detector.

We define the pivot point *P* as the origin of the world coordinate frame *w* (red arrows). For simplicity, we assume that the line joining the focal spot f_0 to the pivot point *P* is orthogonal to the image detector and intersects the detector at *S*. We use the right hand rule for the world coordinate frame. The focal spot position is related to the angle in which the X-ray tube lever arm rotates. The coordinates of each focal spot *i* in the world coordinate frame are $(D\sin\theta_i, 0, -D\cos\theta_i)^w$ if it is θ_i away from the pivot. (Note that as usual a superscript distinguishes which coordinate frame we are using.) We place the origin of the sensor coordinate frame *s* (green arrows), O_s, at the upper left corner of the image detector. The point *S* is *u* mm and *v* mm away from the origin O_s in the *x* and *y* directions respectively, so has coordinates $(u, v, 0)^s$. We can relate the sensor frame coordinates to world frame coordinates straightforwardly by: $(x, y, 0)^s \leftrightarrow (x-u, y-v, L)^w$.

6.5 Epipolar Geometry on DBT

After introducing the DBT geometry, we derive the epipolar lines which the corresponding projection of other views may lie on. We will also put an extra constraint specific to DBT to limit searches.

6.5.1 Derivation of the Epipolar Lines in DBT

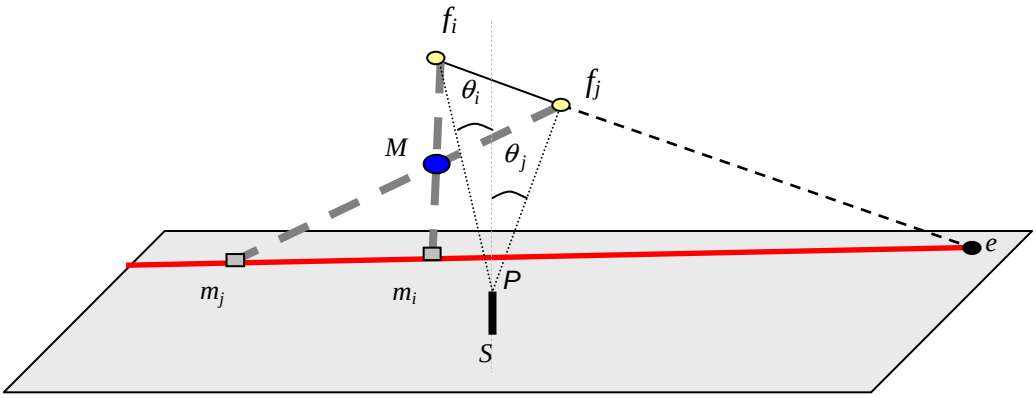

Figure 6.5: Epipolar geometry on digital breast tomosynthesis

Consider a microcalcification M in the 3D breast. In the figure, m_i and m_j are the projections of the microcalcification by focal spot f_i and f_j respectively. Applying epipolar geometry in DBT, we derive the following observations:

1. The image points m_i and m_j, space point M, and the focal spots f_i and f_j are coplanar. Denote this plane by π.
2. The plane π is determined by the baseline $f_i f_j$ and the ray defined by m_i. The plane containing the baseline is the epipolar plane.
3. The ray corresponding to the point m_j lies in plane π. This implies that the point m_j lies on the line of intersection l_e (the red line in the figure) between the plane π and the image plane (the detector). The line of intersection l_e between the epipolar plane and the image plane is called the epipolar line.
4. In DBT, image planes for m_i and m_j are the same (the detector). This means that the epipolar line of the second view corresponding to the image point in the first view is the same line as the epipolar line of the first view corresponding to the image point in the second view.
5. The epipole e is the point of intersection of the line joining the baseline $f_i f_j$ with

the image plane (the detector). In other words, it is the intersection between the baseline $f_i\ f_j$ and the epipolar line l_e.

Now, suppose that the projection m_i has sensor coordinates $(x_i, y_i, 0)^s$ i.e. $(x_i - u, y_i - v, L)^w$ in the world coordinate frame. We also have $f_i = (D\sin\theta_i, 0, -D\cos\theta_i)^w$ and $f_j = (D\sin\theta_j, 0, -D\cos\theta_j)^w$. As noted above, the epipolar line is the intersection of the plane defined by $\{ f_i,\ f_j,\ m_i \}$ and the detector plane i.e. $z = L$ (in the world coordinate frame).

Applying the scalar triple product, the equation of the plane passing through the *3* points $\{ f_i,\ f_j,\ m_i \}$ is

$$\begin{bmatrix} x - x_i + u & y - y_i + v & z - L \\ D\sin\theta_i - x_i + u & v - y_i & -D\cos\theta_i - L \\ D\sin\theta_j - x_i + u & v - y_i & -D\cos\theta_j - L \end{bmatrix} = 0$$

Solving this and putting $z = L$, we get the epipolar line in world coordinates:

$$(x + u - x_i)(v - y_i)2(\sin\frac{\theta_i + \theta_j}{2}\sin\frac{\theta_j - \theta_i}{2}) +$$
$$(y + v - y_i)(D\sin(i - j) + (u - x_i)2\sin\frac{\theta_i + \theta_j}{2}\sin\frac{\theta_i - \theta_j}{2} + 2L(\cos\frac{\theta_i + \theta_j}{2}\sin\frac{\theta_i - \theta_j}{2})) = 0$$

Converting to sensor coordinates, we get:

$$(x - x_i)(v - y_i)2(\sin\frac{\theta_i + \theta_j}{2}\sin\frac{\theta_j - \theta_i}{2}) +$$
$$(y - y_i)(D\sin(i - j) + (u - x_i)2\sin\frac{\theta_i + \theta_j}{2}\sin\frac{\theta_i - \theta_j}{2} + 2L(\cos\frac{\theta_i + \theta_j}{2}\sin\frac{\theta_i - \theta_j}{2})) = 0 \qquad \textit{Eqn. 6.3}$$

Now, given a projection $m_i\ (x_i, y_i, 0)^s$ by focal spot f_i, we know that the corresponding projection by focal spot f_j must lie on the epipolar line *(Eqn. 6.3)*.

6.5.2 Further constraints on the Epipolar Line

As noted above, correspondence matching is reduced from *2D* (the whole image) to *1D* (the epipolar line). The solution space can be further reduced in our DBT situation. Consider the following figure:

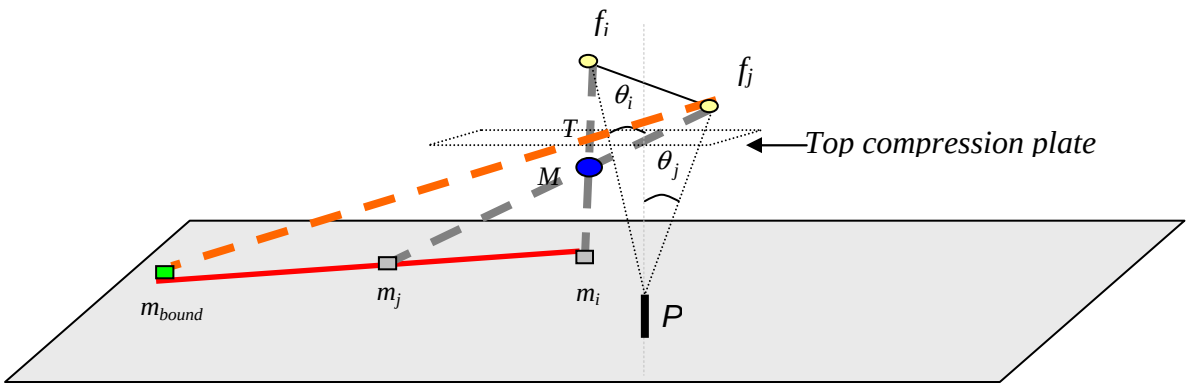

Figure 6.6: Further constraint on the solution space of our correspondence matching problem.

In the figure, we show the top compression plate. Given a projection $m_i\ (x_i, y_i, 0)^s$ by a focal spot f_i, the possible *3D* location of the microcalcification *M* is within *T* (top compression plate) and m_i. Following the geometry, this means that the possible solution space is within m_{bound} and m_i, a line segment of the epipolar line found in the previous section.

The following figures show the results of the epipolar line segment drawn on other DBT views given a projection on a view using our simulated projections:

Figure 6.7: Epipolar line segment. Projection (red circle) on DBT view 7 (0^o) (Left). Epipolar line segment drawn on view 0 (-19.65^o) (Middle). Epipolar line segment drawn on view 15 (19.98^o) (Right).

The results show that the corresponding projection points in other views indeed lie on the corresponding epipolar line segments given a projection point in one view.

6.5.3 Multiple DBT Views

To extend the concept of epipolar geometry in two views, one may think that more constraints can be employed using multiple views. We have investigated and looked for the corresponding epipolar lines in multiple views. However, due to the geometry of DBT that there is only a slight difference in the focal spot positions, the corresponding

epipolar lines are nearly overlapping. The results of using multiple views in this case are not satisfactory for our purpose. On the other hand, we have derived an epipolar curve, a curve of projection points of a 3D point generated by corresponding focal spot positions. In other words, instead of the 1D search space, we now formulate the exact 2D position of the projection points given the 3D position. Of course, we do not know the 3D position in reality, but this formulation gives us a way to solve the correspondence problem, which will be discussed in the coming sections.

6.6 Epipolar Curves: Its Derivation

In the hypothesised DBT geometry, the 2D projection points are related to the 3D position of a microcalcification $\mathbf{M}(a, b, c)^w$ and the focal spot position (which is represented by the angle θ through which the X-ray tube lever arm rotates.). We derive the equations of the projection points given a 3D position of microcalcification **M** at $(a, b, c)^w$ and θ_i.

The line that contains f_0, **M** is given by (in world coordinates):

$$x_0^w = f_o + \lambda(\boldsymbol{M} - f_o) = \begin{bmatrix} 0 \\ 0 \\ -D \end{bmatrix} + \lambda \begin{bmatrix} a \\ b \\ c + D \end{bmatrix} \qquad \textit{Eqn. 6.4}$$

This line intersects the sensor plane $z^w = L$ when $\lambda = \frac{L+D}{c+D}$. Inserting this value into the above equation:

$$\mathbf{x}_0^w = \begin{bmatrix} a\left(\frac{L+D}{c+D}\right) \\ b\left(\frac{L+D}{c+D}\right) \\ L \end{bmatrix} \qquad \textit{Eqn. 6.5}$$

$$\mathbf{x}_0^s = \begin{bmatrix} a\left(\frac{L+D}{c+D}\right) + u \\ b\left(\frac{L+D}{c+D}\right) + v \end{bmatrix}$$

Now consider projection points from equal and opposite focal points f_{+i}, f_{-i}. It is straightforward to show that:

$$\mathbf{x}_{+i}^{s} = \begin{bmatrix} D\sin\theta_i + \left(\frac{L + D\cos\theta_i}{c + D\cos\theta_i}\right)(a - D\sin\theta_i) + u \\ b\left(\frac{L + D\cos\theta_i}{c + D\cos\theta_i}\right) + v \end{bmatrix}$$

$$\mathbf{x}_{-i}^{s} = \begin{bmatrix} -D\sin\theta_i + \left(\frac{L + D\cos\theta_i}{c + D\cos\theta_i}\right)(a + D\sin\theta_i) + u \\ b\left(\frac{L + D\cos\theta_i}{c + D\cos\theta_i}\right) + v \end{bmatrix} \qquad \textit{Eqn. 6.6}$$

After further simplification, for the focal spots at θ_i and -θ_i, the 2D coordinates in the sensor coordinate frame are given by the vectors x_{+i}^{s} and x_{-i}^{s} given $(a, b, c)^{w}$ as follows:

$$\mathbf{x}_{+i}^{s} = \begin{bmatrix} a\left(\frac{L + D\cos\theta_i}{c + D\cos\theta_i}\right) + u \\ b\left(\frac{L + D\cos\theta_i}{c + D\cos\theta_i}\right) + v \end{bmatrix} + \frac{D\sin\theta_i}{c + D\cos\theta_i}\begin{bmatrix} c - L \\ 0 \end{bmatrix} = \mathbf{w}_i^{s} + \mathbf{u}_i^{s}$$

$$\mathbf{x}_{-i}^{s} = \begin{bmatrix} a\left(\frac{L + D\cos\theta_i}{c + D\cos\theta_i}\right) + u \\ b\left(\frac{L + D\cos\theta_i}{c + D\cos\theta_i}\right) + v \end{bmatrix} - \frac{D\sin\theta_i}{c + D\cos\theta_i}\begin{bmatrix} c - L \\ 0 \end{bmatrix} = \mathbf{w}_i^{s} - \mathbf{u}_i^{s} \qquad \textit{Eqn. 6.7}$$

Eqn. 6.8 is the epipolar curve at $(a, b, c)^{w}$. An example of *16* simulated DBT projection points lying on an epipolar curve is shown in *Figure 6.8*. The intersection of any two points on the epipolar curve with the corresponding 3D positions of the focal spot generating the X-rays is the 3D position of the microcalcification in the breast.

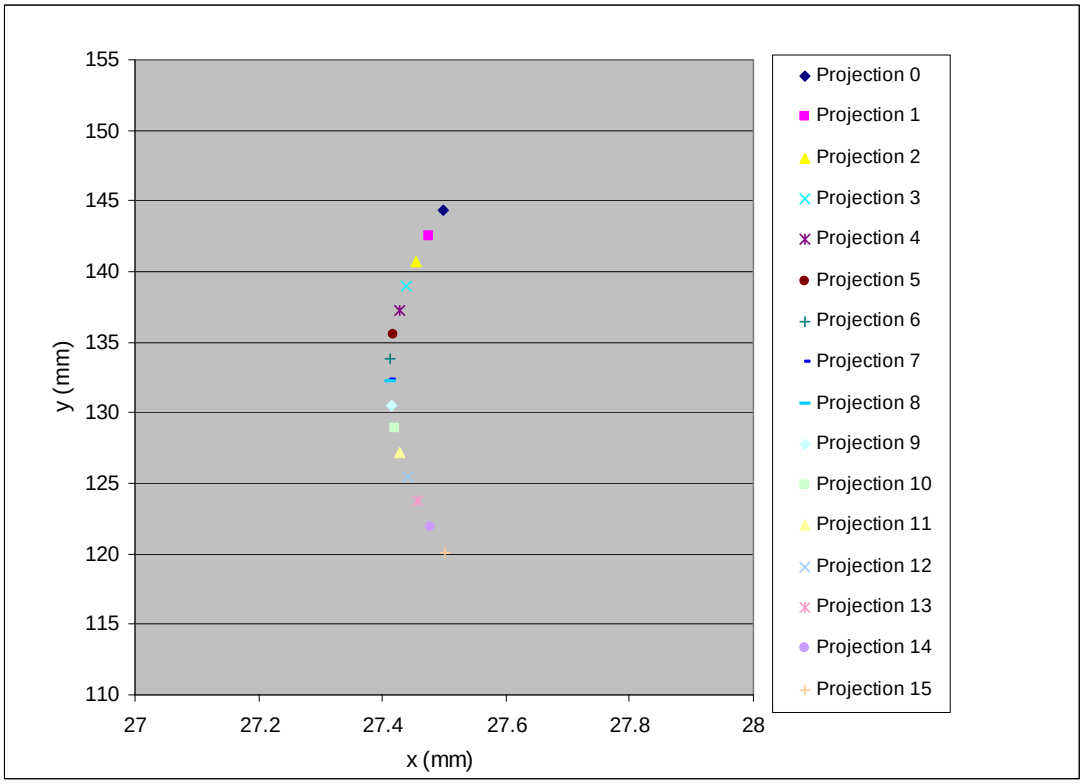

Figure 6.8: An example of an epipolar curve representing a microcalcification

6.7 Benefits of the Epipolar Curves Approach

In this section, we show how our approach helps solve the correspondence problem. We begin through the use of an example. The following figure shows *2* DBT views taken at different focal spot positions of the same simulated breast containing a diffuse cluster of *12* microcalcifications (benign) and a linear cluster of *15* microcalcifications (malignant). For simplicity, the linear cluster of *14* microcalcifications (out of *15*) are magnified and shown here:

Figure 6.9: Two DBT views at different angles obtained from the same simulated breast, magnified with a curvilinear cluster of 14 microcalcifications. Left: -0.16^o. Right: 5.5^o.

Our aim is to find the correspondences of the microcalcifications highlighted in red circles between the views as shown in the figure. We first use the epipolar geometry to address correspondence, and then we discuss how our approach can improve the sensitivity and specificity of microcalcification detection. We also briefly mention other benefits of our approach at the end of this section.

6.7.1 Solving the Correspondence Problem

In the previous section, the derivation of an epipolar curve was presented. To emphasize it, we explain it pictorially here:

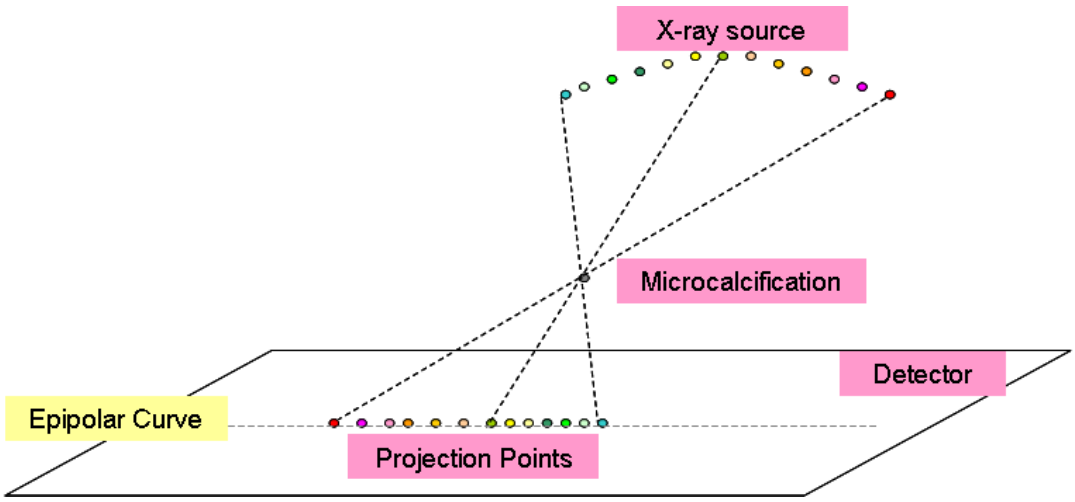

Figure 6.10: An epipolar curve representing a microcalcification

Now, if one microcalcification is represented by one epipolar curve, how about *2, 3, 4, ..., or 10...* or *n* microcalcifications? Evidently, *10* microcalcifications will be represented by *10* epipolar curves:

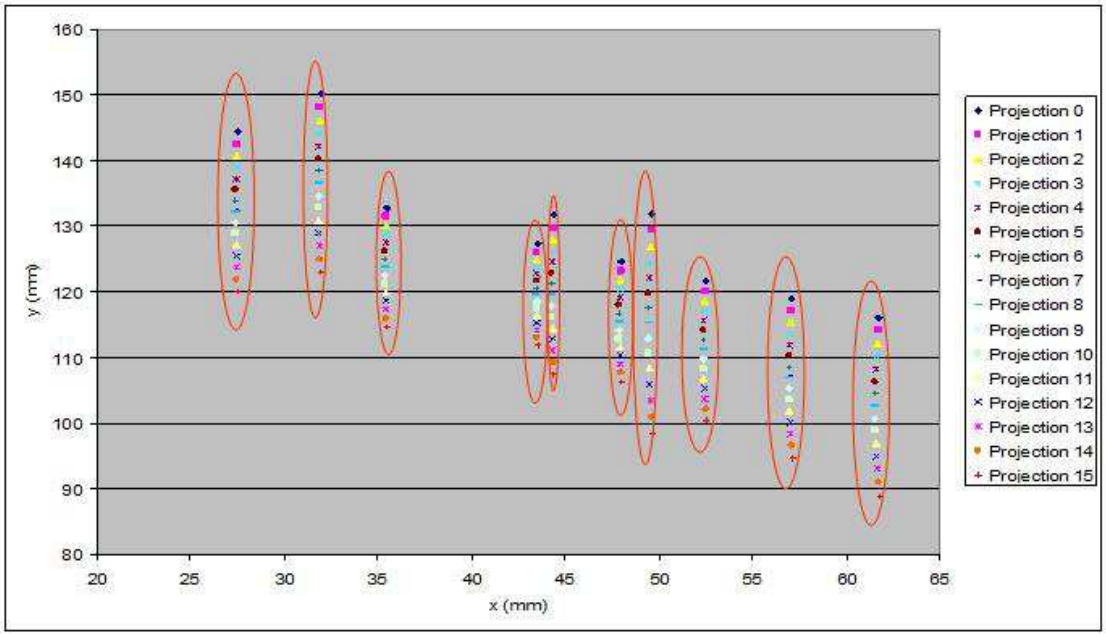

Figure 6.11: An example of 10 epipolar curves representing a cluster of 10 microcalcifications in the ideal case (One red ellipse represents one microcalcification)

So, we observe that by putting all the detected microcalcifications in all projections in the same 2D coordinate system, we can immediately determine the correspondences. Note that the projection points belonging to the same microcalcification automatically form a cluster. (Note the use of "cluster" here. It refers to the group of projection points.)

The correspondence solution to our example is therefore straightforward:

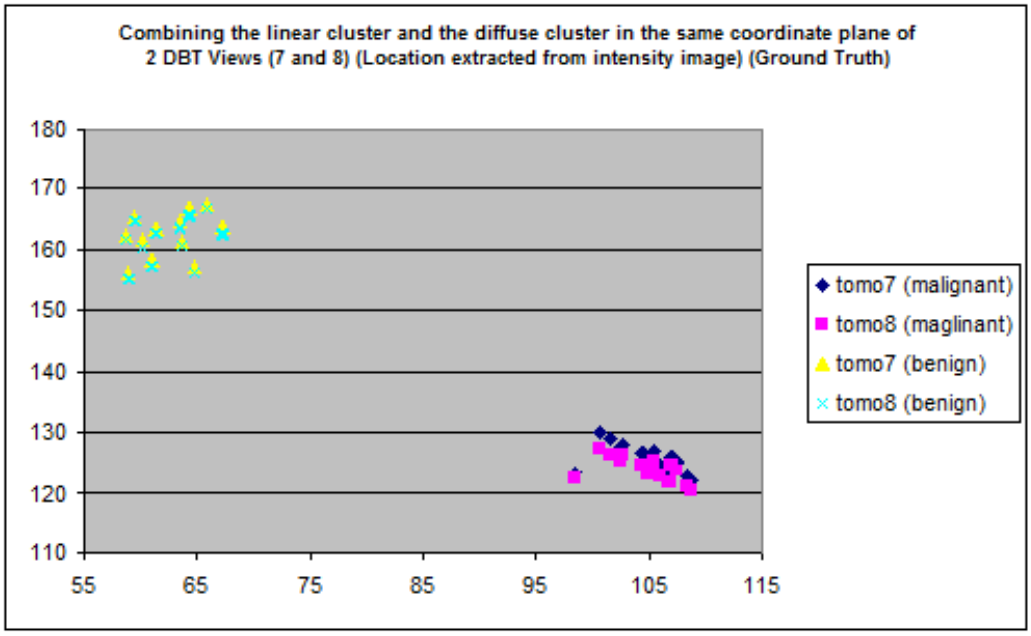

Figure 6.12: All projection points extracted from 2 DBT views in the same 2D coordinate system.

We put all the extracted projections onto the same 2D coordinate system as shown in *Figure 6.12*. For better visualization, we only show *2* DBT views. The projection points of DBT view *7* and *8* showing linear cluster of *15* microcalcifications (malignant) appear at the lower right hand corner in the figure. This is our correspondence solution. With this figure of 2D coordinate system, we can easily tell the corresponding projection points in DBT view *7* and *8*:

Figure 6.13:The correspondence answer of two DBT views at different angles obtained from the same simulated breast, magnified with a curvilinear cluster of 14 microcalcifications. Left: -0.16°. Right: 5.5°.

With the help of our epipolar curves approach, the correspondence problem is straightforward. This can be further highlighted by both circles *4* in the figure. Without

our approach, it may not be noticed at the first instance that they correspond to each other from their 2D positions. With our approach, we can give the correct answer.

6.7.2 Identify Noise Points

Our epipolar curve approach automatically distinguishes noise points from microcalcification points, based on the assumption that noise is usually random. In Section 6.5.1, we mentioned that microcalcification projection points coming from the same microcalcification form a cluster of projection points. It is unlikely that noise points are detected in the majority of DBT views such that it forms a cluster like a true microcalcification. On the other hand, noise points are more likely to be isolated points when they are viewed in the 2D coordinate system. The following figure shows such a scenario:

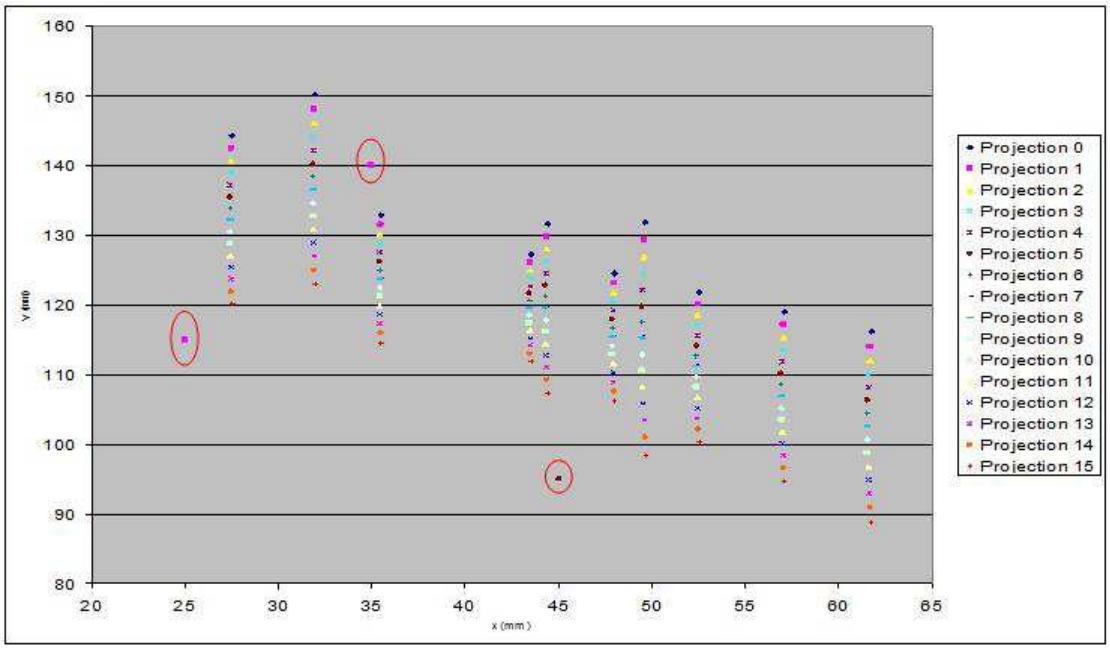

Figure 6.14: An example of 10 epipolar curves representing a cluster of 10 microcalcifications with noise points highlighted as red circle

From the figure, it is very likely that the isolated points are noise, while the other points come from true microcalcifications. This reduces the false positives and improves the specificity of microcalcification detection. This is a benefit of DBT that seems not to have been noted previously.

6.7.3 Identify Missing Points

In addition to reducing noise, another goal of any microcalcification detection algorithm is to find as many true microcalcifications as possible. We know from Section 6.7.1 that true microcalcification projection points automatically form a cluster in an orderly fashion if they come from the same microcalcification. Hence, it is easy to visualize from our epipolar curves approach where there should be microcalcification projection points:

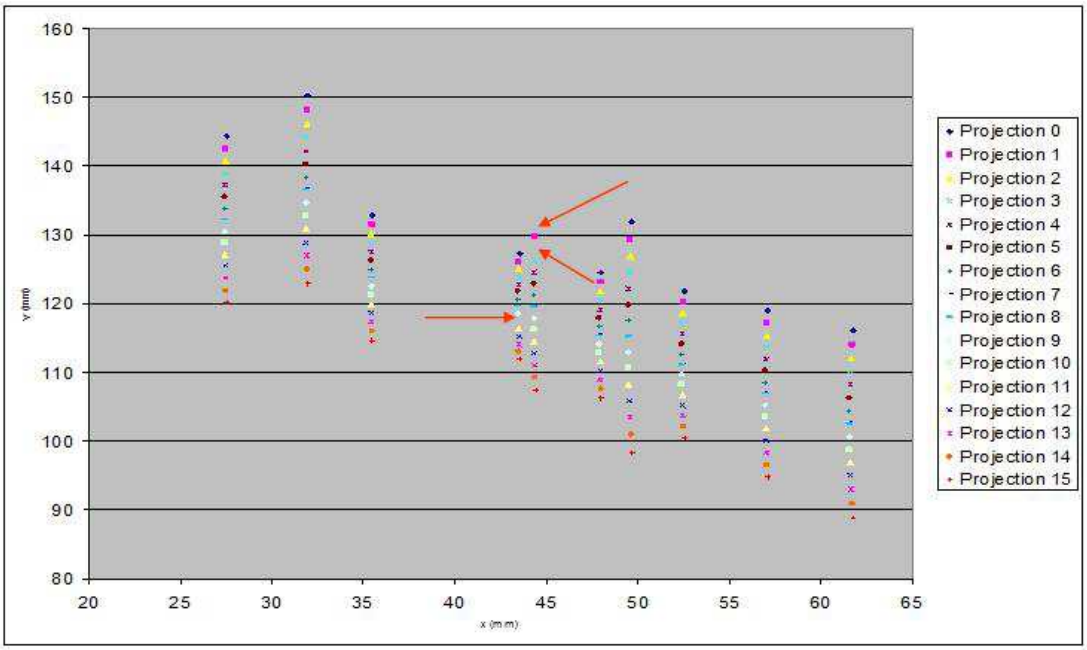

Figure 6.15: An example of 10 epipolar curves representing a cluster of 10 microcalcifications with red arrows showing some points are missed in some projections.

From the figure, it is likely that the locations indicated by the red arrows should contain microcalcification projection points from the corresponding DBT views. This improves the sensitivity in detection in individual projections. Although this may not directly help us find a microcalcification, as other corresponding points have already given us the information, this helps us in further investigation on the detection algorithms and looks for why this missing point is not detected and subsequently helps refine the algorithms.

6.7.4 Other Benefits

Epipolar curves provide a new perspective in DBT research. In addition to the detection improvement mentioned and to be discussed in Chapter 7 and 8, we are now ready to

reconstruct the microcalcification clusters (to be discussed in Chapter 9). Moreover, the approach further helps registration and convention DBT reconstruction (reconstruction of the whole breast). By extending the concepts to simply a normal 3D point, we can add constraints based on our epipolar curves during registration and reconstruction, improving the outcomes (for future work).

6.8 Clustering Methods for the Extraction of Microcalcifications Using Epipolar Curves

To automate the process of detecting microcalcifications using epipolar curves, clustering algorithms are required to group points found in the individual projection images into epipolar curves, alternatively rejecting them as noise. There are many different possible algorithms to serve this purpose. We have developed two such. One is the application of the Hough transform, a feature extraction technique which can help identify lines in an image. We discuss the Hough transform in the next section. In this section, another algorithm is applied. This is because this algorithm highlights the necessary considerations when designing such a clustering algorithm, so that better algorithms can be designed and developed in future based on these observations and considerations.

6.8.1 Background Information

Recall that the first step in the detection process is the application of a detection algorithm to each of the individual projection images in order to identify candidate microcalcifications, similar to the methodology applied in mammography, except now that we apply the detection algorithms to multiple projections. Of course, the poor signal-to-noise ratio of the individual projection images means that some of the candidates will turn out to be noise points, and, equally, some microcalcifications may be missed in some views. Either way, the input to the clustering algorithm is a list of the 2D positions of all the microcalcification candidates. The output of the clustering algorithm is the set of clusters of 2D points, each of which corresponds either to an epipolar curve (hence a microcalcification tracked over most of the projections) or is identified as a noise point. The algorithm also indicates those microcalcifications that

have been missed in which (small number of) views. It also indicates the likely positions in the projection images, potentially enabling a subsequent application of the detection algorithm with adapted parameters, such as local thresholds.

In the initial test reported in this Chapter, in order to evaluate our method against ground truth, we used the X-ray simulation software developed by Tromans [31] to generate simulated DBT views of a cluster containing *15* spherical microcalcifications with radii ranging from *0.0355* to *0.075* mm and lying in a curvilinear arrangement (to simulate a ductal set, to which we return in a later chapter). Statistical noise of the amount expected with current detectors in each acquisition image is added to better simulate reality. As a demonstration, we selected the middle *7* DBT views out of the total *15* views, taken at angles -8.65^o, -5.81^o, -2.99^o, -0.16^o, 2.67^o, 5.5^o, 8.33^o (we refer to these as tomo4, tomo5, tomo6, tomo7, tomo8, tomo9, tomo10 respectively). Note that the angles used follow a plausible DBT acquisition geometry. We have deliberately chosen one of the simplest detection algorithms, namely a top hat transformation, which effectively equates microcalcifications with small, locally bright points, and is expected to miss fainter microcalcifications [124].

In our plausible DBT acquisition system, D = *660* mm, L = *40* mm, *u = 143.36* mm, *v = 232.96* mm and detector resolution = *0.07* mm. We have also used these settings in the demonstration. Also, in this example, the *x*-, *y*- coordinates are directly obtained from the projections and the coordinate frame used is the one used by the simulated software. A coordinate frame transformation is applied to transform it to our sensor coordinate frame used in the derivation of the epipolar curve. Here, for *x*-coordinate, we mean the transformation of the 2^{nd} element in *Eqn. 6.7*; for *y*-coordinate, we mean the transformation of the 1^{st} element in *Eqn. 6.7*.

6.8.2 Observations

Our clustering technique is based on the following observations, which would have analogues in any similar acquisition geometry:

1. *Eqn. 6.7* implies that the DBT views generated from equal but opposite directions (θ_i and $-\theta_i$) will have the same value in one of the coordinates. By assigning typical values used in DBT into the variables in the equation, this implies that the *x* values from the *7* projections are nearly equal.

2. The values in the other axes will follow a specific order with respect to the angles taken to generate the DBT views. In this case, the *y* values are in descending order with respect to the angles taken to generate the DBT views and the differences in *y* values between neighbouring projections are very similar for the same microcalcification.
3. Due to the sizes of the microcalcifications and the viewing angles, the number of projection points for each microcalcifications captured in each DBT view are different.
4. Since noise is assumed to be random and is statically generated randomly, it is expected that a noise point in a projection appear as a single point.
5. The superimposition problem in mammography implies that one projection point may be generated from *2* or more microcalcifications in the breast. However, this situation is unlikely in all but a minority of DBT views, due to different acquisition angles and differences in the 3D positions of the microcalcifications. In Observation *2*, we mentioned that the differences in *y* values between neighbouring projections are very similar for the same microcalcification. For different microcalcifications at different 3D positions, this "differences" varies.

6.8.3 Clustering Steps

Taking account of the above observations, our clustering method comprises *6* steps:

1. Sort all the points in ascending order of *x* values and descending order of *y* values. (Observations *1, 2*)
2. Classify the points into noise points and into groups of same *x* values.
3. If only one point has a particular *x* value, label this point as a noise point. (Observation *4*)
4. Assign points having same *x* values into same group. (Observation *1*)
5. Determine noise points within a group. The noise points are those points whose *y* values do not follow the specific order with respect to the angles. (Observations *2*)
6. Combine groups with *x* and *y* values within a preset range into a cluster. This is because a microcalcification can be larger than one pixel in a projection. (Observation *3*)

6a. Check each cluster and see whether it should be split due to projection points being too close together but actually they are coming from different microcalcifications. (c.f. superimposition problem in mammography or microcalcifications in the breast are being too close to each other.) (Observation *2*, *5*)

6b. Recheck the noise points. If they are within a preset distance from a cluster, include it in the cluster. One cluster corresponds to one microcalcification. (Observation *3*)

6.8.4 Results

Figure 6.16 shows the ground truth of all the projection points of *15* microcalcifications from *7* DBT views obtained visually and manually. We have assigned a number *1* to *15* to each microcalcification for identification. The inputs of our clustering technique are points detected by top hat in each DBT view.

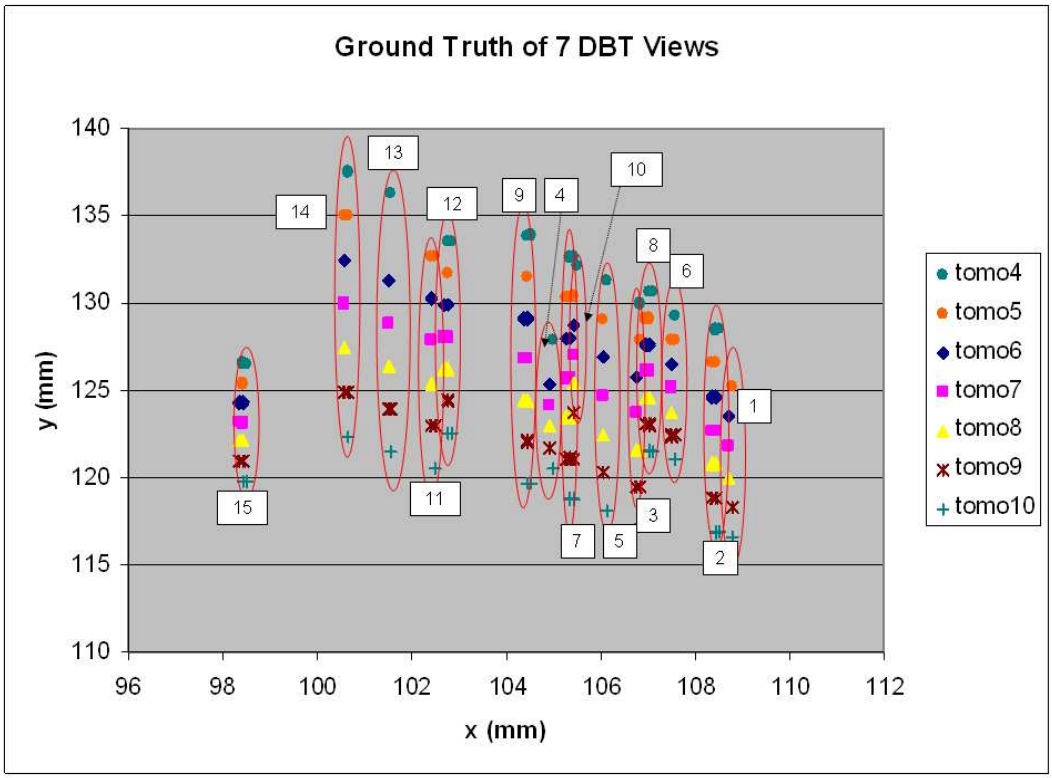

Figure 6.16: Ground truth of all the projection points of 15 microcalcifications from 7 DBT views obtained visually and manually. (Note: Some microcalcifications cannot even be visualized by human eyes in tomo4 (microcalcification 1), tomo5 (microcalcifications 4, 13) and tomo10 (microcalcification 10) due to limitations in acquisition.)

The detection results by top hat in each individual DBT view are recorded in *Table 6.1*:

DBT view	Microcalcification detected	No. of microcalcifications detected in each view	No. of noise points detected
tomo4	2,6,7,8,9,12,14,15	8	2
tomo5	1,2,5,6,7,8,9,11,12,14,15	11	4
tomo6	2,5,6,7,8,9,10,12,14,15	10	1
tomo7	2,7,8,9,11,12,13,14,15	9	5
tomo8	2,3,5,6,7,8,9,11,12,15	10	7
tomo9	2,3,7,8,9,10,11,15	8	1
tomo10	2,7,8,9,11,12,14,15	8	0
		Max no. detected: 11	Total (3 views: 13 7 views: 20)

Table 6.1. Detection results of individual projections (tomo4 to tomo10) using top hat transformation.

To assess the effects of using different number of DBT views, we applied our clustering algorithm using *3* and *7* DBT views. The detection results are shown graphically in *Figure 6.17*:

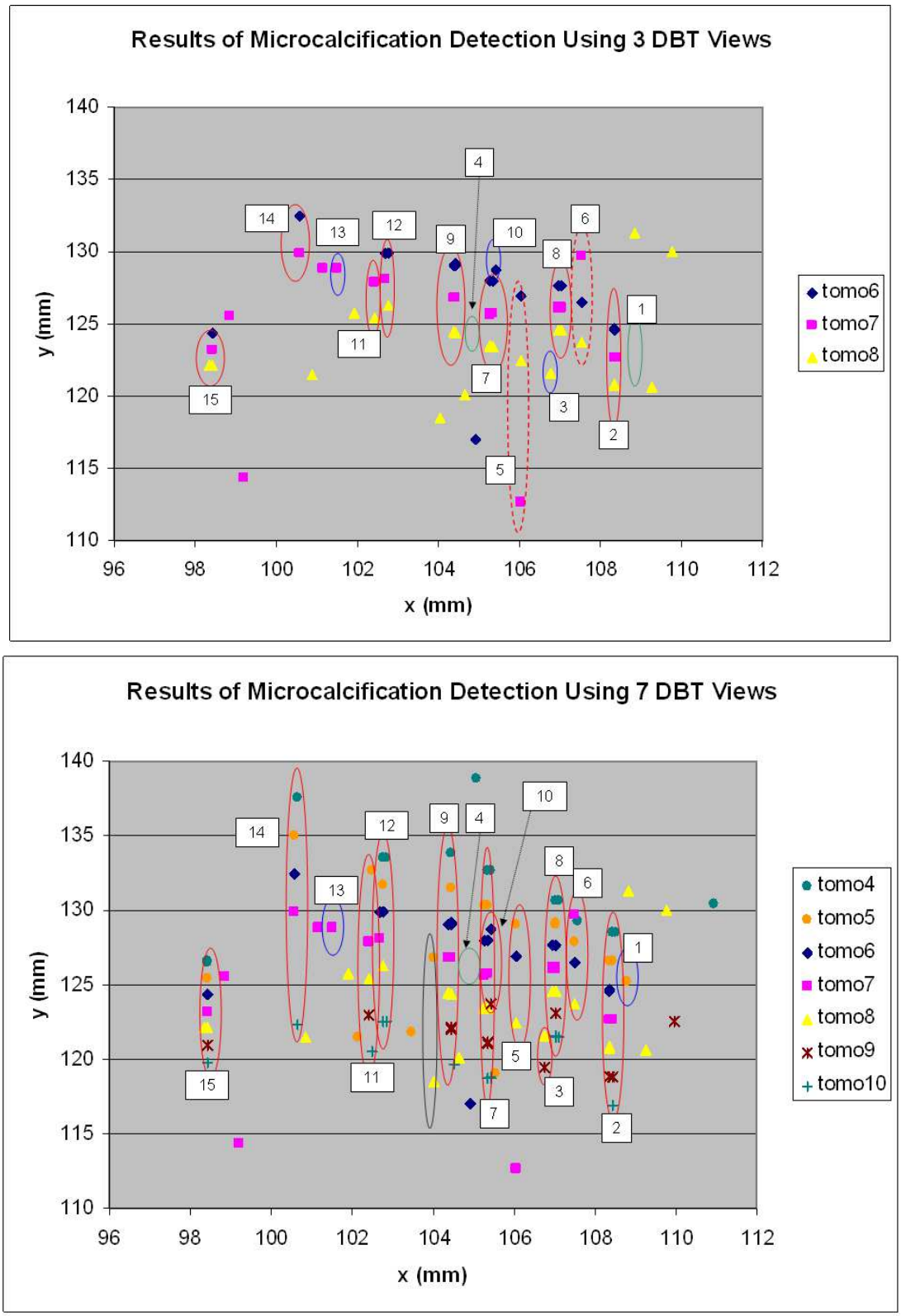

Figure 6.17: Detection results using epipolar curves. Top: 3 views; Bottom: 7 views. (Red Ellipses: True Positives; No Ellipse: True Negatives; Black Ellipses: False Positives; Green/Blue Ellipses: False Negatives; Dotted Red Ellipses: True Positives/False Negatives (depends on implementation.)

and are summarized in *Table 6.2*:

No. of Views used	True Positives (out of 15 microcalc.) (counted as no. of clusters)	True Negatives (counted as isolated points)	False Positives (counted as no. of clusters)	False Negatives (out of 15 microcalc.) (counted as no. of clusters)	Uncertain (counted as no. of clusters)
3	8 (2, 7, 8, 9, 11, 12, 14, 15)*	11	0	5 (1, 3, 4, 10, 13)*	2 (5, 6)*
7	12 (2, 3, 5, 6, 7, 8, 9, 10, 11, 12, 14, 15)*	18	1	3 (1, 4, 13)*	0

* refers to the microcalcifications.

Table 6.2. Detection results of using epipolar curve approach. (The effects of using different no. of views are also shown.)

The algorithm is explained pictorially by magnifying the detection results using *7* DBT views (*Figure 6.17 bottom*) in *Figure 6.18*:

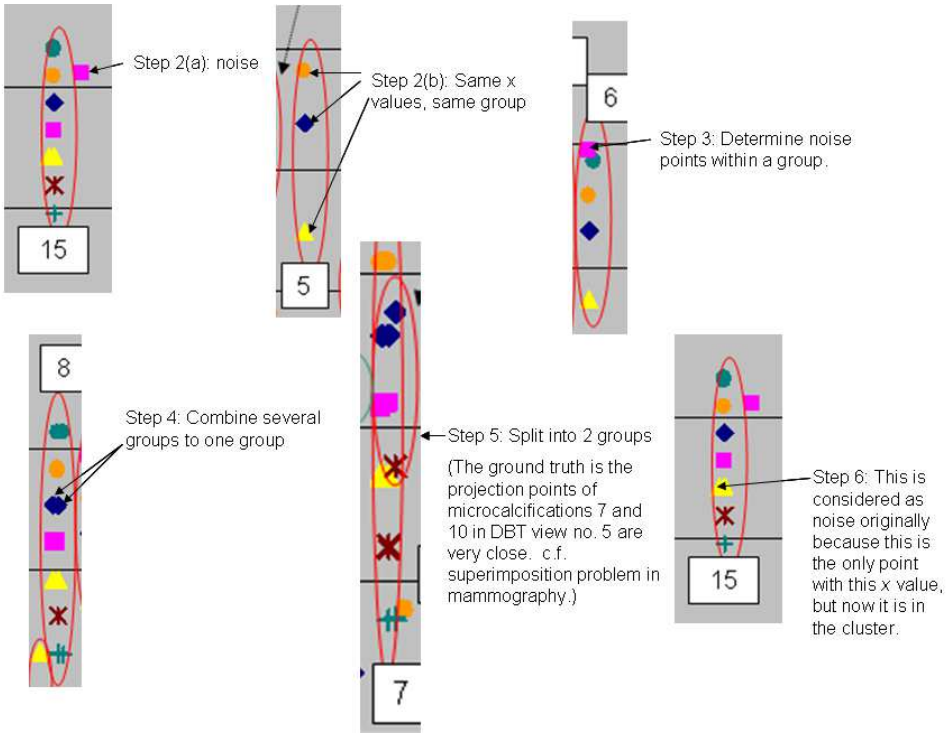

Figure 6.18: Explanation of the clustering algorithm step-by-step pictorially (Extracted from Figure 6.17 Bottom).

It can be seen that the epipolar curves can greatly improve the detection process. Most of the noise points (false positives) can clearly be distinguished. If we use more views (*7* in this example), the results are better than those in any individual projection. We can detect *12* microcalcifications using *7* views while at most *11* microcalcifications are detected in any single projection. In addition, it tells us which points are missing in

the view by looking at the clusters. This allows us to adapt our detection algorithms for better results.

6.9 Application of the Epipolar Curves Approach: A Real Example

In this section, we demonstrate the use of our epipolar curves approach in a real DBT projection image set.

6.9.1 A Real DBT Projection Image Set

We have obtained a real image set showing a region of a breast containing a number of bright white spots which are possibly microcalcifications. In this study, we have extracted these bright white spots for analysis. A magnified view is shown here:

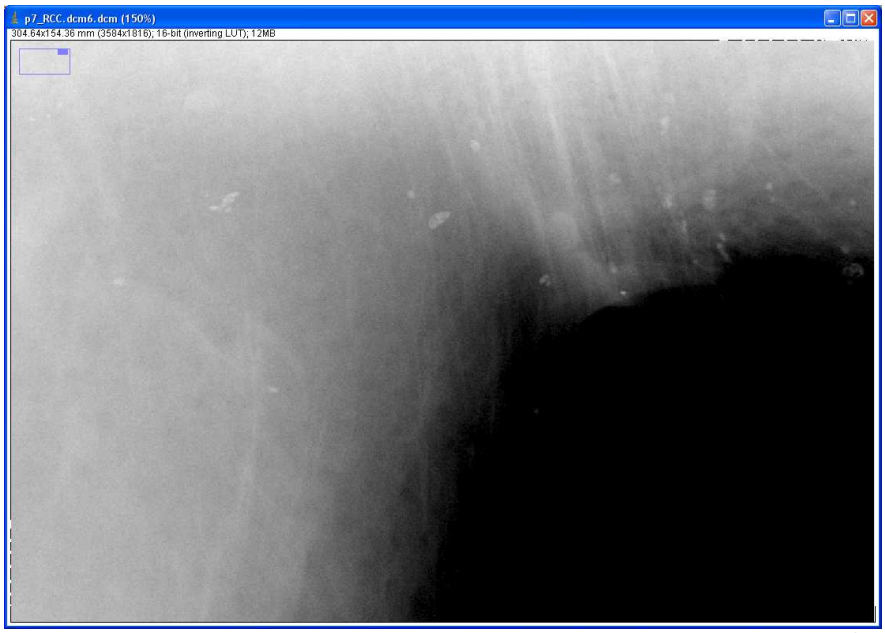

Figure 6.19: A magnified view of one of the 13 real X-ray projection images taken at -0.042^o containing a number of bright white spots.

6.9.2 Geometry of DBT Prototype Machine

The geometry of the commercial prototype machine used to generate the DBT set is almost the same as the one mentioned in Section 6.4, except that there is an offset in the *y*-direction of the world coordinate frame defined, of the source position from the plane containing the pivot point, the origin of the world coordinate frame. It is presented as follows:

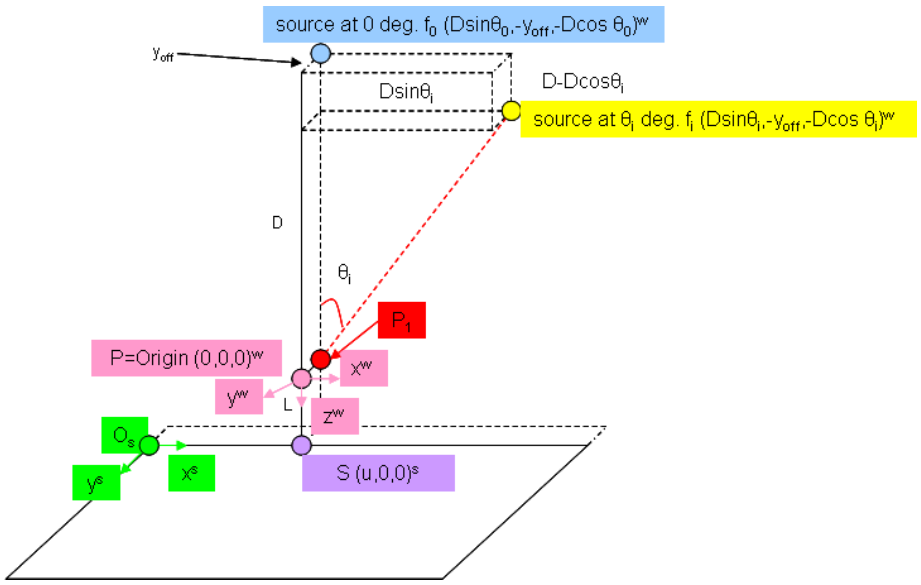

Figure 6.20: Geometry of DBT prototype machine.

Some points regarding the geometry are highlighted:

1. X-ray tube moves in the plane $y^w = y_{off} = 5.95$ mm.
2. z^w is orthogonal to the image plane and is pointing downward.
3. Image plane coordinates are chosen so that x^s and y^s are parallel to x^w and y^w respectively.
4. L (= *53* mm) is the height of the origin P from the detector.
5. D (= *64 0*mm) is the length of the rotation arm.
6. θ_i is the angle the X-ray tube rotates for each view i, ranged between 17.01^o to -17.00^o for *13* projections, approximately 3^o between each view.
7. $S=(u,v,0)^s(=(u,0,0)^s)$ is the intersection point between the line passing through the origin and perpendicular to the image plane and the image plane.

6.9.3 Derivation of an Epipolar Curve

Using the DBT geometry discussed in the previous section and similar derivation in Section 6.6, the equations of the projection points given a 3D position of microcalcification m at $(a, b, c)^w$ and θ_i are derived:

$$\begin{bmatrix} x_i^s \\ y_i^s \end{bmatrix} = \begin{bmatrix} D\left(1-\frac{L+D\cos\theta_i}{c+D\cos\theta_i}\right)\sin\theta_i + \left(u + a\left(\frac{L+D\cos\theta_i}{c+D\cos\theta_i}\right)\right) \\ -y_{off} + v + (b+y_{off})\frac{L+D\cos\theta_i}{c+D\cos\theta_i} \end{bmatrix} \qquad \textit{Eqn. 6.9}$$

6.9.4 All Detected Microcalcification Candidates in the Same 2D Coordinate System

After the detection results of each DBT view are obtained (Detection algorithms are discussed in Chapter 7.), they are put in the same 2D coordinate system as shown:

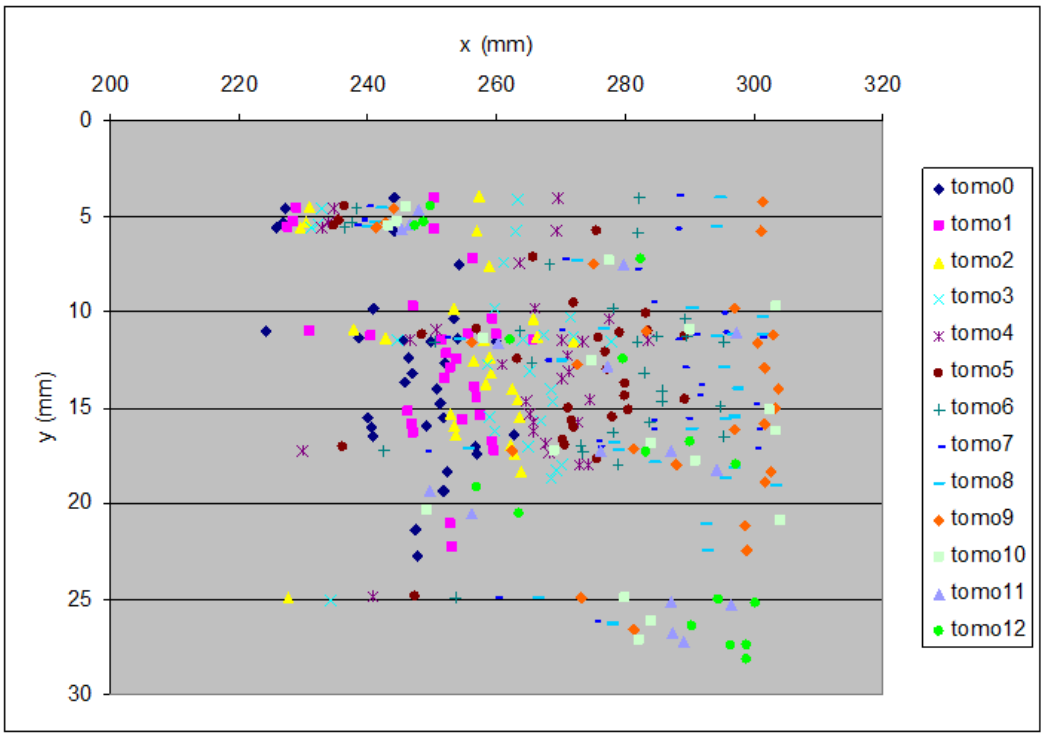

Figure 6.21: All microcalcification candidates detected from 13 DBT views on the same 2D coordinate system.

At a first glance, it seems that reality is more complex than the simulated examples mentioned in previous sections. However, the majority of the detected projection points tend to form different clusters which are consistent with *Eqn. 6.10*, that we say the points in a cluster have similar *y* position. The benefits of our epipolar curves approach can still be applied and are highlighted as follows:

1. Correspondence matching

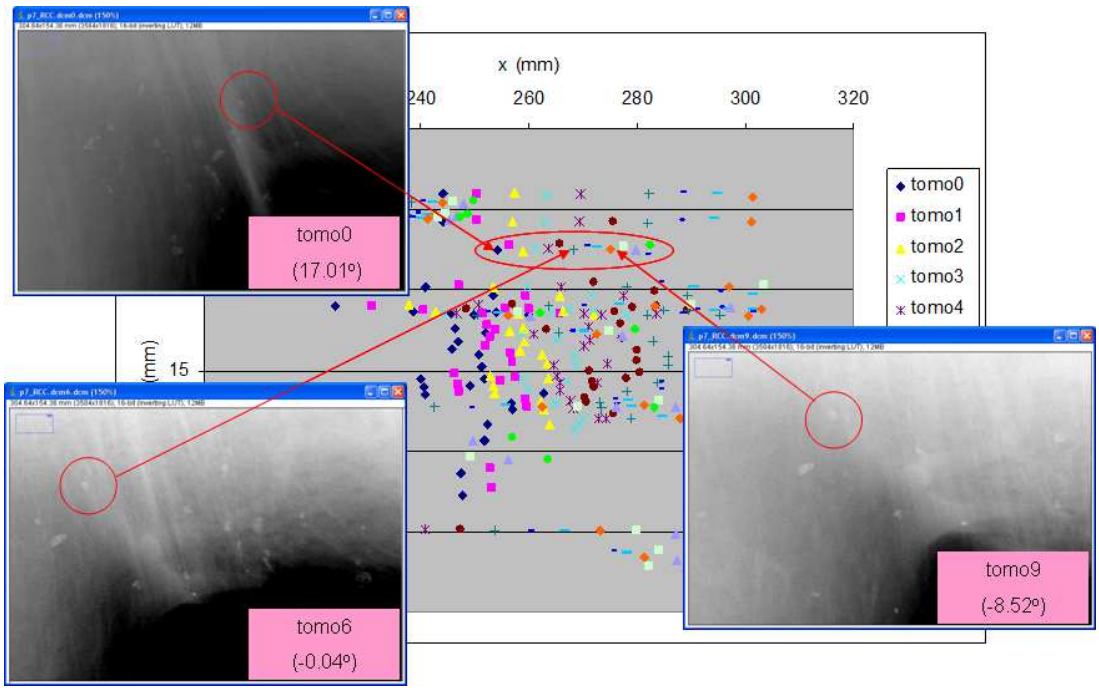

Figure 6.22: Correspondence in 3DBT views.

This is possible to visualize some clusters of projection points generated from same microcalcifications in the breast. In the figure, one of the clusters is circled in red. The corresponding microcalcification projections of *3* of the *13* DBT views are also circled in red.

2. Identification of noise points and missing points

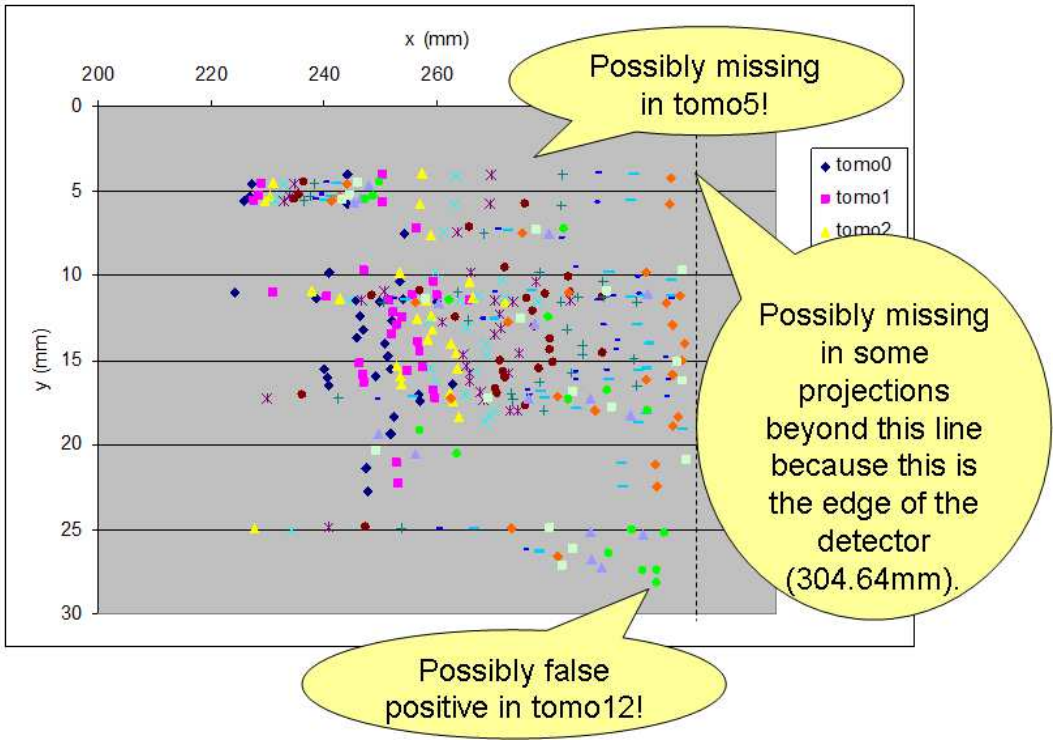

Figure 6.23: Identification of noise points and missing points.

In the figure, *3* cases have been highlighted e.g. a projection point is possibly missed in DBT view *5*; a noise point is wrongly considered as a microcalcification in DBT view *12*. Our approach can also help point out the deficiency of the acquisition system and hence the failure in generating the projection. The dotted line represents the edge of the detector. We can deduce from the figure that some projection points cannot be captured because the detector is too small.

6.9.5 More on Epipolar Curves

As shown in the previous section, some clusters in the 2D coordinates diagram can be easily visualized and grouped both manually and automatically. However, one may argue the feasibility of the epipolar curves approach and question whether any clustering can be applied in situations where it is not that obvious:

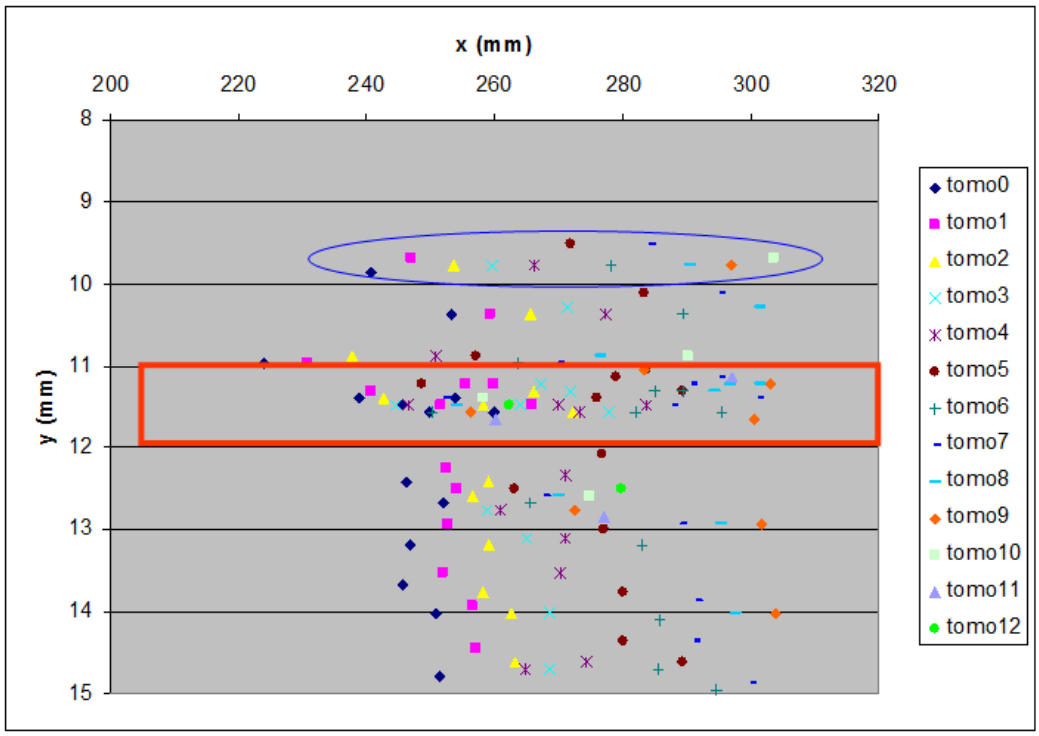

Figure 6.24: A closer look at the 2D coordinates diagram e.g. cluster circled in blue can be visualized easily, clusters inside the red box may not be easily distinguished at the first instance.

In the figure, some clusters may be easily identified e.g. the one in the blue ellipse. Note that the projection points in the same cluster will have similar *y*-coordinates. However, some clusters cannot be distinguished visually e.g. there should be more than one cluster in the red box and some better algorithms are definitely required in order to distinguish the clusters.

In the following, two parts are presented to explain how the clustering method is developed. Our observations regarding the distribution of the projection points are presented first, followed by the mathematical explanation of the phenomenon:

1. Observations

In order to tackle the problems, we have first observed the distribution of the projection points inside the red box. To make the things simple, since the *y*-coordinates of these projection points are all within *11-12* mm, we ignored the *y*-coordinates for the time being and drew the plot of the *x*-coordinates against the projection ID of all the projection points inside the box:

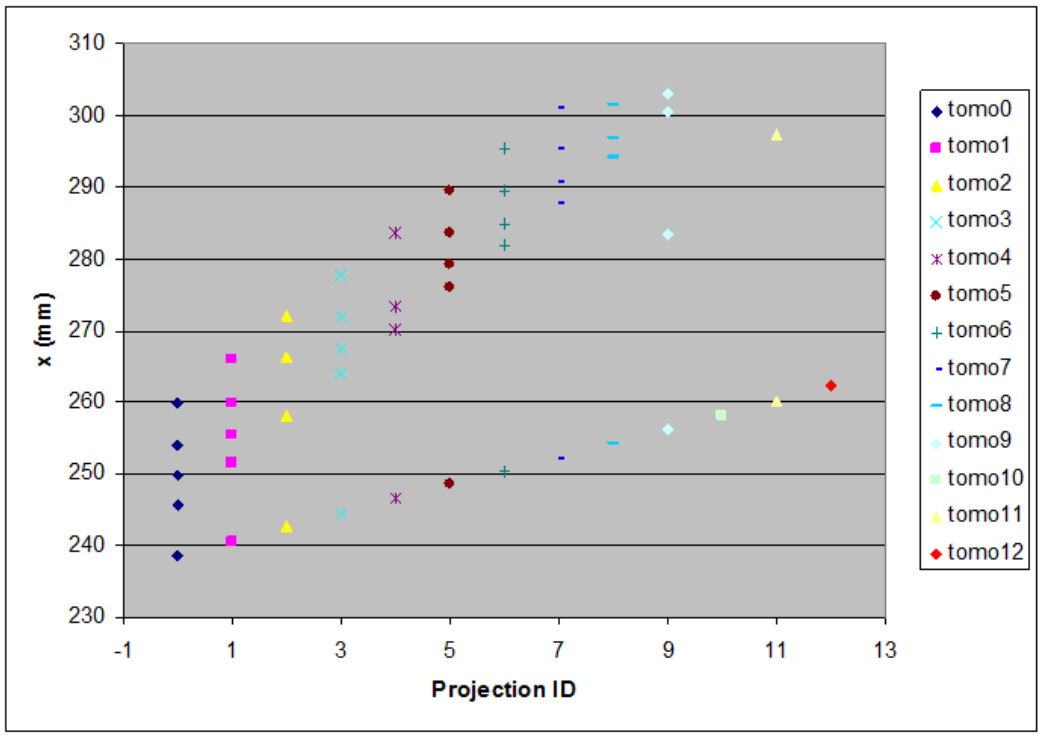

Figure 6.25: A plot of projection points of x-coordinate against the corresponding projection id where y-coordinate is between 11mm and 12mm.

Immediately, it appears that there should be *5* clusters of projection points in this figure. If we develop some mathematical support for this case, then our clustering task will then be solved very easily.

Before we move on, *2* observations regarding the projection points in the same cluster are reiterated as follows:

Observation *1*:

The *y*-coordinates are approximately the same.

Observation *2*:

(a) The *x*-coordinates have approximately equal spacing;

(b) Plotting the *x*-coordinates against projection id gives a straight line with slope *s*.

2. Mathematical Explanation

Recall that we have derived the epipolar curves as:

$$\begin{bmatrix} x_i^s \\ y_i^s \end{bmatrix} = \begin{bmatrix} D(1-\frac{L+D\cos\theta_i}{c+D\cos\theta_i})\sin\theta_i + (u+a(\frac{L+D\cos\theta_i}{c+D\cos\theta_i})) \\ -y_{off} + v + (b+y_{off})\frac{L+D\cos\theta_i}{c+D\cos\theta_i} \end{bmatrix} \qquad \textit{Eqn. 6.11}$$

In the equation, there is a non-linear term $\frac{L + D\cos\theta_i}{c + D\cos\theta_i}$ which is one of the major terms controlling the positions of the projection points of different focal spot positions. Hence, we will take a look at the change between the $(i+1)^{th}$ and the i^{th} term. Note that the angle separation between DBT view $(i+1)$ and view i is approximately 3^o i.e. 0.05 radians. We call it δ_i radians (i.e. $\delta_i = \theta_{i+1} - \theta_i$). It follows that $\cos\delta_i \approx 1$ and $\sin\delta_i \approx \delta_i$.

Using Trigonometry Formula, the approximation we have just made and the Maclaurin Series $(1-x)^{-1} = 1 + x + x^2 + x^3 + \ldots$, we have:

$$
\begin{aligned}
&\frac{L + D\cos\theta_{i+1}}{c + D\cos\theta_{i+1}} \\
&= \frac{L + D\cos(\theta_i + \delta_i)}{c + D\cos(\theta_i + \delta_i)} \\
&\approx \frac{(L + D\cos\theta_i) - D\delta_i \sin\theta_i}{(c + D\cos\theta_i) - D\delta_i \sin\theta_i} \\
&= \frac{L + D\cos\theta_i}{c + D\cos\theta_i}\left(1 - \frac{D\delta_i \sin\theta_i}{(L + D\cos\theta_i)}\right)\left(1 - \frac{D\delta_i \sin\theta_i}{(c + D\cos\theta_i)}\right)^{-1} \\
&= \frac{L + D\cos\theta_i}{c + D\cos\theta_i}\left(1 - \frac{D\delta_i \sin\theta_i}{(L + D\cos\theta_i)}\right)\left(1 + \left(\frac{D\delta_i \sin\theta_i}{(c + D\cos\theta_i)}\right) + \left(\frac{D\delta_i \sin\theta_i}{(c + D\cos\theta_i)}\right)^2 + \ldots\right) \\
&= \frac{L + D\cos\theta_i}{c + D\cos\theta_i}\left(1 + \frac{(L - c)D\delta_i \sin\theta_i}{(L + D\cos\theta_i)(c + D\cos\theta_i)} + O(\delta_i^2)\right)
\end{aligned}
$$

Note that the values of the last 2 terms are negligible when using typical values in our real example. e.g. when $L = 53\ mm$, $D = 640\ mm$, $\theta_i = 17.01^o$, $c = -53\ mm$, $\frac{(L - c)D\delta_i \sin\theta_i}{(L + D\cos\theta_i)(c + D\cos\theta_i)} \approx 0.0027$.

Hence, $\left(\frac{L + D\cos\theta_{i+1}}{c + D\cos\theta_{i+1}}\right) \approx \frac{L + D\cos\theta_i}{c + D\cos\theta_i}$

If we take a look at the epipolar curve again:

$$
\begin{bmatrix} x_i^s \\ y_i^s \end{bmatrix} = \begin{bmatrix} D\left(1 - \frac{L + D\cos\theta_i}{c + D\cos\theta_i}\right)\sin\theta_i + \left(u + a\left(\frac{L + D\cos\theta_i}{c + D\cos\theta_i}\right)\right) \\ -y_{off} + v + (b + y_{off})\frac{L + D\cos\theta_i}{c + D\cos\theta_i} \end{bmatrix} \qquad \textit{Eqn. 6.12}
$$

This justifies the observations presented in the previous section:

Observation 1:

The *y*-coordinates are approximately the same.

Explanation:

Projection points coming from same microcalcification at *(a, b, c)* will have *y*-coordinates approximately equal to a constant $-y_{off}+v+(b+y_{off})\frac{L+D\cos\theta_i}{c+D\cos\theta_i}$.

Observation 2:

(a) The *x*-coordinates have approximately equal spacing;

(b) Plotting the *x*-coordinates against projection id (i.e. view i) gives a straight line with slope *s*.

Explanation:

$x_i^s = D(1-\frac{L+D\cos\theta_i}{c+D\cos\theta_i})\sin\theta_i+(u+a(\frac{L+D\cos\theta_i}{c+D\cos\theta_i})$ is an equation of a straight line where the slope and y-intercept of this line are $D(1-\frac{L+D\cos\theta_i}{c+D\cos\theta_i})$ and $(u+a(\frac{L+D\cos\theta_i}{c+D\cos\theta_i})$ respectively. Plotting the *x*-coordinates against $\sin\theta_i$ results in a straight line. (Since $\sin\theta_{i+1}-\sin\theta_i$ will give an approximate constant for consecutive DBT views, plotting the *x*-coordinates against projection id will give a straight line as well.)

Finally, a better clustering algorithm can be developed for grouping projection points belonging to the same microcalcification.

6.9.6 Epipolar Clustering Algorithm – Hough Transform

With the mathematical explanation discussed in the previous section, now we can use one of the line detection techniques, the Hough transform [125], to perform clustering of *Figure 6.24*.

(a) Brief introduction of the Hough transform

The Hough transform (HT) is a feature extraction technique to detect a particular shape in an image, in this case, a straight line. The following figure explains another form of the equation of a straight line using α, the angle between the line perpendicular to the straight line and the origin, and ρ, the perpendicular distance between the straight line and the origin:

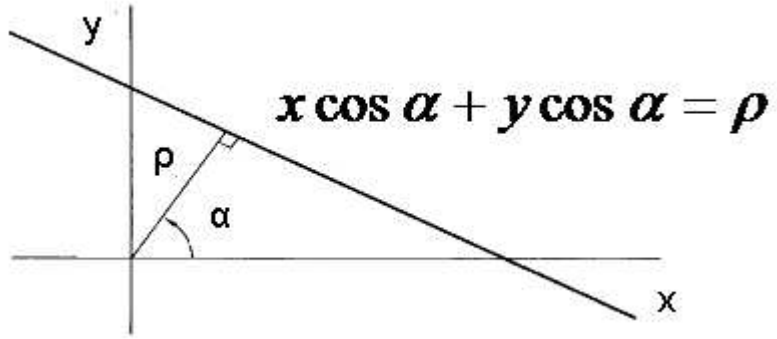

Figure 6.26:Another form of an equation of a straight line using α and ρ .

In other words, any point *(x, y)* lying on the same line will have the same α and ρ. HT is based on the fact that for image points lying on the same straight line, they will have the same pair (ρ,α). Initially, a full set of HT accumulator arrays of all possible combinations of pairs (ρ,α) with counts equal to *0* is set up. Each HT accumulator array will store the votes of pair (ρ,α) representing the straight lines that each image point may lie on. The more the number of votes in the array of (ρ,α), the more image points are contributing to the corresponding straight line (ρ,α). The algorithm returns the (ρ,α) pair if the number of votes exceeds a certain threshold values, indicating that certain number of image points lying on the same straight line (ρ,α).

(b) Applying HT to the real example

In the real example, there are *13* DBT views. For each cluster representing the same microcalcification, we ideally have *13* votes in the HT accumulator array. Of course, due to approximation or detection failure, the number of votes may differ. Our clustering algorithm will try to find the straight line with *13* votes first, then *12* votes, then *11* and so on. After a cluster is found, the projection points in this cluster will then be removed for finding next cluster of points. Here are the clustering results of using HT in our previous example in *Figure 6.27*:

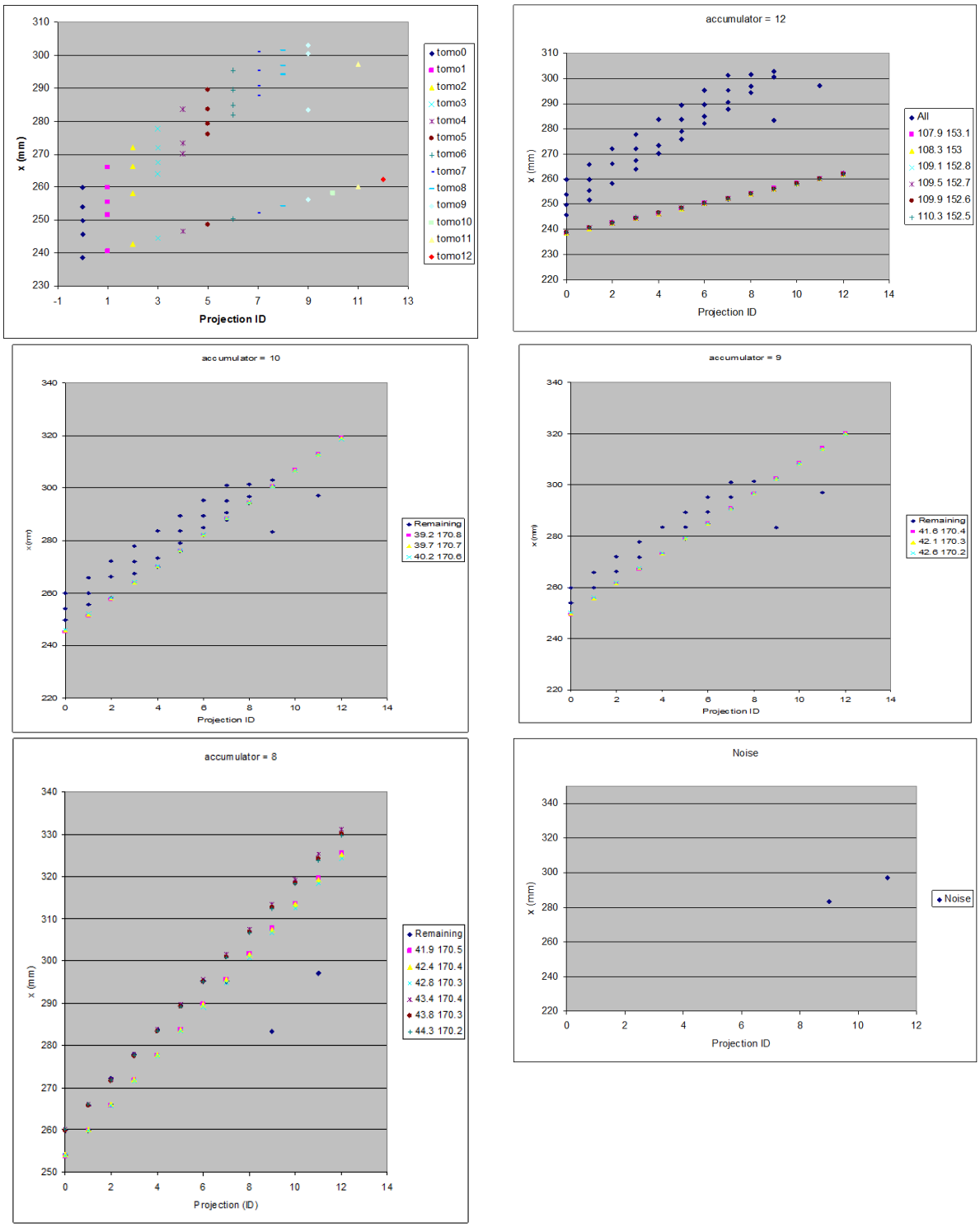

Figure 6.27: Clustering results of using HT. Top Left: The original image of projection points we want to cluster. Bottom Right: The remaining projection points unable to cluster. Other: Projection points belonging to the same straight line found using different threshold values of the accumulator counts in a descending order (Note: the legends represent the (ρ, α) pair.)

In the figure, we can find *5* straight lines using a descending order of threshold values for the accumulator counts.

(c) Other clusters found at different *y*-coordinates

The following shows some more examples of clusters found at different *y*-coordinates:

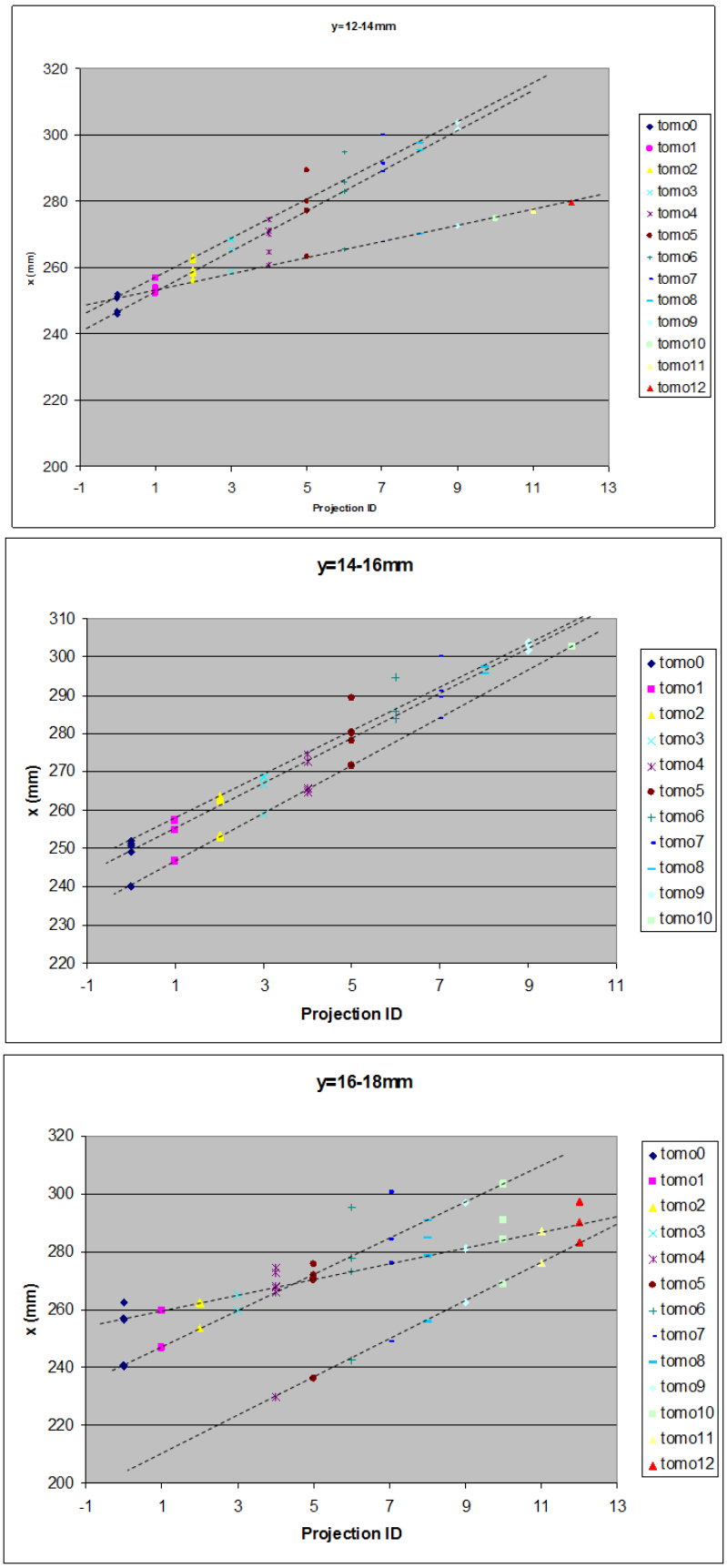

Figure 6.28: 9 clusters are found at different y-coordinates (12-14mm, 14-16mm, 16-18mm).

6.10 Conclusions and Discussion

In this chapter, we have proposed a novel approach to microcalcification detection and reconstruction in DBT. There are a lot of advantages of this approach: Firstly, the correspondence of projection points across different projection views can be determined through different epipolar clustering algorithms. One such algorithm using the Hough transform has been discussed. Secondly, the noise points can be isolated and missing points can be identified. Thirdly, reconstruction is allowed with the correspondence information. In addition to these, the approach has various extensions (to be discussed in the following chapters) which can further improve the detection results.

Chapter 7

Epipolar Curves Approach I: An Adaptive Approach in Microcalcification Detection in Individual DBT Projections

Microcalcification detection is one of the most important tasks in the early detection of breast cancer. In this chapter, we "borrow" and extend some previously described microcalcification detection techniques to DBT projections, and introduce an adaptive approach using our findings about epipolar curves in DBT. We aim to show that such detection algorithms can be adapted so that microcalcifications not detected originally, e.g. due to not passing a threshold, can be detected with the aid of multiple projections in DBT.

In broad outline, the idea is as follows: suppose we have chosen or designed a microcalcification detection algorithm *A* to extract candidates from each DBT projection. Generally, algorithm *A* will have some parameters e.g. *a, b, c* to enable it to deal with noise and sampling. To simplify the discussion, we assume there is just one parameter, *a*, and suppose that there is a default value *a** for *a*. When we apply *A(a*)* to the individual DBT projections, we find many candidate microcalcifications, organised as a set of epipolars. We reject some points as noise because they do not have sufficient epipolar support. In other cases, we may have say *10* microcalcification points in an epipolar and *3* "missing" . Suppose, for example, we do not see the microcalcifications in images *I6, I8, I9*. By changing *a** appropriately (e.g. lowering it) in these *3* images and particularly in the predicted locations, we may find a candidate in, e.g. *I6, I9* but not in *I8*. Nevertheless, this increases our confidence that the points come from a true microcalcification, as there are now *12* points detected instead of the original *10*. The epipolar structure has therefore further increased our true positives (TP) fraction in single DBT projections.

To develop the concept, we need to choose an algorithm to extract microcalcification candidates For simplicity, this algorithm should have a small number of parameters, ideally one. We discuss possible microcalcification detection techniques in Section 7.1 and then choose some among them for our purpose.

The Harris corner detector (Harris) is one of the simplest and most commonly used detectors for "corner" detection (in our case, microcalcifications). It computes a cornerness measure for each pixel in the image and compares the measure with a threshold to determine whether or not the pixel is a corner. Harris therefore fits our requirements well. However, it is very sensitive to noise. On the other hand, anisotropic diffusion (AD) is robust to noise and has been studied by a number of research groups for microcalcification detection. It smooths images to remove noise. Our idea is to combine these two techniques (Harris-AD) to illustrate adaptivity. We discuss the combination approach in Section 7.2. We use some real DBT datasets to show that our concepts help increase the detection rate.

7.1 Microcalcification Detection Techniques in Mammography

Generally, microcalcification detection techniques may be classified into four types: (a) machine learning methods; (b) physics-based approach; (c) statistical approach; and (d) image processing approach. In this section, we briefly review each of these types and comment on their feasibility in being adapted to illustrate our approach.

7.1.1 Machine Learning Methods

Introduction

A machine learning method usually involves two steps: (1) use of an image processing method to extract features in each image; (2) application of a learning algorithm to train the classifier such that the combination of certain sets of features will indicate higher chance of a particular class and other sets may represent other classes. The learning stage always involves large sets of images in order to cover as many cases as possible.

Literature Review

El-Naqa et al. [126] have proposed the use of support vector machines (SVM) for the detection of microcalcifications in mammograms. "Given a training sample, SVM constructs a hyperplane as the decision surface in such a way that the margin of separation between positive and negative examples is maximized." [127]. An illustration from [127] demonstrating the idea of SVM with a linear hyperplane is shown as follows:

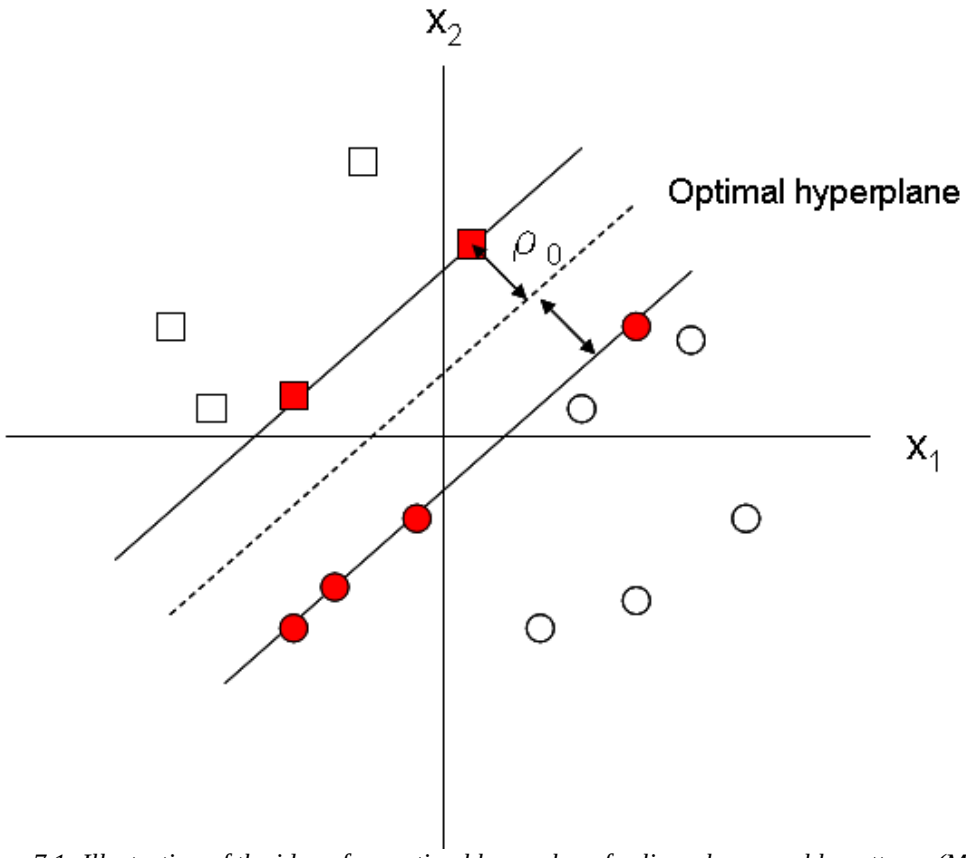

Figure 7.1: Illustration of the idea of an optimal hyperplane for linearly separable patterns (Modified from [127]).

In the figure, data points belong to *2* classes: the circle class and the square class. Many different hyperplanes can be formulated to classify them. The optimum is the one for which the margin of separation between the hyperplane and the closest data point is maximized i.e. ρ_o. The red circles and squares are called support vectors which are elements of the training set that are in essence most difficult to classify.

In an SVM, the discriminant function with testing data vector x, has the form: $g(x) = \sum_{i=1}^{L_s} \alpha_i d_i K(x_i, x) + \alpha_0$ where K is the kernel function, x_i are the support vectors and d_i are the corresponding class indicators (e.g. in microcalcification detection, *+1* represents microcalcification present while *-1* represents microcalcification absent), L_s is the number of support vectors and α_i are constants. These parameters except d_i are

determined during training. (Readers can refer to [127] for more information on SVM and techniques in solving the SVM optimization problems.)

El-Naqa et al. have considered a number of aspects in the design of SVM classifier for microcalcification detection. Regarding the input feature vector, they used pixel values in a *9*9* window because the average size of a microcalcification in their dataset is around *6-7* pixels. Regarding the kernel functions, they studied two common ones: Polynomial kernel $\left(K(x,y)=(x^T y+1)^p\right)$ and Gaussian radial basis functions $\left(K(x,y)=\exp\left(-\frac{\|x-y\|^2}{2\sigma^2}\right)\right)$.

Regarding the training examples, image windows of size *9*9* are collected at the centres of mass of the microcalcifications identified in the database for "MC present" class and a random sampling scheme is adopted to select image windows from those regions of the image containing no microcalcification for the "MC absent" class. Regarding SVM training, the SVM optimization problem is solved using Lagrange multipliers and a successive minimal optimization technique (For details, readers may refer to [128].). Regarding SVM model selection, since a few variables, e.g. the kernel function, have to be determined during the training phase, they have adopted a *m*-fold cross-validation method. In this method, the training datasets are randomly divided into m equal-sized subsets. For each parameter settings, *(m-1)* sets are used for training and the remaining one set is used as a testing set for measuring classification error. This is repeated so that every subset has been used as a testing set. So, an averaged classification error will be obtained for each parameter settings. The parameter settings with the smallest error will be used for the classification.

Comments

Since DBT is still in its infancy, there is insufficient DBT data to perform learning and subsequently to formulate a good classifier. Hence, we will not use learning in our illustration.

7.1.2 Physics-based Approach Using h_{int}

Overview of the method

The fact that the linear attenuation coefficient of microcalcifications is approximately *26* times higher than that of normal tissue has given rise to the development of the detection algorithm to be discussed. The algorithm [129] is based on the mammographic image process model presented in Section 4.1.2.

We first introduce the h_{int} representation proposed by Highnam and Brady [91]. As mentioned in *Table 4.1* of Chapter 4, it is found that fat has a much lower X-ray attenuation than the other tissue types such as fibrous, cancerous tissues which have similar attenuation, while calcification has a much higher one. To distinguish other tissue types from fat and calcification, Highnam and Brady define all other tissue types as "interesting". Mammography is indeed a conversion of the information in the *3D* breast into a *2D* representation as an image. Each pixel in the image actually represents the path the X-ray photons traverse, especially the sub-path within the breast, as we discussed in Chapter 4.1. The energies absorbed by the detector are converted to the intensity values in the image. Thinking from the physical point of view, in this particular sub-path through the breast with thickness *H* (except at the breast edge), the X-ray photons may possibly pass through a certain thickness of fat tissue, h_{fat}, a certain thickness of non-fat tissue (we term this as interesting tissue), h_{int}, in a normal breast assuming no calcification exists. Instead of the intensity of each pixel, the h_{int} representation gives information on the thickness of the interesting tissue the X-ray photons have passed through during their course through the breast. The following figure shows a cross-section across a breast with a path of the X-ray photons passing through fatty tissue and interesting tissue:

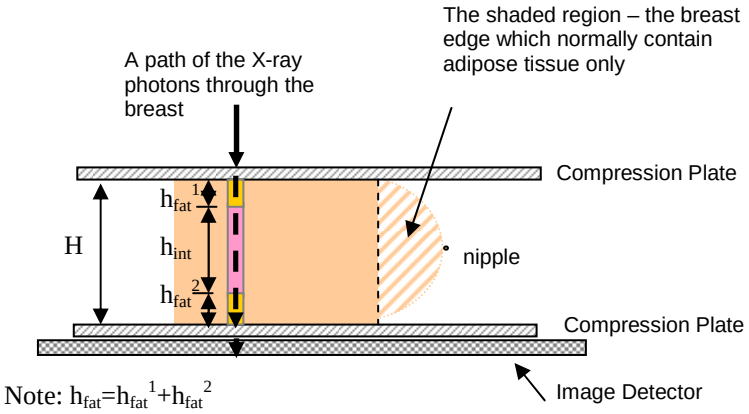

Figure 7.2: A cross-section across a breast showing a path of the X-ray photons passing through fatty tissue and interesting tissue

Indeed,

$$H = h_{\text{int}} + h_{fat} \qquad \textit{Eqn. 7.1}$$

where H can be measured either from the plate separation, or even from the image.

Hence, we can substitute $h\mu(\varepsilon)$, the photons being attenuated at energy ε with linear attenuation coefficient $\mu(\varepsilon)$, by passing through the breast with thickness h in *Eqn. 4.5* for the derivation of the radiation of the primary beam leaving the breast by $h_{\text{int}}(\mu_{\text{int}}(\varepsilon) - \mu_{fat}(\varepsilon)) + H\mu_{fat}(\varepsilon)$, because of *Eqn. 7.1* and $h\mu(\varepsilon) = h_{\text{int}}\mu_{\text{int}}(\varepsilon) + h_{fat}\mu_{fat}(\varepsilon)$. With the experiment results of the linear attenuation coefficients of fat and the interesting tissue (an approximate value), the pixel value of the image, the other components (scattered radiation and extra-focal radiation) and other measured and experimental values, we can therefore solve for h_{int} for each pixel.

So far, we assume that no calcification exists. What if there is a calcification in the X-ray path? It is expected that the h_{int} value computed for pixels with calcification in the path will be much larger than that without calcification, due to the fact that the linear attenuation coefficient of calcification is *26* times higher.

The detection algorithm is based on this observation. It calculates the volume of the interesting tissue in the "suspected" blob, call it v_{int}^{blob}, and compares it with the actual *3D* volume as if it is a calcification with an ellipsoid shape, v_{3D}^{blob}. Assigning v_{int}^{ratio} as the ratio of the volume of the interesting tissue to the actual *3D* volume as if it is a calcification,

i.e. $$v_{\text{int}}^{ratio} = \frac{v_{\text{int}}^{blob}}{v_{3D}^{blob}}$$

Theoretically, if $v_{\text{int}}^{ratio} > 1$, it means that the extracted region is indeed a calcification, because the large value of the linear attenuation coefficient of calcification will lead to an unusually large h_{int} causing an unexpected larger volume than the expected volume. On the other hand, if $v_{\text{int}}^{ratio} \le 1$, it means that the region cannot be a calcification because it contradicts our assumption in deriving h_{int}. In practice this threshold is set experimentally due to the approximation made in the calculations.

The detection algorithm consists of four steps:

(a) Extract the "suspected" region

The mammogram is thresholded at every *K* grey level step from *G* to *G+2K*. Then, the change of area of successive regions is given by, $\Delta A(r_i, r_{i+1}) = (a_i - a_{i+1})/(a_i + a_{i+1})$, where a_i, a_{i+1} are the area of r_i and r_{i+1} respectively and $a_i \geq a_{i+1}$. If $\Delta A(r_G, r_{G+K}) \leq \Delta A_{threshold}$ and $\Delta A(r_{G+K}, r_{G+2K}) \leq \Delta A_{threshold}$ where $\Delta A_{threshold}$ is a preset threshold used to ensure that the extracted "suspected" region r_G is a region such that the area variation is decreased gradually, then r_G is the "suspected" region for the next step, because it is observed in mammograms that the intensity for calcification changes gradually while that for noise is more abrupt.

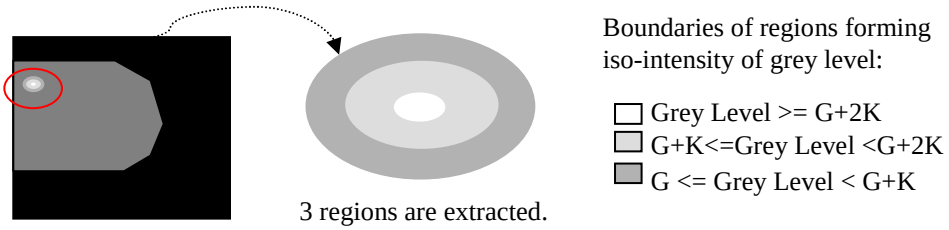

Figure 7.3: Extracted regions for thresholding. A mammogram (Left). 3 regions extracted for thresholding (Middle). The regions are extracted based on the grey level (Right).

(b) Compute the volume of the interesting tissue in the "suspected" blob, v_{int}^{blob}

To compute v_{int}^{blob}, we need to find the volume of the extracted "suspected" region $v_{\text{int}}^{blob+surr}$ and then subtract the volume of the surrounding tissue v_{int}^{surr}.

$v_{\text{int}}^{blob+surr}$ can be calculated by summing the size of each pixel multiplied by the corresponding thickness h_{int}, i.e. $v_{\text{int}}^{blob+surr} = \sum_{i \in r} h_{\text{int}}(i) * p^2$ where *r* is the extracted region and *p* is the pixel size.

v_{int}^{surr} can be calculated by the constant thickness h_{int}^{surr} in the background region close to the extracted region multiplied by the area of the region, i.e. $v_{\text{int}}^{surr} = h_{\text{int}}^{surr} * M * p^2$ where *M* is the number of pixels in the extracted region and *p* is again the pixel size. The constant thickness h_{int}^{surr} can be calculated by finding the average h_{int} values surrounding the extracted region, a dilation ring $r_d \backslash r$.

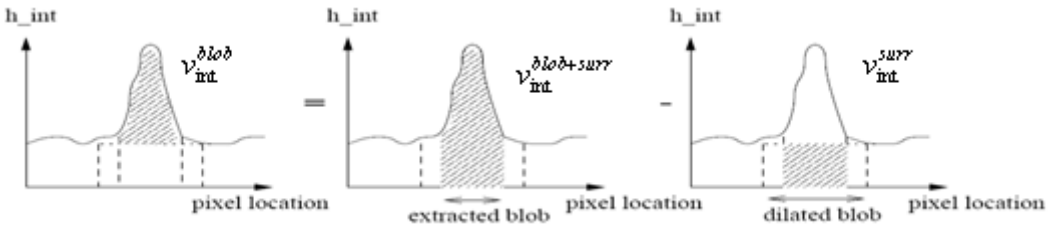

Figure 7.4: A schematic representation of the computation of v_{int}^{blob} *in 1-D (Modified from [129].)*

(c) Estimate the actual 3D volume as if it is a calcification with an ellipsoid shape, v_{3D}^{blob}

Using the formula for the volume of an ellipsoid, we estimate $v_{3D}^{blob} = (4/3)\pi a^2 b$, where *a* and *b* are minor and major axes estimated from the extracted region.

(d) Compute v_{int}^{ratio} and perform thresholding

Finally, we can compute v_{int}^{ratio} as discussed before to check whether the ratio exceeds the selected threshold. If the ratio exceeds the threshold, then the "suspected" region is a calcification.

Comments

The physics-based approach investigates the mechanisms in X-ray formation and uses the physics fundamentals for detection. However, neither h_{int} nor developments of it have been extended to DBT and so we do not (at this stage) adopt the physics approach.

7.1.3 Statistical Methods

There are methods which rely on the statistics of the image for the detection [130] or which uses Markov random fields to model the detection problem [131].

Stochastic Modeling Methods

Gurcan et al. [130] have proposed a method of using higher order statistics, namely skewness and kurtosis, in finding the regions containing clusters of microcalcifications in mammograms. In their study, they investigated the impact of microcalcifications in lowpass, bandpass and highpass subimages as well as the original image, from the datasets employed. Experimentally, they found that the bandpass subimage is the best one to differentiate between regions with microcalcifications and those without. In their tests, they divided the subimage into regions of size *30*30* with an overlap size of *15*. For each region, the statistical measurements of skewness (a measure of the symmetry of the distribution) and kurtosis (a measure of the heaviness of the tails in a distribution) were calculated. It was found that both values were distinctly greater than *0* if the regions contained microcalcifications and were very close to *0* for those without. *Figure 7.5* shows *2* histograms of *2* regions, one with a microcalcification cluster and one without, in the bandpass image. The skewness and kurtosis of the region with a

cluster were *1.5616* and *9.0307* respectively, while the measurements of the region without a cluster were close to *0*.

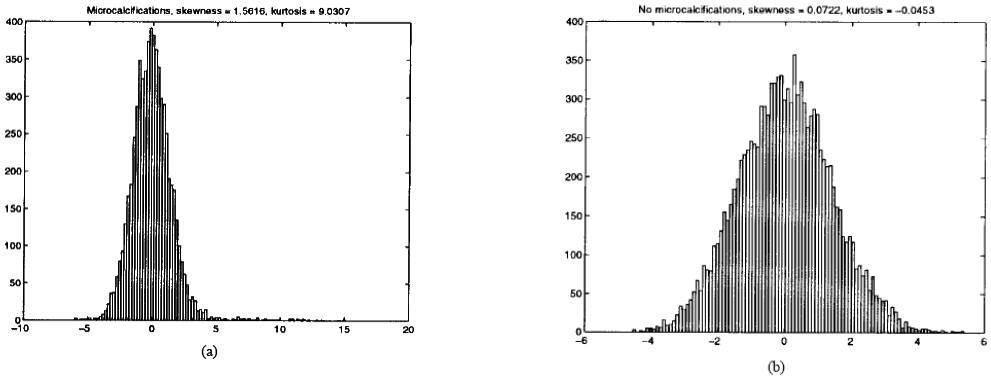

Figure 7.5: Histogram of a region (a) with a microcalcification cluster and (b) without microcalcifications in the bandpass image (Extract from [130]).

Then, thresholding (i.e. the values of skewness and kurtosis measurements were greater than thresholds found experimentally) was applied to extract the regions which were considered as containing microcalcifications.

Bayesian Statistical Methods

Karssemeijer [131] tackled the microcalcification detection problem using Markov random fields (MRF), based on both image data and prior beliefs. The detection problem becomes a labeling problem, in which every pixel is assigned to one of the *3* labels (Label *1* corresponds to background; Label *2* corresponds to calcification; Label *3* corresponds to line shaped structures.). Using Bayes' Theorem and the Markov property, the aim is to maximize the probability:

$$p(x_i = k \mid Y, \hat{X}_{S/i}) \propto p(Y \mid x_i = k, \hat{X}_{S/i})\, p(x_i = k \mid \hat{x}_{\Delta i}) \qquad \textit{Eqn. 7.2}$$

where x_i is the pixel label of pixel *i*; *k* is the label *(1, 2 or 3)*; Y is the image data; $\hat{X}_{S/i}$ is the current estimate of the rest of the labelling; $\hat{x}_{\Delta i}$ is the current estimate of the labelling of the neighbourhood Δi of pixel i.

There are *2* terms in the RHS of the probability. Note that regarding the current labelling $\hat{X}_{S/i}$, the standard approach is to replace it by the true segmentation. The first term $p(Y \mid x_i = k, \hat{X}_{S/i})$ models the likelihood of the image data Y given the label of pixel i. Using the assumption of conditional independence of the image data of pixel i, y_i, the first term is then reduced to $p(y_i \mid x_i)$. This is obtained by the distribution

$f(y_i', \theta_i \mid x_i)$ where y_i' is the relative pixel value with the consideration of the pixel values of the neighbourhood and θ_i is a shape parameter extracted from the image data in a small neighbourhood of i. This shape parameter indicates whether or not a line or dot feature at site i is likely. The author uses the Hough transform in the calculation of the shape parameter. Both the densities $f(y_i' \mid x_i)$ and $f(\theta_i \mid x_i)$ were estimated from a given set of labelled training examples.

Regarding the second term $p(x_i = k \mid \hat{x}_{\Delta i})$ which is based on the contextual relations between neighbouring pixels, the author models this as

$$p(x_i = k \mid \hat{x}_{\Delta i}) \propto \exp\left[- A(k) - B'(k) N_{c,i} - \sum_{n=1}^{3} B(k,n) G_{\partial i}(n) \right] \qquad \textit{Eqn. 7.3}$$

In the expression, the values for the model parameters were determined experimentally.

A(k) models the probability the pixel i is assigned to the label *k* and they are set to: *A(1)=0; A(2)=4.0; A(3)=2.0.*

B'(k) models a cluster of microcalcifications, which normally spans a large neighbourhood of *i*. $N_{c,i}$ is the number of calcification sites in this large neighbourhood. In the study, all sites within *30* pixels distance are considered, making up a total of about *2,800* distant neighbours. Both *B'(1)* and *B'(3)* are assigned to *0* and *B'(2)=-250/* $N_{\Delta i}$ (where $N_{\Delta i}$ denotes the number of pixels in the "large" neighbourhood).

Finally, *B(k, n)* models the nearest neighbour interaction. A second order neighbourhood is used. $G_{\partial i}(n)$ is the number of pixels labelled as *n* in the neighbourhood of *i*. In setting the values of *B(k, n)*, the author has a few principles: Modelling the interaction between calcification and line labels must be chosen high to disallow patches consisting of a mixture of these two classes; Interaction with the background class has to be chosen small or zero to allow calcifications consisting of only one or a few pixels to survive if they are bright enough. The values of *B(1,2)=0.2, B(1,3)=0.5, B(2,3)=2.0.* Other values follow from symmetry conditions, or else were put to zero.

The following figures compare the detection results by using local thresholding and the Bayesian statistical method:

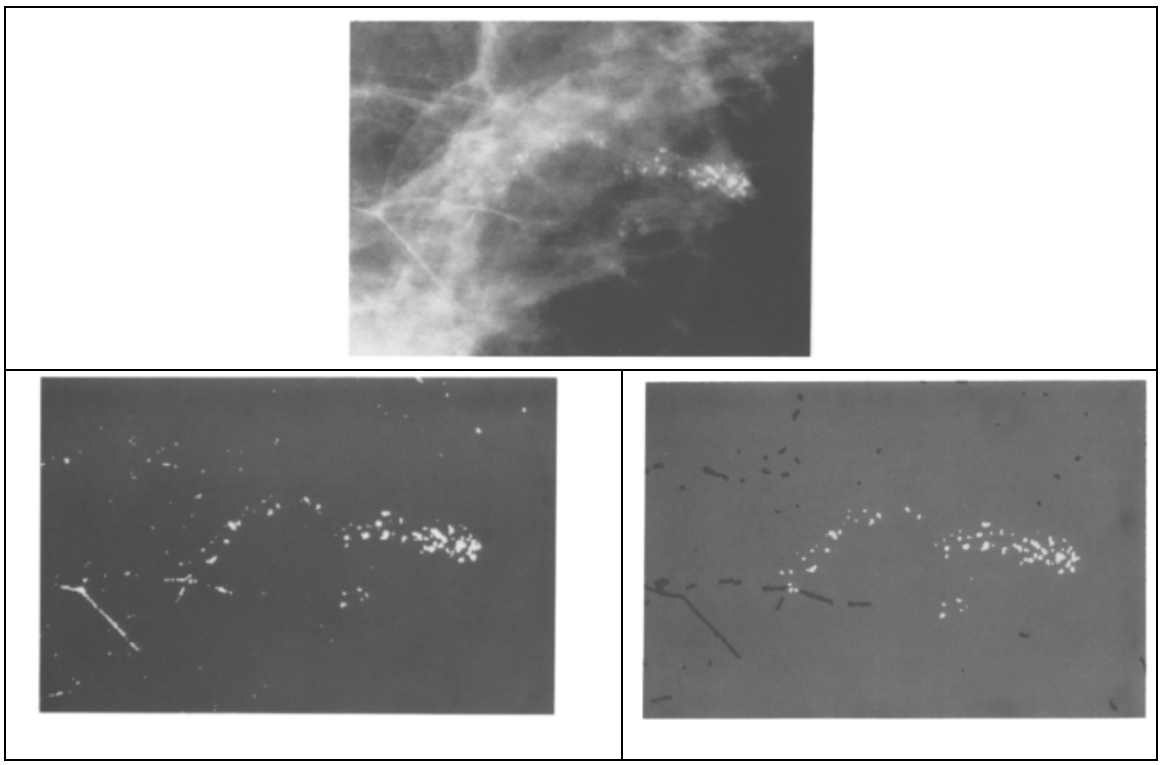

Figure 7.6: (Top) A region containing a cluster of microcalcifications; (Bottom Left) Detection by local thresholding; (Bottom Right) Detection by Bayesian statistical method. (Extracted from [131])

From the figure, local thresholding results are unsatisfactory because the connective tissues are also extracted, while the Bayesian technique can extract microcalcifications in a cluster.

Comments

The stochastic modelling method is not applicable to our problem because we do not have sufficient datasets to perform a reasonable statistical analysis. For the Bayesian statistical method, instead of applying it to our adaptive approach, we will adopt the MRF method with multiple projections and epipolar curves using belief propagation to illustrate the improvement in microaclfication detection in the next chapter.

7.1.4 Image Processing Approach

There are basically three categories in this approach regarding microcalcification detection: (1) Methods which aim to find candidate points; (2) Methods which aim to increase SNR by smoothing the image, but without deleting microcalcifications; and (3) Methods that apply various image filters or feature detectors.

7.1.4.1 Methods which aim at finding candidate points

Given any digital image, regardless of its contents, we are always interested in finding the features in the image, e.g. point detection, edge detection. Hence, a lot of fundamental detection algorithms have been developed by the digital image processing community. In this section, we highlight two feature detectors: the Harris corner detector [132-134] and a salient region detector [135, 136], as they can detect interest points, which are similar to the detection of microcalcifications. After each discussion, we will show detection results by applying the detectors on our simulated images containing microcalcifications.

Harris Corner Detector

The Harris corner detector finds locally distinctive points in an image by computing the average changes of image intensity of a local window in the image when the window is shifted by a very small amount in various directions. It is an improved version of the Moravec corner detector in that both of them use the idea that a corner is within a window if shifting a window results in a large change in intensity no matter in which direction. Three cases are considered: flat region, edge and corner. Consider the following figure:

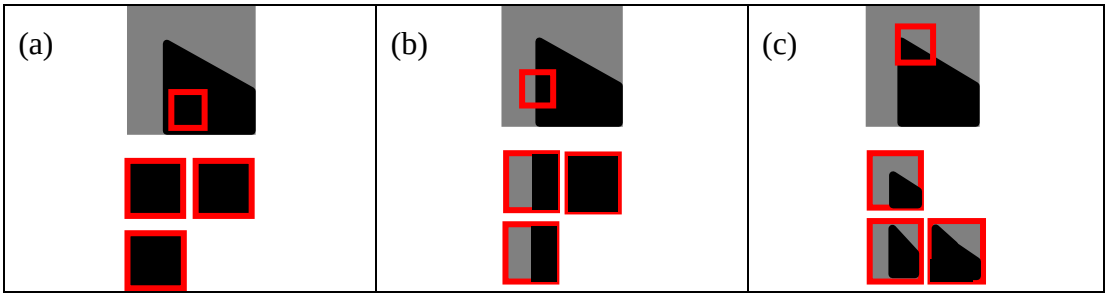

Figure 7.7: Image with a window (red box) some windows after shifting (bottom boxes). (a) When window is extracted at a flat region; (b) When window contains an edge; (c) When window contains a corner. (Extracted from [133]).

In case (a), when the window is within a flat region, the change in intensity is minimal when it shifts a little bit in any direction. In case (b), when the window contains an edge feature, a shift in the vertical direction does not cause any change in intensity, but a shift in the horizontal direction results in a large change in intensity. Finally in case (c), when the window contains a corner feature, small shifts in all directions will lead to a large change in intensity in the windows.

How the image function *I(u, v)* at point *(u, v)* is self-similar when shifted by a small amount *(x, y)* is given by the auto-correlation function, which measures the local changes of the image signal:

$$E(x,y) = \sum_{u,v} w(u,v)(I(u+x,v+y) - I(u,v))^2 \qquad \textit{Eqn. 7.4}$$

where *w(u, v)* is a window function which can either be constant (for binary or rectangular window) or Gaussian (for a smooth circular window). A Gaussian filter is often used as it smoothes the image:

$$w(u,v) = \exp(-\frac{(u^2+v^2)}{2\sigma^2}) \qquad \textit{Eqn. 7.5}$$

By Taylor's first order approximation of *I(u+x, v+y)* in the auto-correlation function:

$$E(x,y) \cong [x,y]M\begin{bmatrix} x \\ y \end{bmatrix} \qquad \textit{Eqn. 7.6}$$

where

$$M = \sum_{u,v} w(u,v)\begin{bmatrix} I_x^2 & I_x I_y \\ I_x I_y & I_y^2 \end{bmatrix} \qquad \textit{Eqn. 7.7}$$

I_x, I_y are partial derivatives of *I(u, v)* in *x* and *y* respectively.

Note: *E(x, y) = constant* is the equation of an ellipse. *M* is a *2-by-2* symmetric matrix which has exactly *2* positive eigenvalues and *2* mutually orthogonal eigenvectors which give the orientation of the ellipse. Elongation and size of the ellipse are governed by the size of the eigenvalues λ_1, λ_2, since the length of the major and minor axis of the ellipse relates to $(\lambda_1)^{-1/2}$ and $(\lambda_2)^{-1/2}$ respectively for $\lambda_1 < \lambda_2$. Different eigenvalues correspond to different shapes of ellipse which correspond to either flat region (both eigenvalues are small), edge feature (one large, one small eigenvalues) or corner feature (both eigenvalues are large) in the image as shown:

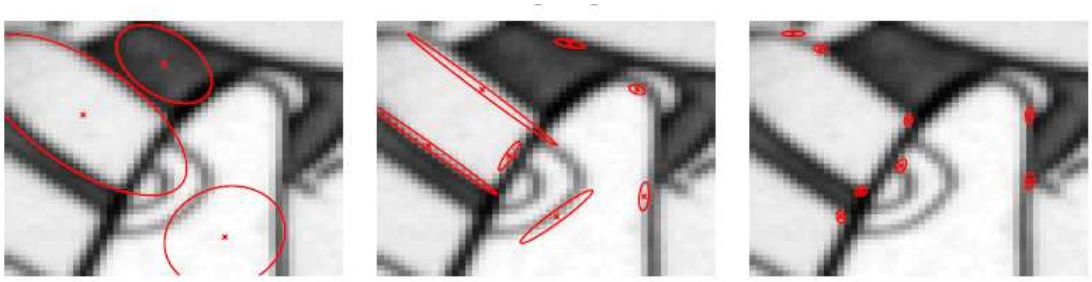

Figure 7.8: Eigenvalues and the corresponding ellipses. Flat region (Left). Edge feature (Middle). Corner feature (Right). (Extract from [134])

Given the same shift *(x, y)*, larger eigenvalues in the LHS of the equation of an ellipse will give larger *E(x, y)* for the same constant in the RHS of the equation of an ellipse,

implying larger intensity change. This explains why small eigenvalues give rise to the flat region and large eigenvalues give rise to corner feature. For the edge case, one large and one small eigenvalues will lead to a larger change in *E(x, y)* when shifting in one direction and a smaller change when shifting in another direction.

Instead of calculating the eigenvalues directly, Harris et al. suggested determining the cases in the image by finding *det(M)* ($= \lambda_1\lambda_2$) and *trace(M)* ($=\lambda_1 + \lambda_2$). They also suggested a measure of "corner" response $R = \lambda_1\lambda_2 - k(\lambda_1 + \lambda_2)^2$ with a typical value of $k = 0.04$. R is positive for corner, negative for edge and small in flat region.

We have generated an image with microcalcifications from our simulation model of tomosynthesis projection and applied the Harris corner detector using a freely available implementation. A preliminary result is shown as follows:

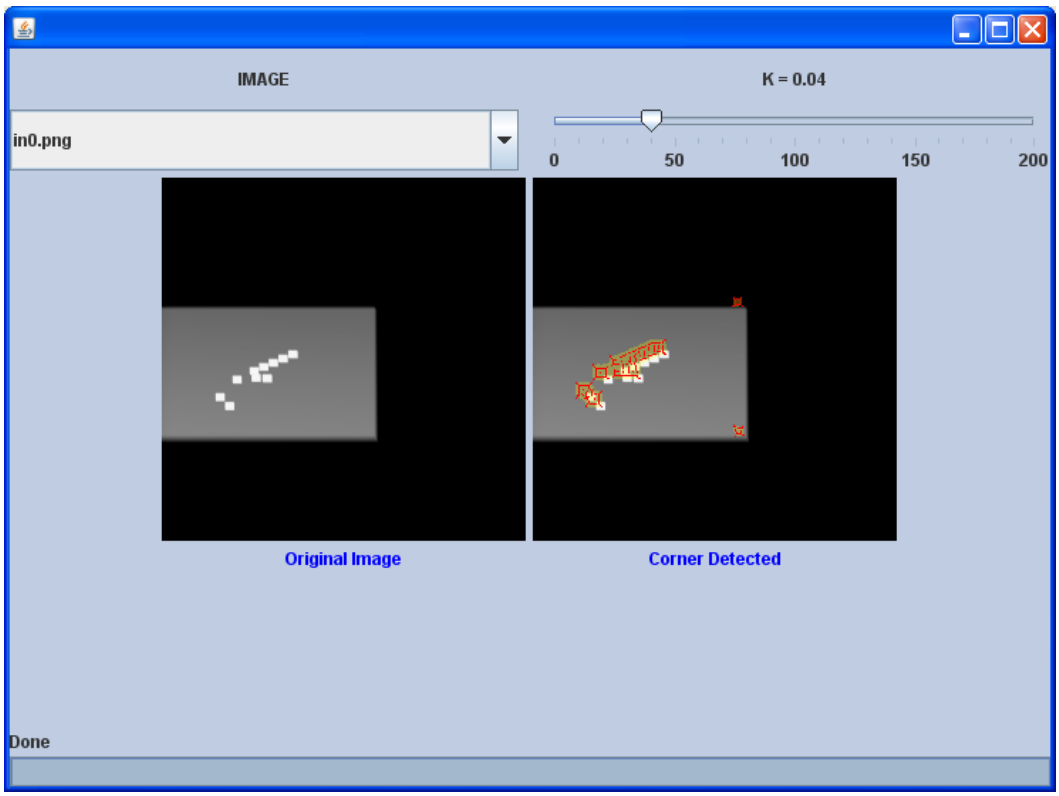

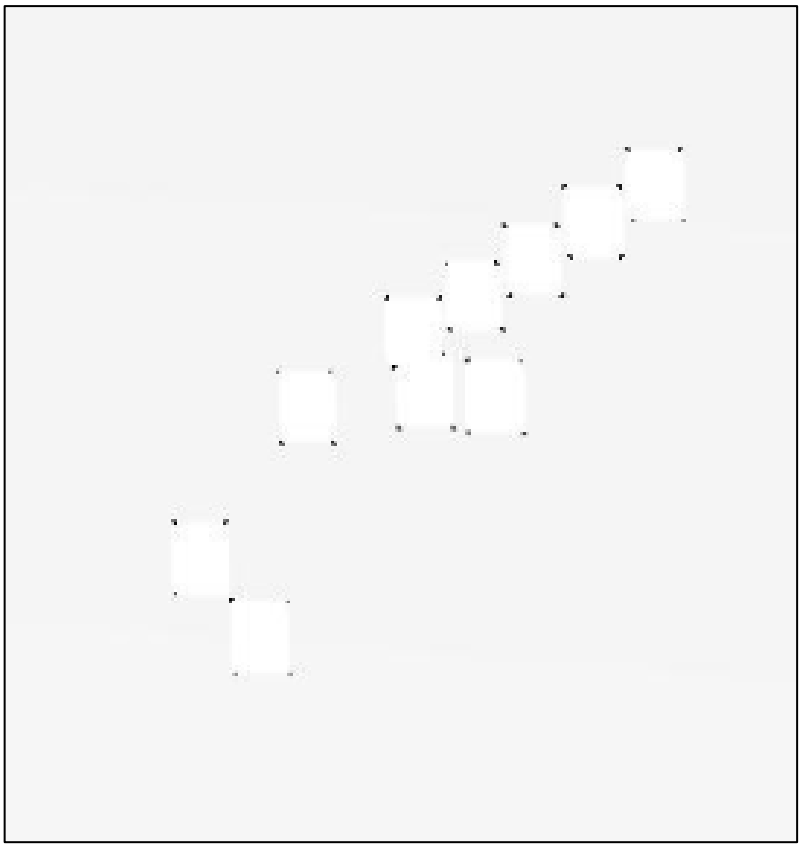

Figure 7.9: The sample outputs of our simulated microcalcification image by the Harris Corner Detector using Java implementation [137] (Left); MatLab implementation [138] (Right).

From the figure, it can be seen that the white rectangles representing microcalcifications can be detected by both implementations of the Harris corner detector.

A Salient Region Detector by Kadir and Brady

Salient image regions refer to the "surprise" (i.e. saliency) in their local attributes over a small range of scales.

(a) Saliency

Given an image, a region with a probability distribution function of intensity following a normal distribution is less complex than a region with a flatter distribution. An example is the human face. The eye is a more complex region than the cheek. Complexity is related to predictability. The intensity in the cheek region can be easily predicted, as they have similar intensity. However, the eye region is more complex and hence the local intensity is more unpredictable.

A measure of the predictability of a region can be obtained by evaluating the entropy of local attributes. Entropy measures the randomness of a variable [139]. The more uncertain a variable is, the higher its entropy. In information theory, entropy measures average information content. Consider an example of transmission of *1,000* bits. If these bits are known beforehand, then it is considered that no information has been transmitted. On the other hand, if the probability of transmitting *0* or *1* is equal, then *1,000*-bit of information is transmitted, because we cannot predict *0* or *1* in the transmission and we need to get all *1,000* bits of information. Using a similar concept, we are looking for image regions with high average information content (salient regions e.g. eye), rather than image regions with no information at all (e.g. cheek in our example). Hence, entropy values will be computed for the saliency in each region. The higher the entropy, the more salient the region is.

(b) Scale

Scale is the size of the region in which the entropy is calculated. Consider the following example:

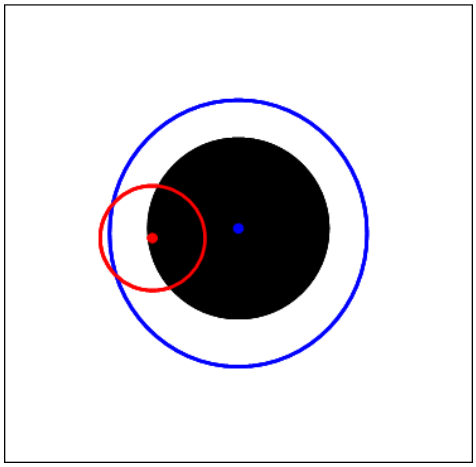

Figure 7.10: Regions of different scales in an image. (Redrawn from [135].)

Both the red point and blue point exhibit the same highest entropy values in the corresponding circular region, because the proportions of black and white pixels are the same in both regions (high unpredictability). However, we consider the blue region to be our salient region in the image visually. In an image, different local scales are required for different salient regions. Imagine another smaller black dot in our example image. Then, the optimal scale used for this other salient region will be smaller. Hence, local scale selection is required. To determine the scale, we will look for complex regions. Complexity is assumed to be rare. If a region is unpredictable at all scales, then it means it is not rare and it may only be a random image. This will not be considered as a salient region. Hence, a measure of self-similarity over different scales is designed.

(c) Scale Saliency Algorithm

After a brief discussion on saliency and scale, the scale saliency algorithm is presented. The algorithm consists of four steps:

(1) Calculation of Shannon entropy $H_D(s,x)$:

Using the equation of Shannon entropy, we first calculate the entropy $H_D(s,x)$ using the probability density of the intensity I as a function of scale s and position x, $p(I,s,x)$:

$$H_D(s,x) = -\int p(I,s,x)\log_2 p(I,s,x)dI \qquad \textit{Eqn. 7.8}$$

(2) Finding the scales at which the entropy is maximum s_p:

Next, we use the second derivative to find the scales for the peaked entropy:

$$s_p = \left\{ s : \frac{\partial H_D(s,x)}{\partial s} = 0, \frac{\partial^2 H_D(s,x)}{\partial s^2} < 0 \right\} \qquad \textit{Eqn. 7.9}$$

Using our previous example, the entropy against scale is plotted. For the red region, it is found that the scale at which entropy peaks is approximately *7* while that for the blue region is *15*.

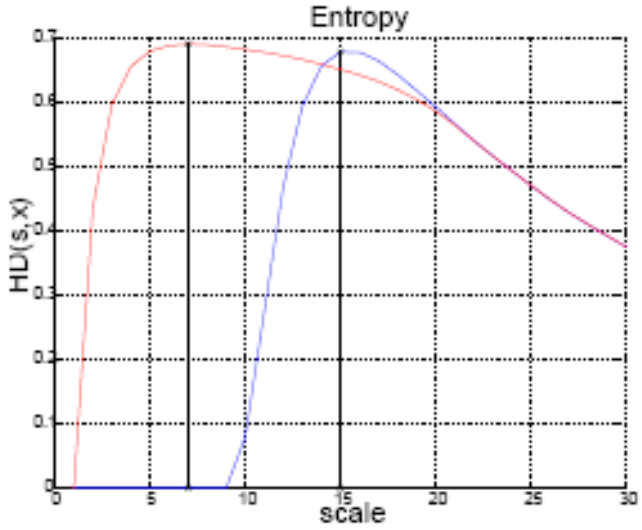

Figure 7.11: Graph showing entropy against scale in the example. (Extracted from [135].)

(3) Finding the inter-scale unpredictability measure $W_D(s,x)$:

Now, we need to find the optimal scale as a salient region. To do this, we calculate the magnitude change of the probability density as a function of scale. If the region is similar over a large range of scales, then a smaller weight $W_D(s,x)$ will be resulted. We aim at finding a large $W_D(s,x)$, meaning the region is self-dissimilar i.e. salient. $W_D(s,x)$ can be found as follows:

$$W_D(s,x) = s\int \left| \frac{\partial}{\partial s} p(I,s,x) \right| dI \qquad \textit{Eqn. 7.10}$$

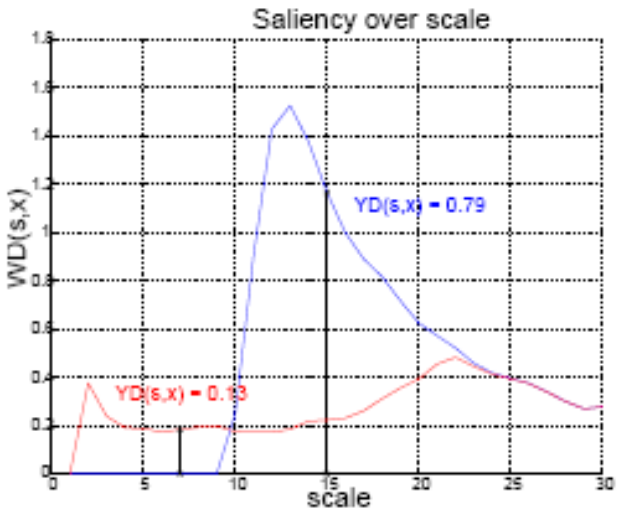

Figure 7.12: Graph showing saliency over scale in the example. (Extracted from [135].)

It is seen from the graph in *Figure 7.12* that although both red and blue region in our example give the same maximum entropy values, the weight calculated for the red one is much smaller than for the blue one.

(4) Finding the saliency measure $Y_D(s_p , x)$:

Finally, the saliency measure can be computed by the product of the entropy and the weight of inter-scale unpredictability:

$$Y_D(s_p, x) = H_D(s_p, x)W_D(s_p, x) \qquad \textit{Eqn. 7.11}$$

The larger the value of $Y_D(s_p ,x)$, the more salient the region is. From *Figure*, $Y_D(s_p ,x)$ for the blue region is greater than that for the red one. A threshold can be set for $Y_D(s_p ,x)$ to select those regions with values above the threshold.

The following figure shows an application of the algorithm using our simulated tomosynthesis image of microcalcifications:

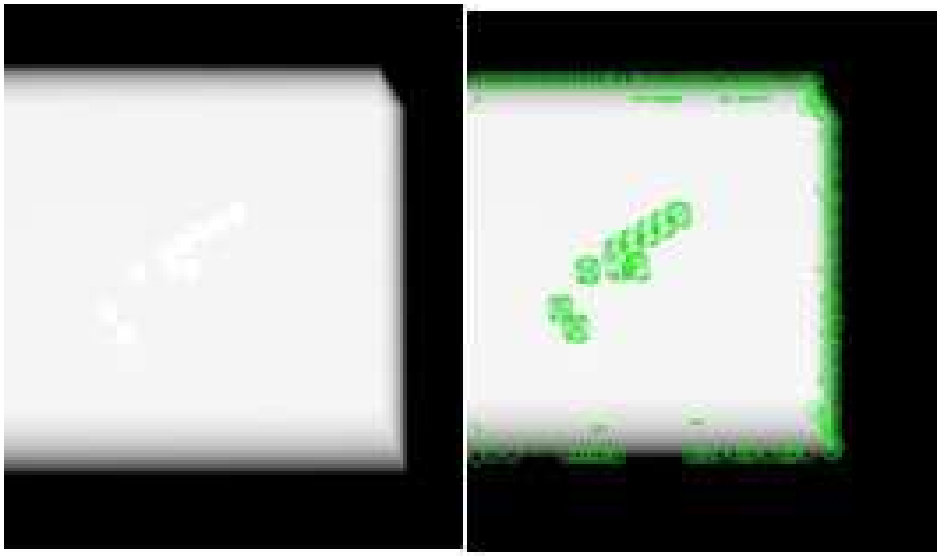

Figure 7.13: Detection outputs of our simulated microcalcification image by the Scale Saliency algorithm. Original image (Left). Salient points shown in green circles (Right) (Implementation from [135, 136])

From the figure, it can be seen that the white rectangles representing microcalcifications can be detected by the Scale Saliency algorithm.

7.1.4.2 Methods which aim at smoothing the images and increasing SNR without removing microcalcifications in the image

In this section, two smoothing methods will be reviewed: the Laplacian of a Gaussian, and anisotropic diffusion. To illustrate the smoothing effect, we have chosen one of

them – anisotropic diffusion and apply it to the Mammography BR3D Phantom to give some insight into filtering and detection in a single DBT projection.

Methods Using Laplacian Scale-space Representation

The Laplacian *L(x,y)* of an image with pixel intensity values *I(x,y)* is a 2D isotropic measure and is obtained by the 2nd spatial derivative:

$$L(x,y) = \frac{\partial^2 I}{\partial x^2} + \frac{\partial^2 I}{\partial y^2} \qquad \textit{Eqn. 7.12}$$

Regions of sharp intensity change e.g. edges will have a large value. In order to reduce its sensitivity of noise, the image is always smoothed with a smoothing filter, specifically a Gaussian, before applying the Laplacian filter. Combining the two, we obtain a LoG (Laplacian of Gaussian) with Gaussian standard deviation σ:

$$LoG(x,y) = -\frac{1}{\pi\sigma^4}\left[1 - \frac{x^2+y^2}{2\sigma^2}\right]e^{-\frac{x^2+y^2}{2\sigma^2}} \qquad \textit{Eqn. 7.13}$$

Using the findings that bright spots correspond to local maxima in Laplacian convolved images if the size of the filter kernel is chosen appropriately, Netsch et al. [140] have proposed a method using Laplacian scale-space representation for the detection of clustered microcalcifications.

There are *3* steps in their approach: (1) find bright, almost circular spots in the mammogram; (2) estimate the size D and local contrast C of each spot; (3) mark a spot as a microcalcification if $C > C_T(D)$ where C_T is given threshold depending on the estimated size *D* of the spot.

Given a mammogram, the authors first looked for the centres of bright spots as potential microcalcification candidates, by finding the local maxima in the Laplacian filtered image at different scales *h*, where $h = 2\sqrt{2}\sigma$. It is important that spots are marked at their true centre. Hence, a path tracking technique is used. This technique starts a path with a candidate pixel at the finest scale *h=2* and ends at some coarser scale if no appropriate candidate pixel is found in the *3*3* neighbourhood. The following figure shows an example of locating centre of bright spots:

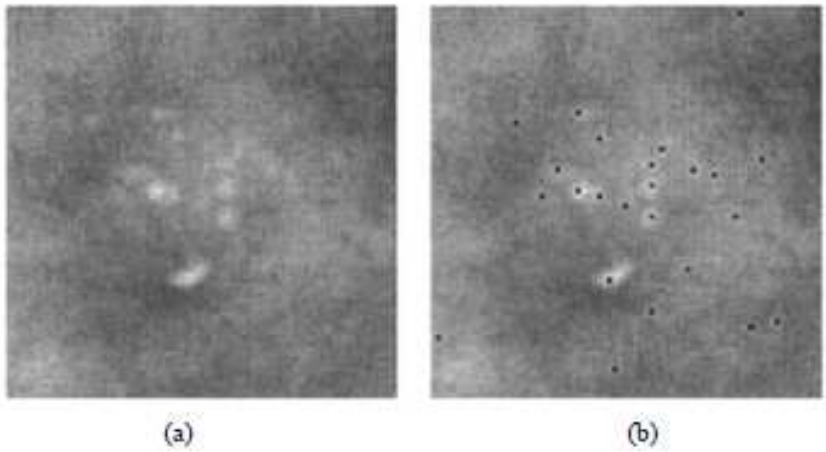

Figure 7.14: (a) A region containing a cluster of microcalcifications; (b) Potential microcalcification candidates are marked by the Laplacian detection as black dots. (Extract from [140]).

Next, the authors estimated the local contrast and size of a spot based on the scale-space representation of the image. A microcalcification is modelled by a cylinder of a specific height *C* and diameter *D* which corresponds to the local contrast and the diameter of the spot in the image respectively. It is found in the paper that the local contrast *C** and the size *D** of the spot are determined from the peak of the signature of the cylindrical microcalcification model, which is the peak values of LoG response and the corresponding scale h of the signature curve. The following figure shows *3* example curves of the signature of the cylindrical microcalcification model:

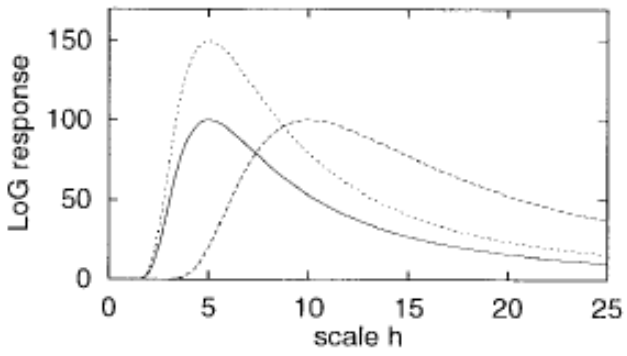

Figure 7.15: Signature of the cylindrical microcalcification model. The solid curve shows the Laplacian response of the model for C=100 and D=5. The dashed curves refer to a change to C=150 (higher peak) or D=10 (peak to the right) respectively. (Extract from [140]).

Finally, for threshold decision, different sizes of the bright spot are subjected to different contrast threshold C_T, which is chosen by visual inspection of several candidate pixels using a set of true microcalcifications. Those potential microcalcification candidates having a contrast *C* greater than the corresponding C_T are considered to be real microcalcifications.

In the paper, the authors have also considered image noise in their model, so as to estimate the local contrast correctly.

Methods Using Anisotropic Diffusion

Anisotropic diffusion is a scale-space and edge detection technique based on partial differential equations. This idea comes from the physical process, the diffusion process that equilibrates concentration differences without creating or destroying mass [141]. Using Fick's law and continuity equation, the diffusion equation is employed into the fields of image processing and computer vision: $I_t = div(c(x,y,t)\nabla I) = c(x,y,t)\nabla^2 I + \nabla c \cdot \nabla I$, where $I(x,y)$ is the image at x and y; I_t is the smoothed image at time (scale) t; div is the divergence operation; ∇ and ∇^2 are the gradient and Laplacian operators; $c(x,y,t)$ is the diffusion tensor as in the diffusion equation in the physical process, or conduction coefficient. This is the anisotropic diffusion equation used in the Perona-Malik model [142]. Perona et al. has shown how a suitable choice of $c(x,y,t)$ will be useful in scale-space and edge detection. Their idea is that smoothing within a region is preferred to smoothing across the boundaries. They have chosen c to be a function of the gradient of I, i.e. $c(x,y,t) = g(I_x(x,y,t))$. Further to this, they have proposed a few choice of $g(I_x)$ (or $g(\nabla I)$) e.g. $g(\nabla I) = e^{(-(\|\nabla I\|/K)^2}$ and $g(\nabla I) = \dfrac{1}{1+\left(\dfrac{\|\nabla I\|}{K}\right)^2}$

where $\|\nabla I\|$ is the norm of the gradient of the image and K is a constant. The anisotropic diffusion equation is thus controlled by 2 parameters: t, the time or the iteration of the diffusion (or the scale); K, a constant which is related to the contrast of the features and the background. Some subsequent literature has introduced the Gaussian convolution of the gradient of the image and hence has introduced another parameter σ to control the sensitivity in filtering the size of the structures.

The application of anisotropic diffusion to digital mammography was first studied by Linguraru et al. [143]. By subtracting the anisotropically diffused image from the less blurred original, they found that microcalcifications and noise points are diffused differently. After a certain number of iterations, the surface of the difference image contains significant changes for noise only, for an appropriate choice of parameters and diffusion tensors [144].

Application of Anisotropic Diffusion on Mammography BR3D Phantom

We have applied the techniques of anisotropic diffusion to the Mammography BR3D Phantom (discussed in Chapter 5) using the Java implementation developed by [145]. Using suitable parameter settings, it is possible to discriminate noise points and the Calcium compounds in our phantom. The results are similar to those obtained by Linguraru, namely that the noise points and *6* Calcicum compound $CaCO_3$ can be distinguished in the difference image:

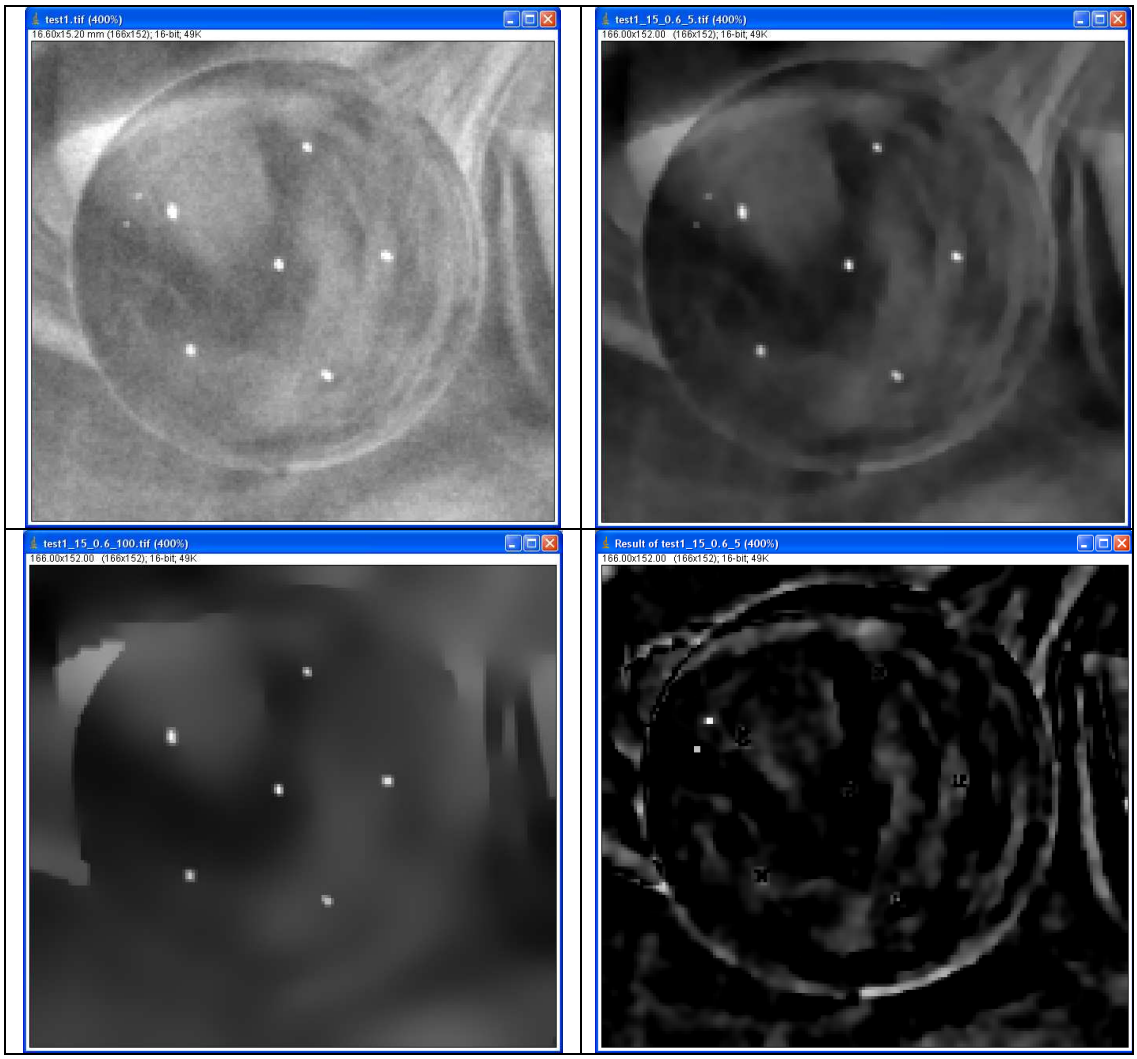

Figure 7.16: (Top Left) The original image with 6 Calcium compounds (pentagon-like arrangement) and 2 noise points (2 faded white points near the left); (Top Right) Anisotropic Diffusion using K=15, sigma=0.6, t=5; (Bottom Left) Anisotropic Diffusion using K=15, sigma=0.6, t=100; (Bottom Right) Difference image of Upper Right and Bottom Left ones.

Experiment of Filtering/Detection in a Single DBT Projection Using Anisotropic Diffusion

In this section, we have adopted the anisotropic diffusion methods in a real DBT dataset. In the experiment, we have extracted a region of a breast containing *3* microcalcifications. We show that anisotropic diffusion technique can facilitate their extraction:

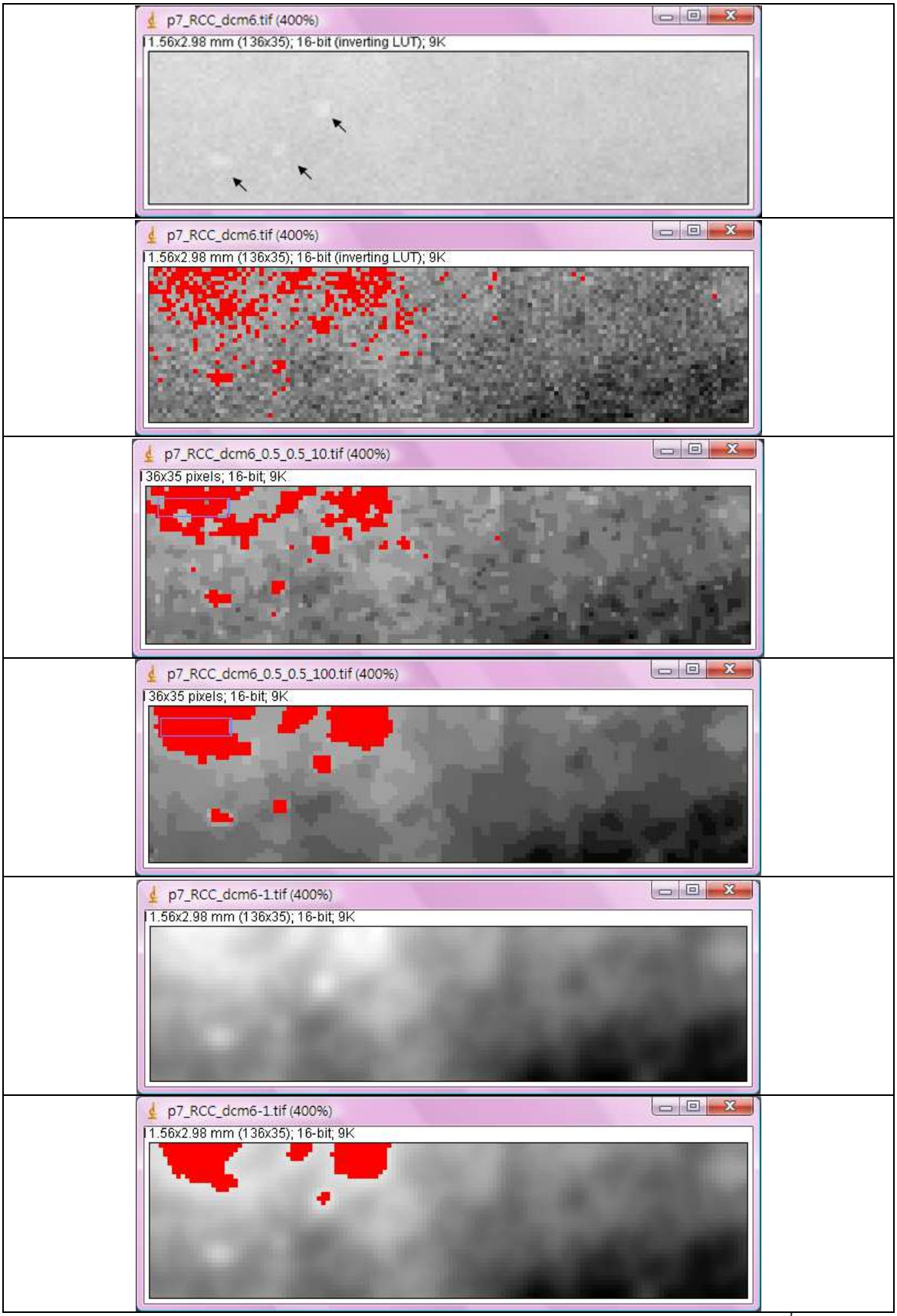

Figure 7.17: (Top Row) Original DBT projection with 3 microcalcifications (arrows); (2nd Row) Thresholding (pixel values between 1980 and 2100 are chosen for all images) (in red); (3rd Row) Anisotropic Diffusion using K=0.5, sigma=0.5, t=10 and then thresholding; (4th Row) Anisotropic Diffusion using K=0.5, sigma=0.5, t=100 and then thresholding; (5th Row) Gaussian blur of sigma 0.5 of 20 times; (6th Row); (6th Row) Gaussian blur of the image in the 5th Row and then thresholding.

From the figure, we can see the effect of using anisotropic diffusion. We have also compared the result with basic (isotropic) Gaussian blur. Anisotropic diffusion can preserve the microcalcifications over many iterations; even after *100* iterations, they are not smoothed away. On the other hand, Gaussian smoothing has blurred the microcalcifications completely, even after *20* iterations. Also, anisotropic diffusion can help the subsequent thresholding. If suitable parameters are set, it is possible to extract only microcalcifications and eliminate the isolated points and noise points.

7.1.4.3 Methods by applying various image filters or feature detectors

Local Adaptive Thresholding and Feature Extraction Approach

Due to the fact that microcalcifications appear as bright spots with a higher contrast than other local breast structures, many detection methods are based on local adaptive thresholding. An example is the algorithm designed by Davies et al. [146]. They used a local area thresholding process and then use a feature analysis step to detect microcalcifications.

In their method, the original image is partitioned into square sub-images. Each sub-image is smoothed using a median filter to remove local maxima and minima. A local threshold will then be set by evaluating the resulting histogram obtained from the smoothed sub-image, depending on whether the histogram is bimodal or unimodal. The threshold is set at the valley if it is bimodal; else the threshold is set initially at the maximum and then set to a value interpolated from neighbouring sub-images. In order to get the pixels with high local contrast as microcalcifications, the region of interest in one sub-image will overlap with four other sub-images, so that any pixel has actually undergone five threshold values. The pixel is chosen as potential microcalcification candidate if it is above at least a pre-determined number of thresholds from these five values.

Next, five features including the area and mean grey level are selected and analyzed in the training set. For example, the areas of calcifications range from *0.3-2.5* mm^2, the grey level ranges from *25* for faintest calcifications to *245* for the brightest one. In addition, they also consider microcalcification clusters by considering the distance between the neighbours. A cluster exists if the distance between

microcalcifications is less than *5*mm and there are at least *3* microcalcifications in the cluster.

Comments

The image processing approach is the most suitable approach for consideration, because it is the most straightforward and direct. Specifically, we have combined the Harris corner detection (Harris) and anisotropic diffusion (AD) because Harris has an adjustable threshold applicable for our purpose while AD can help smooth the noise in our noisy DBT images.

7.2 Combination of Harris Corner Detector and Anisotropic Diffusion Approach

In this section, we will evaluate both Harris corner detector and the anisotropic diffusion approach in more detail. In order to have a relevant evaluation especially for detection in a single DBT projection, we first look at the requirements of a microcalcification detection algorithm in a single DBT projection. We will then evaluate the two approaches from this basis. Finally, we will have a detection analysis using this combination approach.

7.2.1 Requirements of a microcalcification detection algorithm in a single DBT projection

A microcalcification detection algorithm shares similar criteria to corner detectors discussed in [147], with more emphasis on microcalcifications, instead of corners. We highlight and discuss the requirements as follows:

1. All the microcalcifications should be detected. (Criterion 1)

Having said that, we are aware there exists cases in reality that some microcalcifications cannot be detected even using the perfect microcalcification detection algorithm, due to the physical constraints e.g. the microcalcification is blocked by another microcalcification in the direction when the X-ray projection is taken.

2. *No false microcalcifications should be detected. (Criterion 1)*

Sometimes, the detection algorithm misclassifies breast structures e.g. fibroglandular tissues or blood vessels as microcalcifications, in addition to the misclassification of noise points. A good detection algorithm should minimize these misclassification cases as often as possible.

3. *The detection algorithm should be robust with respect to noise. (Criterion 2)*

The signal-to-noise ratio in DBT is even worse than that in mammography. So, an important criterion of a microcalcification detection algorithm in a single DBT projection is its robostness to noise.

4. *Microcalcifications should be well localized at different scales. (Criterion 3)*

Since microcalcifications vary in size, shape, boundary and intensity, a good detection algorithm should detect microcalcifications at the same correct coordinates at different scales.

5. *Microcalcifications detected in one projection should also be detected in other projections. (Criterion 4)*

This is to say, a good detection algorithm should be transformation invariant, so that microcalcifications should be detected in all DBT projections if all the projections are taken under the same conditions. Of course, the conditions in DBT are never the same and microcalcifications may be detected in some projections but not the others.

6. *Microcalcifications should be detected even the contrast to the surrounding tissues is small. (Criterion 5)*

In general, there are *2* classes of tissues, namely adipose and fibroglandular tissues, surrounding a microcalcification, making different contrasts. A good detection algorithm should be able to distinguish the microcalcification from any surrounding tissue.

7. *The detection algorithm should be efficient. (Criterion 6)*

The requirement is even more demanding in DBT because multiple projections will be processed instead of *2* projections in mammography.

7.2.2 Evaluation of Harris corner detector and anisotropic diffusion approach

Criterion 1: Applicability and performance in microcalcification detection in mammography

Harris corner detector

No literature has been found using this technique specifically for microcalcification detection. Having said that, the detector is historically significant and has been widely used in image processing. There exists many improved version of the detector based on the fundamental idea e.g. using derivatives of a Gaussian or using different cornerness measure. The literature suggests that its detection performance in other images used in the experiments is good in general.

Anisotropic diffusion approach

A few researchers have applied the technique in microcalcification detection in mammography e.g. [148, 149]. The results are promising. In [148], it suggests that "the tissue structure of background can be further suppressed and microcalcifications be greatly enhanced" using this filtering. In [149], it suggests that "the method provides excellent true positive rates in both detection of isolated coarse calcifications and microcalcifications with a very low number of false positives per image" in their experiment settings.

Criterion 2: Robustness to noise

Harris corner detector

In [150], the detectors' sensitivity to different levels of noise is evaluated. It is found that Harris corner detector performs poorly and the detection rate of true corners goes down sharply from low to high level of noise.

Anisotropic diffusion approach

The principle of this approach is to remove noise from the images without blurring edges. If an appropriate diffusion coefficient is chosen e.g. in Perona and Malik, the resulting equations encourage diffusion (hence smoothing) within regions and prohibit it across strong edges. So, the edges can be preserved while removing noise from the image. Hence, the approach is reasonably resistant to noise.

Criterion 3: Multi-scale detection and localization accuracy

Harris corner detector

Harris method detects corner points at a single scale and it rarely captures all the corner points that contain much information of the structure in the image [151]. Also, it suffers from poor localization [150].

Anisotropic diffusion approach

The scale-space and immediate localization are the properties of anisotropic diffusion approach developed by Perona and Malik [142].

Criterion 4: Transformation invariant

Harris corner detector

The Harris method is rotation invariant but not scale invariant.

Anisotropic diffusion approach

The approach is both rotation invariant and image scale invariant.

Criterion 5: Sensitivity to contrast

Harris corner detector

By assigning different threshold values for the cornerness measure, its sensitivity to contrast can be adjusted.

Anisotropic diffusion approach

Similarly, the sensitivity to contrast can be adjusted by changing the value of the parameter (K) used in the diffusion coefficient.

Criterion 6: Speed

Harris corner detector

It is slow because every pixel is involved in the computation. Also, the convolution step using a Gaussian filter is very time consuming [152].

Anisotropic diffusion approach

It is slow on sequential machines because in the diffusion process a continuum of scales are generated instead of a small fixed number.

Summary

	Harris corner Detector	**Anisotropic diffusion approach**
Criterion 1: Applicability and performance in microcalcification detection in mammography	N/A (Detection performance is good in other images.)	✓✓
Criterion 2: Robustness to noise	×	✓
Criterion 3: Multi-scale detection and localization accuracy	×	✓
Criterion 4: Transformation invariant	Partially	✓
Criterion 5: Sensitivity to contrast	✓	✓
Criterion 6: Speed	×	×

Table 7.1: Summary of comparison between Harris corner detector and aniostropic diffusion approach.

7.2.3 Detection Analysis Using the Combination Approach (Harris-AD)

Our choice of detection algorithm is the combination of Harris corner detector (Harris) and anisotropic diffusion (AD), because we want to take both advantages that Harris is a well-known good corner detector and AD is robust to noise. In this section, by using a

real DBT dataset, we will discuss the impact of the cornerness measures of the microcalcifications after the DBT projections are smoothed by AD.

(1) Microcalcifications will not be smoothed away even after many iterations in AD, provided that a suitable contrast parameter K is chosen.

We start our analysis using the real DBT dataset of *Patient 7* and we have extracted a region containing *3* microcalcifications. We applied AD on tomo4 with *K=10* and *K=30* at iterations *10, 100* and *1,000*. The smoothed images are shown in *Figure 7.18* and *Figure 7.19*:

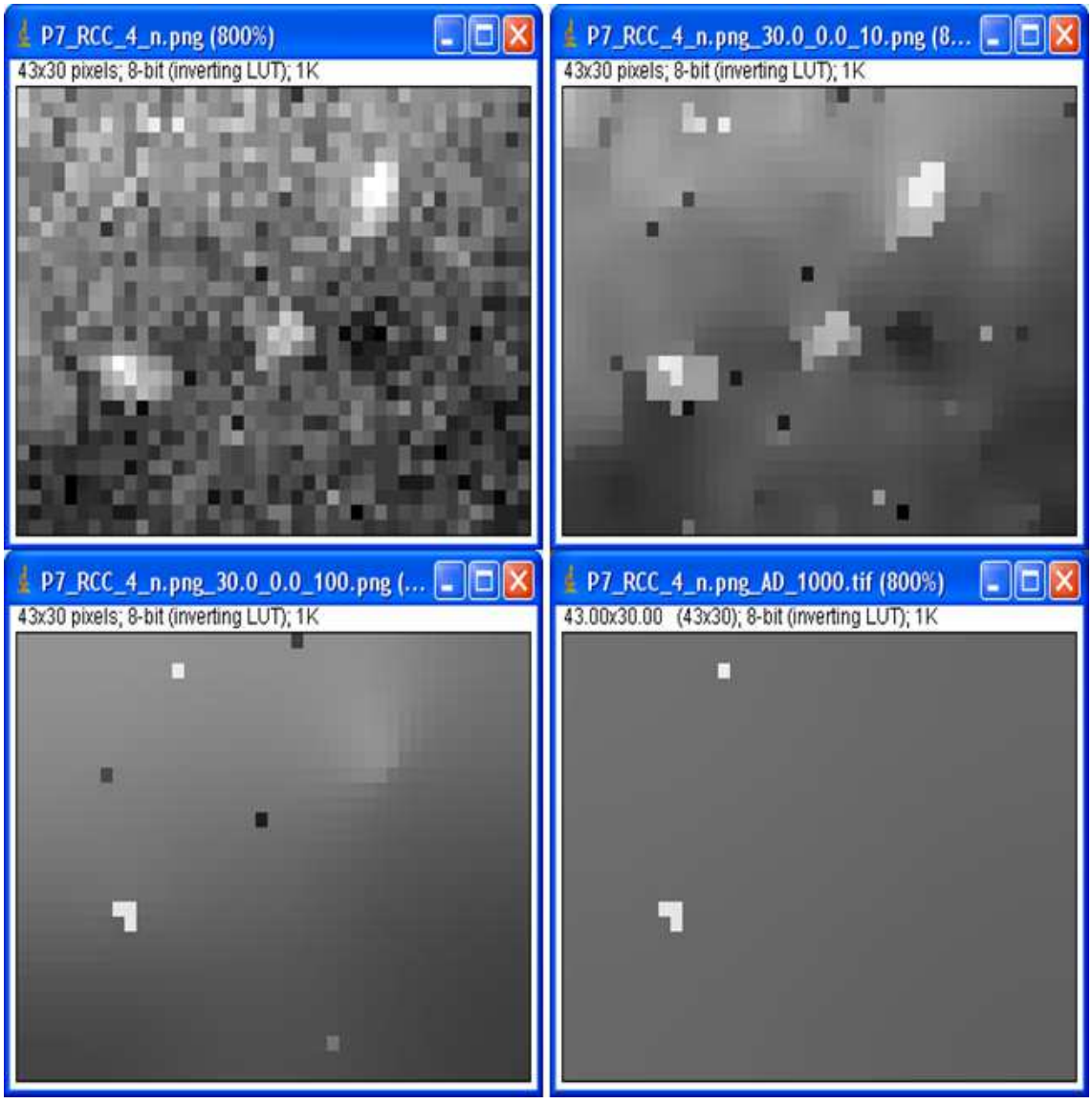

Figure 7.18: AD smoothed images of Patient 7 at 0 (original), 10, 100, 1000 iterations (from left to right, top to bottom) at K=30.

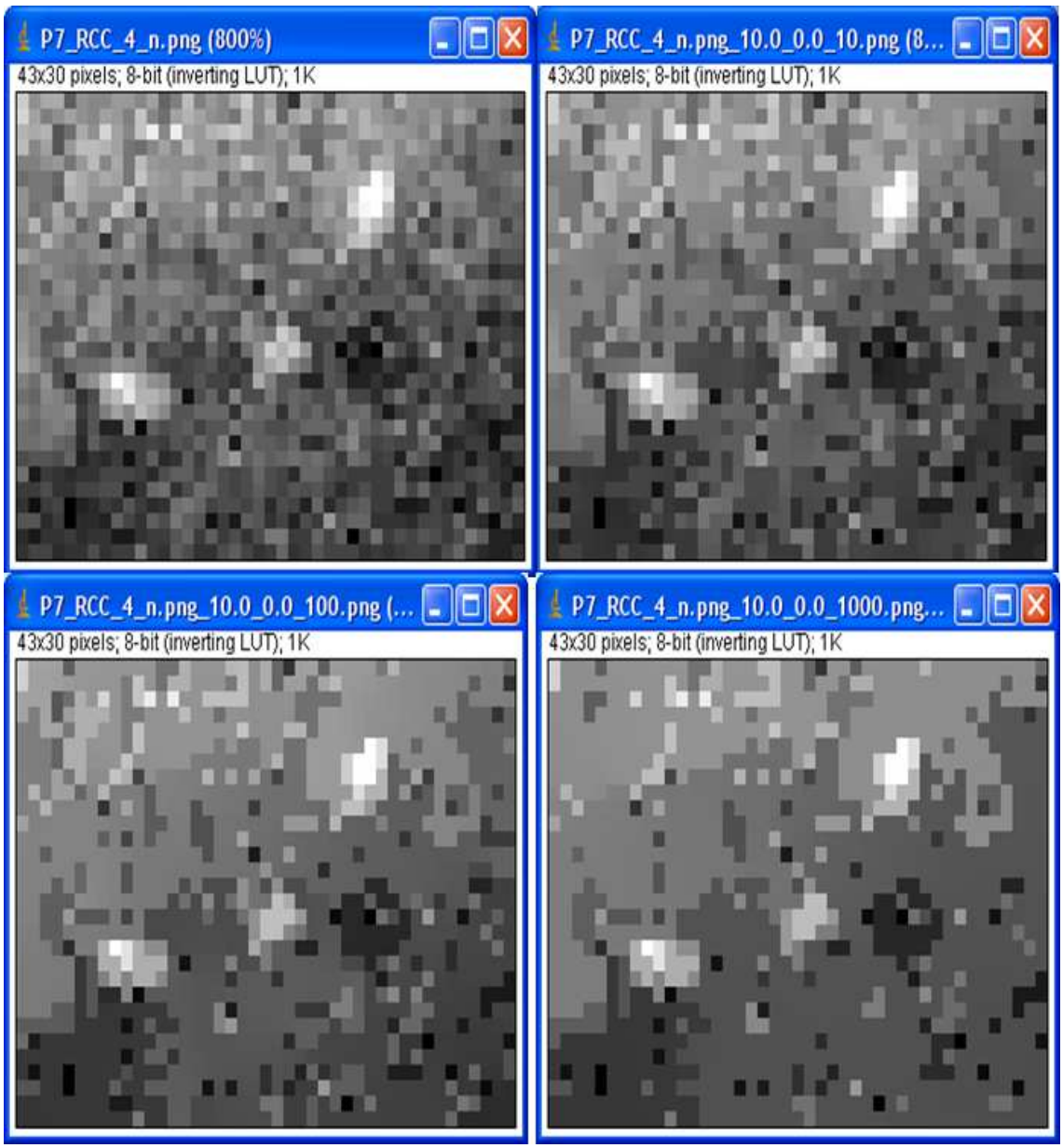

Figure 7.19: AD smoothed images of Patient 7 at 0 (original), 10, 100, 1000 iterations (from left to right, top to bottom) at K=10.

The contrast of microcalcifications to the tissues in typical DBT projections should not be too large. In this example, if K is *30* (too large), then the microcalcifications are smoothed out at large number of iterations e.g. even *100* iterations. When a suitable K (a smaller one) is chosen, e.g. *10*, the microcalcifications can still be seen even at *1000* iterations.

(2) At certain iterations of AD, the cornerness measures of the microcalcifications will be "saturated". This means large smoothing lets microcalcification "stands out" while at the same time the noise points are smoothed away.

We have observed the change of cornerness measures at different number of iterations for the *3* microcalcifications at *5* DBT projections of *Patient 7* (tomo4, tomo5, tomo6, tomo7, tomo8). We found that after a certain number of iterations, the cornerness measures "saturates" (decreases slowly, flattens or even increases). This is because noise is smoothed away after a number of iterations and the cornerness measure after this stage will mostly reflect the contrast between microcalcifications and the surrounding tissues. The following plots show the average cornerness measures (Harris) against number of iterations (AD) of *3* microcalcifications in *5* DBT projections at K=*30*:

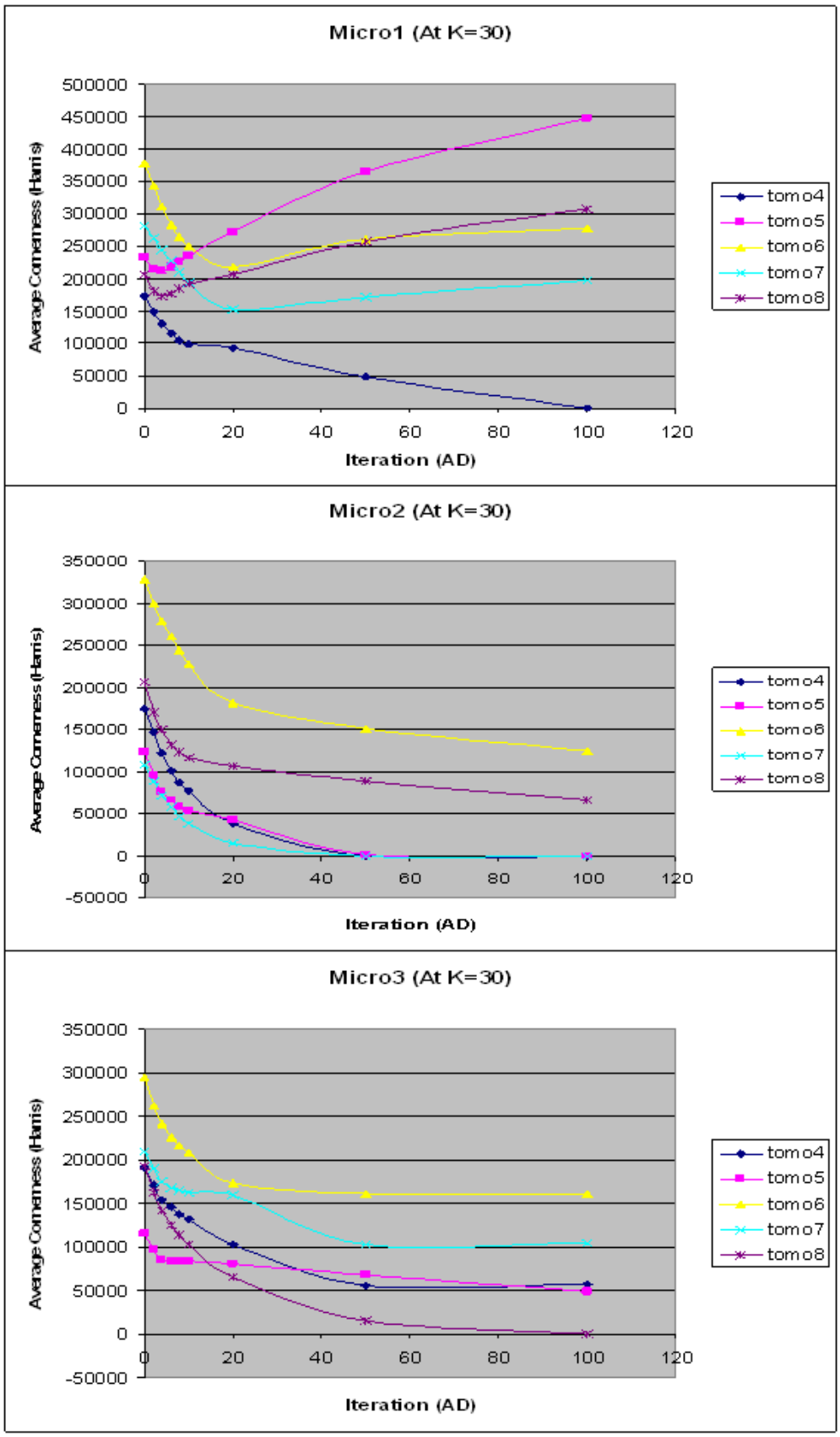

Figure 7.20: Plots of the average cornerness measures (Harris) against number of iterations (AD) of 3 microcalcifications in 5 DBT projections of Patient 7 at K=30.

As mentioned before, a poorly chosen K will lead to microcalcifications being smoothed away and that is why the cornerness measures of some microcalcification in some projections are *0*.

Now if we used a better (smaller) K, e.g. K=*10*, then we can see that the cornerness measures will be “saturated” at certain values:

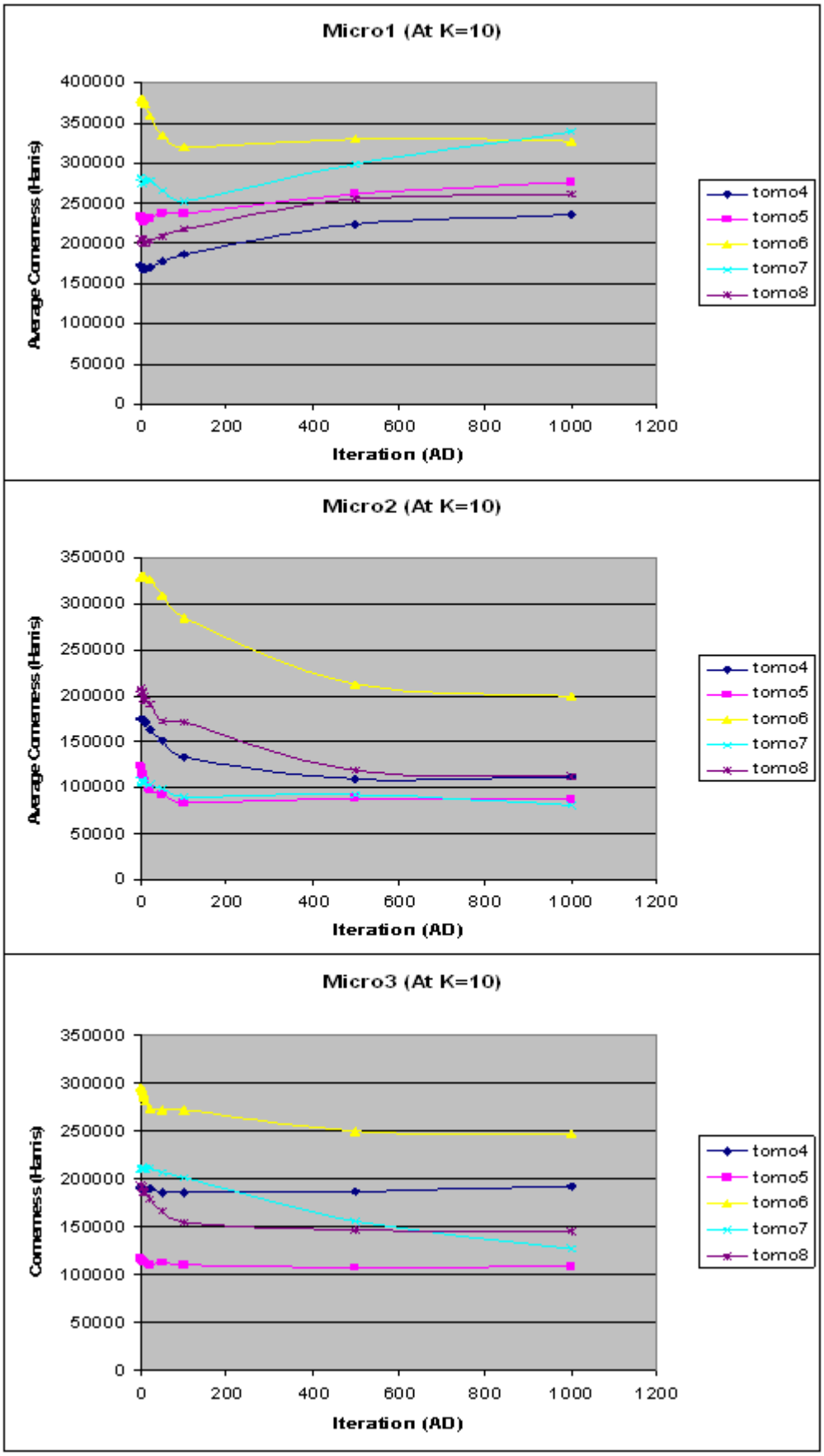

Figure 7.21: Plots of the average cornerness measures (Harris) against number of iterations (AD) of 3 microcalcifications in 5 DBT projections of Patient 7 at K=10.

From this illustration, Harris-AD serves as a better algorithm than either of them individually because microcalcification detection is more dependent on the tissue composition in the breast. The widely used Harris and its simplicity that it only needs a threshold to detect corners (in our case, microcalcifications), together with AD which can be used to smooth out the noises, will therefore be a suitable choice to demonstrate our epipolar-constrained adaptive image analysis to be discussed in the next section.

7.3 Epipolar-constrained Adaptive Image Analysis

In our case of using Harris-AD detector, our detection is based on submitting a threshold, determined by the percentage of pixels with the cornerness measures. In a realistic environment, it is possible that some relatively slightly dimmer microcalcifications may not pass this threshold in some DBT projections and cannot be detected, while the corresponding pixels in some projections may pass the threshold. We may then not be confident enough to conclude that those pixels passing the thresholds are microcalcifications. To address this problem, we propose an adaptive approach based on the benefits of epipolar curves that they can help predict the position of microcalcifications being missed in some projections. By slightly adjusting (lowering) the threshold in those projections missing the pixels, if those missing pixels at the predicted positions appear, then our confidence in believing those pixels are true microcalcifications increases.

7.3.1 An Illustration: Using a DBT dataset of Patient 24

We illustrate our concept using the middle *5* projections of patient *24* (tomo4, tomo5, tomo6, tomo7, tomo8). The following figure shows the original images and the detection results of our Harris-AD detection algorithms by setting the threshold of *0.1*% of the cornerness measures of each projection:

Figure 7.22(a)

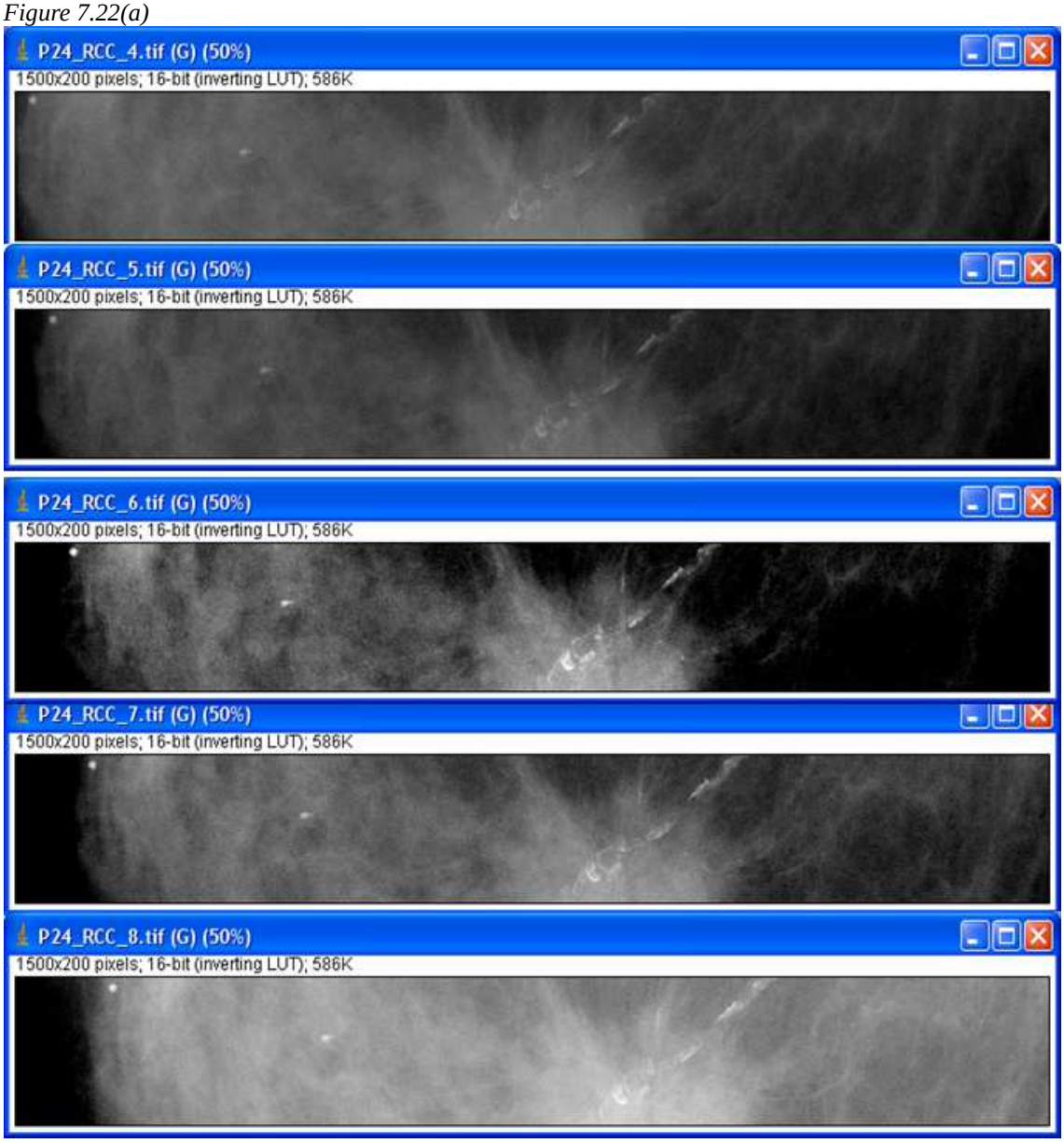
P24_RCC_4.tif (G) (50%)
1500x200 pixels; 16-bit (inverting LUT); 586K
P24_RCC_5.tif (G) (50%)
1500x200 pixels; 16-bit (inverting LUT); 586K
P24_RCC_6.tif (G) (50%)
1500x200 pixels; 16-bit (inverting LUT); 586K
P24_RCC_7.tif (G) (50%)
1500x200 pixels; 16-bit (inverting LUT); 586K
P24_RCC_8.tif (G) (50%)
1500x200 pixels; 16-bit (inverting LUT); 586K

Figure 7.22(b)

Figure 7.22: Original image (a) and the detection results using our Harris-AD algorithm (b) of patient 24.

From the figure, we can visualize that there is something missing in tomo5 (red arrow). A clearer picture will be seen if we draw out the 2D coordinates of the points detected in the region of these *5* projections:

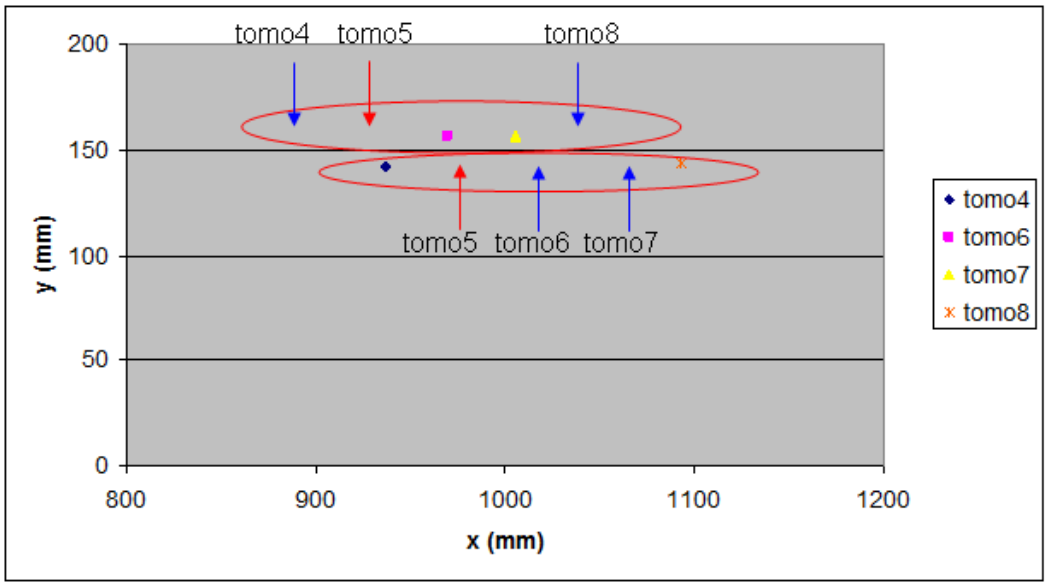

Figure 7.23: 2D plot of the detected points (4 points inside the red circles in Figure 7.22).

In fact, *2* microcalcifications are suspected in the region around the red circles in *Figure 7.22 (b)*, although we have only detected *4* points out of *5* DBT projections. The *2* microcalcifications are highlighted as red ellipses in *Figure 7.23*. For the top ellipse (microcalcification), points are missing in tomo4, tomo5 and tomo8 (the predicted positions are indicated by blue arrow, red arrow and blue arrow respectively); for the bottom one, points are missing in tomo5, tomo6 and tomo7 (the predicted positions are indicated by red arrow, blue arrow and blue arrow respectively). For illustration, we perform our analysis on tomo5 (the red arrows). Using epipolar curve analysis, we predict the locations of the *2* points are *(929, 156)* (for the top one in the figure) and *(976, 143)* (for the bottom one in the figure) if they are microcalcifications. Our adaptive approach tries to adjust the threshold in tomo5 a little bit, let's say, by setting the threshold of *0.2*% of the cornerness measures of tomo5. This means we lower the threshold a little bit, allowing more points to be detected. Here are the detected results:

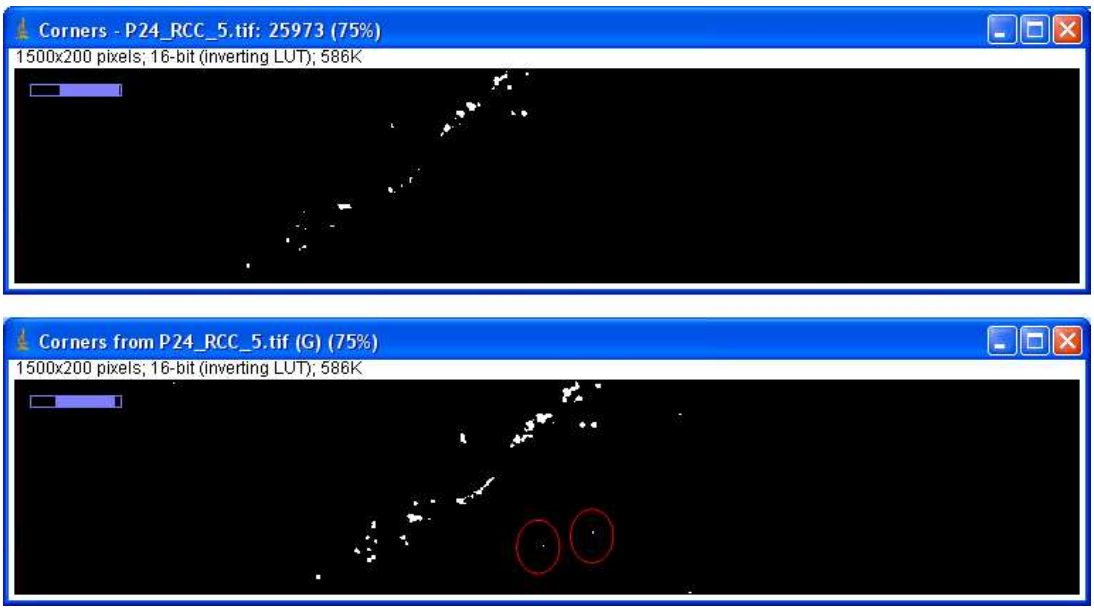

Figure 7.24:Detected results of tomo5: Using 0.1% of cornerness measures (Top); Using 0.2% of cornerness measures (Bottom).

The detected positions of the two points are *(976, 143)* and *(930, 157)* where we have predicted the positions as *(976, 143)* and *(929, 156)* respectively. The magnified region is shown in the following figure:

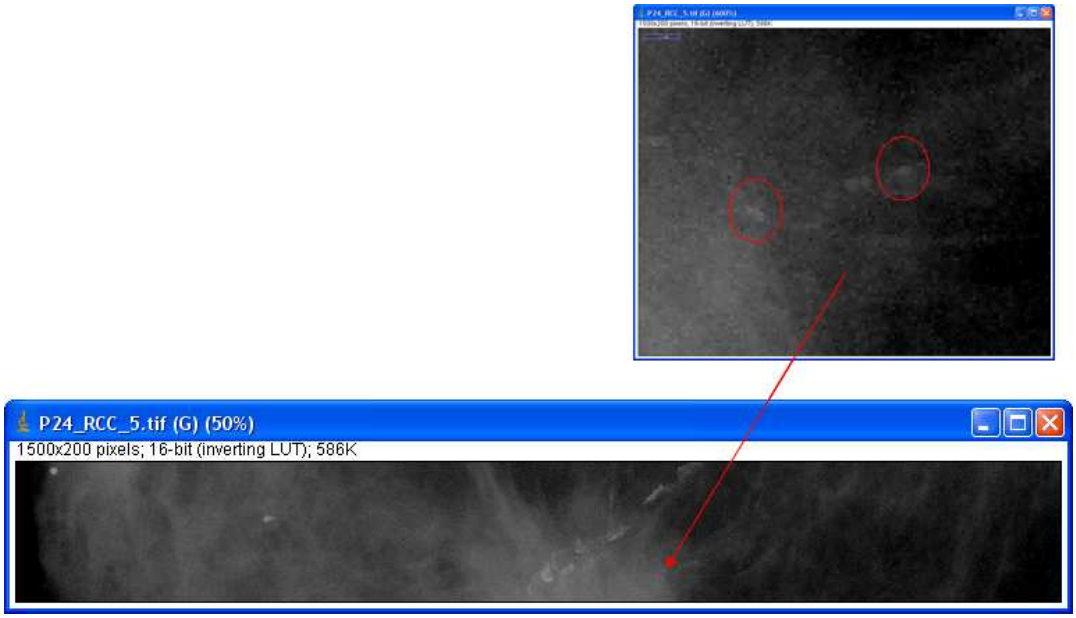

Figure 7.25: Detected results of tomo5: Using 0.1% of cornerness measures (Top); Using 0.2% of cornerness measures (Bottom).

It is therefore likely that the microcalcifications are at the positions.

7.3.2 Results of More Real DBT Examples

We now show some more results using real DBT datasets. (Note: The purpose of the experiments is to illustrate the adaptive approach only and we focus only on the suspected points. The *%* of cornerness measures are chosen differently and deliberately

so that the suspected points can be shown after adaptation. Having said that, all examples show only small adjustments in the threshold values. In reality, the % of cornerness can be determined empirically and a discussion on the consideration of the adjustment is given in Section 7.3.3.)

(1) Patient 13 (P13_LCC):

The points appear in tomo4 when the threshold value changes from *0.7*% to *1.0*% of cornerness measures:

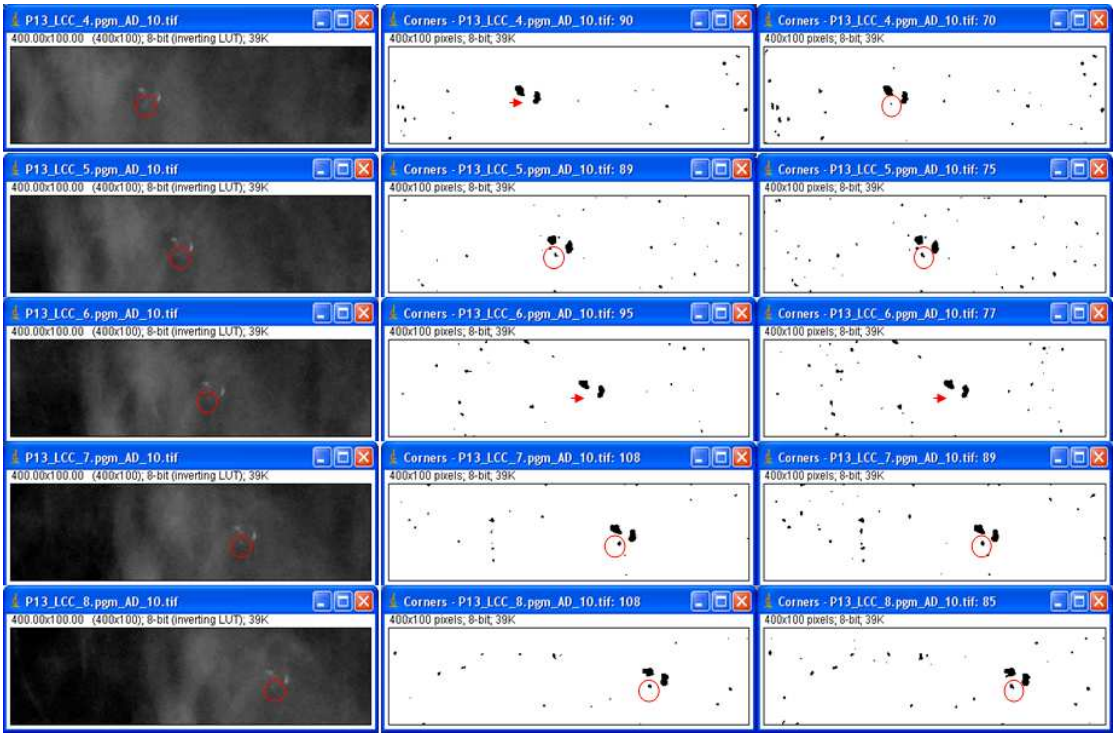

Figure 7.26: Original images (Left); Detection results initially (red arrow indicating possible missing point) (Middle); Detection results after threshold adjustment (Right) of patient 13.

(2) Patient 16 (P16_LCC):

The points appear in tomo7 when the threshold value changes from *1.2*% to *1.3*% of cornerness measures:

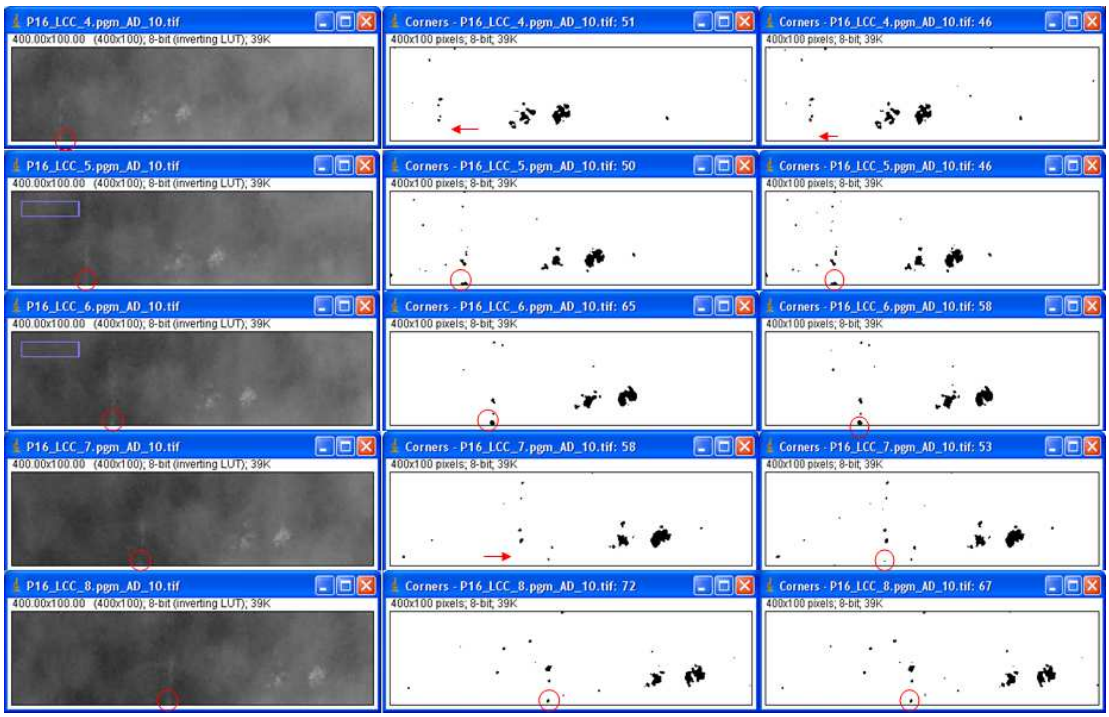

Figure 7.27: Original images (Left); Detection results initially (red arrow indicating possible missing point) (Middle); Detection results after threshold adjustment (Right) of patient 16.

(3) Patient 19 (P19_RCC):

The points appear in tomo5 when the threshold value changes from *0.3*% to *0.5*% of cornerness measures:

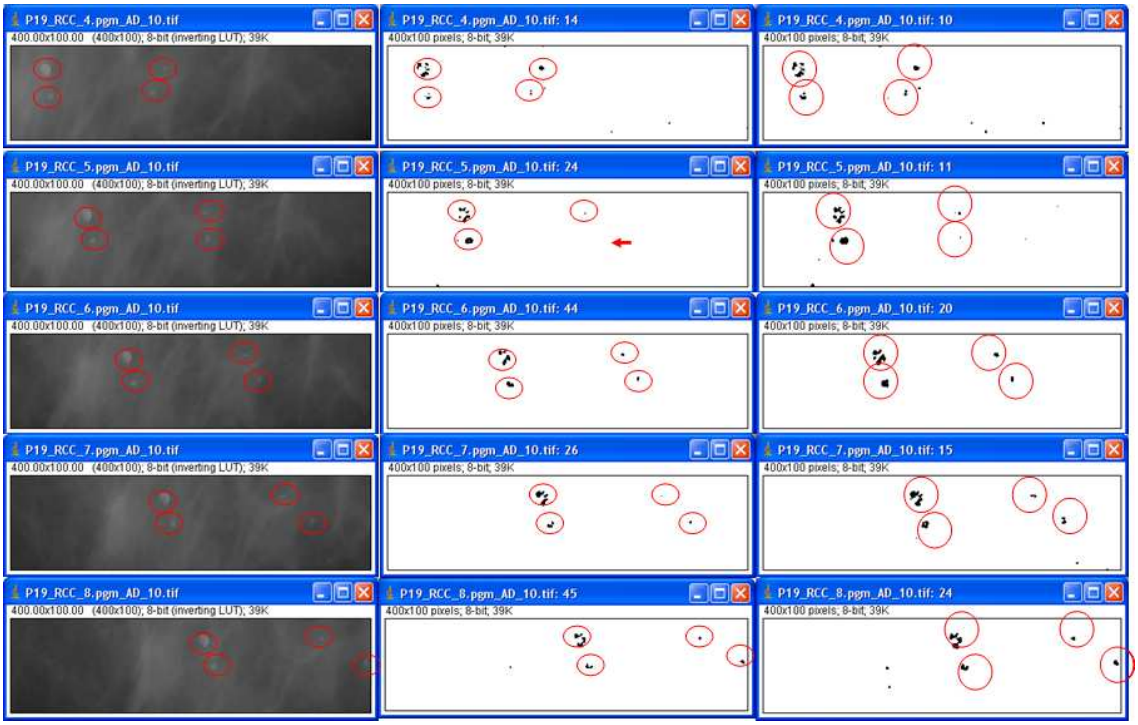

Figure 7.28: Original images (Left); Detection results initially (red arrow indicating possible missing point) (Middle); Detection results after threshold adjustment (Right) of patient 19.

7.3.3 Considerations in Threshold Adjustments

In the previous examples, initially the threshold values are chosen according to the top *a*% of cornerness measures in the projections. Then, we slightly increase *a* to *a'* incrementally. By doing so, the threshold is lowered, so that more points are detected and the missing points can hopefully appear.

Two parameters, to be determined empirically, can be considered in setting *a'*: a_{max}, the maximum *%* of cornerness measures (which controls the minimum threshold values allowed for detection); *b*, the belief that the detected projection points representing one same microcalcification (To fulfil the belief, the number of DBT views that the same suspected microcalcification is detected / the total number of DBT views, should be greater than the belief. If so, we are confident that the detected points represent one same microcalcification.).

For example, assume there are *13* DBT views. Initially we set a = *0.1* of cornerness measures for detection. Suppose, say, that a suspected microcalcification is detected in *5* DBT views (e.g. in DBT views: *1, 2, 5, 6, 7*). Suppose that we want a belief of *0.5*. In other words, we are confident only if the projection points representing the same microcalcification is detected in at least *7* DBT views. So, we need to adapt the threshold values to see whether it can fulfil our belief, i.e. we adjust *a* to *a'*. By incrementally setting *a'* ($\leq a_{max}$) in those DBT views that the points are not detected (i.e. in DBT views: *3, 4, 8, 9, 10, 11, 12, 13*), we check whether the points can be detected in the predicted corresponding positions using a'. Let say, when *a' = 0.3* ($\leq a_{max} = 1$), the points can be detected in the predicted positions in DBT views *10, 11, 12*. Now, we have *8* DBT views. *8/13 = 0.62* is larger than our belief (which is equal to *0.5*). So now, we are confident that these corresponding points in these 8 DBT views come from the same microcalcification. It is noted that the microcalfication points may not be detected in some DBT views (e.g. DBT views *3, 4, 8, 9, 13* in this example.) no matter how we adjust the threshold. This may be caused by the poor contrast with the surrounding tissues when X-rays are captured in those particular angles.

7.4 Conclusions and Discussion

In this chapter, we have illustrated an adaptive approach to microcalcification detection in an individual projection in DBT using a combination of Harris corner detector and anisotropic diffusion. We have shown that in some real DBT datasets, microcalcifications originally not detected in some projections can appear by adjusting slightly the thresholds. This assists our decision in determining whether the detected points come from a true microcalcification.

Chapter 8

Epipolar Curves Approach II: Belief Propagation for Microcalcifications Detection in DBT

Markov random field (MRF) models have been widely used in solving problems in image analysis and computer vision e.g. the segmentation of a medical image into tissue classes; image restoration from noise; predicting disparities in stereo vision; and finding displacements in registration. Applying the MRF framework for the segmentation of microcalcifications from other tissue classes (i.e. microcalcification detection) in a mammogram has also been studied and demonstrated e.g. [131]. Contextual relations between the pixel labels of a neighbourhood is modelled using a random field so that a labelling (assigning pixels to microcalcification class or other tissue classes) is found with maximum posterior probability (MAP). With the multiple projections available in DBT and with our epipolar curves approach providing geometric information, contextual constraints with other projections can be utilized. This includes the cross correlation constraint across neighbouring projections and the consensus constraint in all projections. By applying these constraints, a novel approach based on using MRFs in microcalcification detection in DBT is developed in this chapter. Since the MRF framework yields an optimization problem that is NP hard, good approximation techniques based on belief propagation have been developed. Specifically, an implementation of the max-product belief propagation (BP) from [153] has been adopted.

The outline of this chapter is as follows: First, a brief introduction to the MRF framework will be given. We then discuss how our detection problem can be formulated within the MRF framework. Instead of following the instinctive assumption that microcalcifications and non-microcalcifications classes are labelled for each pixel,

we move one step further and assign to microcalcification pixels a label that is an integer depth *d*, indicating the depth of the corresponding microcalcification in the breast, while all non-microcalcification pixels are assigned a label that amounts to a meaningless value. Our aim is to find a labelling using MAP. We do this by converting the problem to an equivalent energy minimization problem. The formulation of the energy minimization function, which consists of a data cost term and a discontinuity cost term, will be detailed. The data cost term measures how much it costs to assign a particular label f_p to the pixel *p*, while the discontinuity cost term measures how much it costs to have differences in the label f_q for a neighbouring pixel *q* having given that the label of pixel *p* is f_p. In our case, the cost terms are related to the costs in assigning a depth *d* to pixel *p*. We define our cost terms using the detection results, cross correlation with neighbouring projections and depths predicted from other projections. Next, the BP approach will be reviewed for performing inference on our MRFs. The message passing mechanism of BP and the computation of message updates is presented. We then propose a workflow for our algorithm. The algorithm consists of three steps: Step 1) Detection in a single projection; Step 2) Initialization – Generation of depth maps using neighbouring projections only; Step 3) Iteration – Generation of depth maps using all the projections. To illustrate the method, a step by step example is presented. Following this, we will show results using real DBT datasets obtained as part of the TSB collaborative project with Dexela Ltd. The results are promising in that the depths assigned by the BP are consistent with those obtained from a state of the art DBT reconstruction algorithm. Using our BP approach, not only can the microcalcifications be detected, their approximate depths in the breast can also be determined concurrently. Finally, a conclusion and discussion section will be given.

8.1 Markov Random Fields (MRFs)

A Markov random field [154, 155] is an undirected graphical model which has a set of nodes (pixels in the case of an image) representing a set of random variables (8.1.1) satisfying Markov properties (8.1.3), connecting by a set of undirected links (relationship with neighbouring pixels) (8.1.2).

8.1.1 Labelling Problem

MRF theory is a branch of probability theory for analyzing the spatial or contextual relationships of physical phenomena. In image processing, it is about analyzing the spatial dependencies between neighbouring pixels, by following the probability distributions according to the image content. (An excellent discussion on MRF in image analysis can be referred to [155].)

The labelling problem is to assign a label to each pixel p in $\mathcal{P}$ where a rectangular lattice for a 2D image of size $m \times n$ can be denoted by:

$$\mathcal{P} = \{(i, j) \mid 1 \le i \le m, 1 \le j \le n\} \qquad \textit{Eqn. 8.1}$$

Each random variable corresponds to a node and takes values from a set of labels $f_p \in \mathcal{L}$. It has a set of probabilities corresponding to each label f_p. A label can be discrete or continuous. For example, the labels may correspond to tissue classes in the case of image segmentation, intensities in the case of image restoration, disparities (depths) in stereo vision, or displacements in the case of image registration. Our ultimate goal is to find a labelling with MAP for the whole image. In other words, we wish to determine the best labelling configuration for the image and this is determined by the contextual constraints in the image.

Contextual constraints are expressed locally in terms of conditional probabilities $P(f_i \mid \{f_{i'}\})$, where $\{f_{i'}\}$ denotes the set of labels at the other sites $i' \neq i$, or globally as the joint probabilities $P(f)$. Generally, the labels are assumed to be independent (no context), in which case the joint probability is the product of the local ones:

$$P(f) = \prod_{i \in \mathcal{P}} P(f_i) \qquad \textit{Eqn. 8.2}$$

This implies the conditional independence:

$$P(f_i \mid \{f_{i'}\}) = P(f_i) \quad i' \neq i \qquad \textit{Eqn. 8.3}$$

In the presence of context, the labels are in fact mutually dependent. Usually, however, they are primarily dependent to their neighbours.

8.1.2 Neighbourhood System

The pixels in $\mathcal{P}$ are related to one another via a neighbourhood system $\mathcal{N}$ which is defined by:

$$\mathcal{N} = \{\mathcal{N}_p \mid \forall p \in \mathcal{P}\} \qquad \textit{Eqn. 8.4}$$

For a regular lattice $\mathcal{P}$, in the first-order neighbourhood system, also called the *4*-neighbourhood system, every (interior) pixel has four neighbours (Figure 8.1):

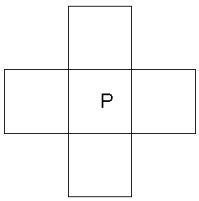

Figure 8.1: The 4-neighbourhood system.

There are other neighbourhood systems such as *8*-neighbourhood system and so on. In our discussion, we will use the first-order neighbourhood since it is sufficient to demonstrate our concepts.

In a MRF, a node (pixel) *p* is connected with its neighbours with links. Each link shows the interaction of pixel *p* with its neighbour $\mathcal{N}_p$. Regarding the labelling problem, it concerns the relationship between pixel *p* being assigned label f_p and its neighbour, pixel *q*, being assigned label f_q.

8.1.3 Markov Property

A MRF on image $\mathcal{P}$ w.r.t. a neighbourhood system $\mathcal{N}$ is defined if it fulfils the Markov property that a variable is conditionally independent of all other variables which are not its neighbours. It means that the assignment of labels in any two pixels is independent if the pixels are not neighbours to one another.

8.1.4 Definition of Markov Random Fields

Now the MRF can be defined and rewritten using random variables, labels, neighbourhood system, probability theory and the Markov property together.

Let $F = \{F_1,...,F_m\}$ be a family of random variables defined on the image $\mathcal{P}$ in which each random variable F_i takes a value f_i in $\mathcal{L}$. F is said to be a MRF on image $\mathcal{P}$ w.r.t. neighbourhood system $\mathcal{N}$ if and only if the following two conditions are satisfied:

$$(1)\quad P(f) > 0, \forall f \in \mathcal{F} \qquad \textit{Eqn. 8.5}$$

$$(2)\quad P(f_i \mid f_{\mathcal{P}-\{i\}}) = P(f_i \mid f_{\mathcal{N}_i}) \qquad \textit{Eqn. 8.6}$$

where $P(f)$ is the joint event of all random variables at one configuration *f*, $\mathcal{F}$ is the set of all configurations, $f_{\mathcal{P}-\{i\}}$ is the set of labels at pixels other than *i* and $f_{\mathcal{N}_i}$ is the set of labels at the neighbourhood of *i*. This means that the joint probability $P(f)$ is uniquely

identified by the local conditional probabilities (from (1)) and only neighbouring labels have interactions with each other (from (2)).

8.2 Labelling for Microcalcification Detection in DBT – Depth of a Microcalcification in the Breast

8.2.1 Our Label Set

The microcalcification detection problem can be modelled as a labelling problem. Combining the concepts in: [131] which models the microcalcification problem as tissue classification problem using MRF, [153] which corresponds the labels to different disparities in early vision problem, and [156] which predicts displacements across two images in image registration, we develop a MRF approach using the depth *d* of a microcalcification in the breast as the label to be assigned to each pixel in a DBT projection that corresponds to that microcalcification.

It is important to note that our definition of depth refers to the world coordinate system defined in the geometry of DBT acquisition system as discussed in Chapter 6. In the notation introduced in that chapter, depth *d* means the coordinate *c* of the microcalcification *m (a, b, c)* in world coordinates. More precisely, this refers to the depth of the microcalcification in the breast from the defined reference point which is set at the pivot of the rotation arm. Different pixel positions across different projections representing the same microcalcification therefore share the same depth *d*.

In a DBT projection, it is only meaningful to identify the depth *d* for a microcalcification pixel. Here, we model *d* as discrete and adopt the resolution as used in DBT slices. More precisely, *d* is an integer representing the depth from the pivot point. For example, if the breast is *80 mm* thick and is *20 mm* above the pivot and *60 mm* below the pivot, and the resolution is *1 mm*, we have *81* discrete depth *d* values, ranging from *-20, -19, -18,…, 0, 1, 2, …, 60*. (Note: for implementation purposes, we can simply shift the *d* values so that they range from *0* to *80*.)

There is no concept of depth for non-microcalcification pixels, because each pixel represents the integrated X-ray attenuation over the whole trajectory of the primary ray through the breast tissues. So, for pixels other than microcalcifications, the

depth label assigned to them is "MEANINGLESS". (Note: for the purposes of implementation, we can simply give it a value of *81* in this example.)

Our label set $\mathcal{L}$ is therefore defined by:

$$\mathcal{L} = \{0,1,2,3,..., d_{\max} - 1, d_{\max}, "MEANINGLESS"\} \qquad \textit{Eqn. 8.7}$$

where $d_{\max}$ is the maximum depth of the breast and label *0* to $d_{\max}$ are integer values (shifting for illustration and implementation purposes only), and a non-integer "MEANINGLESS" meaning the pixel does not have a depth. In other words, if a pixel is assigned to an integer label, it means it is a microcalcification; otherwise it is not a microcalcification.

By solving such a labelling problem, not only can we solve the microcalcification detection problem, we can also estimate the depth of the microcalcifications in the breast. The two critical tasks in the early detection of breast cancer are solved in one go.

8.2.2 Relationship of Depth and Displacement Across DBT Projections

Instead of labelling the pixel with a displacement value or disparity as in [153, 156], our label corresponds to the depth of a microcalcification in the breast. But a depth *d* in the breast actually represents a pixel displacement, +ve or –ve, *disp*, across neighbouring projections. This is derived from the geometry of epipolar curves developed in Chapter 6.

Recall that the equations of epipolar curves can be derived as follows:

$$\begin{bmatrix} x_i^s \\ y_i^s \end{bmatrix} = \begin{bmatrix} D(1-\frac{L+D\cos\theta_i}{c+D\cos\theta_i})\sin\theta_i + (u + a(\frac{L+D\cos\theta_i}{c+D\cos\theta_i})) \\ -y_{off} + v + (b + y_{off})\frac{L+D\cos\theta_i}{c+D\cos\theta_i} \end{bmatrix} \qquad \textit{Eqn. 8.8}$$

We have noted that for the non-linear terms, we have $\left(\frac{L+D\cos\theta_{i+1}}{c+D\cos\theta_{i+1}}\right) \approx \frac{L+D\cos\theta_i}{c+D\cos\theta_i}$. So, we make the following approximations and remarks:

(1) For the same microcalcification ***M(a, b, c)***, the *y*-coordinates are approximately the same in all projections.

(2) Since $\sin\theta_{i+1} - \sin\theta_i \approx 0.05$ with θ in our range, this gives nearly a straight line with slope = $D(1-\frac{L+D\cos\theta_i}{c+D\cos\theta_i})$ and y-intercept = $(u+a(\frac{L+D\cos\theta_i}{c+D\cos\theta_i})$. Hence, for the same microcalcification *m(a, b, c)*, the spacing in *x*-dimension between consecutive projections is approximately equal, to $(D(1-\frac{L+D\cos\theta_i}{c+D\cos\theta_i})(\sin\theta_{i+1}-\theta_i))$, which displacement we denote by *disp*. In other words, a microcalcification appears on pixel *p* in projection *i* should appear on pixel *(p + (i+1-i)*disp)* (= *p + 1*disp*) in projection *i+1* and pixel (*p + 2*disp*) in projection *i+2* and pixel (*p + m*disp*) in projection *i+m* and so on.

Given the epipolar curves, each depth *d* (which equals coordinate *c* in this case) corresponds to a single displacement *disp*. So for a depth at pixel *p*, we now know one corresponding pixel in each of the other projections. This is useful in the design of the cost terms in the energy minimization function that it is now feasible to include the information from other projections for the computation. In our approach, the label f_p is determined based on the correlation with neighbouring projections and the number of counts of same depth in the corresponding pixels in other projections. More details will be given in Section 8.4.

8.3 MAP-MRF Labelling

Our aim is to find a labelling for each DBT projection with maximum posterior probability (MAP) (MAP-MRF labelling problem). In other words, we want to assign a depth to each pixel in each DBT projection so that the joint posterior probability is maximized in each DBT projection.

This labelling problem can be converted to an equivalent energy minimization problem, given by the energy function [153, 155-157]:

$$E(f) = w_{data}\sum_{p\in\mathcal{P}} D_p(f_p) + w_{disc}\sum_{(p,q)\in\mathcal{N}} V(f_p - f_q) \qquad \textit{Eqn. 8.9}$$

where $D_p(f_p)$ is the data cost which measures the cost of assigning label f_p to pixel *p*; $V(f_p - f_q)$ is the discontinuity cost which measures the cost of assigning labels f_p to pixel *p* and f_q to pixel *q* which is a neighbour of *p* in a *4*-connected neighbourhood; w_{data} and w_{disc} are the weights of the data cost and the discontinuity cost in the function.

The reason why the MAP-MRF labelling problem can be converted to an energy minimization problem is because of a theoretical result that establishes the equivalence between MRFs and Gibbs distributions (Hammersley and Clifford Theorem) [158] which provides a mathematically tractable means of specifying the joint probability of a

MRF. The theorem states that F is a MRF on lattice S (in our case image $\mathcal{P}$) w.r.t. the neighbourhood system $\mathcal{N}$ if and only if F is a Gibbs Random Field (GRF) on S w.r.t. to $\mathcal{N}$.

8.3.1 Gibbs Random Fields (GRFs)

A set of random variables F is said to be a GRF on S w.r.t. to $\mathcal{N}$ if and only if its configurations follow a Gibbs distribution. A Gibbs distribution is in the form:

$$p(f) = \frac{1}{Z}\exp[-U(f)] \qquad \textit{Eqn. 8.10}$$

where f is a configuration of F, $U(f)$ is called the energy function and Z is a constant for normalization.

8.3.2 Energy function is a sum of clique potentials

The energy $U(f)$ is a sum of clique potentials $V_c(f)$ over all possible cliques C:

$$U(f) = \sum_{c \in C} V_c(f) \qquad \textit{Eqn. 8.11}$$

Note a clique c for (S to $\mathcal{N}$) is defined as a subset of sites (in our case, pixels) in S. In our case of 4-neighbourhood system, it consists of either a single-site $c = \{i\}$, a pair of neighbouring sites $c = \{i, i'\}$ where i and i' are neighbours to each other. The following figure shows the cliques in the neighbourhood system we used:

Figure 8.2: Cliques of the 4-neighbourhood system.

So, in our case, the energy can also be written as:

$$U(f) = \sum_{i \in \mathcal{P}} V_1(f_i) + \sum_{i \in S} \sum_{i' \in \mathcal{N}_i} V_2(f_i, f_{i'}) \qquad \textit{Eqn. 8.12}$$

This is exactly the form as the one we have discussed (*Eqn. 8.9*). Hence, to maximize the joint probability of labelling, what we need is to minimize the energy function.

8.4 Energy Minimization Function

The design of the data cost term and the discontinuity cost term is crucial in solving our microcalcification detection problem in DBT. It is noted that the cost assignment is different for labels with an integer depth value (a microcalcification pixel) and label as

"MEANINGLESS" (a non-microcalcification pixel). The principle of the assignment is discussed as follows:

8.4.1 Data Cost

Data cost term $D_p(f_p)$ is the data cost of assigning the depth *d* to pixel *p* in projection *i*. There are *2* situations when data cost is considered: (1) When only information of neighbouring projections is considered (during the initialization step); (2) When depth information of all projections are available (in the iteration step).

8.4.1.1 When only information of neighbouring projections are considered

(a) Labels with an integer depth value

Principle 1: The cost is related to the detection results of projection *i*. The more likely the pixel is to be a microcalcification, the lower is the cost to assign to this label (depth with integer value).

As an illustration, for the reasons outlined in the previous chapter, we used the Harris-AD as our detection algorithm. For each pixel in a projection, the algorithm returns a cornerness measure, representing a score that a pixel is a corner (in our case a microcalcification). The higher the measure, the more likely the pixel is a microcalcification. To represent this measure relative to other pixels in the projection, we use a cornerness ratio, which is:

cornerness_ratio
= cornerness of pixel *p* / max_cornerness in the projection *Eqn. 8.13*

So our data cost term depends on the pixel's own cornerness measure represented by its "cornerness_ratio". The larger this ratio, the smaller the cost.

Principle 2: The cost is related to the cross correlation value of region centred at pixel *p* with the corresponding regions in the neighbouring projections. The more correlated they are, the less the cost to assign to this label (this specific depth) is.

One approach to identifying a pattern within an image uses cross correlation of the image with a suitable mask [159]. It is likely that a microcalcification region centered at pixel *p* in projection *i* will have high correlation with a corresponding region in projections *(i-1)* or *(i+1)*. When the depth at a pixel *p* is *d*, for projection *(i-1)*, the

region should be centered at (*p-disp(d)*); for projection *(i+1)*, the region should be centered at (*p+disp(d)*). The correlation is calculated by:

$$r[i][j] = \sum_{jj=-Nj/2}^{jj<Nj/2} \sum_{ii=-Ni/2}^{ii<Ni/2} (neighbour[i+disp+ii][j+jj] - \overline{neighbour}) * (current\_projection[i+ii][j+jj] - \overline{current\_projection})$$

Eqn. 8.14

where $\overline{neighbour}$ and $\overline{current\_projection}$ are the mean of neighbour regions and the mean of current projection regions respectively; *Ni*Nj* are the size of the region for computing the correlation.

So our data cost term depends on this correlation value (absolute value). The larger this value, the smaller the cost.

Hence, we come up with our data cost term for labels with an integer value:

$$D_p(f_p) = 1\text{-cornerness\_ratio}*\text{correlation}$$

Eqn. 8.15

The data cost will then range from *0* to *1* since both cornerness_ratio and correlation are between *0* and *1*.

A point to note here that a problem with using cross correlation in general is the computational complexity, because the transformation between the two regions for which the cross correlations are computed may be affine: in our case, a translation in *x* and *y*, as well as a rotation and possibly a scaling. However, as a direct result of the epipolar analysis, there is no rotation, no translation in *y*, and no scaling, and so the search for the *disp* value is one-dimensional.

(b) Labels "MEANINGLESS"

The cost is a relative value compared with the costs when other integer labels are assigned to the same pixel *p*. If the minimum data cost computed in other integer labels is smaller than, say, *0.5*, this means it is likely that this pixel is a microcalcification, a large data cost value should be assigned, let say, *1*. Otherwise it is likely that it is a non-microcalcification, a small data cost value should be assigned, say, *0*.

8.4.1.2 When depth information of all projections are available

(a) Labels with an integer depth value

The more the corresponding pixels in other projections having similar depth with pixel *p* (count), the more likely that *p* has this depth (this label), the less the cost to assign to this label is. We term this: *multi_cost = (1 – count/NO_OF_PROJECTION).*

Hence, we propose the following data cost term for labels with an integer value:

$$D_p(f_p) = w_{neigh}(\text{1-cornerness\_ratio*correlation}) + w_{multi}*\text{multi\_cost} \quad \textit{Eqn. 8.16}$$

where w_{neigh} and w_{multi} are the weights of the cost with neighbouring projections only and the multiple projection cost respectively.

(b) Labels "MEANINGLESS"

The cost is determined by the maximum count among all integer labels (max_count). If there exists some count which is very large, this means that it is likely that the pixel has a depth, implying that it is a microcalcification. So the multi_cost is computed as max_count/NO_OF_PROJECTION.

8.4.2 Discontinuity Cost

$V(f_p - f_q)$ is the discontinuity cost which measures the cost of assigning labels f_p to pixel *p* and f_q to pixel *q* which is a neighbour of *p* in a *4*-connected neighbourhood. It measures how similar the depth of pixel *p* with its neighbour *q*. If both depths are integers, the smaller the difference, the more they are similar, the smaller the cost . It is noted that there is no preference if any of them is "MEANINGLESS" because it may be possible to have a microcalcification among the tissues or the pixel may be part of the tissue. So the cost is undetermined in these cases. The computation of discontinuity cost is the same for both situations whether depth information of all projections are available.

(a) For both pixel *p* and neighbouring pixel *q* having integer depth values

The cost is based on the difference between labels, rather than on their actual values. The cost of assigning a pair of labels to neighbouring pixels is based on the degree of difference between the labels. Neighbouring pixels with similar depth should have a smaller cost. Since a microcalcification has a size and so it may span a few pixels, the depth of its neighbours should share similar depth as pixel *p*. So, it is favourable if $f_p - f_q$ is small. The cost increases if depth of pixel *p* is very different from its neighbour.

(b) For pixel *p* having a "MEANINGLESS" label and neighbouring pixel *q* having integer depth values

We do not need to bother with this case because what we need is the minimum cost among all the labels of pixel *p* in the message computation of the BP algorithm. So, we will return the minimum cost when pixel *p* is an integer during the computation. (More details will be given in the discussion of BP in next section.)

(c) For pixel *p* having any label and neighbouring pixel *q* having a label "MEANINGLESS"

Since we do not have preference if the neighbour's depth is "MEANINGLESS", we have no way to assign the discontinuity cost (which is about the similarity between neighbouring pixel *q* and itself (pixel *p*).) But we anyway need to assign a cost when the neighbour *q* is "MEANINGLESS" and *p* is some label. Hence, we look for an alternative way to assign cost. This is based on pixel *q*'s cornerness measure and from this we will determine whether *q* is worth to be "MEANINGLESS" in this situation.

If *q* has a large cornerness value, this means it is likely that it is a microcalcification and it is likely that it has an integer depth, but here we say it is "MEANINGLESS" (contradiction), so the cost is large for pixel *q* to be "MEANINGLESS". Similar, if *q* has a small cornerness value, it is likely that it is "MEANINGLESS", so the cost is small.

Now we know the "relative" cost assignment, which is related to the cornerness value of *q*. In order to have a basis to perform the assignment, the maximum and minimum of the discontinuity cost when *p* and *q* are integer labels are adopted when pixel *q*'s cornerness value is small and large respectively.

8.5 Max-Product Belief Propagation (BP)

We follow the BP implementation in [153].

The max-product BP algorithm is an iterative method in which messages are passed from all nodes around the graph defined by the four-connected image grid in parallel. Let $m^{t}_{p->q}$ be the message that pixel *p* sends to a neighbouring pixel *q* at iteration *t*. All entries in $m^{0}_{p->q}$ are initialized to zero, and at each iteration new messages are computed as:

$$m^{t}_{p->q}(f_q) = \min_{f_p}\left(V(f_p - f_q) + D_p(f_p) + \sum_{s\in\mathcal{N}(p)\setminus q} m^{t-1}_{s->p}(f_p) \right) \qquad \textit{Eqn. 8.17}$$

where $\mathcal{N}(p) \setminus q$ denotes the neighbours of p other than q. After T iterations, a belief vector is computed for each node,

$$b_q(f_q) = D_q(f_q) + \sum_{p\in\mathcal{N}(q)} m^{T}_{p->q}(f_q) \qquad \textit{Eqn. 8.18}$$

Finally, the label f_q^* that minimized $b_q(f_q)$ individually at each pixel is selected.

8.6 Workflow of Our Algorithm and a Step-by-Step Example

Our algorithm consists of three steps:

8.6.1 Step 1) Detection in individual projections

The algorithm starts by detection in each of the DBT projections individually, using the Harris-AD. The output of the algorithm is that every pixel will have a cornerness measure, indicating its likelihood of being a bright white spot. The larger the value, the more likely it is a microcalcification. Note that we do not expect the detector to give us "near perfect" microcalcification detections, in the sense of maximising the true positive fraction (TPF), while minimising the number of false positives (FP), rather we need to find a suitably high TPF and sufficiently low FP that the epipolar constraint can improve both.

As an illustration, we will detection microcalcifications in *4* projections in our dataset Patient 7 P7_RCC, namely tomo4, tomo5, tomo6, tomo7.

Figure 8.3:Original images (Left) and detection results (Right) of Patient 7.

From the figure, we noted the three bright white spots in the projections (in red circle), which have a slight shift across projections. We first used the detection algorithm to generate *4* lists of cornerness measures. The figure shows the results if we use a threshold of *20*.

8.6.2 Step 2) Initialization – Generation of depth maps using neighbouring projections only;

In this step, we generate a depth map for each projection using only neighbouring projections. As discussed previously, the neighbouring projections are used for the computation of the correlation during the data cost calculation. As an illustration, we used the next projection as the neighbouring projection, e.g. for generating the depth map of tomo4, we used tomo5. Here are the depths maps:

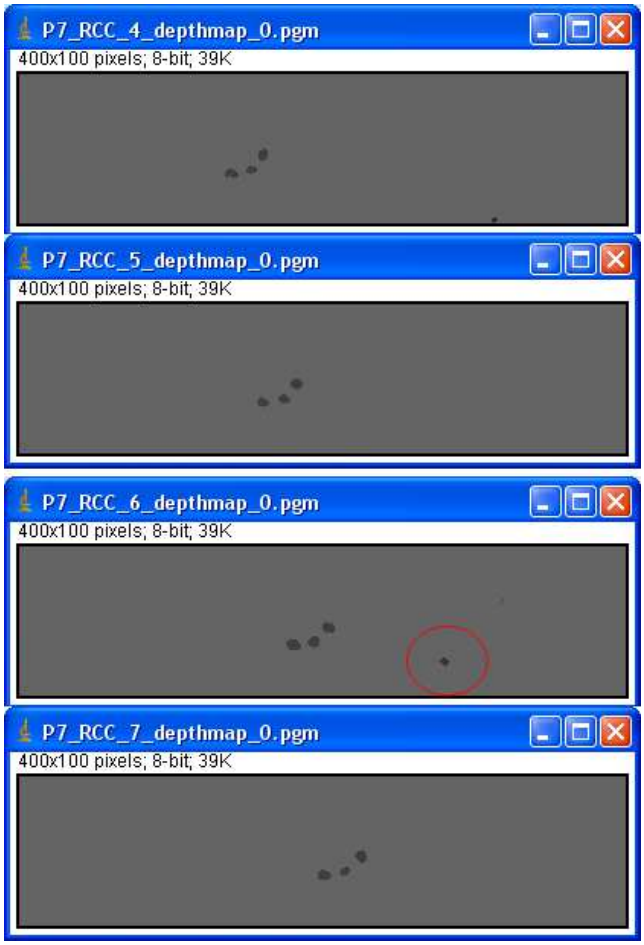

Figure 8.4: Depth maps using neighbouring projections only.

From the figure, we showed that the results of BP algorithm using just neighbouring projections are promising and at least comparable with other single detection algorithms, in our case, Harris-AD. In addition, the depths of the microcalcifications are also estimated. In this illustration, the depths for those *3* microcalcifications are between *15 mm* and *18 mm*. When we tried to reconstruct them in 3D using a reconstruction method based on our epipolar curves formulas (to be discussed in Chapter 9), we found that the estimated depths are consistent. Using the reconstruction method, the depths of these 3 microcalcifications are *15.64 mm*, *17.42 mm* and *17.62 mm*. We have also compared these with the slice numbers generated using typical DBT reconstruction algorithms and found that the results are consistent.

Note in the projection tomo6, there is *1* obvious spot on the right (red circle). It will be removed after we consider the depths maps of all projections in the next step.

8.6.3 Step 3) Iteration – Generation of depth maps using all projections

After the initial depth maps are generated for each projection, we can now utilize this information to enhance the computation of the joint probability of the MRF-MAP

labelling problem. We include the multiple projections constraint into the data cost computation.

In our example, we now obtained *4* depth maps from Step 2. By adding the consensus constraint of counting the number of similar depths in the corresponding pixels, we obtained *4* new depth maps:

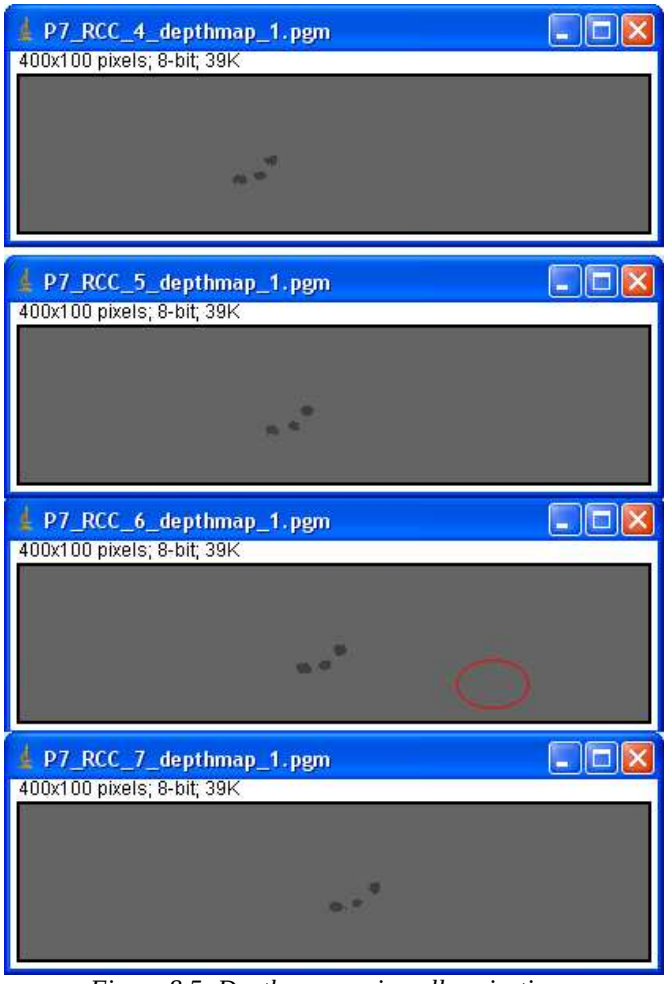

Figure 8.5: Depth maps using all projections.

From the figure, we can see that the spot originally in projection tomo6 is removed since it does not get the consensus from other projections.

8.7 Results Using Real DBT Datasets

Here, we show some more results after running a few more real DBT datasets on our BP algorithm using multiple projections:

(1) Patient 12 (P12_LCC):

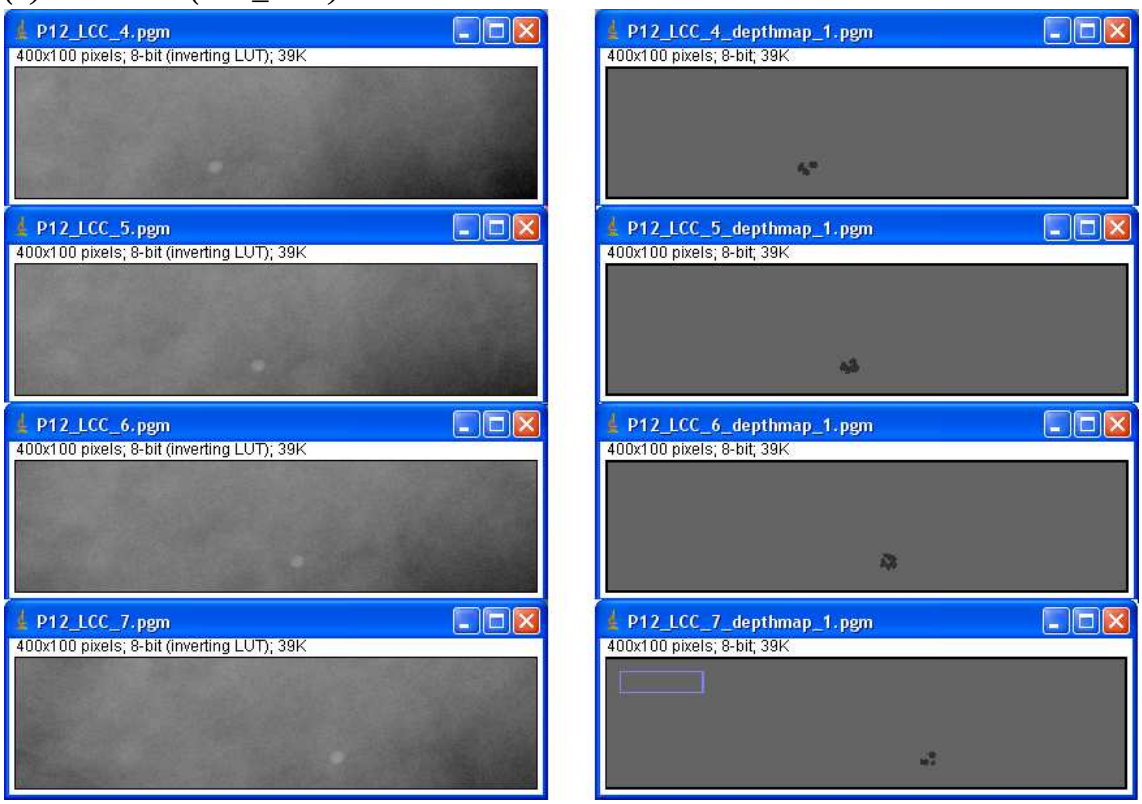

Figure 8.6: Original image (Left) and depth maps using multiple projections (Right) of patient 12.

(2) Patient 13 (P13_LCC):

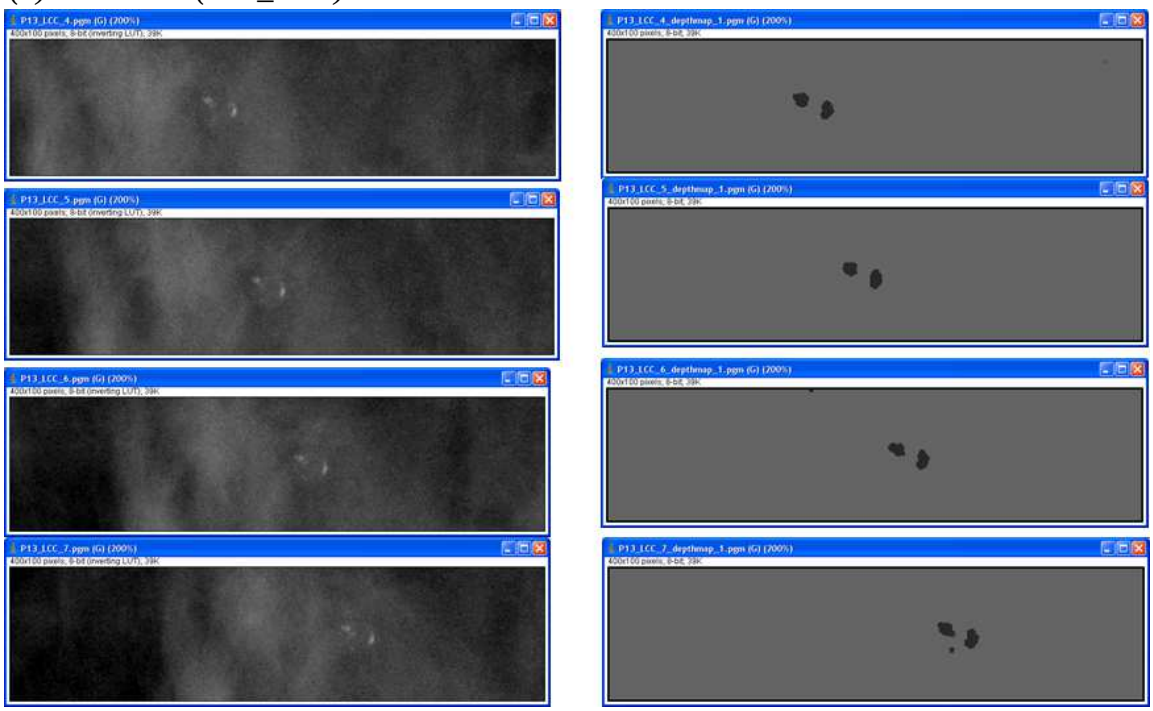

Figure 8.7: Original image (Left) and depth maps using multiple projections (Right) of patient 13.

(3) Patient 16 (P16_LCC):

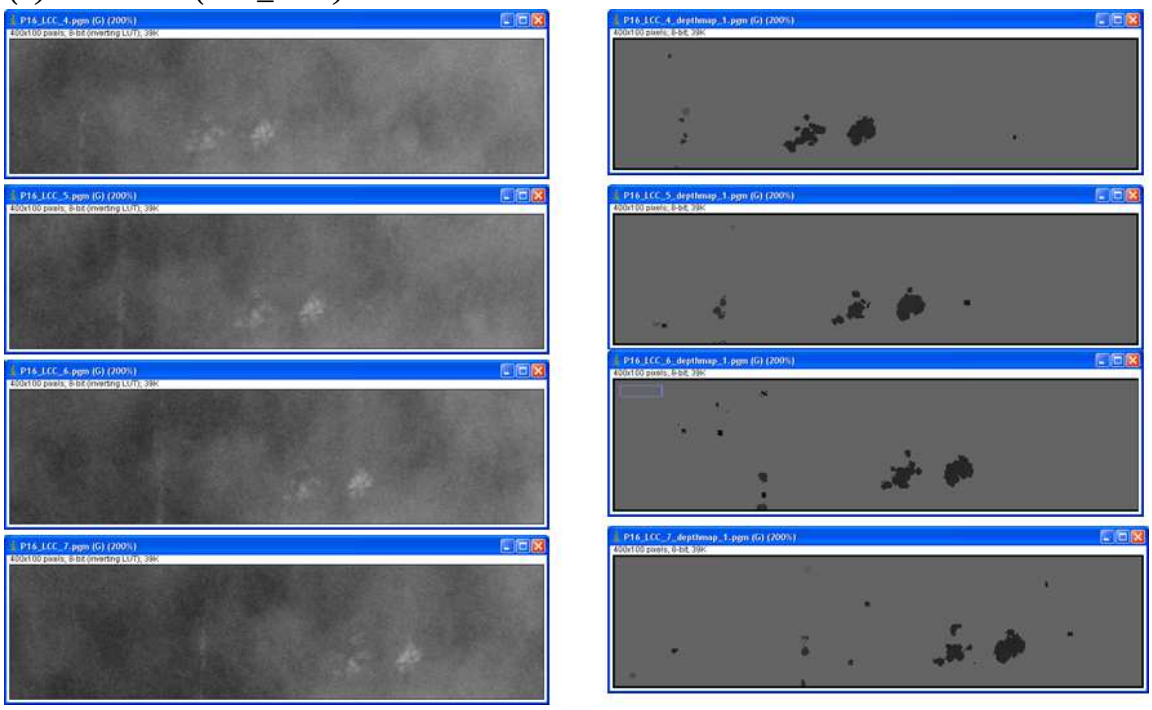

Figure 8.8: Original image (Left) and depth maps using multiple projections (Right) of patient 16.

(4) Patient 17 (P17_RCC):

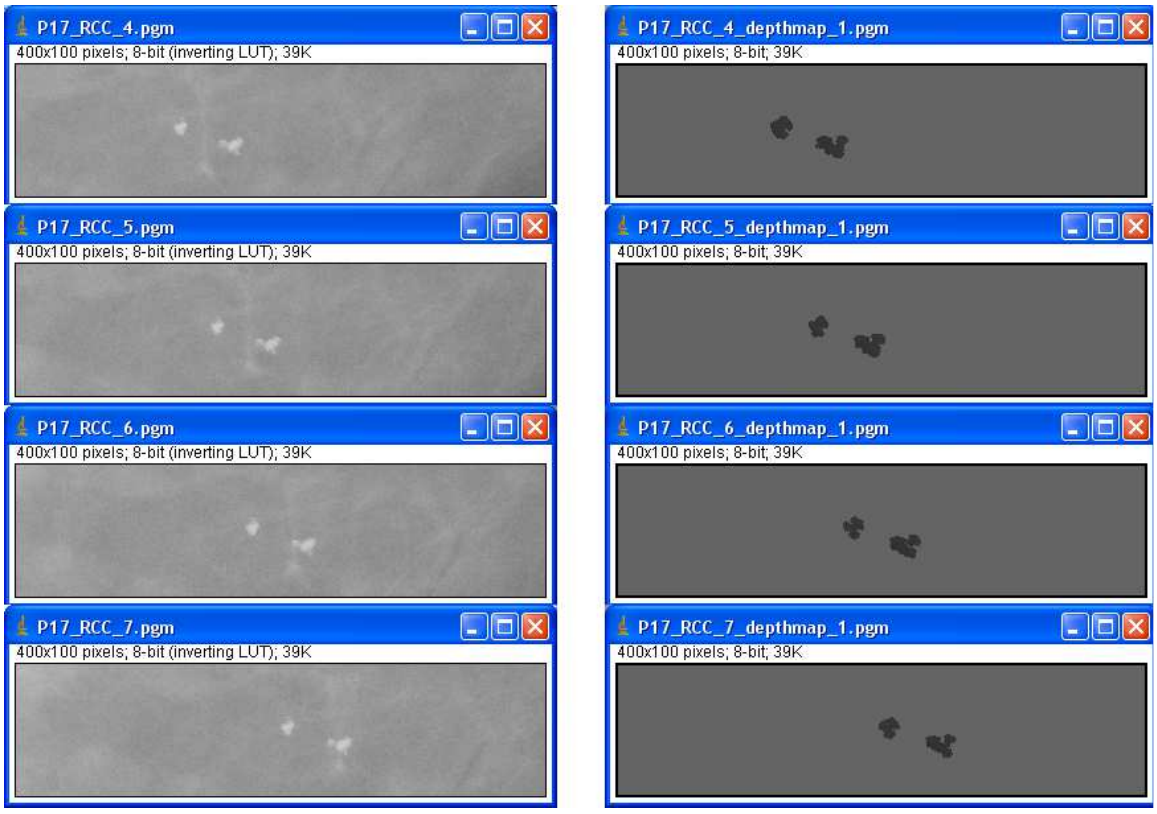

Figure 8.9: Original image (Left) and depth maps using multiple projections (Right) of patient 17.

(5) Patient 19 (P19_RCC):

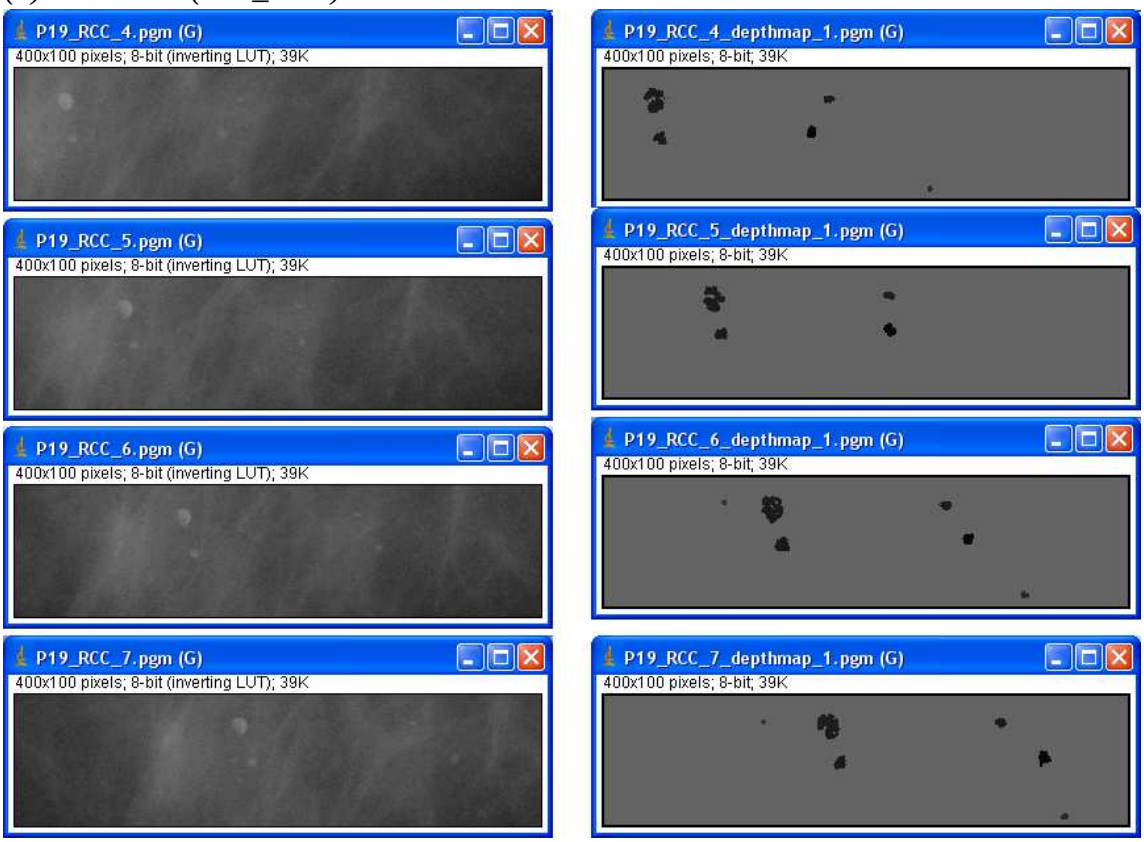

Figure 8.10: Original image (Left) and depth maps using multiple projections (Right) of patient 19.

(6) Patient 20 (P20_RCC):

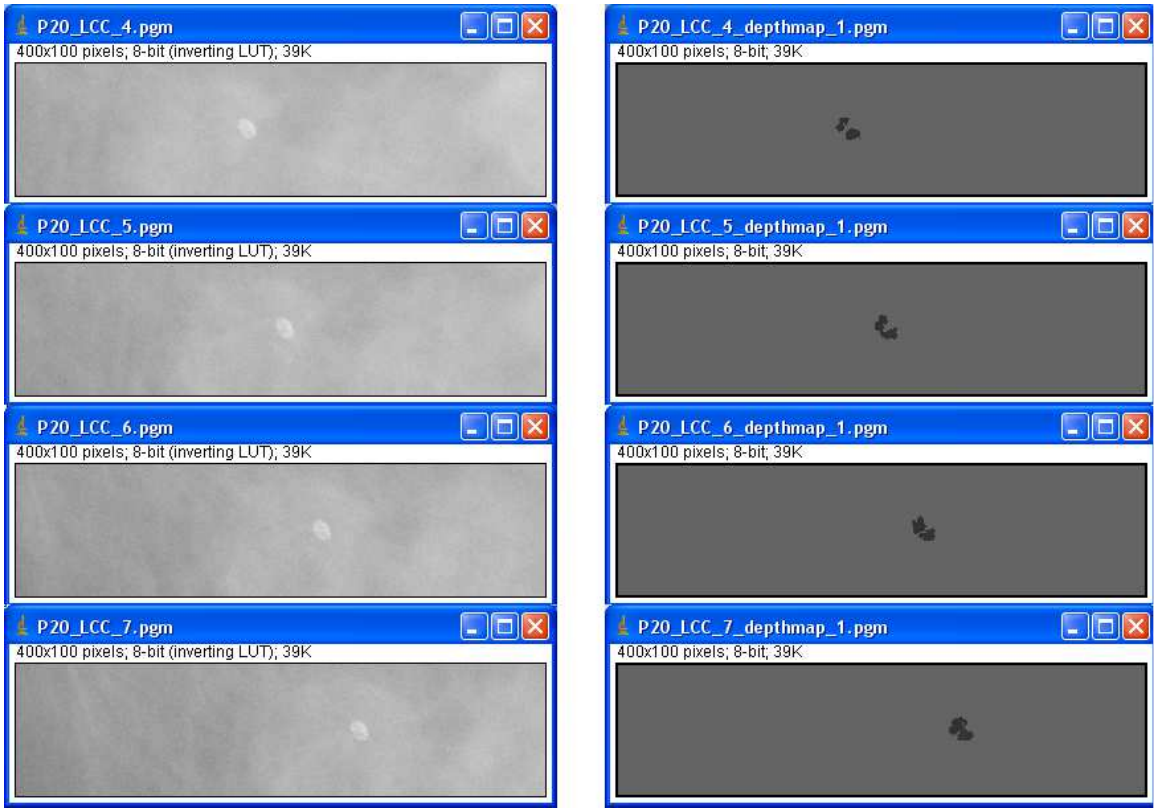

Figure 8.11: Original image (Left) and depth maps using multiple projections (Right) of patient 20.

(7) Patient 24 (P24_RCC):

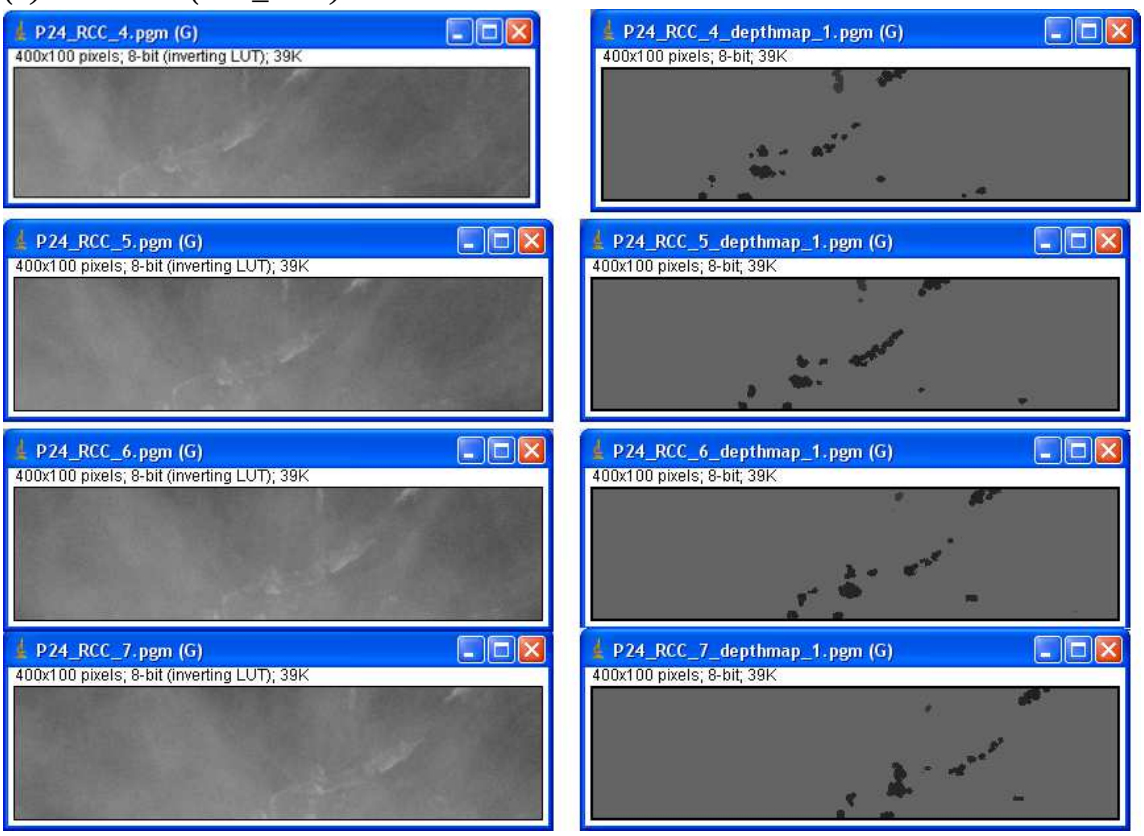

Figure 8.12: Original image (Left) and depth maps using multiple projections (Right) of patient 24.

8.8 Conclusions and Discussion

In this chapter, we have proposed a novel approach in microcalcification detection in DBT using MRF and BP. We have also shown some results using real DBT datasets using our approach. The results are promising. In terms of detection results, it is comparable with a single detection algorithm (e.g. Harris-AD in our case.). In addition, the depths of the microcalcifications in the breast can be estimated at the same time that no single detection algorithm can give us such information.

Chapter 9

Epipolar Curves Approach III: The Reconstruction of Microcalcification Clusters in DBT

In the two previous chapters, we showed how our epipolar curves approach improves microcalcification detection in individual DBT projections adaptively (Chapter 7) and leads to novel algorithms based on MRF and BP for simultaneous microcalcification detection and depth estimation (Chapter 8). In this chapter, we apply our derivations of epipolar curves to determine the 3D positions of microcalcifications. From this reconstruction, we will be able to visualise and approximate more accurately the shape and distribution of the microcalcifications in a cluster, which provides one of the fundamental criteria in deciding whether the cluster is evidence for malignant or benign disease.

Section 9.1 reviews some reconstruction algorithms developed for mammography, and then Section 9.2 presents some of the existing reconstruction algorithms in DBT, all of which are focussed on developing a representation of the entire breast. However, the reconstruction of a 3D volume from a DBT data set continues to have substantial limitations due to the null space problem, which makes the reconstruction under-determined.

In a breast, the vast majority of tissue is normal. We may be interested in normal tissue to some extent, but we are definitely more concerned with potentially abnormal tissue. One such kind of abnormality is microcalcification clusters. Instead of investigating the common reconstruction approach in building up the whole breast and extracting the parts of microcalcification clusters, we adopt an approach of considering only that portion of the breast – reconstruction of microcalcification clusters only. In Section 9.3, we continue our discussion of epipolar curves and

introduce methods for finding the 3D positions of microcalcifications. Following this, we illustrate some results with real DBT datasets and compare them against results with slices following reconstruction in Section 9.4. We will discuss some analysis on geometric accuracy using simulated data in Section 9.5. The chapter ends with a conclusion and discussion section.

9.1 Reconstruction in Mammography

In this section, we will briefly review two studies of the 3D reconstruction of microcalcifications in mammography.

9.1.1 Reconstruction of Uncompressed Breast from Two Mammograms

Yam et al. propose a method [160] for the reconstruction of microcalcification clusters from a pair of CC and MLO views. They developed a model of the three-dimensional uncompressed breast and a model of breast compression to impose a geometric constraint regarding the possible three-dimensional location of a calcification in the uncompressed breast. A two-dimensional point corresponding to a calcification in a mammographic view is represented by a curve in three-dimensions. The intersection (or the midpoint of the closest distance) between the two curves obtained from the two mammographic views is then considered to be the location of the microcalcification in three-dimensions. We reimplemented and modified their C++ implementation. A reconstructed three-dimensional breast is shown in the following figure:

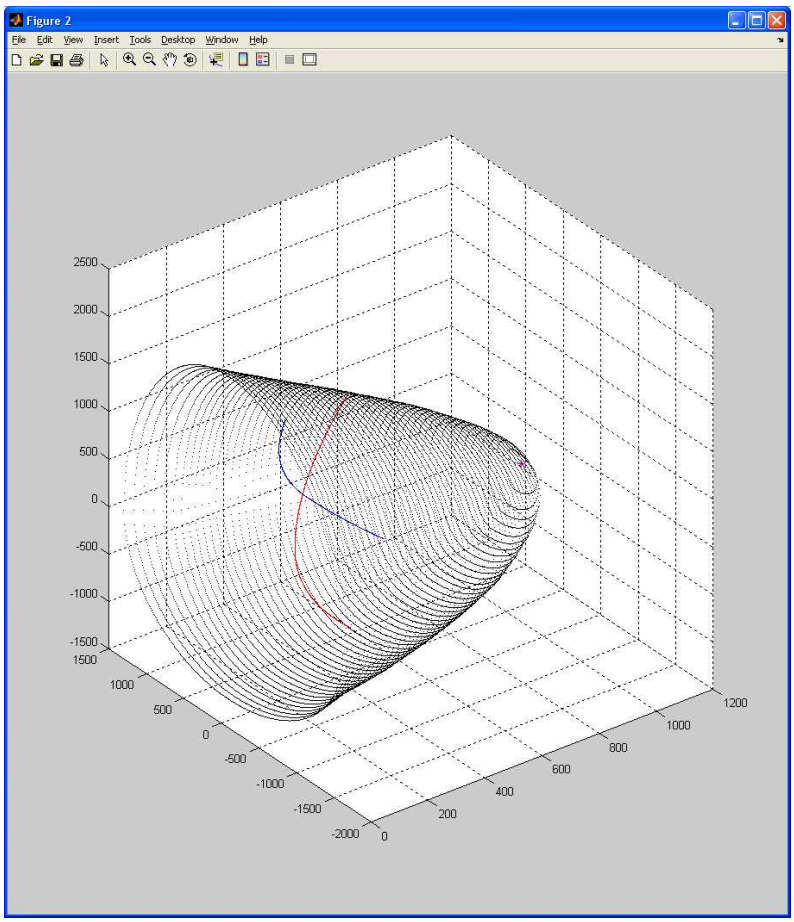

Figure 9.1: Reconstructed three-dimensional uncompressed breast with an intersection representing a microcalcification

Their method makes use of the physical X-ray generation process, the geometry of mammography, the concept of h_{int} and the microcalcification detection algorithm described in Section 7.1.2, they have converted from two images of a compressed breast to an uncompressed breast in 3D and estimated the 3D positions of microcalcifications. This enables the classification of microcalcification clusters. The following shows the reconstruction of two clusters (one benign and one malignant) with the use of CC and MLO views:

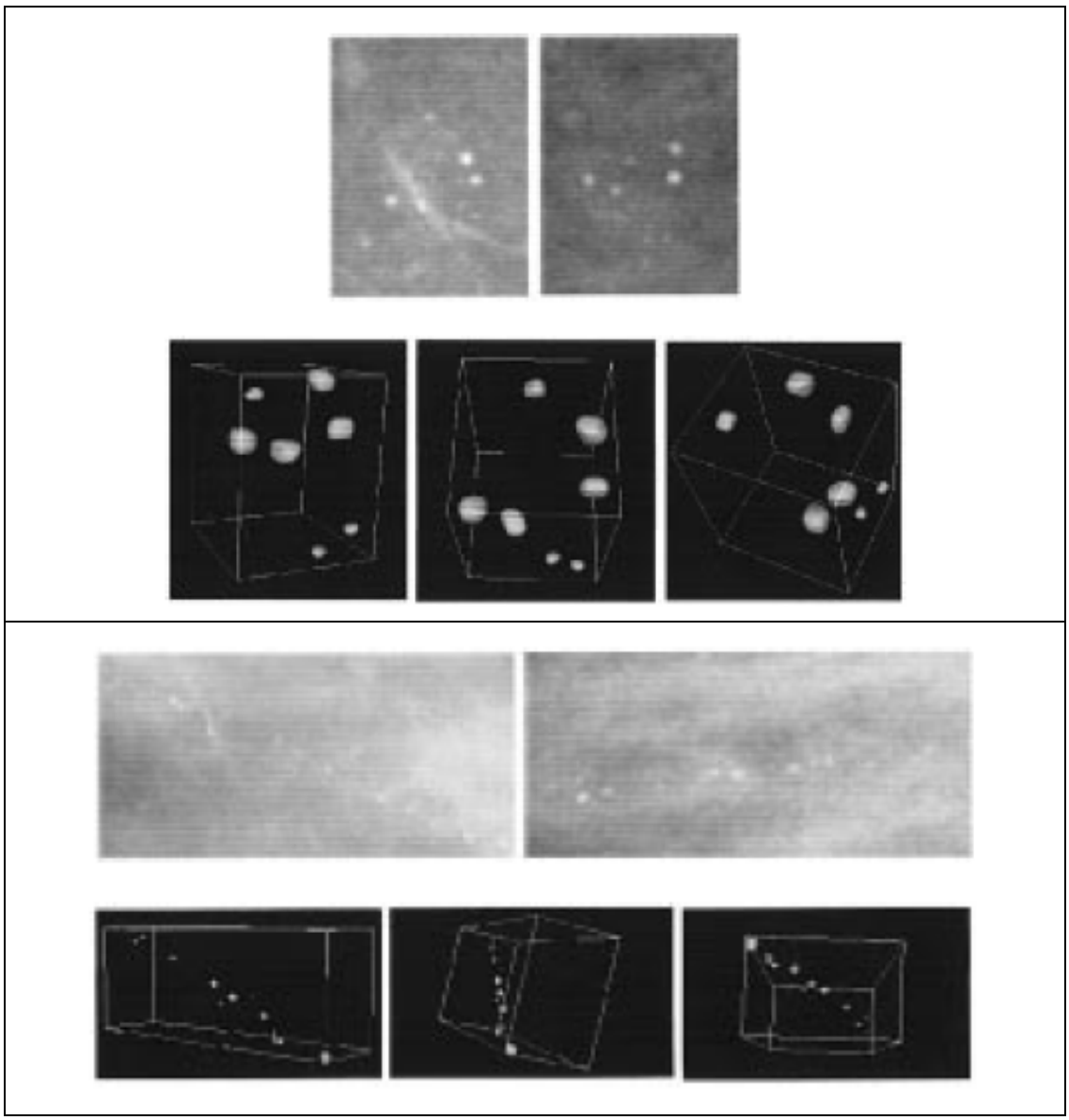

Figure 9.2: (Top) A benign cluster with a diffuse configuration; (Bottom) A malignant cluster (DCIS) with a linear configuration. (Pictures extracted from [160].)

As the figure shows, a benign cluster appears as a scattered and diffuse configuration, whereas a malignant cluster appears as a curvilinear (ductal) configuration. This provides room for future investigation on cluster shape and the spatial distribution of calcifications within the cluster, and hopefully may help improve the classification of benignancy and malignancy.

However, since they only had available two projections and since strong - and different - compression is applied when the images are taken, they have to make a number of assumptions in their model and these may lead to inaccurate reconstruction. For instance, the uncompressed breast outlines are approximated by the outlines of the uniformly eroded breast region. However, in reality, it is possible that the amount of change caused by compression will not be uniform around the breast outline. Another

assumption is that the mapping of points between the compressed and uncompressed breast surface using simple ratios; while the skin surface may stretch non-uniformly.

9.1.2 3D Localization of Clustered Microcalcifications Using CC and MLO Views

Yang et al. proposed another method in localization of the clustered microcalcifications in 3D [161]. Their method includes three main steps: (1) Registration of clustered microcalcifications in CC and MLO views; (2) 3D localization of clustered microcalcifications; (3) Coordinate correction resulting from breast compression.

In the first step, they studied three types of features: a gradient code which keeps track of changes in gray levels of each of clustered microcalcifications; an energy code which describes the energy of each of clustered microcalcifications and is defined by the largest eigenvalues of the correlation matrix of each image block in a mammogram; and a local entropy code which measures the information content in each set of clustered microcalcifications. After the feature values have been computed, the registration procedures are started by dividing the CC and MLO views into image blocks which are then prioritized in the order of the three features using a binary decision tree. The leaves of this tree represents the different levels of matching using the three features are the registered regions in the images.

For 3D localization, they used the nipple as the controlling point to reconstruct the 3D position of any point of interest such as microcalcifications and taken it as the origin of a 3D coordinate system. They assume that the CC and MLO views are represented by the XZ and YZ planes. Since both views share a common coordinate axis, z-axis, they used this as a base for the 3D spatial coordinate computation.

Finally, they performed coordinate correction to include the compression effect in their model. Similar to Yam's, they have also made a few assumptions due to compression e.g. both of them assumed that the volume of a breast is the same before and after compression. In addition, in their computation, the shape of an uncompressed breast and compressed breast are modelled by a hemisphere and a semi-cylinder respectively. However, as one can imagine, the validity of these assumptions is suspicious and the results should not be expected to be too reliable.

Comments:

As we have discussed, some assumptions made in the computation in both papers are questionable and this will surely affect the correctness of the results. From both papers, it is indicated that both models suffer from errors of about *10-20 mm* in the estimation of the 3D locations of lesions. This may be acceptable as an initial study in the research environment. However, this should not be accepted for diagnosis in the real clinical environment. Hence, further improvements are required.

On the other hand, in DBT, we have far more projections than two. Also, minimal compression is applied to the breasts, sufficient only to keep the breast immobile, and all projections are generated with the same compression force. With all these improvements, it may be imagined that the reconstruction of microcalcification clusters in DBT will be more accurate and this will be discussed in later sections.

9.2 Reconstruction in DBT – A Common Approach (Reconstruction of the Whole Breast)

The reconstruction algorithms rebuild a 3D breast from the set of 2D projections. The breast tissue, blood vessels, ducts and breast abnormalities, which are usually viewed in 2D in mammography can now be visualised in 3D, in the form of reconstruction slices with x and y dimensions and stacked along the z direction. In this section, we briefly review four different reconstruction methods: (1) Shift-And-Add; (2) Fourier-based; (3) Algebraic; and (4) Statistical. (The following review is based on the thesis of Dominique Van de Sompel, whose research concerned reconstruction in limited view tomography [71]. Note that we only highlight very briefly the basic concept of the reconstruction methods here, since the topic is not our main focus in this thesis. For more details, readers should refer to [71].) Finally, we explain the null space problem in DBT. This fundamental data insufficiency problem in limited view tomography is one of the motivations leading us to our proposed approach in considering only the reconstruction of microcalcification clusters instead of the whole breast.

9.2.1 Review of Reconstruction Algorithms

(1) Shift-And-Add Method

Shift-and-add method is the simplest method. The principle can be explained and illustrated using the following figure:

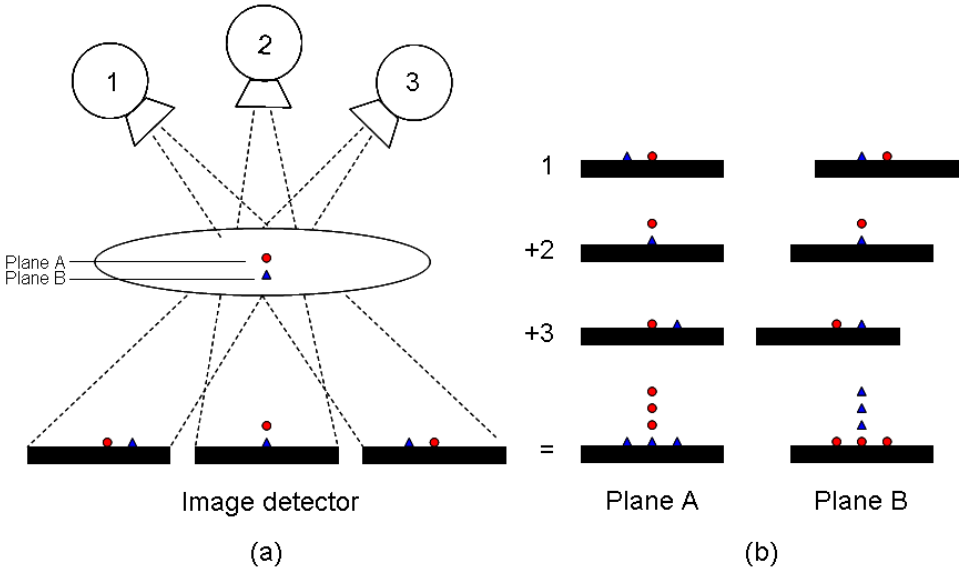

Figure 9.3: Principle of shift-and-add. (a) Three positions of the X-tube (1,2,3) and two structures to be imaged (A, B). (b) Planes of interest can be brought into focus by shifting the projections appropriately and summing them. (Figures redrawn from [162].)

The reconstruction slices, i.e. the horizontal planes A and B in the figure, are brought into focus by shifting and adding the projections. Note that artefacts are serious within the plane. For example, in Plane A, our focus is the circular object. However, in this slice, we may find the artefacts caused by the triangle object. Plane B shows similar artefacts caused by the circle object.

(2) Fourier Methods

The Fourier method is based on the Fourier transform of parallel projections of an object and the subsequent reconstruction from the transform. There are two reconstruction methods: direct Fourier methods and filtered backprojection (FBP). In the following, we briefly overview it in 2D for the purpose of understanding the basic concepts. For its extension to 3D and more details, readers can refer to [71].

(a) Parallel projections of a 2D object $f(x,y)$

In assuming the rays are in parallel during the imaging process, the projection of a 2D object *f(x,y)* at an angle ϕ can be written as the line integral:

$$\boldsymbol{p}_{\phi}(\boldsymbol{x}_r) = \int_{-\infty}^{\infty} \boldsymbol{f}(\boldsymbol{x}, \boldsymbol{y}) \boldsymbol{dy}_r \qquad \textit{Eqn. 9.1}$$

where the rotated coordinates $\boldsymbol{x}_r$ and $\boldsymbol{y}_r$ are related to *x* and *y* respectively by

$$\begin{bmatrix} \boldsymbol{x}_r \\ \boldsymbol{y}_r \end{bmatrix} = \begin{bmatrix} \cos\phi & \sin\phi \\ -\sin\phi & \cos\phi \end{bmatrix} \begin{bmatrix} \boldsymbol{x} \\ \boldsymbol{y} \end{bmatrix} \qquad \textit{Eqn. 9.2}$$

The function $\boldsymbol{p}_{\phi}(\boldsymbol{x}_r)$ is also known as the X-ray or Radon transform of the function *f(x,y)*. (See *Figure 9.4* (Left)). Then, the Fourier transform of $\boldsymbol{p}_{\phi}(\boldsymbol{x}_r)$ gives the values of $\boldsymbol{F}(\boldsymbol{v}_x, \boldsymbol{v}_y)$ along the line BB as shown in *Figure 9.4* (Right). Mathematically,

$$\boldsymbol{p}_{\phi}(\boldsymbol{v}_{xr}) = \boldsymbol{F}(\boldsymbol{v}_{xr}, \phi) \qquad \textit{Eqn. 9.3}$$

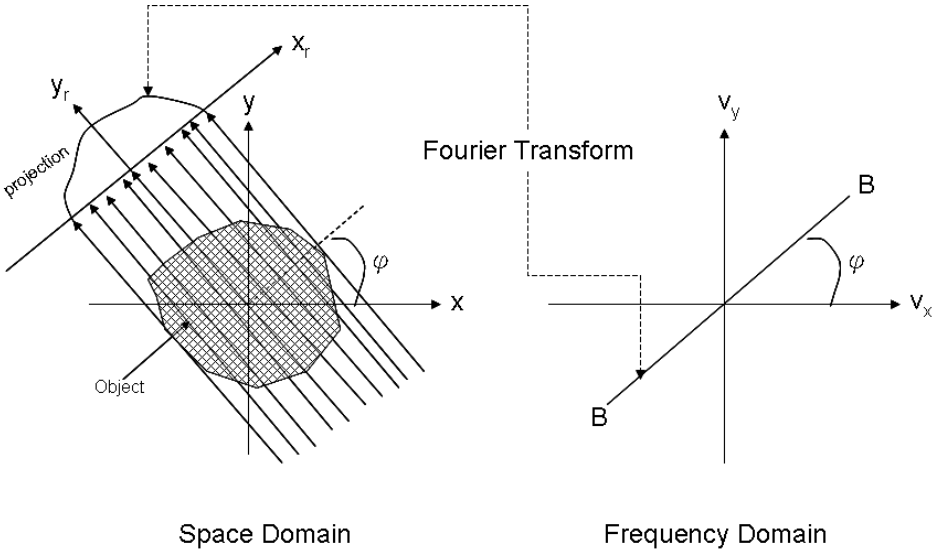

Figure 9.4: The Fourier transform of a projection. (Figures redrawn from [163])

(b) The 2D Fourier Slice Theorem

Refer to [71], the Fourier Slice Theorem states that "the Fourier transform of a parallel projection of an image *f* gives a slice through the Fourier domain *F* of the image perpendicular to the direction of the projection". (Later in this section, we will discuss the null space problem which can be explained by the Theorem and the null space problem is still one of the major research challenges in DBT reconstruction.)

(c) Reconstruction by direct Fourier methods

It follows that the object can then be recovered by direct inversion of the sampled Fourier domain after the Fourier space of the object is populated with slices collected over a full angular range as shown:

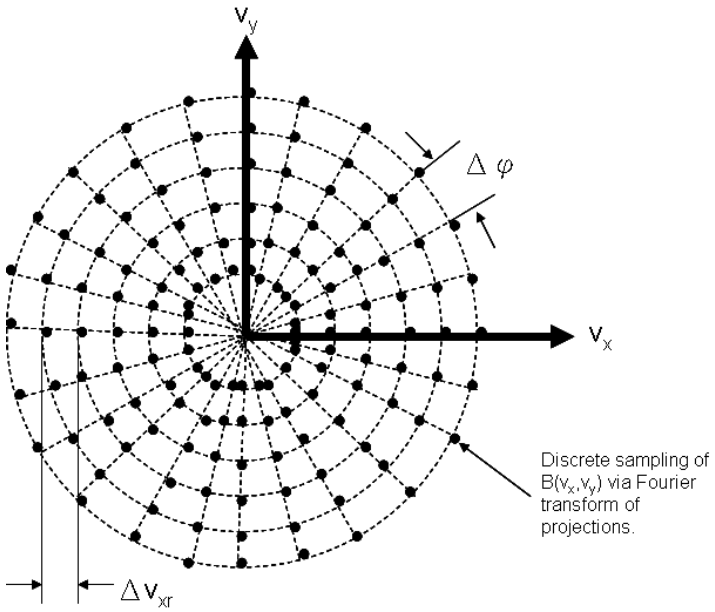

Figure 9.5: Sampling of the Fourier domain. (Figures redrawn from [164])

The direct Fourier methods suffer from interpolation errors when using the inverse Fast Fourier Transform algorithms that the frequency data needs to be interpolated from a polar to a rectangular grid. The data points become sparser at higher frequencies, leading to larger interpolation errors. Due to the global nature of the Fourier transform, these errors are unavoidable throughout the entire image.

(d) Reconstruction by filtered backprojection (FBP)

To address the problems by direct Fourier methods, it is more common to use the FBP method which performs the required interpolations in the image domain such that the errors affect the final image only locally. In the continuous case, the image *f(x,y)* can be recovered using:

$$f(x,y) = \int_0^{\pi} Q_{\phi}(x_r)\, d\phi \qquad \textit{Eqn. 9.4}$$

where

$$Q_{\phi}(x_r) = \int_{-\infty}^{\infty} P_{\phi}(v_r)\,|\,v_r\,|\, e^{j2\pi v_r x_r}\, dv_r \qquad \textit{Eqn. 9.5}$$

It is a backprojection of the ramp-filtered projection $\boldsymbol{p}_{\phi}(\boldsymbol{x}_r)$. The Fourier domain is oversampled at lower radial frequencies and the frequency factor $|\boldsymbol{v}_r|$ can compensate for that, otherwise a radial blur or halo effect will be seen.

However, FBP is not very good in limited view tomography (in our case DBT). This is because the limited projection data i.e. the undersampling, leads to sharp streak artefacts along the projection directions, and an over-suppression of low spatial

frequencies. The former confuses the small features e.g. microcalcifications, and the latter reduces the visibility of large masses.

(3) Algebraic Methods

The algebraic methods can be explained by a ray tracing model:

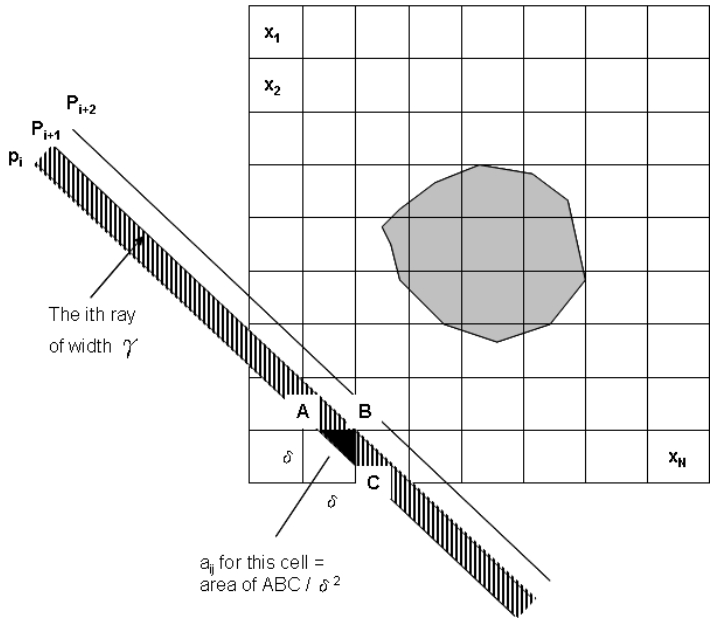

Figure 9.6: Ray tracing model. (Figures redrawn from [163].)

In the model, each projection value $\boldsymbol{p_i}$ is given by the ray sum

$$\sum_{j=1}^{N} a_{ij} x_j = p_i, \quad i = 1,...,M \qquad \textit{Eqn. 9.6}$$

where $\boldsymbol{a_{ij}}$ is the fraction of the area of the $\boldsymbol{j^{th}}$ cell intersected by the $\boldsymbol{i^{th}}$ ray, N is the number of pixels, $\boldsymbol{x_j}$ is the intensity or density of the $\boldsymbol{j^{th}}$ pixel, and M is the number of rays.

The image is discretised into a finite set of pixel cells. The measured projection values are modelled as a sum of weighted contributions from each pixel cell. The reconstruction task is to solve the simultaneous equations to obtain $\boldsymbol{a_{ij}}$.

Despite of their advantages e.g. fewer projections are required for a given image quality than FBP, the methods suffer from some other limitations, e.g. the computation time is large and the nature of the noise in the projection data is not modelled explicitly.

(4) Statistical Methods

The likelihood function $\boldsymbol{P}(\boldsymbol{r} \mid \boldsymbol{x})$ describes the probability of observing a set of projection data *r* given an estimate of the reconstructed object *x*. It corresponds to the statistical noise model such as Gaussian and Poisson statistical noise models in the simplest setting, without considering effects such as scattering and bean hardening. However, the data likelihood is usually ill-conditioned in DBT, because of the data insufficiency problem (the null space problem). To constrain the space of solutions, an additional penalty function (or image prior) called a regulariser is usually used. The likelihood function and the penalty function are then combined using Bayes' rule into the posterior probability:

$$P(x \mid r) = \frac{P(r \mid x)P(x)}{P(r)} \qquad \textit{Eqn. 9.7}$$

The objective of the statistical reconstruction algorithm is then to find the optimal estimator $\hat{\boldsymbol{x}}$ which is normally the maximiser of the probability distribution $\boldsymbol{P}(\boldsymbol{x} \mid \boldsymbol{r})$. While the likelihood function can be modelled using statistical noise model, one of the most common forms of the image priors $\boldsymbol{P}(\boldsymbol{x})$ relies on Markov random field (MRF) models to account for spatial interactions within the image. $\boldsymbol{P}(\boldsymbol{r})$ is usually constant when optimising for *x*.

Similar to algebraic methods, the disadvantages of statistical methods are longer computation times and higher memory requirements. Having said that, such methods allow for better physical models of the imaging process and the inclusion of regularizing penalty functions to constrain the reconstruction solutions.

9.2.2 The "Null Space" Problem in DBT

A major and fundamental issue in reconstruction applied to DBT is the null space problem. The problem is caused by the nature of DBT that only limited angular range of projections are taken. The following figure illustrates the null space problem for a *384*370* head CT image:

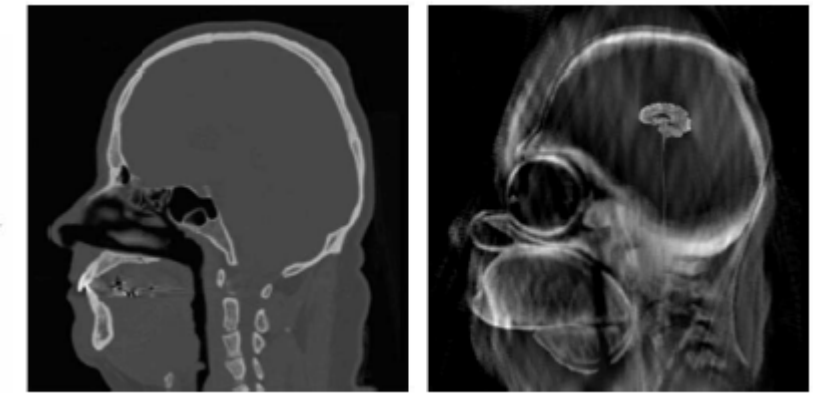

*Figure 9.7: Illustration of the null space problem for a 384*370 head of CT image. (Figures extracted from [71])*

Both reconstruction images satisfy the same projection data (*15* noiseless projections distributed uniformly over $\pm 30^0$). Since a limited range of projections is available, there can be many possible reconstruction solutions given the same set of projection data.

To explain the problem, we can continue our previous discussion of the Fourier Slice Theorem. Since only slices perpendicular to the direction of the projection can be obtained and only limited angular range of projections are inputted, the reconstruction in the "?" region in the following figure is unknown.

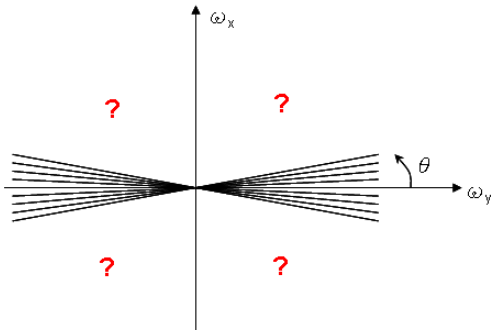

*Figure 9.8: Illustration of the null space problem for a 384*370 head of CT image. (Figures modified from [71])*

To solve the problem, researchers try to incorporate anatomical priors into the reconstruction process. Though a great deal of progress continues to be made, considerably more research effort is still required.

9.3 Reconstruction in DBT – Our Proposed Approach (Reconstruction of the Microcalcification Clusters Only)

As discussed in the previous section, the reconstruction of the whole breast is fundamentally under-constrained, due to the fact that DBT projections are taken over a

limited angular range. DBT reconstruction continues to be the subject of considerable research. Judging by the papers at three successive International Workshops on Digital Mammography *(2006, 2008,* and *2010*), the frenzied debate in 2006 on the relative merits of variants of FBP, algebraic methods (e.g. simultaneous algebraic reconstruction technique (SART)), and statistical reconstruction, with the implicit assumption that the problem of generating a robust and accurate algorithm ready for unsupervised clinical application had been replaced in *2010* by a frank recognition that there remain major mathematical and implementation issues to be overcome. If the general reconstruction problem remains to be solved, we may note both that the vast majority of breast tissue is normal, and also that one of the primary indicators of possible breast disease is the appearance of microcalcifications, in particular their shapes and distribution in the breast. These motivate our investigation into reconstructing just those portions, initially microcalcifications clusters, instead of the whole breast.

With the geometry of DBT acquisition system, one can roughly estimate the 3D position given at least two corresponding projection points from two different projections using basic geometry arithmetic:

Method 1: Intersection Method

The situation of finding the intersection between *2* rays is depicted in the following figure:

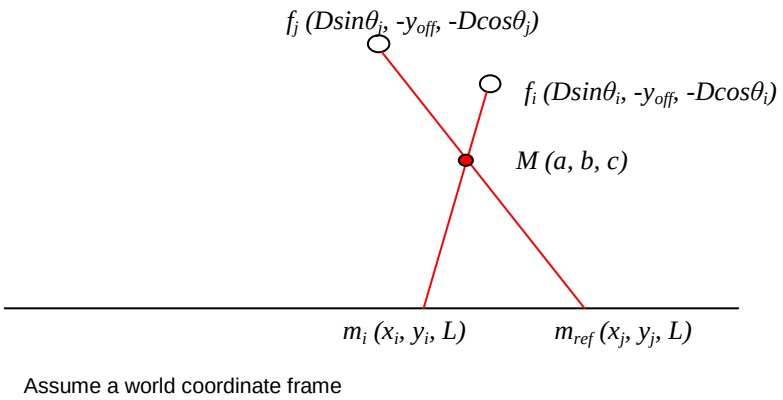

Figure 9.9: A simplified geometry for DBT given a microcalcification .

Our aim is to find *a, b, c* in the figure. Theoretically, the intersection of the two rays in 3D is the solution. However, due to noise, approximations such as quantisation, or small errors, the two rays may not exactly intersect in 3D space. Instead, the two rays will pass close by each other. The midpoint between the two closest points of the rays will then be considered as the intersection point, i.e. the 3D position of the microcalcification. The following figure shows the situation when two rays cross each other:

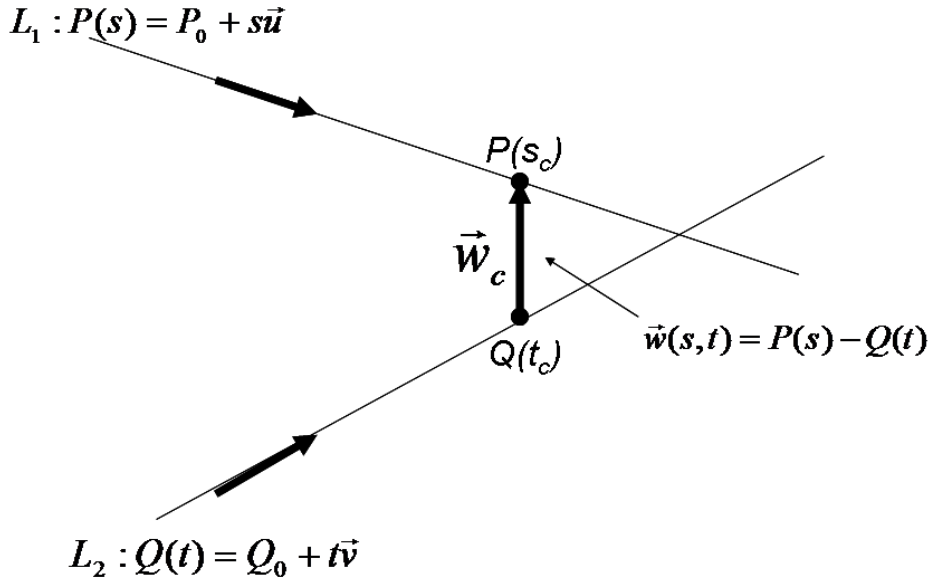

Figure 9.10: Two rays crossing each other.

In the figure, the *2* rays are represented as $L_1 : P(s) = P_0 + s\vec{u}$ and $L_2 : Q(t) = Q_0 + t\vec{v}$ where *s* and *t* denote the specific position along the corresponding ray. Let $\vec{w}(s,t) = P(s) - Q(t)$ be a vector between points on the two lines. We need to find the $\vec{w}(s,t)$ that has a minimum length for all *s* and *t* i.e. $\vec{w}_c$. This is a standard exercise in vector algebra. The midpoint of $P(s_c)$ and $Q(t_c)$ is the point we want.

In our reconstruction of a microcalcification, at least *2* rays forming from any *2* projection points in the same epipolar cluster and their corresponding focal spot positions can be used to estimate the microcalcification position. A robust average from all pairs can be used if all projections are taken into consideration at the same time.

The intersection method is very easy to understand. However, it cannot provide a good mathematical foundation and framework for us to perform future analysis of the geometric accuracy of the 3D positions obtained. On the other hand, to

continue our discussion of our epipolar curves approach, the following method is suggested:

Method 2: Epipolar Curve Formulas Method

Another method uses the epipolar curves formulae derived in Chapter 6 directly.

Recall that the *x* coordinates of the epipolar curve are:

$$x_i^s = D(1-\frac{L+D\cos\theta_i}{c+D\cos\theta_i})\sin\theta_i + (u + a(\frac{L+D\cos\theta_i}{c+D\cos\theta_i})) \qquad \textit{Eqn. 9.8}$$

and that $\frac{L+D\cos\theta_i}{c+D\cos\theta_i} = \lambda(c)$ is a constant to a good approximation (the exact value depends on *c*), we note that this takes form of a straight line $x_i^s = A\sin\theta_i + B$. If we estimate A, then we find that

$$A = D(1-\lambda(c)), \text{ and so } \lambda(c) = 1-\frac{A}{D} \qquad \textit{Eqn. 9.9}$$

From which we find *c*, i.e.

$$c = \frac{L+D\cos\theta_i}{(1-A/D)} - D\cos\theta_i \qquad \textit{Eqn. 9.10}$$

and,

$$a = (B-u)*\frac{c+D\cos\theta_i}{L+D\cos\theta_i} \qquad \textit{Eqn. 9.11}$$

if we know the slope (*A*) and the *y*-intercept (B) of the line x_i^s against $\sin\theta_i$. An example of line fitting is shown:

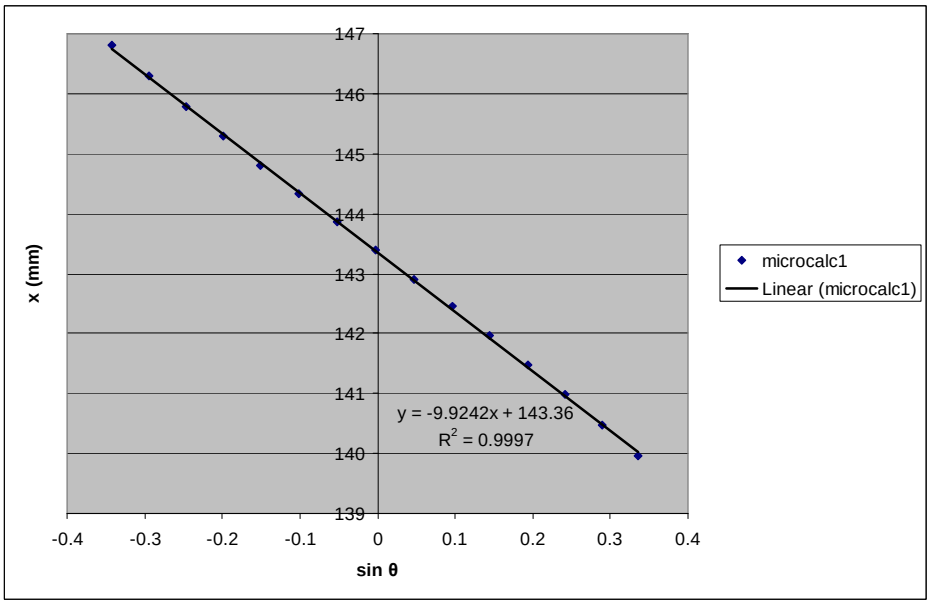

Figure 9.11: An example of line fitting after epipolar clustering of 15 projection points.

Now, we can approximate the slope and *y*-intercept using the projection points, we can estimate *c* and *a*.

For *b*, we can use the *y* coordinates: $y_i^s = -y_{off} + v + (b + y_{off})\frac{L + D\cos\theta_i}{c + D\cos\theta_i}$ so that

$$b = (y^s + y_{off} - v - y_{off} * \frac{L + D\cos\theta_i}{c + D\cos\theta_i}) * \frac{c + D\cos\theta_i}{L + D\cos\theta_i} \qquad \textit{Eqn. 9.12}$$

Putting them together, we have a method to estimate the 3D position of a microcalcification *(a, b, c)*.

9.4 Results of Reconstruction of the Microcalcification Clusters on Real DBT Datasets

(Note: For better illustration of 3D reconstruction, the reconstruction results are saved as animation gif format and can be found in the attached CD Rom.)

9.4.1 Reconstruction Results for Patient 7

(a) Reconstruction results

The right breast in CC view of *Patient 7* using a DBT prototype machine with the same geometry as discussed in Chapter 6. The following figure shows one of the

projections containing the bright white spots and the reconstruction results using our approach:

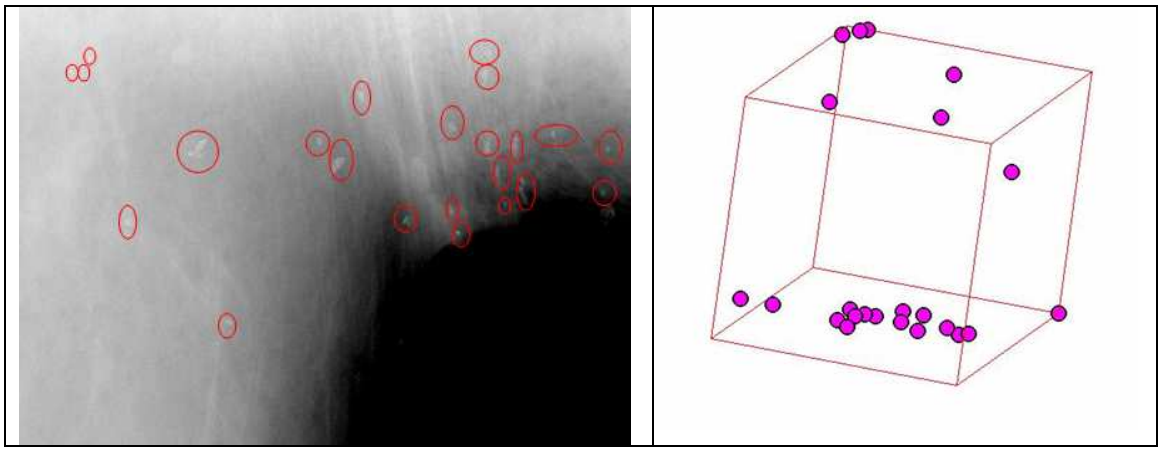

Figure 9.12: A magnified region from one of the real DBT projections showing a number of bright white spots (Left); The reconstructed 3D positions (Right) of Patient 7.

We have reconstructed the 3D positions of the bright white spots; an impression of their 3D positions can be seen in the display in the right of this figure. It can be seen that the spots cluster into two different depth distributions.

(b) Comparison with one common reconstruction algorithm

A corresponding DBT reconstruction version using a statistical algorithm is obtained from Dexela Ltd. For illustration, we will focus on the *3* microcalcifications near the top left corner of the projection in previous figure (ROI):

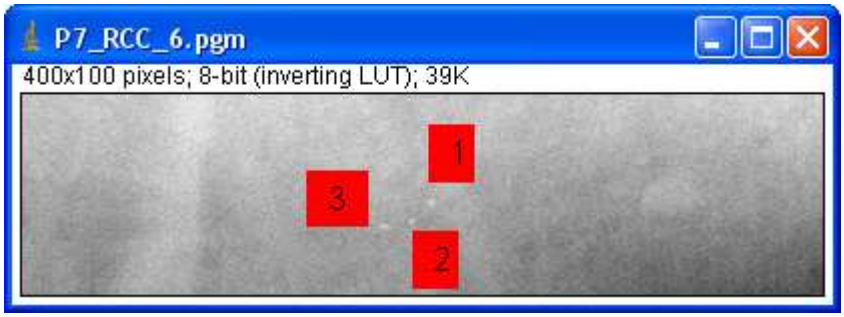

Figure 9.13: The extracted ROI with 3 microcalfications of one of the projections.

We have extracted the relevant slices as shown:

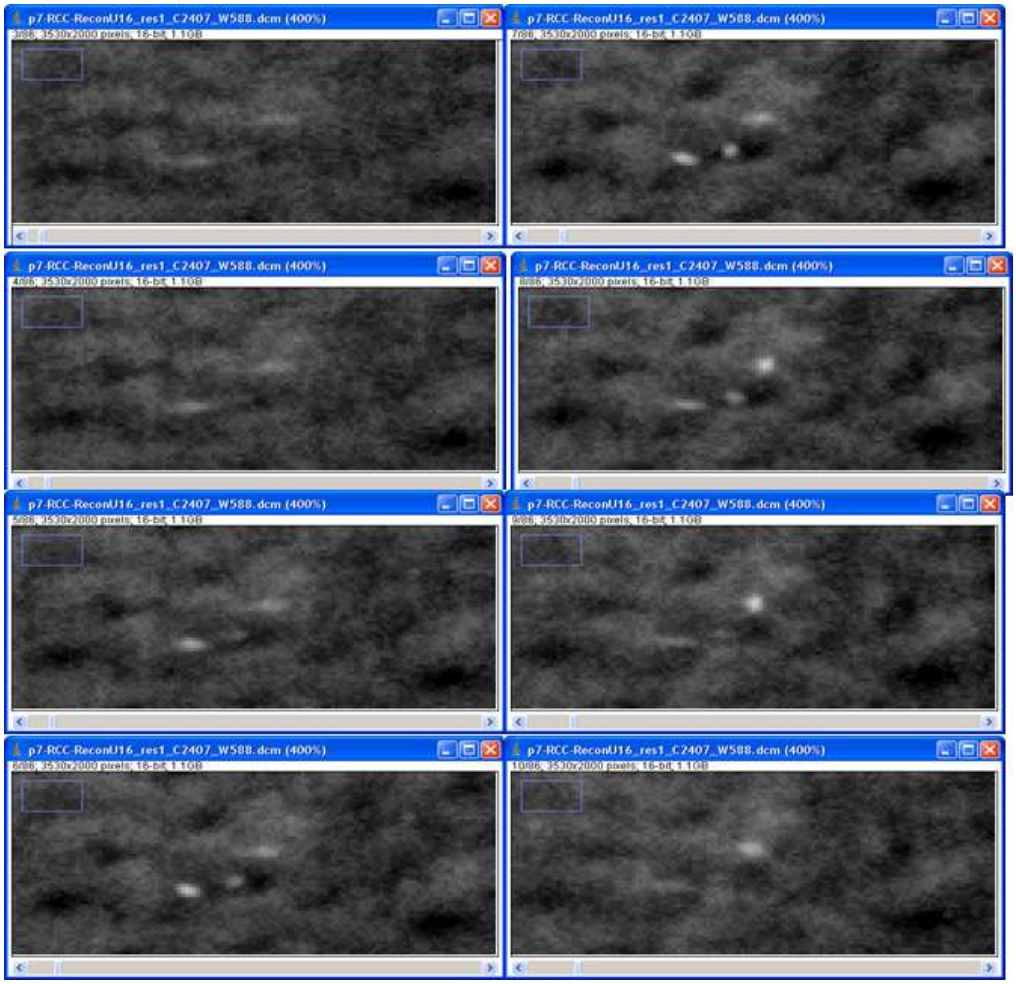

Figure 9.14: Reconstruction slices 3 to 10 (from top left to bottom left, then top right to bottom right) of the ROI .

From visualization, a rough estimate of the depths of the 3 microcalicifications in terms of slice numbers are slices *7-10* for microcalicification *1* and *5-8* for microcalcifications *2* and *3.*

To further verify our reconstruction with the reconstruction results obtained by a statistical reconstruction algorithm, we have compared with *2* other regions in the same projection:

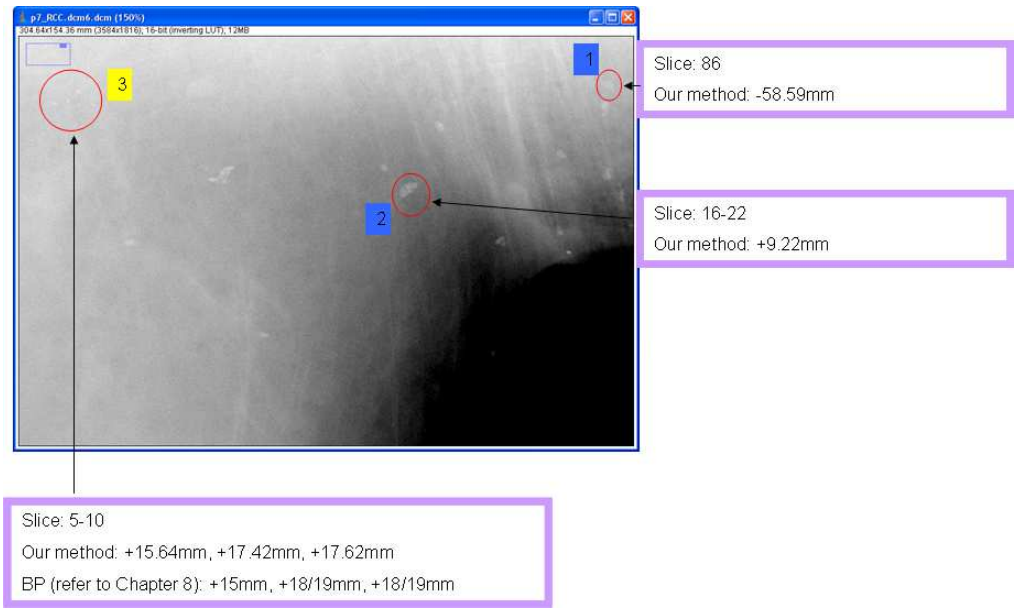

Figure 9.15:Comparison of depth calculated of our method with reconstruction results using statistical algorithm in 3 regions.

With the slice resolution is *1 mm*, our results (both using this epipolar curve formulas method and belief propagation method as discussed in Chapter 8) are consistent with the reconstruction results, which can be shown more clearly with the following figure:

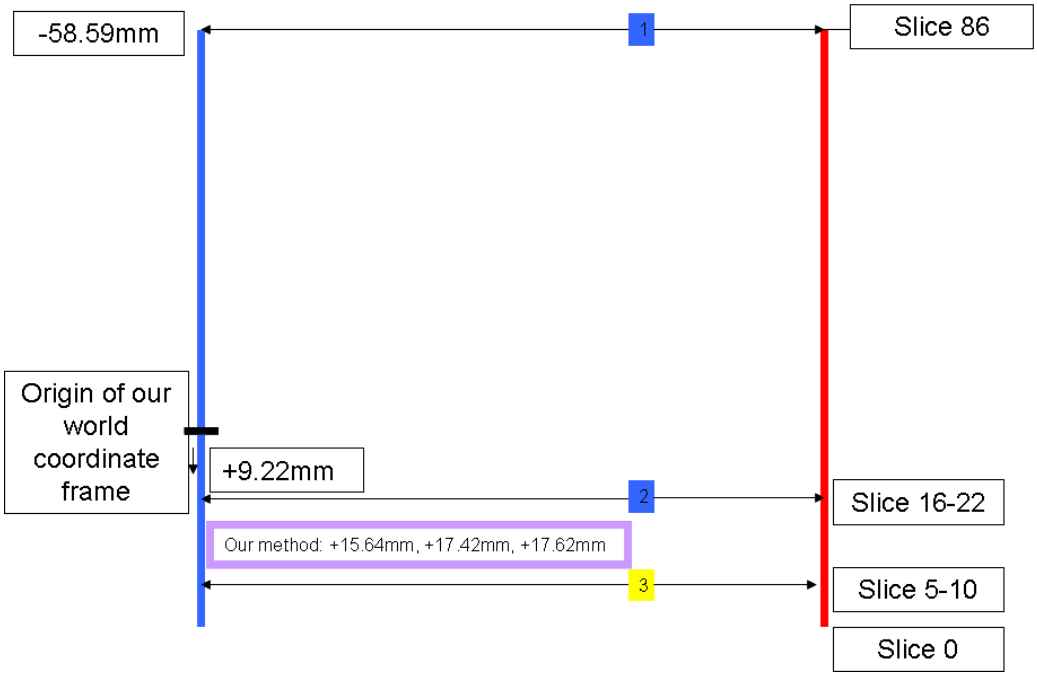

Figure 9.16: A mapping of our computed depths with the slice numbers of the 3 regions.

Our reconstruction method gives a more precise depth for a microcalcification, while typical DBT reconstruction algorithms can only provide a rough estimate of depth in a range of slices.

9.4.2 Reconstruction Results of Other Patients

The following shows *2* more results from *Patient 16* and *Patient 24*:

(a) Patient 16

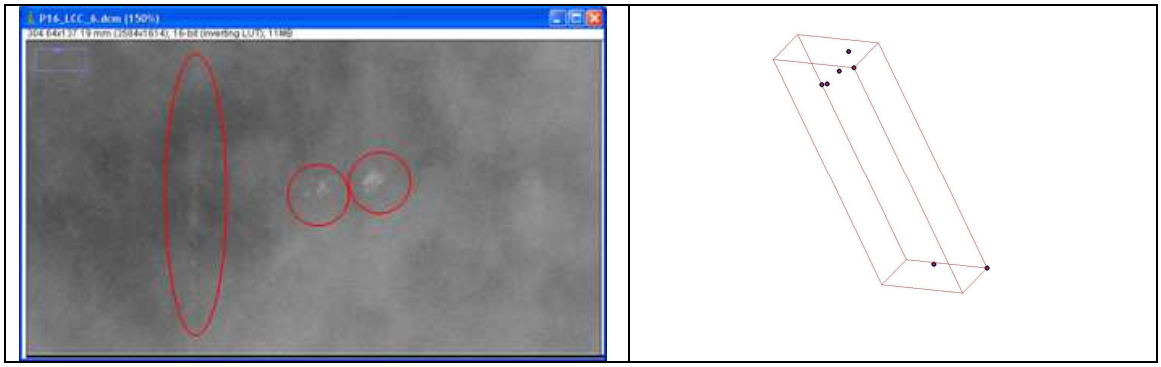

Figure 9.17: A magnified region from one of the real DBT projections showing a number of bright *white spots (Left); The reconstructed 3D positions (Right) of Patient 16.*

(b) Patient 24

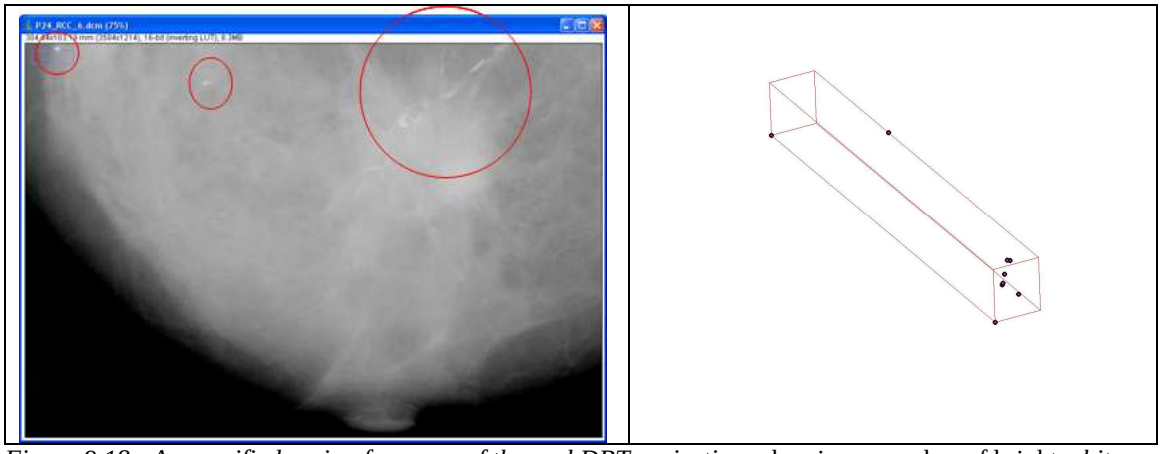

Figure 9.18: A magnified region from one of the real DBT projections showing a number of bright *white spots (Left); The reconstructed 3D positions (Right) of Patient 24.*

9.5 Analysis of Geometric Accuracy

In the previous sections we proposed a method using our epipolar curve formulae to estimate the 3D coordinates $\left\{\begin{bmatrix} a & b & c \end{bmatrix}^T\right\}$ of a set of microcalcifications. In this section, a series of experiments on different 3D positions of microcalcifications are

carried out on simulated data. In these experiments, simulated datasets containing microcalcifications at different positions are generated using Tromans et al's software [31] (discussed in Chapter 5). Simulated datasets are required so that we can have the ground truth for analysis. Our goal is to study issues such as discretisation and other approximations have, ignoring, in the first instance, factors affecting the estimation such as noise, or the imperfect of the detection algorithms in the extraction of microcalcification candidates.

Four different sets of experiments have been carried out: (a) microcalcifications at different 3D locations (in *mm*) with all other values fixed (Experiments *1-3*); and (b) 3D estimation using different subsets of DBT views (Experiment *4*). For (a), one of the coordinates are varied while the others are fixed. For (b), the impact of using different combinations of DBT views in finding the parameters in the formulae of epipolar curves and subsequently the 3D positions of microcalcifications, will be analyzed. For experiments in (a), a cluster of *5* microcalcifications, spherical in shape with radius *0.3* mm, at *5* different 3D locations with all other values fixed are generated. Experiments in (b) are based on microcalcifications generated in (a).

9.5.1 Geometry and parameters used

In these experiments, we have used the geometry for generation of simulated data sets as discussed in Chapter 5. *15* DBT views (starting from DBT view *0* to DBT view *14*) have been generated at angles: -19.98^o, -17.14^o, -14.31^o, -11.48^o, -8.65^o, -5.82^o, -2.99^o, -0.16^o, 2.67^o, 5.50^o, 8.33^o, 11.16^o, 13.99^o, 16.82^o, 19.65^o. The parameter values used are: $D = 620$ mm, $L = 40$ mm, $u = 143.36$ mm, $v = 232.96$mm, $y_{off} = 0$ mm.

The first three sets of experiments consist of *5* microcalcifications with different *c* values, then different *a* values, and finally different *b* values. The reason that we are more concerned with the change in *c* is because it is the ability to estimate *c* that makes DBT useful, and second, the calculation of *c* precedes the calculations of *a*, *b*, so that any problems with *c* will impact on those *a*, *b*. For the 4^{th} experiment, the position of a microcalcification at *(0, -30, -30)* are chosen and estimated using a selective number of DBT views.

The presentation of the first three sets of experiments will be as follows: First, the actual microcalcification positions in the experiment will be given first. Then, *3* out of *15* DBT views will be displayed. As 2D plots are useful for visualization in our epipolar curves analysis, they will also be included. Finally, we present the results of each experiment. The results will include the actual and estimated positions, the difference between them and the estimated position in all projections, and the Euclidean distance which is defined by $\sqrt{(a_A - a_E)^2 + (b_A - b_E)^2 + (c_A - c_E)^2}$, where the subscript *A* means actual position and subscript *E* means estimated position. Finally, it comes with our comments. For the 4^{th} one, results and comments will be given.

9.5.2 Details of the Experiments

Experiment 1: Experiments on different "c" values

(a) Actual microcalcification positions:

5 microcalcifications at 3D positions with different "*c*" values are generated:

Microcalcification No.	A	b	c
1	0	-30	30
2	0	-30	15
3	0	-30	0
4	0	-30	-15
5	0	-30	-30

Table 9.1: 5 microcalcification with different "c" values.

(b) DBT views:

15 DBT views are generated and *3* of them are shown here:

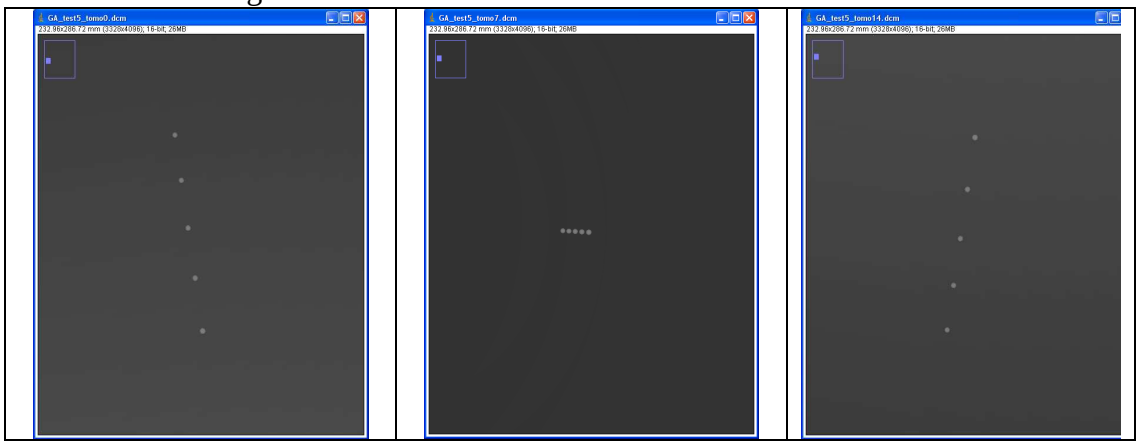

Figure 9.19: DBT views containing a cluster of 5 microcalcifications with different "c" values and fixed "a" and "b" values, generated at -19.98°*(Left),,* -0.16°*(Middle),* 19.65°*(Right).*

(c) 2D plots of all extracted microcalcification candidates:

Two 2D plots are drawn for visualization of the epipolar curves and epipolar clustering:

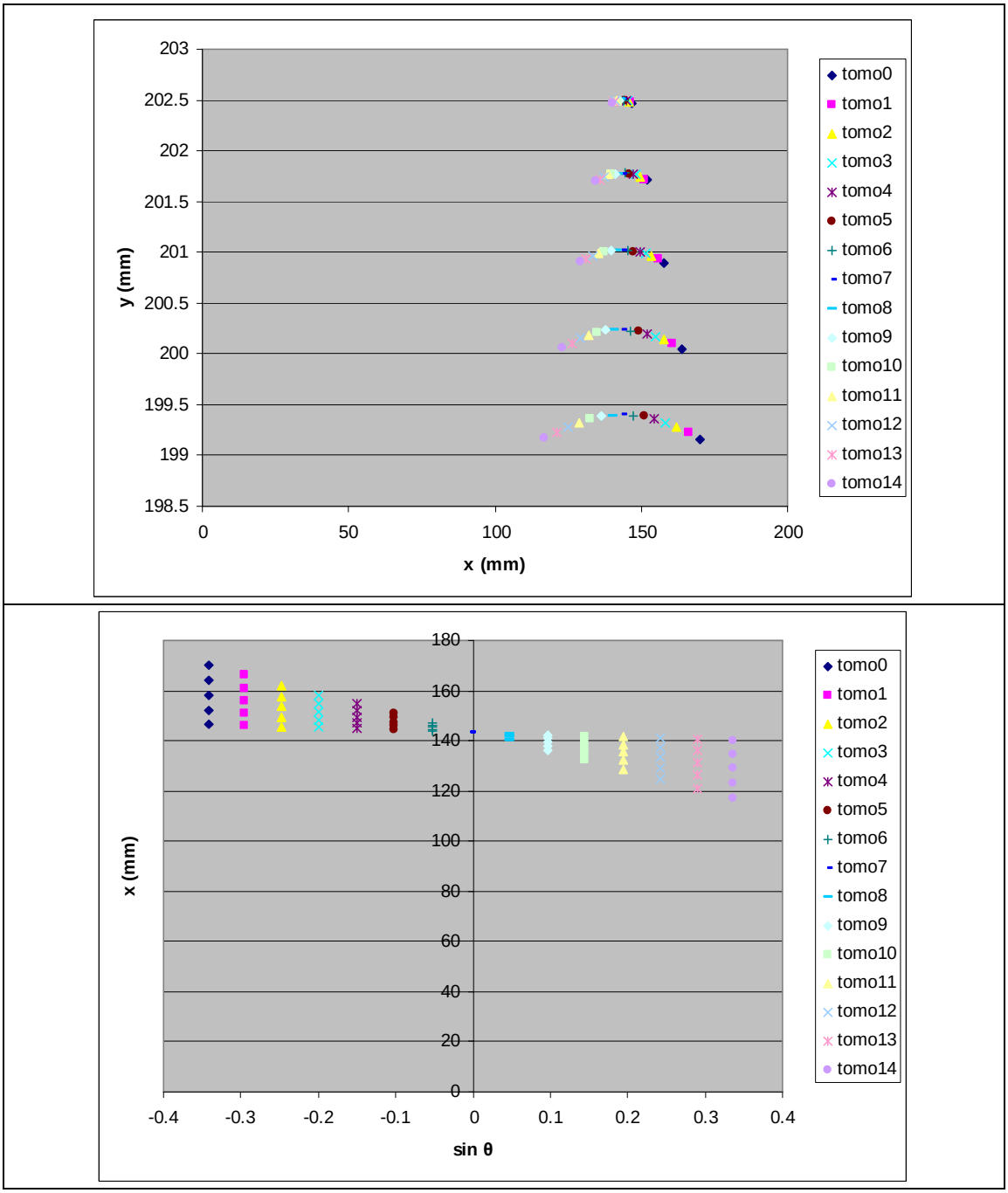

Figure 9.20: 2D plots of all extracted microcalcification candidates. Left: sensor y versus sensor x; Right: sensor x versus sin θ.

(d) Results:

Microcalc. No.	Actual (a,b,c)	Estimated (a,b,c)	Diff. (a, b, c)	Euclidean Distance
1	(0,-30,30)	(0,-29.99,29.82)	(0,-0.01,0.18)	0.18
2	(0,-30,15)	(0,-29.98,14.56)	(0,-0.02,0.44)	0.44
3	(0,-30,0)	(0,-29.97,-0.70)	(0,-0.03,0.70)	0.70
4	(0,-30,-15)	(0.01,-29.95,-15.96)	(-0.01,-0.05,0.96)	0.96
5	(0,-30,-30)	(0.01,-29.94,-31.22)	(-0.01,-0.06,1.22)	1.23

Table 9.2: Actual and estimated (a, b, c) of Experiment 1.

(e) Comments

The value of *c* affects the accuracy of the estimation of the microcalfication position. The closer it is to the sensor, the more accurately it can be estimated. It is also found that the estimated values of *a* and *b* are nearly the same as the actual ones, while the errors are mostly due to the estimated values of *c*.

Experiment 2: Experiments on different "a" values

(a) Actual microcalcification positions:

5 microcalcifications at 3D positions with different "*a*" values are generated:

Microcalcification No.	A	b	c
1	-30	-10	20
2	-25	-10	20
3	-20	-10	20
4	-15	-10	20
5	-10	-10	20

Table 9.3: 5 microcalcification with different "a" values.

(b) DBT views:

15 DBT views are generated and *3* of them are shown here:

Figure 9.21 DBT views containing a cluster of 5 microcalcifications with different "a" values and fixed "b" and "c" values, generated at -19.98°*(Left),,* -0.16°*(Middle),* 19.65°*(Right).*

(c) 2D plots of all extracted microcalcification candidates:

Two 2D plots are drawn for visualization of the epipolar curves and epipolar clustering:

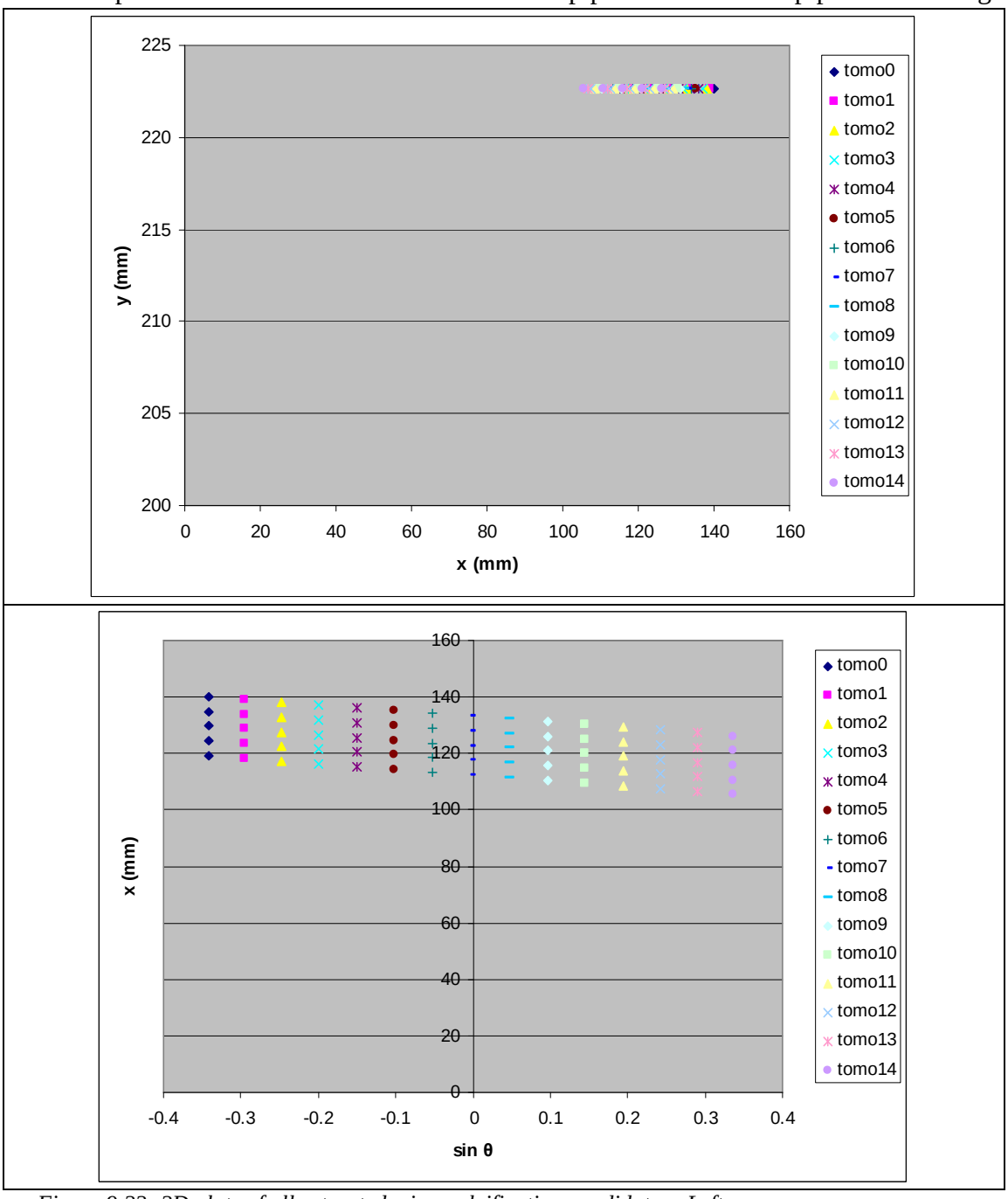

Figure 9.22: 2D plots of all extracted microcalcification candidates. Left: sensor y versus sensor x; Right: sensor x versus sin θ.

(d) Results:

Microcalc. No.	Actual (a,b,c)	Estimated (a,b,c)	Diff. (a, b, c)	Euclidean Distance
1	(-30,-10,20)	(-29.98,-10.00,19.65)	(-0.02,-0.00,0.35)	0.35
2	(-25,-10,20)	(-24.99,-10.00,19.65)	(-0.01,-0.00,0.35)	0.35
3	(-20,-10,20)	(-10.99,-9.99,19.65)	(-0.01,-0.01,0.35)	0.35
4	(-15,-10,20)	(-14.99,-10.00,19.65)	(-0.01,-0.00,0.35)	0.35
5	(-10,-10,20)	(-9.99,-10.00,19.65)	(-0.01,-0.00,0.35)	0.35

Table 9.4: Actual and estimated (a, b, c) of Experiment 2.

(e) Comments

The change of the value of *a* will give a similar Euclidean distance. Similar to Experiment *1*, the estimated values of *a* and *b* are nearly the same as the actual ones, while the errors are mostly due to the estimated values of *c*.

Experiment 3: Experiments on different "b" values

(a) Actual microcalcification positions:

5 microcalcifications at 3D positions with different "*b*" values are generated:

Microcalcification No.	A	b	c
1	-30	-10	20
2	-30	-20	20
3	-30	-30	20
4	-30	-40	20
5	-30	-50	20

Table 9.5: 5 microcalcification with different "b" values.

(b) DBT views:

15 DBT views are generated and *3* of them are shown here:

Figure 9.23: DBT views containing a cluster of 5 microcalcifications with different "b" values and fixed "a" and "c" values, generated at -19.98°*(Left),,* -0.16°*(Middle),* 19.65°*(Right).*

(c) 2D plots of all extracted microcalcification candidates:

Two 2D plots are drawn for visualization of the epipolar curves and epipolar clustering:

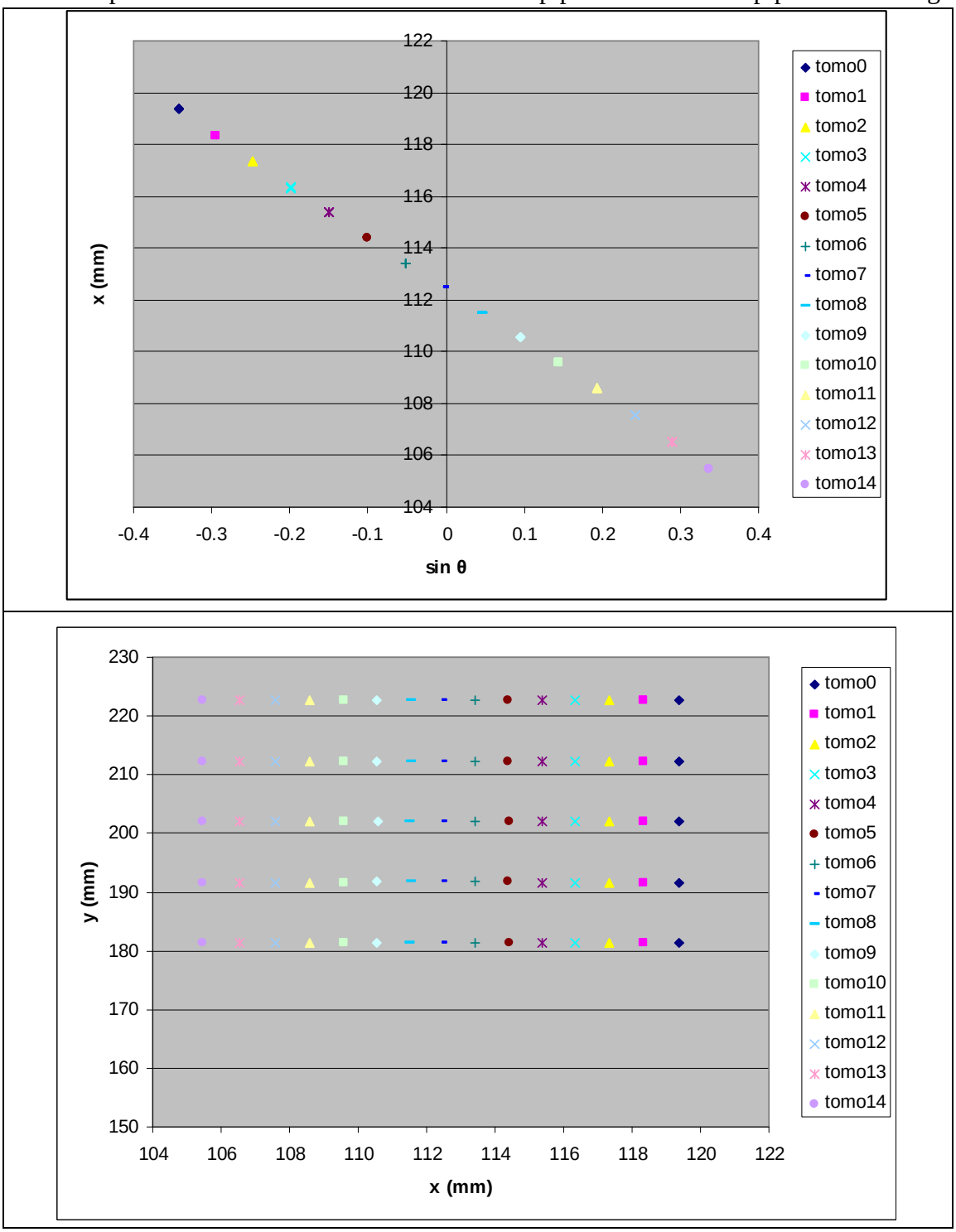

Figure 9.24: 2D plots of all extracted microcalcification candidates. Left: sensor y versus sensor x; Right: sensor x versus sin θ.

(d) Results:

Microcalc. No.	Actual (a,b,c)	Estimated (a,b,c)	Diff. (a, b, c)	Euclidean Distance
1	(-30,-10,20)	(-29.98,-10.00,19.65)	(-0.02,-0.00,0.35)	0.35
2	(-30,-20,20)	(-29.98,-19.99,19.65)	(-0.02,-0.01,0.35)	0.35
3	(-30,-30,20)	(-29.98,-29.98,19.65)	(-0.02,-0.02,0.35)	0.35
4	(-30,-40,20)	(-29.98,-39.98,19.65)	(-0.02,-0.02,0.35)	0.35
5	(-30,-50,20)	(-29.98,-49.97,19.65)	(-0.02,-0.03,0.35)	0.35

Table 9.6: Actual and estimated (a, b, c) of Experiment 3.

(e) Comments

The change to the value of *b* gives a similar Euclidean distance. As in Experiments *1* and *2*, the estimated values of *a* and *b* are nearly the same as the actual ones, with a very slight increase in errors in the estimation of *b* for smaller *b* , while the errors are mostly due to the estimated values of *c*.

Experiment 4: Experiments on using different DBT views

In this experiment, a microcalcification is chosen: one at *(0, -30, -30)* because it gives the largest error among all other experiments. We simply see whether using different selection of projections may improve it. Projection points on selective DBT views are used for the estimation of the slope and y-intercept during the line fitting process, and subsequently for the estimation of *(a, b, c)* in the EC Formulas Method. The results are shown in the following table:

DBT Views Used	Actual (a,b,c)	Estimated (a,b,c)	Diff. (a, b, c)	Euclidean Distance
All	(0,-30,-30)	(0.01,-29.94,-31.22)	(-0.01,-0.06,1.22)	1.23
5,6,7,8,9	(0,-30,-30)	(0.09,-29.99,-30.12)	(-0.01,-0.01,0.12	0.12
6,7,8	(0,-30,-30)	(0.01,-30.00,-30.09)	(-0.01,-0.00,0.09)	0.09
0,14,1,13, 2,12	(0,-30,-30)	(0.01,-29.84,-30.22)	(-0.01,-0.16,0.22)	0.27
0,14,1,13	(0,-30,-30)	(0.01,-29.82,-30.08)	(-0.01,-0.18,0.08)	0.20

Table 9.7: Actual and estimated (a, b, c) of Experiment 4.

(e) Comments

From the results, it seems that the errors can be reduced using fewer number of views and it is more favourable to use the projections near the CC positions. More experiments and analysis should be done in future to have a more valid conclusion.

9.5.3 Comparison with Reconstruction in Mammography

From our experiments, the maximum error found using our epipolar curve formulas method in DBT is *1.23 mm*. Compared with those reconstructed in mammography which ranged from *10-20 mm*, our reconstruction method is a vast improvement.

9.6 Conclusions and Discussion

In this chapter, following our derivation of epipolar curves, we have proposed a method to estimate the 3D positions of the microcalcifications from the formulae. We have shown a number of reconstruction examples using real DBT datasets. In some examples, we can now discover the depths of the microcalcifications in the breast, instead of viewing them in 2D. Our method can provide a definite depth while common reconstruction methods can only give us a very rough estimation in terms of slice numbers. In addition, we have tried a few experiments to analyze the geometric accuracy of our method using simulated data. The estimation is promising and is much more accurate than those methods in mammography.

Chapter 10

Feasibility Study of Classification of Clusters of Microcalcifications in DBT

In this chapter, we investigate the feasibility of microcalcification classification in DBT based on the detection and reconstruction approach proposed in the previous chapters. We generated *15* simulated datasets, each with a microcalcification cluster organised spatially according to an ellipsoidal shape. We estimated the 3D positions of the microcalcifications in each of the clusters and reconstructed the clusters as ellipsoids. We classify each cluster as malignant or benign based on the parameters of the ellipsoids. The classification result is compared with the "ground truth". Our results show that the deviations between the actual and estimated 3D positions of the microcalcification, and the actual and estimated parameters of the ellipsoids are sufficiently small that the classification results are *100%* correct. This encourages us to investigate the feasibility in cluster classification using 3D features.

We first review observations and analysis of factors in differentiation between malignant and benign, in both individual microcalcifications and clusters of microcalcifications. Then we note current clinical practice in Section 10.2. We consider classification of microcalcification clusters for mammography in Section 10.3, then review a study on 3D features for microcalcification cluster classification in mammography in Section 10.4. Next, we present results of a preliminary study in classification based on the ellipsoidal shapes of the clusters using simulated datasets in DBT. This study does not give answers to, e.g. which 3D features are desirable for classification, or which classifiers are good. On the other hand, it shows that classification is feasible in DBT after using our reconstruction methods. The clusters can be reconstructed very similarly to the original shape, that it is possible to classify them correctly. This gives an important message that when more data is available in

future, we can use 3D features in the study of classification for more accurate results, as our real world is 3D but not 2D.

Finally, we will show two minimum volume enclosing ellipsoids of microcalcifications of two real patient datasets. The chapter will be ended with conclusions and discussion section.

10.1 Factors Affecting Classification of Microcalcifications

Extensive studies have related the seriousness of the breast diseases by the morphology and distribution of individual calcifications and clustered calcifications. To understand it, we start from the breast anatomy.

The basic functional unit in the breast is the lobule, also named as the terminal ductal lobular unit (TDLU), which contains acini, the berry-shaped termination of the mammary glands for secretion, that drain into the duct network and to the nipple. Supporting the network is a layer of fatty connective tissue called stroma. Calcifications can be found in breast stroma, within the acini (lobular calcifications) or within the terminal ducts (intraductal calcifications) [165].

Calcifications found in breast stroma are always benign. Due to some mechanical injury such as trauma or surgery, calcifications form in the skin or sutures may become calcified. Damage to an area of the fatty breast tissue will form a lump called fat necrosis and calcifications can be found surrounding the wall of the lump. Therefore, the shape and distribution of calcifications are variable in such cases.

For other cases like lobular calcifications or intraductal calcifications, their shape and distribution can be explained as follows:

Lobular calcifications fill the acini in the TDLU. Hence, the calcifications seen on a mammogram are usually uniform, homogeneous and sharply outlined, and are often punctate or round. They usually have a diffuse or scattered distribution, because their distribution follows how the acini are distributed. Lobular calcifications are always benign. They are formed by fibrocystic changes, fibroadenoma and lobular neoplasia or LCIS.

Figure 10.1 : Lobular calcifications (Extracted from [165].)

Intraductal calcifications are calcified cellular debris or secretions within the milk ducts. They have variable size, density and form. Since they form within the ducts, these calcifications often have a fine linear or branching form and distribution. Intraductal calcifications have a higher probability of malignancy because they are usually associated with DCIS.

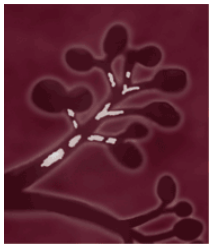

Figure 10.2: Intraductal calcifications (Extracted from [165].)

10.1.1 Classification Based on Morphology of Individual Calcifications (Le Gal's Classification)

Understanding that the morphologic character of calcification may correlate with the benignancy / malignancy of breast disease, Le Gal et al. [114] performed excisions with histological examination of breast microcalcifications. They classified the microcalcifications into five types:

Type 1: Annular	Type 2: Regularly Punctiform	Type 3: Dusty	Type 4: Irregularly Punctiform	Type 5: Vermicular
				

Figure 10.3: Le Gal's Classification (Pictures extracted from [114].)

In their study, they diagnosed *227* cases of breast microcalcifications. All benign lesions have Type *1* calcifications. All Type *5* calcifications are malignant. In terms of malignancy, the higher the type number, the higher the percentage of malignant lesions. Other studies [166, 167] have shown similar results according to Le Gal's classification. They are summarized as follows:

Type	***Le Gal et al. [114]***	***E. Foundrinier et al. [166]***	***Z. Sun et al. [167]***
Type 1 (Annular)	0%	0%	Not available
Type 2 (Regularly Punctiform)	22%	27%	37.0%
Type 3 (Dusty)	40%	32%	60.0%
Type 4 (Irregularly Punctiform)	66%	65%	78.8%
Type 5 (Vermicular)	100%	100%	88.9%
Total No. of lesions	227	211	103
Malignant	101 (+ 27 borderline lesions)	99	67
Benign	99	112	36

(Note: Values of % refer to the % of malignancy)

Table 10.1: Studies of malignancy according to Le Gal's classification

10.1.2 Classification Based on Shape of Calcification Clusters

In addition to the shapes of the individual calcifications and their distribution, Lanyi undertook a comprehensive analysis of calcifications, within and outside the lobular and ductal system of the breast, and calcifications in fibroadenomas [168]:

(i) Breast Carcinomas

Most mammograms of breasts with carcinomas contain calcification clusters with shapes such as triangular or trapezoidal; square or rectangular, possibly with a tapered end; bottle- or club-shaped; propeller- or butterfly-shaped; rhomboid or kite-shaped; linear or branched.

(ii) Fibroadenoma

The calcifications form rounded clusters in the majority of cases.

The following figures show a malignant calcification cluster which is linear, and a benign cluster which is round in shape:

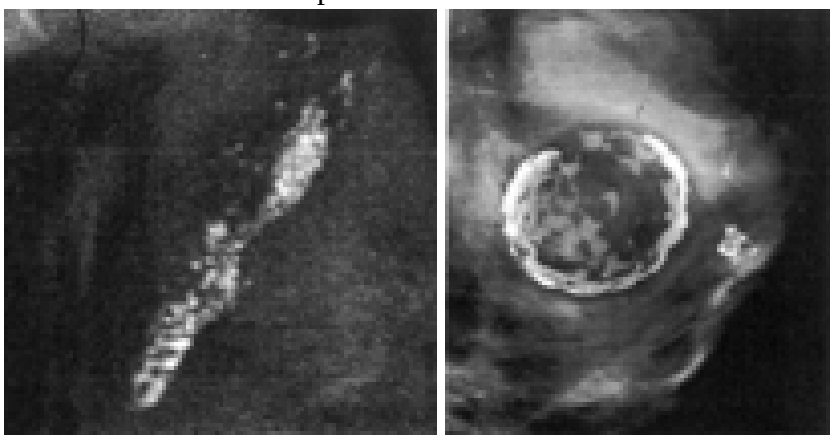

Figure 10.4: Linear shape in a duct segment filled with microcalcifications (Left). Calcified fibroadenoma (Right). (Extracted from [168])

10.2 Current Radiological Practice – BI-RADS

The Breast Imaging Reporting and Data System (BI-RADS), developed by the American College of Radiology, provides a standardized classification for mammographic studies [165, 169, 170]. The system demonstrates good correlation with the likelihood of breast malignancy. Given a mammogram, the radiologist will assess the breast condition and classify it into seven categories: requiring additional imaging evaluation, negative findings, benign findings, probably benign, suspicious abnormality, highly suggestive of malignancy and known biopsy proven malignancy. BI-RADS provides classifications of calcifications according to calcification morphology and the distribution pattern.

In terms of morphology, calcifications are classified into three types: Benign, Intermediate concern, and Malignant. For benign calcifications, their patterns or shapes can be lucent centred deposits of skin calcifications, vascular, popcorn, large rod like, round, eggshell or rim, milk of calcium, suture, dystrophic or punctuate. For intermediate concern, they are amorphous and coarsely heterogeneous. For the malignant type, they are fine linear, branching or pleomorphic. (*Figure 10.5*)

In terms of distribution modifiers, there are in general five different calcification distributions: (1) diffuse or scattered (calcifications that are distributed randomly

throughout the breast), (2) regional (calcifications within a relatively large volume of breast tissue (> *2* cm^3), (3) grouped or clustered (when there are at least *5* calcifications occurring in a small volume (< *1* cm^3), (4) linear (calcifications arrayed in a line that may have branching points, it is typically seen when DCIS fills the entire duct and its branches with calcifications), (5) segmental (deposits within a duct and its branches). (*Figure 10.5*) It is noted, however, that the differentiation in many cases may be problematical and depends on radiologist experience.

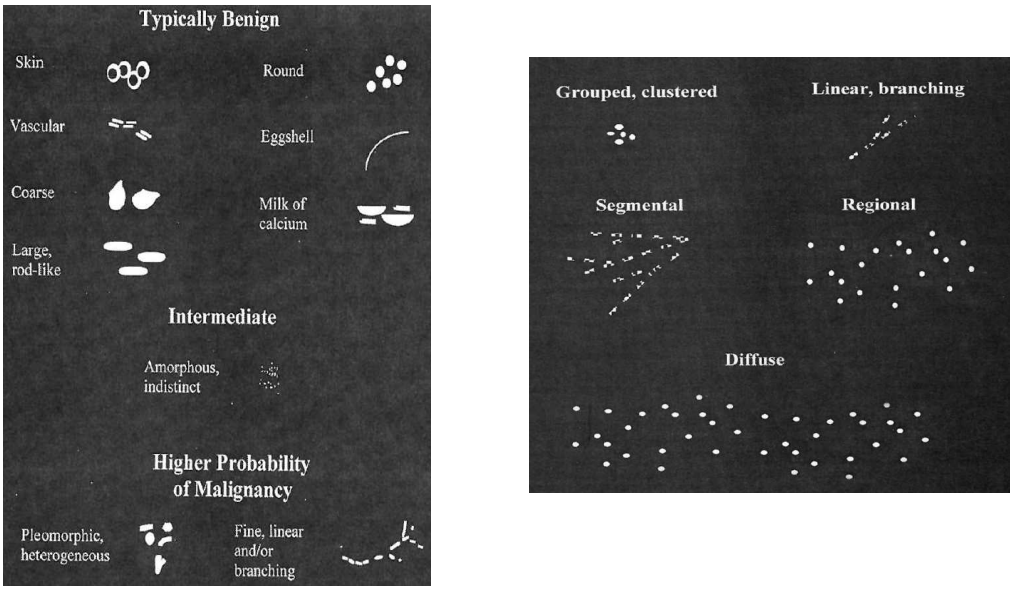

Figure 10.5: BI-RADS classification: morphology (Left); distribution modifiers (Right) (Extracted from [171].)

10.3 Automated Classification

The NHS Breast Screening Programme screens about *1.8* million women a year [106]. Given the large amount of data that the radiologist needs to review, CAD may play an important role in assisting radiologists if a case is suspected as breast cancer. A recent study [172], published in *2008*, was performed on *231,221* screening mammograms interpreted by experienced mammographers from *2001* through *2005* in a community-based mammography program. The study compared the efficacy of single reading with CAD to double reading and also to the first reader (without CAD) in a double-reading program. Their results indicated that CAD enhances performance of a single reader, resulting in an increased sensitivity with only a minor increase in recall rate. Hence, it is worth to investigate how to automate the classification task.

10.3.1 Problem Statement of Classification

Classification is the problem of predicting the class to which new observations belong, on the basis of a training set of data containing observations whose class is known. Given a set of training data $\{(x_1, y_1),...,(x_n, y_n)\}$, a classifier *h* is developed so that for any *x*, the output $\hat{y} = h(x)$ can be predicted as close and accurate as the true *y*.

Here, we identify *3* elements in classification: (1) the classifier; (2) the features (which are the values of the *x* term in the training data and *x* can either represent a single feature, or multiple features in terms of a feature vector); (3) feature selection algorithm. In the following, we will give an introduction of these *3* elements and have a literature review specifically on microcalcification clusters classification.

10.3.2 Classifiers: ANN and KNN

There are various supervised machine learning classification techniques. Kotsiantis [173] has provided a useful review of such techniques. Among all the algorithms, we briefly introduce two of the most popular ones: Artificial Neural Network (ANN) and K-Nearest Neighbours technique (KNN).

(a) Artificial Neural Network (ANN)

(i) Introduction

(For a detailed discussion on neural network, please refer to the book [127].)

Given the set of input data *x* and the set of synaptic weights *w*, a neural network can be considered as a set of mathematical functions $y_k(x;w)$, which provides a non-linear mapping of *x* to a class label *y*. The form of the mapping is governed by the network architecture and the values of the adjustable weights.

To illustrate the concept in a very simple way, we show in the following figure the decision boundary given *2* input variables x_1 and x_2. There are *2* synaptic weights w_1 and w_2 and a bias *b* which does not depend on the input variables. The decision boundary takes the form of a straight line (or a hyperplane for multiple inputs). Those points (x_1, x_2) fall on the right of the decision boundary belong to class *1* while others belong to class *2*. The task here is to determine the weights and the bias given the training datasets.

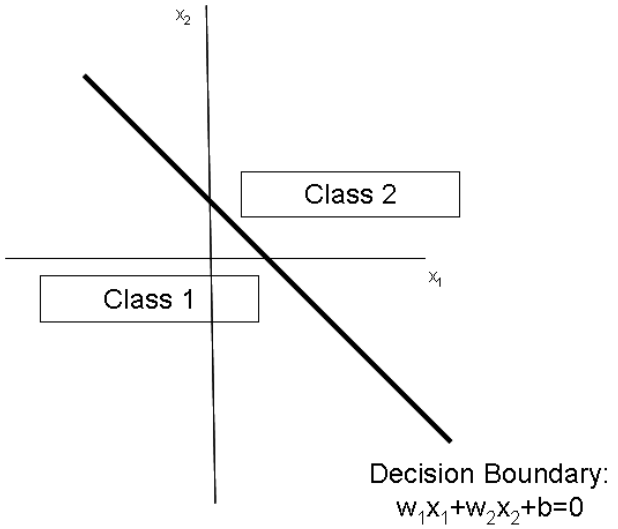

Figure 10.6: Illustration of a decision boundary for a 2D and 2-class pattern recognition problem.

To find the weights and the bias, one common approach is the back propagation algorithm. Readers can refer to [174] which gives a very simple example in explaining how back propagation works.

(ii) ANN on Microcalcification Clusters Classification

After a brief introduction of ANN, we will review an application of ANN on microcalcification clusters classification, so as to demonstrate the idea concretely.

Classification of microcalcifications in mammograms using artificial neural networks [175]

Nguyen et al. introduced the use of a multi-layer feedforward neural network to help microcalcification classification using *122* cases. Their neural network had *7* input neurons, *11* hidden neurons and *1* output neuron. There were *2* weight matrices for the neural network: the hidden layer weight matrix $\overline{w}$ and the output layer weight matrix W. They used *6* features which are some qualitative parameters assigning by clinicians, including shape, uniformity of size, uniformity of shape, uniformity of density, shape of cluster and distribution. The clinicians assigned a range of *1-5* to all the parameters except distribution which was ranged between *0* and *1*. The pathological results were also available for the training.

To formulate it mathematically:

$$x = \begin{bmatrix} x_1 \\ x_2 \\ x_3 \\ x_4 \\ x_5 \\ x_6 \\ -1 \end{bmatrix} = \begin{bmatrix} FSIZE \\ DISTRIB \\ FSHAPE \\ SHAPE \\ FDENSE \\ CLUSTER \\ -1 \end{bmatrix}, y = \begin{bmatrix} y_1 \\ y_2 \\ ... \\ y_{10} \\ -1 \end{bmatrix} = \begin{bmatrix} f(\overline{wx}) \\ -1 \end{bmatrix}, z = f(Wy)$$

where the author has chosen f as a bipolar activation function $f(v) = \frac{1-e^{-v}}{1+e^{-v}}$ and x represents the input features, y is the hidden neurons and z is the output. *-1* acts as a bias term which does not depend on the input.

The input data is classified as typical benign if z is between *-1* and *-0.35*, probably benign if z is between *-0.35* and *0*, suspicious if z is between *0* and *0.35* and typical malignant if z is between *0.35* and *1*. Using this dataset, the authors reported that a sensitivity of *86.11%* and a specificity of *84.21%* have been achieved. However, the authors did not mention how they distributed the *122* datasets for training and testing.

The paper demonstrates one way in which neural network may be used for classification. Of course, a lot of improvements are required, e.g. the features they used are some qualitative parameters which require inputs from radiologists. Feature extraction from the mammograms automatically should be performed instead for a truly computer-aided diagnosis. We will discuss more about the common features extracted later in this section.

(b) K-Nearest Neighbours (KNN)

(i) Introduction

KNN is a non-parametric method to decide to which class a feature sample belongs. Classification of a feature vector is performed by searching for the k closest training vectors based on some distance metric, usually Euclidean distance. The test vector is assigned to the class to which the majority of these k nearest neighbours belong. The advantage of KNN is that it provides an efficient and robust classification scheme without requiring significant initialisation and training time. Unlike ANN which normally needs quite a large size of datasets, KNN is capable for classification with small datasets. Normally, the classifier was trained and tested using the leave-out-n method, or sometimes called leave-one-patient-out method if n is *1*. This method takes the N available samples, trains the network on N-n samples and uses the remaining

n samples as test cases. Classification is continued in this manner until all the *N* samples have been used as test cases. Despite the advantages of KNN, as the example shows, it needs to choose *k* very carefully.

(ii) KNN on Microcalcification Clusters Classification

There are quite a number of works using KNN for classification by different research groups e.g. [176-178]. Instead of focusing on the classifiers, different authors defined their own feature sets, tried different number of features and different *k* values for the best performance. (More on feature sets will be discussing in the coming section.)

10.3.3 Features for Classification

In microcalcification cluster classification, there are, in general, *3* different types of features: (1) Individual calcification features; (2) Cluster features; (3) Texture features. The following table shows some common features used in classification [129, 176-178]:

Types	Features
Individual Calcification Features	Regarding the size, shape and spatial distribution [129, 176]: e.g. Mean and standard deviation of calcification area, compactness, eccentricity, elongation, orientation, distance to cluster centre, nearest neighbour distance.
	Regarding the gray level of the microcalcification in the cluster [177]: e.g. Average gray level, standard deviation of the mean of the microcalcification gray levels, maximum standard deviation of the gray levels in each calcification, average standard deviation of the gray levels in each calcification.
Cluster Features	Regarding the size, shape, location and number [129, 176, 177]: e.g. cluster area, compactness, eccentricity, elongation,

	orientation, relative distance to pectoral muscle, relative distance to breastedge, total number of calcifications, calcification density, radius of the circle that best fits the cluster.
Texture Features	Haralick texture features [177, 178]: angular second moment, contrast, correlation, variance, inverse difference moment, sum average, sum variance, sum entropy, entropy, difference variance, difference entropy, information measures of correlation.
	Wavelet texture signatures [178]: energy, entropy and root texture signatures for the approximation and detail wavelet coefficients.

Table 10.2: Common features used in classification.

10.3.4 Feature Selection Algorithms

The choice of features input to the classifier is vital to both the classification performance and results, because many of the features may not contain any significant discriminatory information, or there may also be correlation between features [178].

A feature selection algorithm consists of *2* parts: the selection criterion and the search strategy. The selection criterion indicates the discriminative power of features, e.g. Veldkamp et al. [176] used the area under the ROC curve as a criterion such that features having larger area are chosen. There are a few search strategies. e.g. Krammer et al. [178] employed *3* search strategies: The Uni-dimensional Search ("Best Features") (Selection of the best d features from the total feature set); The sequential forward selection (SFT) (This starts with the best feature which is put in an empty list. Then, the algorithm sequentially adds the next feature to the list when this feature combines with the features already in the list scores the highest.); The Sequential Backward Selection (SBS). (This works in a similar way to SFT except it starts with the complete feature set and successively removes the least discriminatory features.)

10.4 3D Features for Microcalcification Cluster Classification in Mammography

Most studies (as discussed in Section 10.3), or even in the current practice by radiologists (as discussed in Section 10.2) on cluster classification are in 2D, due to the limitation of the current mammography technologies. There is always a doubt in the accuracy in the classification results. We have already shown graphically in Chapter 2.2. that a 2D image cannot sometimes reflect the true picture of the shape or distribution of microcalcifications. Hence, to strive for a more accurate result, 3D features analysis is required. Using CC and MLO views of the mammograms, Yam et al. [129] have proposed a reconstruction method of microcalcifications in 3D (as discussed in Chapter 9). They examined six 3D features computed from the reconstruction using a total of *15* malignant and *15* benign clusters and compared with the 2D counterparts. As our focus is 3D, we will only discuss their findings of these six 3D features in the following briefly. (Readers are advised to refer to Yam's thesis [129] for more details.)

10.4.1 Calcification Distance to Cluster Centre (d_{cen})

It is believed that malignant clusters are typically more likely to have a linear or branching shape. Hence, it is expected that the variation of d_{cen} should be larger than those benign clusters which are typically more likely to have a round for oval shape. So, the authors have calculated the mean and standard deviation of d_{cen} in the *30* clusters for analysis. As expected, it is found that the mean and standard deviation tend to be larger in the malignant clusters.

10.4.2 Nearest Neighbour Distance of Calcifications (d_{nn})

This measures the separation between adjacent calcifications within the cluster. It is believed that malignant clusters are typically denser and hence should have a smaller d_{nn}. Similar to d_{cen}, the authors have calculated the mean and standard deviation of d_{nn} in the *30* clusters for analysis. Surprisingly, it is unexpected that the results showed benign clusters tend to have a smaller mean than malignant ones, which is not consistent to our

belief. There is no noticeable difference between the standard deviation of the two groups.

10.4.3 Calcification Compactness (*c*)

Compactness is a common shape descriptor used for calcification classification in 2D. Yam et al. have extended the definition of compactness to 3D volumes using calcifications' surface area *A* and their volume *V*. It is defined as $c = \frac{A^{\frac{3}{2}}}{6\pi^{\frac{1}{2}}V}$ such that a sphere will have the smallest value of *1*. It is believed that malignant calcifications are expected to have a larger value of compactness, because they should have an elongated or irregular shape, or a more jagged outline, causing a larger area to volume ratio that that of benign ones. Again, the mean and standard deviation of calcification compactness are calculated. It is found that a subset of benign clusters can be isolated from the remaining clusters by having a smaller mean and standard deviation.

10.4.4 Calcification Orientation (θ)

This is measured relative to the nipple position and is defined as the (smaller) angle between the principal direction of the cluster and the line connecting the nipple and the cluster centre. It is expected that malignant clusters associated with DCIS are more likely to have a smaller mean value than benign ones, because the calcifications lie along ducts and hence tend to be oriented towards the nipple. It is no conclusion on the favoured orientation, however. Overall, the results of the distribution pattern of the mean value of the *30* clusters agree with the theory that malignant calcifications are expected to have a smaller angle.

10.4.5 Calcification Volume (*v*)

It is believed that malignant clusters are more likely to have calcifications of mixed sizes, while the size of benign clustered calcifications tend to be more homogeneous. Hence, malignant clusters tend to have a larger variation of calcification size. However,

the results showed that the volume feature appeared not to be a good discriminator for this particular dataset.

10.4.6 Cluster Location Features (d_{pec} and d_{edge})

They are the measures of the relative distance of the cluster centroid to the pectoral muscle d_{pec} and to the breast edge d_{edge}. The reasons of using these features are based on the finding that malignant clusters are more likely to be located in the upper part of the breast, meaning that they are more likely to be closer to the pectoral muscle and the breast skin. However, the results showed that the features do not appear to be significant differentiation between benign and malignant clusters using this particular dataset.

10.4.7 Discussion

The study by Yam et al. is one of the first few using 3D features for classification. It is encouraging that some of the features used follow our expectation and they can help differentiate between malignant and benign clusters. However, the classification resuls using some other features are deviated from what we expect. This can easily be explained by the small datasets used in their experiment and the reconstruction method they used in estimating the 3D locations of the microcalcifications. The reconstruction method is only an approximation based on only *2* views with certain degree of compression. Hence, there must exist some discrepancies in the 3D features used and our expectation. With DBT, we have proposed a reconstruction method, presented in previous chapters. This is expected that the reconstruction, and subsequently the classification, should be more accurate, as we have more information (views) and also the compression is negligible in DBT. In the following section, we will show an example of using one 3D feature of cluster shape in *15* simulated datasets in the classification of clustered microcalcifications in DBT. This illustrates the feasibility and perhaps will help future development in breast classification when more datasets are available and more different 3D features can be identified.

10.5 Classification of Clustered Microcalcifications In DBT

In the following section, we describe a study in classification of microcalcifications in DBT using *15* simulated datasets generated by our simulation model.

10.5.1 Generation of Simulated Data

As discussed in Chapter 5, we have developed a simulation model to facilitate our study. The simulation model consists of *2* parts: (1) Simulation of microcalcification clusters; (2) Mammography/DBT projections generation. For Part (1), a model is developed to randomly generate microcalcification clusters. Recall that it has been reported that microcalcification clusters which are curvilinear in shape are far more likely to be malignant than those that appear to lie on the surface of a 3D surface shaped like a potato. For the purpose of demonstration of classification in DBT, currently we deliberately generate the clusters based on an ellipsoidal envelope, since it enables us to simulate both benign (diffuse shape) and another representing malignant (linear shape) clusters simply by varying the parameters of the ellipsoid. For a diffuse shape, one expects the *3* radii of the ellipsoids to be similar. For a linear structure, one expects one of the radii of the ellipsoid to be large relative to the other *2*. Hence, the shape of the ellipsoid is considered as the feature descriptor in the classification task (See *Figure 10.7*).

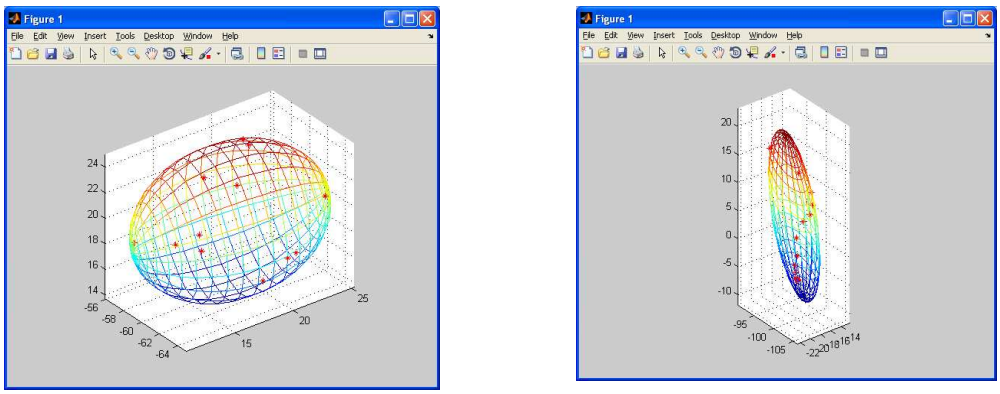

Figure 10.7: Ellipsoids of benign (Left) and malignant (Right) clusters.

Of course other feature descriptors may be considered in future. We randomly generate microcalcifications within the ellipsoidal envelope. We note, in passing, that the likelihood of malignancy is also suggested by the shapes of individual microcalcifications [114]. In the future, we intend to extend our model to generate

different shaped microcalcifications. The shape of the cluster is ellipsoidal with radii r_1, r_2, r_3 generated randomly, to represent different cluster shapes.

For Part (2), we use the X-ray simulation software developed by Tromans et al. [179]. This software generates X-ray projections comparable with real X-ray images, according to the input X-ray parameters. It also accepts the size and 3D positions of the microcalcifications.

10.5.2 Reconstruction of Microcalcification Clusters

As an initial experiment, we have used our simulation model to generate *15* sets of DBT views each containing a cluster of microcalcifications of various sizes. We have compared the difference between the actual and estimated 3D positions of the microcalcifications in each clusters using our epipolar curves approach and found that the average of the absolute difference of the 3D positions is between *0.028* and *0.197*. (*Table 10.3*):

Test No.	**No. of microcalcifications**	**Average of the absolute difference between actual and estimated 3D positions**		
		x	**y**	**z**
0	6	0.038	0.030	0.128
1	6	0.034	0.030	0.095
2	16	0.033	0.034	0.162
3	7	0.044	0.029	0.143
4	14	0.030	0.032	0.163
5	11	0.032	0.034	0.123
6	25	0.035	0.034	0.184
7	19	0.031	0.040	0.195
8	22	0.036	0.033	0.197
9	13	0.033	0.036	0.172
10	9	0.033	0.042	0.180
11	10	0.028	0.039	0.124
12	10	0.034	0.033	0.113
13	20	0.045	0.046	0.148

14	12	0.035	0.037	0.165

Table 10.3: Comparison between actual and estimated 3D positions of the microcalcifications in the clusters

10.5.3 Shape and Distribution Analysis of Microcalcification Clusters

After the reconstruction of microcalcification clusters, we analyse the 3D shape and distribution of the cluster. We computed the minimum volume enclosing ellipsoid (developed in Matlab code by [180]) for each cluster based on the estimated 3D positions of the microcalcifications obtained. We then compare the parameters of the ellipsoids (radii r_1, r_2, r_3 with $r_1 \le r_2 \le r_3$) with the ground truth.

Table 10.4 shows the comparison of the radii of the microcalcification clusters (as ellipsoid) in *15* simulated datasets. It is found that the estimated values do not deviate too much from the actual ones. The message here is that it is feasible to apply epipolar curves in the 3D positions estimation and subsequently perform classification of clustered microcalcifications.

Test No	**Comparison between the actual (left) and estimated (right) radii of the ellipsoidal clusters**					
	r_1		**r_2**		**r_3**	
0	3.58	3.62	8.66	8.65	22.87	22.89
1	4.91	4.93	9.98	9.97	13.95	13.83
2	12.92	12.72	14.38	14.56	18.33	18.71
3	3.09	3.12	13.72	13.70	17.51	17.43
4	5.77	5.73	12.00	12.17	18.92	19.27
5	5.68	5.67	13.18	13.12	16.47	16.53
6	5.65	5.76	6.62	6.71	16.67	16.61
7	9.91	9.64	10.25	10.60	16.52	16.58
8	9.73	9.74	14.59	14.71	19.33	19.07
9	8.40	8.40	16.39	16.17	20.85	21.34
10	4.84	4.82	13.22	13.22	19.67	19.61
11	8.82	8.81	9.73	9.71	15.19	15.16
12	6.69	6.64	8.69	8.73	10.70	10.85

13	7.85	7.80	8.50	8.85	10.20	10.34
14	11.19	11.14	14.48	14.39	19.42	19.40

Table 10.4: Comparison between actual and estimated radii of the ellipsoidal clusters

To demonstrate the use of feature descriptors in classification, we defined a classification rule:

IF $(r_3 / r_1 > t_1 \wedge r_3 / r_2 > t_2)$

THEN: The cluster is malignant;

ELSE: The cluster is benign

(where t_1, t_2 are the thresholds for comparison of the radii of the ellipsoid)

This rule implies that the longest radius r_3 should have a larger value than the other two radii with appropriate values of t_1, t_2 for a malignant cluster. Here, we have used $t_1 = 2.8$ and $t_2 = 1.4$. Out of *15* simulated datasets, we have *4* malignant clusters (Test No. *0, 4, 6, 10*) and *11* benign clusters. Our classification shows *100%* correctness after reconstruction using epipolar curves. Note the data is generated randomly. For all testing datasets, we can reconstruct the clusters and come up with similar ratios as the ground truth, leading to same classification results as in ground truth.

10.5.4 DBT vs Mammography

Classification results based on cluster features such as its shape, should be more accurate in DBT than in mammography. We have chosen *1* malignant test case (Test No. *0*) and *1* benign test case (Test No. *1*) for comparison. We correctly classified both test cases based on our classification rule on the ratios of the radii of the ellipsoids (cluster shape in 3D). However, it is difficult to make the same judgement by simply analyzing one 2D projection in these *2* test cases e.g. both can give linear structure with connected microcalcifications, misleading to classifying them both as malignant (*Figure 10.8* (top)). *Figure 10.8* (bottom) also shows the corresponding ellipsoids of the *2* test cases for reference.

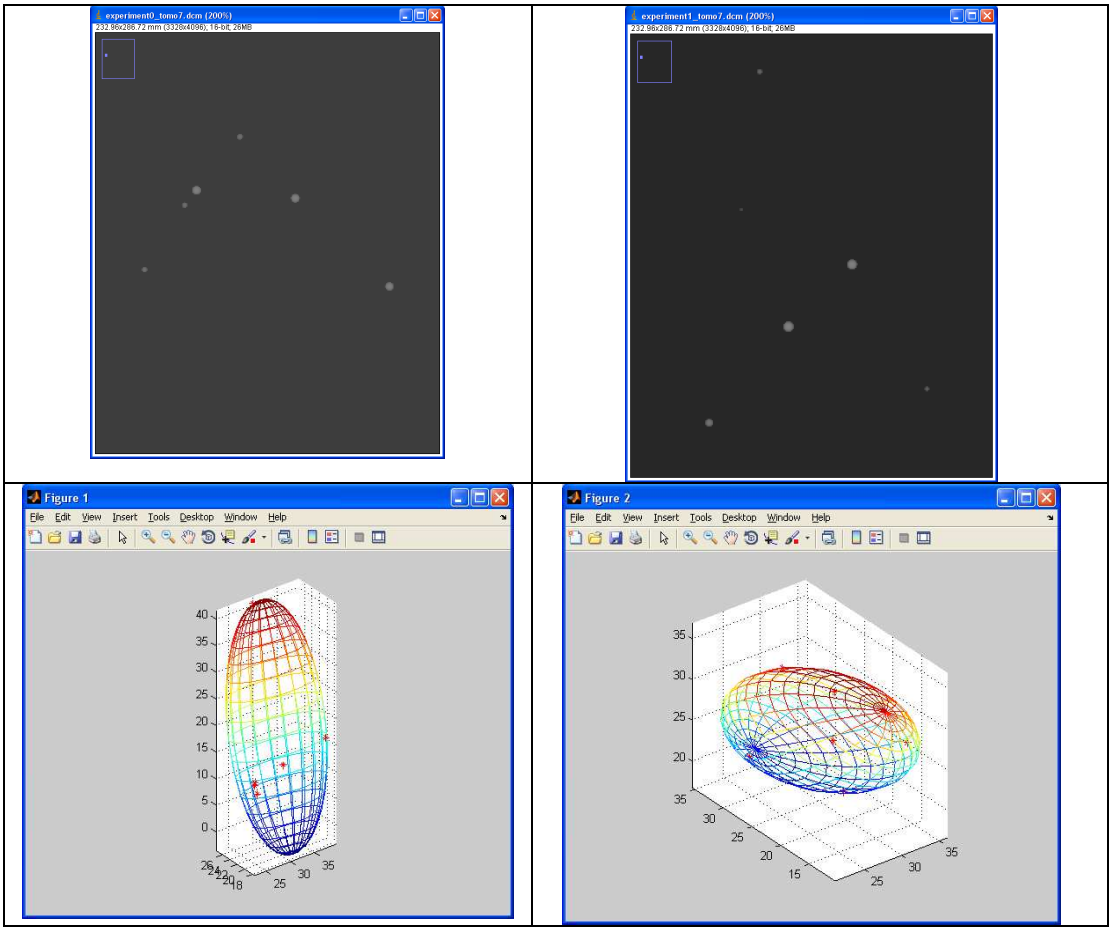

Figure 10.8. 2D projection in CC view (Top) and ellipsoid enclosing the microcalcifications (Bottom) of Test No. 0 (malignant) (Left) and Test No. 1 (benign) (Right).

10.6 Some Real Examples

We have computed the minimum volume enclosing ellipsoid as we have done for the simulated datasets for each cluster based on the estimated 3D positions of the microcalcifications obtained using DBT datasets of *Patient 16* and *Patient 24*:

(a) *Patient 16*

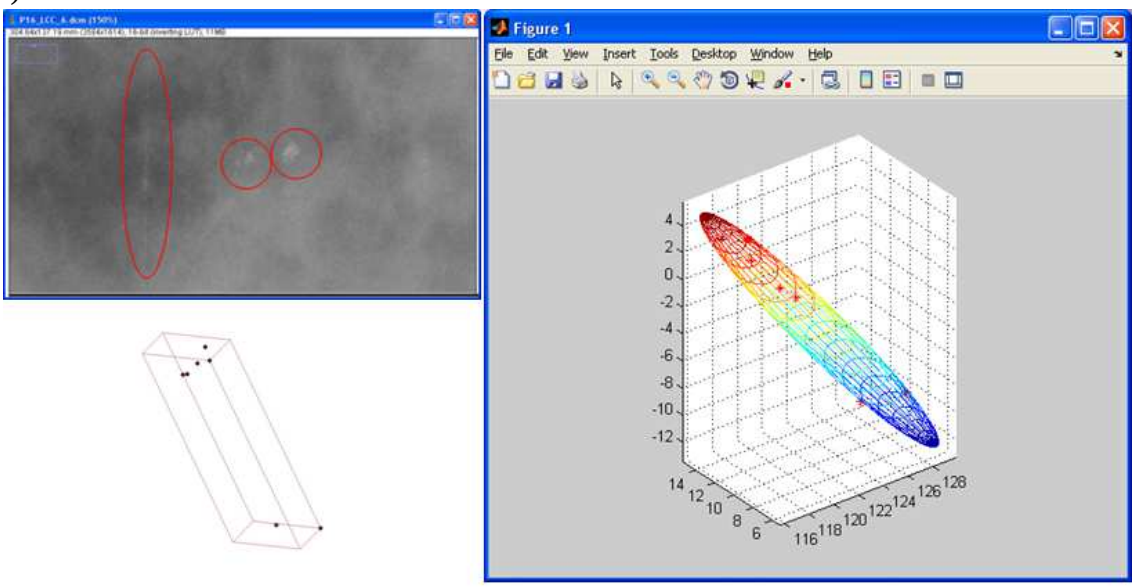

Figure 10.9: A magnified region from one of the real DBT projections showing a number of bright white spots (Top Left); The reconstructed 3D positions (Bottom Left); Ellipsoid enclosing the microcalcifications (Right) of Patient 16.

(b) *Patient 24*

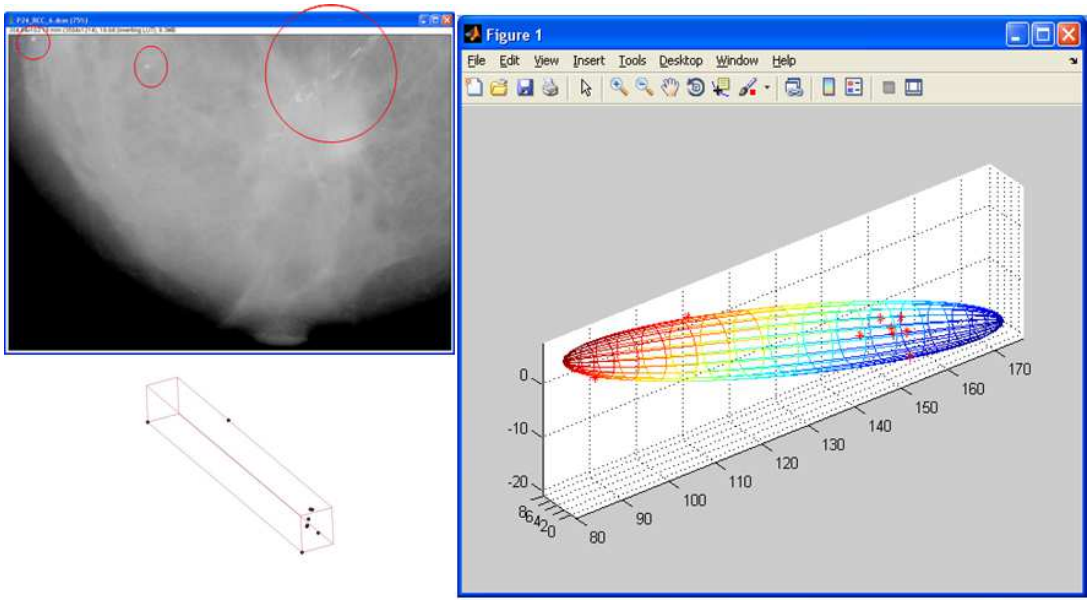

Figure 10.10: A magnified region from one of the real DBT projections showing a number of bright white spots (Top Left); The reconstructed 3D positions (Bottom Left) Ellipsoid enclosing the microcalcifications (Right) of Patient 24.

The following table shows the estimated radii of the ellipsoids generated for the clusters:

Patient No	r_1	r_2	r_3
16	1.52	4.28	12.18
24	3.72	5.81	50.02

Table 10.5: Estimated radii of the ellipsoidal clusters

Both patients have been diagnosed as Invasive/Infiltrating Ductal Carcinoma and both ellipsoids appear to have a longitudinal shape. Of course, we have not defined what a cluster is, nor the malignancy criteria, which are only meaningful with more real DBT datasets later in future. However, the message here is that we have demonstrated the feasibility in classification in DBT.

10.7 Conclusions and Discussion

DBT brings a new opportunity in the early detection of breast cancer. We have discussed a framework for computerized detection and classification of clustered microcalcifications using our epipolar curves approach. We demonstrated one possible way of 3D shape analysis by estimating the 3D positions of microcalcifications through epipolar curves and finding the minimum volume enclosing ellipsoids. In future when more DBT datasets are available, other 3D features such as distance to the nipple, volume of the clusters as ellipsoid can also be calculated for further analysis. This can help further investigation on the classification of clustered microcalcifications as malignant or benign.

Chapter 11

Conclusions and Future Work

In this concluding chapter, we will summarize the work in this thesis and identify possibilities for further research.

11.1 Epipolar Curves Approach in CAD in DBT

There have been few investigations on microcalcification detection algorithms in DBT, either using slices or projections. The technical challenge derives from the poor image quality in both types of images. Consequently, the performance of these detection algorithms is not too satisfactory and most vendors do not even have a solution of CAD for DBT.

Our epipolar curves approach offers a new method in microcalcification detection and reconstruction. By using the multiple projections produced during the acquisition process and the geometry of the system, it is possible to derive the trajectory of each microcalcification in the breast, provided that they are detected in the 2D X-ray images. The latter part of the previous statement is not always possible. It is interesting that the detection process is iterative and adaptive. Even if the microcalcifications are not detected at some projections in the first instance, the detection performance can be improved with our epipolar curves approach.

Our epipolar analysis also brings a new novel detection algorithm in DBT using Bayesian statistics method. The method estimates a maximum a posterior (MAP) labelling in each individual image and subsequently for all projections iteratively. Not only does this algorithm output the binary decision of whether a pixel is a microcalcification, it can predict the approximate depth of the microcalcification in the breast if it is.

With our epipolar ideas, reconstruction of only the region of interest (ROI) e.g. microcalcification clusters is possible and it is more accurate than any existing method

which we can find. This allows the future classification of breast cancer when more clinical data is available.

11.2 A New Branch of Research in DBT – Epipolar Analysis [181]

Over the last few decades, a major branch of research in DBT has concerned reconstruction algorithms in which the conventional meaning of reconstruction usually stands for the reconstruction of the whole breast, in the form of DBT slices. However, as we have seen, reconstruction algorithms remain work-in-progress not least because of the substantial null space problem.

On the other hand, our epipolar curves approach brings a new branch of research in DBT. With the DBT projections, by analogy with stereovision, a reconstruction of the whole breast for "fly through" and represented as "thick slab" for visualisation is likely not to have the required precision to evaluate quantitatively a region of interest (ROI), while reconstruction by epipolar analysis on the ROI is possibly better. As a result, reconstruction (the convention meaning) may not necessarily be a prior requirement for 3D analysis of structures of interest, for example microcalcification clusters. Epipolar analysis can provide detailed analysis and visualisation of ROI instead. The outcomes by DBT through reconstruction and/or epipolar analysis can further fuse with other 3D imaging modalities and mammography for better diagnosis of breast cancer:

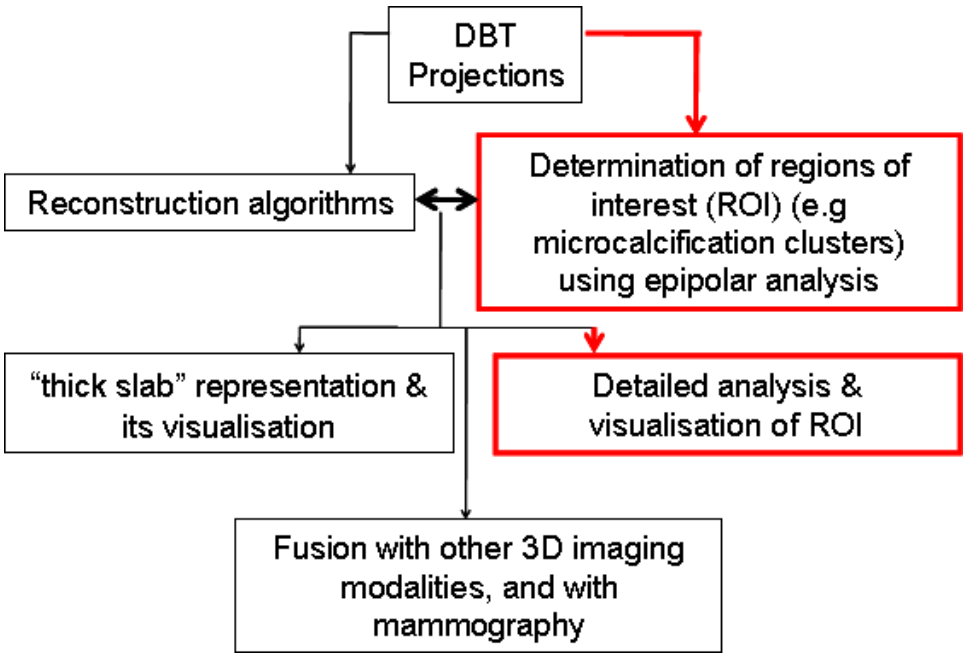

Figure 11.1:.Epipolar analysis as a new branch of research in DBT [181].

The following areas are some of the possible extensions or new interactions with other existing major areas in DBT:

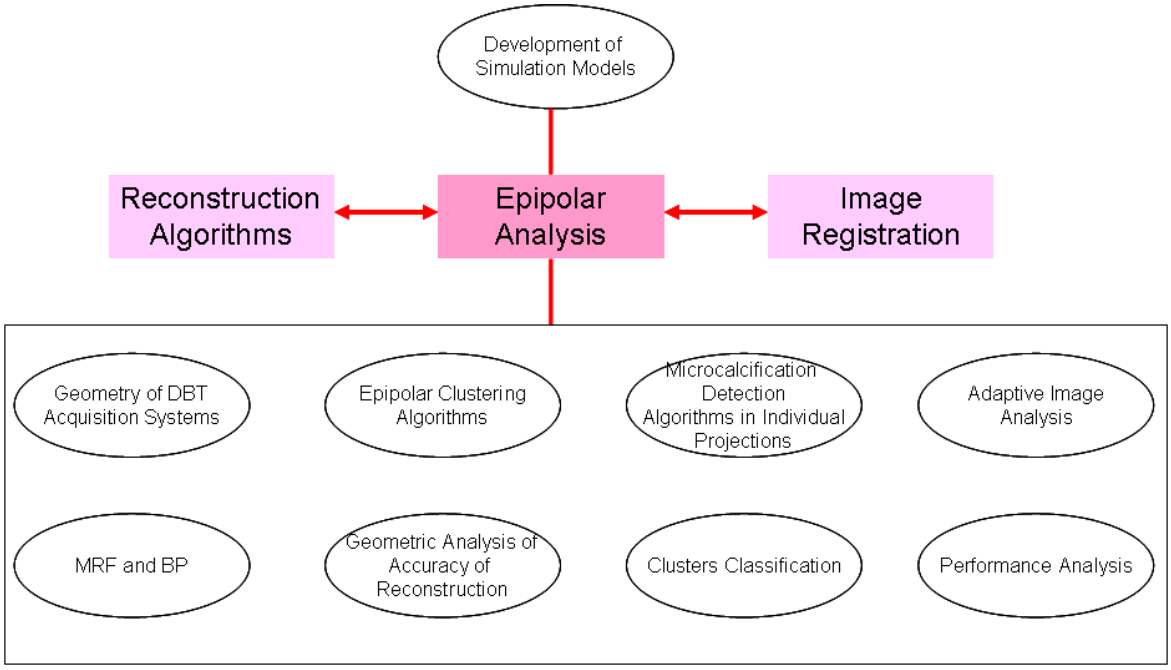

Figure 11.2:.Summary of Further Work

11.1.1 Development of Simulation Models

We have developed a simulation model which allows us to develop and illustrate our epipolar curve ideas. Currently, the model can only generate images with a uniform background. Further development and implementation can be carried on for a more comprehensive simulation model showing more realistic breast tissue compositions.

11.1.2 Geometry of DBT Acquisition Systems

In Chapter 6, we illustrated our concepts using a non-isocentric configuration. As mentioned in Chapter 2, there are other available configurations for the DBT acquisition systems. Also, since the development of DBT is ongoing, there may be some other geometries not yet covered and may arise in future. Although our concepts are developed on one geometry, our ideas of epipolar curves can be applied on any geometry. Work on other geometries can be further developed. A comparison analysis on different geometries can also be performed.

11.1.3 Epipolar Clustering Algorithms

An epipolar clustering algorithm aims at finding correspondence of projection points from the multiple projections. In this thesis, we have proposed the use of the Hough transform and line fitting to relate points coming from the same microcalcification in the breast, after the derivation of the epipolar curves. The development of epipolar clustering algorithms will be an important topic in the branch of epipolar analysis in DBT.

11.1.4 Microcalcification Detection Algorithms for Individual DBT Projections

Microcalcification detection algorithms are always one of the most active areas in mammography. In this thesis, we have applied a modified algorithm which is the combination of Harris corner detector and anisotropic diffusion on the individual DBT projections, as an illustration, specifically, of our concepts of adaptive image analysis and the development of a new DBT detection algorithm using multiple projections. The technical challenge of DBT over mammography is its poorer signal to noise ratio in the images. Enhancing the existing detection algorithms in mammography or image

processing areas can be one direction; developing new ones suitable for DBT can be another.

11.1.5 Adaptive Image Analysis

Multiple projections provide information which may not be perceived in a single projection. The epipolar curves help us tune up the single detection algorithms e.g. by a slightly adjustment of the thresholds, so that information e.g. the image position of the microcalcification being missed in the initial detection, can be estimated. We have discussed some ways to adaptively adjust the thresholds. More experiments should be carried out on more clinical data, to come up with a more real generalization.

11.1.6 Markov Random Fields (MRF) and Belief Propagation (BP)

Statistical analysis in image processing and computer vision is always an important topic. We have presented a novel algorithm using MRF and BP to detect microcalcification with an energy minimization functions using first-order neighbourhood system. In the future, other neighbouring systems used in the labelling problem and other cost terms and discontinuity terms can be considered in the energy minimization function. The memory and speed requirements are always demanding in MRF and BP. Improvement on computation performance can be further investigated.

11.1.7 Geometric Analysis of Accuracy of Reconstruction

Using the simulated data generated by our simulation model, we have compared the estimated 3D positions found using our epipolar curve formulas and the ground truth. The maximum error found using our epipolar curve formulas method in DBT is 1.23mm, which is a good approximation, when comparing with reconstruction methods in mammography or slice resolution which is about 1mm. More analysis on the accuracy, such as the impact of different line fitting methods when finding the parameters *(a, b, c)* (the 3D positions of microcalcification), the impact of using different combination of projection views, the impact of X-ray sources at different angular range, the impact of microcalcifications at different positions, can be studied in future.

11.1.8 Clusters Classification

In Chapter 10, we have a feasibility study on performing classification in our simulated clusters composing mainly on two different ellipsoidal shapes. Now, with a more accurate estimation of 3D positions of microcalcifications by our method, numerous experiments can be conducted on both simulated data and, when more freely available, real clinical data, regarding classification based on morphology and distribution of individual microcalcifications or shapes of clusters of microcalcifications.

11.1.9 Performance Analysis

As more clinical data becomes available, it would be valuable to compare the detection and classification performance with human observers and different imaging modalities.

11.1.10DBT Reconstruction Algorithms

Epipolar analysis can facilitate developments in other areas. With expectation-maximization algorithms, statistical reconstruction algorithms allow regularization so that additional constraints can be added for a more accurate reconstruction. The epipolar constraints provide further information for reconstruction.

11.1.11Image Registration

Image registration is another big topic. After the feature points are detected in each projection, these feature points, together with the epipolar constraints can be added during registration.

Appendix A

Glossary

ACR	American College of Radiology
AD	Anisotropic Diffusion
ANN	Artificial Neural Network
BI-RADS	Brast Imagaing Reporting and Data System
BP	Belief Propagation
CAD	Computer-aided detection and classification of microcalcifications
CC	Cranio-caudal view
CT	Computed Tomography
DBT	Digital Breast Tomosynthesis
DCIS	Ductal Carcinoma in Situ
DCE MRI	Dynamic Contrast Enhanced Magnetic Resonance Imaging
DM	Digital Mammography
EC Formulas Method	Epipolar Curve Formulas Method
FDA	United States Food and Drug Administration
FBP	Filtered backprojection
FP	False Positives
GRF	Gibbs Random Fields
keV	Kilo-electron Volts
KNN	K-Neares Neighbours
kVp	Peak of the waveform of the kilo-Voltages against time
LCIS	Lobular Carcinoma in Situ
MAP	Maximum Posterior Probability
MIP	Maximum intensity projection
MLO	Mediolateal-oblique view
MRF	Markov Random Field
MRI	Magnetic Resonance Imaging
NHS	National Health Service (United Kingdom)
PMMA	Polymethyl methacrylate
PTHrP	Parathyroid hormone-related protein
PZT	Lead zirconate titanate
ROC	Receiver Operating Characteristic
ROI	Region of Interest
SBS	Sequential Backwad Selection
SFM	Screen-Film Mammography
SFT	Sequential Forward Selection
SNR	Signal-to-noise Ratio
SVM	Support Vector Machine
T	Tesla
TDLU	Terminal Ductal Lobular Unit

TPF	True Positive Fraction
USI	Ultrasound Imaging

Bibliography

[1] National Cancer Institute. *SEER Stat Fact Sheets: Breast*. Accessed at: http://seer.cancer.gov/statfacts/html/breast.html. Cited on: 8 July, 2011.

[2] Hong Kong Cancer Registry, Hospital Authority. *Hong Kong Cancer Stat 2007*. Accessed at: http://www3.ha.org.hk/cancereg/e_canstat2007.pdf

[3] Office for National Statistics, United Kingdom. *Health Statistics Quarterly No. 40, Winter 2008*. Accessed at: http://www.statistics.gov.uk/downloads/theme_health/HSQ40-winter-2008.pdf.

[4] GLOBOCAN, International Agency for Research on Cancer (IARC), World Health Organization (WHO). *Breast Cancer Incidence and Mortality Worldwide in 2008*. Accessed at: http://globocan.iarc.fr/factsheets/cancers/breast.asp

[5] Kopans, D. B., *Breast Imaging*, 3rd ed. Piladelphia: Lippincott Williams & Wilkins, 2007.

[6] Breastcancer.org. *What Is Breast Cancer?* Accessed at: http://www.breastcancer.org/symptoms/understand_bc/what_is_bc.jsp

[7] Lynch, P. J. Wikipedia. *Breast Anatomy Normal Scheme*. Accessed at: http://en.wikipedia.org/wiki/File:Breast_anatomy_normal_scheme.png

[8] Mayo Foundation for Medical Education and Research. *Breast with Stroma, Lobule, Duct, Lymph Nodes and Vessels*. Accessed at: http://www.mayoclinic.com/health/medical/IM01880.

[9] Healthsearches. *What is DCIS?* Accessed at: http://www.healthsearches.org/Categories_of_Q&A/Diagnosis/1253.php.

[10] Cancer Research UK. *Types of breast cancer*. Accessed at: http://cancerhelp.cancerresearchuk.org/type/breast-cancer/about/types/

[11] Pam, S. About.com. *Types of Breast Cancer*. Accessed at: http://breastcancer.about.com/od/types/a/bc_types.htm

[12] American Cancer Society. *What Causes Breast Cancer?* Accessed at: http://www.cancer.org/Cancer/BreastCancer/OverviewGuide/breast-cancer-overview-what-causes

[13] Autier, P., Boniol, M., LaVecchia, C., Vatten, L., Gavin, A., Héry, C., and Heanue, M., "Disparities in breast cancer mortality trends between 30 European

countries: retrospective trend analysis of WHO mortality database," *BMJ*, 341((2010).

[14] van den Akker-van Marle, E., de Koning, H., Boer, R., and van der Maas, P., "Reduction in breast cancer mortality due to the introduction of mass screening in the Netherlands: comparison with the United Kingdom," *J Med Screen*, 6(1), (1999).

[15] Payne, D., "Ireland announces national breast screening programme," *BMJ*, 318(7190), (1999).

[16] Sofia News Agency - novinite.com. *Bulgarian oncology doctor raises alarm over lack of cancer screening*. Accessed at: http://www.novinite.com/view_news.php?id=117516

[17] Nick, T. *Breast cancer deaths fall in UK*. Accessed at: http://www.bbc.co.uk/news/health-10944826 Cited on: 12 August 2010.

[18] International Agency for Research on Cancer (IARC), World Health Organization (WHO). *Breast Cancer Screening, IARC Handbook of Cancer Prevention Volume 7*. Accessed at: http://www.iarc.fr/en/publications/pdfs-online/prev/handbook7/index.php

[19] Allgood, P. C., Warwick, J., Warren, R. M. L., Day, N. E., and Duffy, S. W., "A case-control study of the impact of the East Anglian breast screening programme on breast cancer mortality," *Br J Cancer*, 98(1), (2007).

[20] International Cancer Screening Network. *Characteristics of Breast Cancer Screening Programs in 19 ICSN Countries Responding to a Survey in 2002*. Accessed at: http://appliedresearch.cancer.gov/icsn/breast/policies1.html Cited on: 20 March 2009.

[21] Mammographic Image Analysis Homepage. *Signs of disease*. Accessed at: http://www.mammoimage.org/signs-of-disease/

[22] Laurance, J. The Independent Health News. *Review puts merits of breast cancer screening under the microscope*. Accessed at: http://www.independent.co.uk/life-style/health-and-families/health-news/review-puts-merits-of-breast-cancer-screening-under-the-microscope-2042584.html Cited on: 4 August 2010.

[23] Hope, J. Mail Online. *259 breast cancer screenings 'will save only one life'*. Accessed at: http://www.dailymail.co.uk/health/article-1300169/Breast-cancer-screening-harm-women-helps.html Cited on: 5 August, 2010.

[24] Jørgensen, K. J., Zahl, P.-H., and Gøtzsche , P. C., "Breast cancer mortality in organised mammography screening in Denmark: comparative study," *BMJ*, 340(

[25] Boone, J. M., Nelson, T. R., Lindfors, K. K., and Seibert, J. A., "Dedicated Breast CT: Radiation Dose and Image Quality Evaluation," *Radiology*, 221((2001).

[26] Yee, K. M. AuntMinnie.com. *DBT beats digital mammo for microcalcifications*. Accessed at: http://www.auntminnie.com/index.asp?sec=ser&sub=def&pag=dis&ItemID=95228. Cited on: 9 July, 2011.

[27] Hologic, Inc. *Hologic's R2 ImageChecker Digital CAD*. Accessed at: http://www.hologic.com/en/breast-screening/imagechecker/.

[28] Gilbert, F. J., Young, K. C., Astley, S. M., Whelehan, P., and Gillan, M. G. C. NHS Cancer Screening Programmes. *Digital Breast Tomosynthesis, NHSBSP Publication No 69, September 2010*. Accessed at: http://www.cancerscreening.nhs.uk/breastscreen/publications/nhsbsp69.pdf

[29] Bolan, C., "Breast screening's trade-offs," *Applied Radiology*, 40(3), (2011).

[30] Hologic, Inc. *Hologic Selenia Digital Mammography* Accessed at: http://www.hologic.com/en/selenia-s/.

[31] Tromans, C., "Measuring Breast Density from X-Ray Mammograms," DPhil, Engineering Science, University of Oxford, Oxford, 2006.

[32] About.com. *Mammogram views for routine and diagnostic screening*. Accessed at: http://breastcancer.about.com/od/mammograms/a/mamm_views.htm. Cited on: 20 March, 2009.

[33] Peters, G., "Computer-aided Detection for Digital Breast Tomosynthesis," PhD, TSI Research Group, ENST, Paris, France, 2007.

[34] Warren, R., Solomonides, A. E., del Frate, C., Warsi, I., Ding, J., Odeh, M., McClatchey, R., Tromans, C., Brady, M., Highnam, R., Cordell, M., Estrella, F., Bazzocchi, M., and Amendolia, S. R., "MammoGrid -- a prototype distributed mammographic database for Europe," *Clinical Radiology*, 62(11), (2007).

[35] Pruthi, S. Mayo Foundation for Medical Education and Research. *Mammogram: Can it find cancer in dense breast?* Accessed at: http://www.mayoclinic.com/health/mammogram/AN01137

[36] Miller, J. C. M. Department of Radiology, Massachusetts General Hospital. *When should breast MRI be used?* Accessed at: http://www.mghradrounds.org/index.php?src=gendocs&link=2005_october

[37] Hashemi, R. H., Bradley, W. G., and Lisanti, C. J., *MRI: The Basics*: Lippincott Williams & Wilkins, a Wolters Kluwer Business, 2010.

[38] Noterdaeme, O., "Magnetic Resonance Imaging of the Liver," DPhil, Engineering Science, University of Oxford, 2008.

[39] Tanner, L. N., "Functional Imaging Markers for Tumour Characterisation," DPhil, Engineering Science, University of Oxford, 2010.

[40] RadiologyInfo.org. *MRI of the breast*. Accessed at: http://www.radiologyinfo.org/en/info.cfm?pg=breastmr Cited on: 1 June 2011.

[41] El Khouli, R. H., Thomasson, D., Macura, K., Mezban, S., Liu, W., Jacobs, M., Edden, R., Barker, P., and Bluemke, D., "Detection of breast micro-calcifications with MRI at 3T," in *International Society for Magnetic Resonance in Medicine*, Stockholm, Sweden, 2010.

[42] Safir, M. D. J., Zito, M. D. J. L., Gershwind, M. D. M. E., Faegenburg, M. D. D., Tobin, M. D. C. E., Cayea, M. D. P. D., Wortman, M. D. W. J., Sclafani, M. D. L. M., and Maurer, M. D. V. E., "Contrast-enhanced breast mri for cancer detection using a commercially available system--a perspective," *Clinical Imaging*, 22(3), (1998).

[43] Safir, J., Zito, J. L. Z., Gershwind, M. E., Faegenburg, D., Tobin, C. E., Cayea, P. D., Wortman, W. J., Sclafani, L. M., and Maurer, V. E., "Contrast-enhanced breast mri for cancer detection using a commercially available system - a perspective," *Clinical Imaging*, 22((1998).

[44] FDA Drug Safety Newsletter. *Questions and answers on Gadolinium-based contrast agents*. Accessed at: http://www.fda.gov/Drugs/DrugSafety/DrugSafetyNewsletter/ucm142889.htm

[45] RadiologySpirit. *Ultrasound image with a fluid filled cyst*. Accessed at: http://radiologyspirit.blogspot.com/.

[46] Merz, E., *Ultrasound in Obstetrics nd Gynecology Vol.: Gynecology*, 2nd ed. New York: Georg Thieme Verlg, 2007.

[47] Hughes, S., "Medical ultrasound imaging," *Physics Education*, 36(6), (2001).

[48] Women's Imaging Specialists in HealthCare (W.I.S.H.). *Breast ultrasound unit*. Accessed at: http://www.wishmd.com/services/ultrasound.html.

[49] Stavros, A. T., *Breast ultrasound*. Phildelphia: Lippincott Williams & Wilkins, 2004.

[50] Yang, W. T., Suen, M., Ahuja, A., and Metreweli, C., "In vivo demonstration of microcalcification in breast cancer using high resolution ultrasound," *The British Journal of Radiology*, 70(835), (1997).

[51] Sehgal, C. M., Weinstein, S. P., Arger, P. H., and Conant, E. F., "A review of breast ultrasound," *Journal of Mammary Gland Biol Neoplasia*, 11((2006).

[52] Muhammed, H. H., KTH Royal Institute of Technology, "Lecture 5, Computed Tomography and The Radon Transform, Medical Image Analysis."

[53] Nilsson, J., "Computer Tomography for Mammography," Master of Science, Engineering Physics, Royal Insitute of Technology, KTH, 2007.

[54] Rehani, M. M., "CT: Caution on radiation dose," *Indian Journal of Radiology and Imaging*, 10(1), (2000).

[55] Boone, J. M., Packard, N. J., and Abbey, C. K., "Ideal Observer Comparison between Tomographic and Projection X-ray Images of the Breast," in *International Workshop on Digital Mammography*, Girona, Spain, 2010, pp. 591-597.

[56] Doheny, K. HealthDay. *Breast CT Scans Could Be Comfortable Alternative to Mammograms*. Accessed at: http://news.healingwell.com/index.php?p=news1&id=618031

[57] Bates, S. P., Astley, S. M., Davies, J. D., and Sharp, S., "Three-dimensional reconstruction and shape classification of microcalcification clusters in breast lesions," in *Int. Workshop Digital Mammography*, 1996.

[58] Astley, S. M., "Evaluation of computer-aided detection (CAD) prompting techniques for mammography," *Br J Radiol*, 78(suppl_1), (2005).

[59] RadiologyInfo.org. *Mammography (Breast compression)*. Accessed at: http://www.radiologyinfo.org/en/info.cfm?PG=mammo

[60] Sechopoulos, Suryanarayana, S., Vedantham, S., D'Orsi, C. J., and Krellas, A., "Scatter radiation in digital tomosynthesis of the breast," *Medical Physics*, 34(2), (2007).

[61] International Medical Service. *GE Senographe Essential*. Accessed at: http://www.internedservice.ru/content/view/849/209/.

[62] MedicExchange.com. *Hologic's Selenia Dimensions System*. Accessed at: http://www.medicexchange.com/Hologic-Inc/fda-approves-first-3-d-mammography-imaging-system.html.

[63] RadSource Imaging Technologies. *IMS's Giotto System*. Accessed at: http://www.radsource.net/solutions_listing.php?category=8.

[64] Siemens Healthcare Sector. *Siemens Mammomat Inspiration* Accessed at: http://www.siemens.com/press/en/pressrelease/?press=/en/pressrelease/2009/workflow_solutions/hws200906046.htm.

[65] Deller, T., Jabri, K. N., Sabol, J. M., Ni, X., Avinash, G., Saunders, R., and Uppaluri, R., "Effect of acquisition parameters on image quality in digital tomosynthesis," in *SPIE - Medical Imaging*, 2007.

[66] Machida, H., Yuhara, T., Mori, T., Ueno, E., Moribe, y., and Sbol, J. M., "Optimizing Parameters for Flat-Panel Detector Digital Tomosynthesis," *RadioGraphics - The journal of continuing medicl education in radiology*, 30((2010).

[67] Dexela Ltd. *Dexela Flat Panel CMOS X-ray Detectors*. Accessed at: http://www.dexela.com/cmos.aspx.

[68] Analogic Corporation. *ANRAD's amorphous Selenium flat-panel detector*. Accessed at: http://www.analogic.com/products-medical-digital-radiography.htm.

[69] Smith, A. *Fundamentals of breast tomosynthesis - Improving the performance of mammography*. Accessed at: http://www.hologic.com/data/WP-00007_Tomo_08-08.pdf.

[70] AuntMinnie.com. *Selenia digital mammography is 1st to meet or exceed rigorous new European image quality and patient dose standards*. Accessed at: http://www.auntminnie.com/index.aspx?sec=eba&sub=eml&pag=dis&ItemID=91314

[71] Van de Sompel, D., "Limited View Tomography," DPhil, Engineering Science, University of Oxford, 2010.

[72] Forrest, W. AuntMinnie.com. *FDA approves Hologic's 3D digital breast tomosynthesis system*. Accessed at: http://www.auntminnie.com/index.aspx?sec=sup%sub=wom&pag=dis&ItemID=94199.

[73] Gur, D., Abrams, G. S., Chough, D. M., GAnott, M. A., Hakim, C. M., Perrin, R. L., Rathfon, G. Y., Sumkin, J. H., Zuley, M. L., and Bandos, A. I., "Digital Breast Tomosynthesis: Observer Performance Study," *American Journal of Roentgenology*, 193((2009).

[74] Gennaro, G., Baldan, E., Bezzon, E., La Grassa, M., Pescarini, L., and Maggio, C. d., "Clinical Performance of Digital Breast Tomosynthesis Versus Full-Field Digital Mammography: Preliminary Results," in *International Workshop on Digital Mammography 2008*, 2008, pp. 477-482.

[75] Lin, J. Medscape Reference. *3D Mammography*. Accessed at: http://emedicine.medscape.com/article/1970908-overview#showall.

[76] Bassett, L. W., *Holland-Frei Cancer Medicine (Chapter 36f)*: BC Decker, 2003.

[77] Fandos-Morera, A., Prats-Esteve, M., Tura-Soteras, J. M., and Traveria-Cros, A., "Breast tumors: composition of microcalcifications," *Radiology*, 169((1988).

[78] National Cancer Institute, National Institutes of Health. *Understanding breast changes: a health guide for women*. Accessed at: http://www.cancer.gov/cancertopics/screening/understanding-breast-changes/page6.

[79] Poissonier, M., "Iconic normalisation and segmentation in x-ray mammograms," DPhil, Engineering Science, University of Oxford, Oxford, 2003.

[80] Moynihan, T. Taiwan Adventist Hospital. *Breast calcifications: Are they breast cancer?* Accessed at: http://www.tahsda.org.tw/warm_association/uploaded/file/37-01.pdf.

[81] Tse, G. M., Tan, P. H., Pang, A. L. M., Tang, A. P. Y., and Cheung, H. S., "Calcification in breast lesions: pathologists' perspective," *J. Clin. Pathol,* 61((2008).

[82] Radi, M. J., "Calcium oxalate crystals in breast biopsies. An overlooked form of microcalcification associated with benign breast disease.," *Arch Pathol Lab Med,* 113(12), (1989).

[83] Morgan, M., Cooke, M., and McCarthy, G., "Microcalcifications associated with breast cancer: an epiphenomenon or biologically significant feature of selected tumors?," *J Mammary Gland Biol Neoplasia,* 10(2), (2005).

[84] Halls, S. B. *Microcalcifications*. Accessed at: http://www.breast-cancer.ca/type/microcalcifications.htm.

[85] Harvard Medical School - Harvard Women's Health Watch. *Calcium beyond the bones*. Accessed at: http://www2.massgeneral.org/bmg/harvard_health/Women_Mar_10.pdf.

[86] Birch, M. A., Carron, J. A., Scott, M., Fraser, W. D., and Gllagher, J. A., "Parathyroid hormone (PTH)/PTH-related protein (PTHrP) receptor expression and mitogenic responses in human breast cancer cell lines.," *British Journal of Cancer,* 72(1), (1995).

[87] Devys, A., Lortholary, A., and Audran, M., "PTHrP and breast cancer," *Bull Cancer,* 88(11), (2001).

[88] Dunbar, M. E. and Wysolmerski, J. J., "Parathyroid Hormone-Related Protein: A Developmental Regulatory Molecule Necessary for Mammary Gland Development," *Journal of Mammary Gland Biology and Neoplasia,* 4(1), (1999).

[89] parathyroid.com. *High Blood Calcium (too much calcium in the blood)*. Accessed at: http://parathyroid.com/high-calcium.htm.

[90] Falzon, M. and Du, P., "Enhanced growth of MCF-7 breast cancer cells overexpressing parathyroid hormone-related peptide," *Endocrinology,* 141(5), (2000).

[91] Highnam, R. and Brady, M., *Mammographic Image Analysis*, 1st ed.: Kluwer Academic Publishers, 1999.

[92] Sprawls, P. *The Physical Principles of Medical Imaging*. Accessed at: http://www.sprawls.org/ppmi2/.

[93] Smith, A. *Full Field Breast Tomosynthesis*. Accessed at: http://www.guttahu.hu/users/749034/files/Mamografia/Tomosyntezas.pdf.

[94] McGill Faculty of Medicine - Interactive Mammography Analysis Web Tutorial. *MLO view of the normal breast*. Accessed at: http://sprojects.mmi.mcgill.ca/mammography/normal.htm.

[95] Boyd, N. F., Lockwood, G. A., Mrtin, L. J., Knight, J. A., Byng, J. W., Yaffe, M. J., and Tritchler, D. L., "Mammographic densities and breast cancer risk," *Breast Dis.*, 10(3-4), (1998).

[96] Byrne, C. and Spernak, S., "What is breast density?," *Breast Cancer Online*, 8(10), (2005).

[97] Yaffe, M., "Mammographic density. Measurement of mammographic density," *Breast Cancer Research*, 10(3), (2008).

[98] "Different mammographic appearance showing different breast composition," McGill Faculty oof Medicine - Interactive Mammography Analysis Web Tutorial.

[99] Boyd, N. F., Guo, H., Martin, L. J., Sun, L., Stone, J., Fishell, E., Jong, R. A., Hislop, G., Chiarelli, A., Minkin, S., and Yaffe, M. J., "Mammographic Density and the Risk and Detection of Breast Cancer," *New England Journal of Medicine*, 356(3), (2007).

[100] Dance, D., Thilander, A., Sandborg, M., Skinner, C., Castellano, I., and Carlsson, G., "Influence of anode/filter material and tube potential on contrast, signal-to-noise ratio and average absorbed dose in mammography: A Monte Carlo study," *The British Journal of Radiology*, 73(874), (2000).

[101] Schie, G. v. and Karssemeijer, N., "Noise model for microcalcification detection in reconstructed tomosynthesis slices," in *SPIE Medical Imaging*, Lake Buena Vista, FL, USA, 2009.

[102] Karssemeijer, N., "Adaptive Noise Equalization and Image Analysis in Mammography," in *13th International Conference on Information Processing in Medical Imaging*, Arizona, USA, 1993, pp. 472-486.

[103] Badea, C., Bliznakowa, K., Kolitsi, Z., and Pallikarakis, N., "Noise removal in tomosynthestic mammographic imaging," in *IFMBE Proc. 2nd European Medical and Biological Engineering Conf. BMBEC' 02*, Vienna, 2002, pp. 924-5.

[104] Smith, A. *Tomosynthesis - The New Imaging Modality for Breast Imaging*. Accessed at: http://www.acmp.org/meetings/lasvegas2006/Smith.Tomosynthesis.pdf. Cited on: 20 March, 2009.

[105] Smith, A. *Full Field Breast Tomosynthesis*. Accessed at: http://www.papapostolou.gr/pdf/Tomosynthesis.pdf. Cited on: 20th March, 2009.

[106] The NHS Information Centre, Workforce and Facilities. *Breast Screening Programme, England 2008-09*. Accessed at: http://www.ic.nhs.uk/webfiles/publications/breast_screening/Breast_Screening_Programme_Report_2008_09.pdf.

[107] Lefebvre, F., Benali, H., Gilles, R., and Paola, R. D., "A simulation model of clustered breast microcalcifications," *Med. Phys.*, 21(12), (1994).

[108] Maria J. Lado, A. J. M., Pablo G. Tahoces, Miguel Souto, Jose Correa, Juan J. Vidal, "Comparison of real and computer-simulated clustered microcalcifications on digital mammograms. ROC study.," in *International Conference on Image Processing*, Lausanne, Switzerland, 1996, pp. 355-358.

[109] Bliznakova, K., Bliznakov, Z., Bravou, V., Kolitsi, Z., and Pallikarakis, N., "A three-dimensional breast software phantom for mammography simulation," *Phys. Med. Biol.*, 48((2003).

[110] Nappi, J., Dean, P. B., Nevalainen, O., and Toikkanen, S., "Algorithmic 3D simulation of breast calcifications for digital mammography," *Computer Methods and Programs in Biomedicine*, 66((2001).

[111] Fernandez, D., Mossi, J. M., and Albiol, A., "Image capture prototype for the analysis and development of algorithms applied to the identification and visualization of clustered microcalcifications in tomosynthesis," in *Pattern Recognition and Image Analysis*, Benicasim (Castellon), Spain, 2001.

[112] Martí, J., Oliver, A., Freixenet, J., Martí, R., Shaheen, E., Van Ongeval, C., Cockmartin, L., Zanca, F., Marshall, N., Jacobs, J., and Bosmans, H., "Realistic Simulation of Microcalcifications in Breast Tomosynthesis," in *Digital Mammography*. vol. 6136, ed: Springer Berlin / Heidelberg, p. 235.

[113] CIRS. *CIRS Model 020 BR3D Mammography Phantom*. Accessed at: http://www.cirsinc.com/020_mammo.html.

[114] LeGal, M., Chavanne, G., and Pellier, D., "Diagnostic value of clustered microcalcifications discovered by mammography (apropos of 227 cases with histological verification and without a palpable breast tumor)," *Bull. Cancer*, 71(57), (1984).

[115] Forsyth, D. and Ponce, J., *Computer Vision -- A modern approach*: Prentice Hall, 2002.

[116] Faugeras, O., *Three Dimensional Computer Vision (A Geometric Viewpoint)*: MIT Press, 1993.

[117] Trucco, E. and Verri, A., *Introductory Techniques for 3D Computer Vision*: Prentice Hall, 1998.

[118] Hartley, R. and Zisserman, A., *Multiple View Geometry in Computer Vision*, Second ed.: University Press, Cambridge, 2003.

[119] Cyganek, B. and Siebert, J. P., *An Introduction to 3D Computer Vision Techniques and Algorithms (Volume 10)*: Wiley, 2009.

[120] Goshtasby, A. A., *2-D and 3-D Image Registration for Medical, Remote Sensing, and Industrial Applications*: Wiley-Interscience, 2005.

[121] Kolitsi, Z., Panayiotakis, G., and Pallikarakis, N., "A method for selective removal of out-of-plane structures in digital tomosynthesis," *Med Phys*, 20(1), (1993).

[122] Wheeler, F. W., Perera, A. G. A., Claus, B. E., Muller, S. L., Peters, G., and Kaufhold, J. P., "Micro-calcification detection in digital tomosynthesis mammography," in *SPIE*, 2006, pp. 671-682.

[123] Reiser, I., Nishikawa, R. M., Edwards, A. V., Kopans, D. B., Schmidt, R. A., Papaioannou, J., and Moore, R. H., "Automated detection of microcalcification clusters for digital breast tomosynthesis using projection data only: A preliminary study," *Medical Physics*, 35(4), (2008).

[124] Rick, A., Muller, S., Bothorel, S., and Grimaud, M., "Quantitative Modelling of Microcalcification Detection in Digital Mammography," in *Second International Conference on Medical Image Computing and Computer-Assisted Intervention*, 1999, pp. 32-41.

[125] Duda, R. O. and Hart, P. E. H., "Use of the Hough Transformation to Detect Lines and Curves in Pictures," *Comm. ACM*, 15(1), (1972).

[126] El-Naqa, I., Yang, Y., Wernick, M. N., Galatsanos, N. P., and Nishikawa, R., "Support vector machine learning for detection of microcalcifications in mammograms," in *IEEE International Symposium on Biomedical Imaging*, 2002, pp. 201-204.

[127] Haykin, S. S., *Neural Networks and Learning Machines* vol. 10: Prentice Hall, 2009.

[128] Platt, J. C. Microsoft Research. *Fast Training of Support Vector Machines Using Sequential Minimal Optimization*. Accessed at: http://research.microsoft.com/pps/pubs/?id=68391.

[129] Yam, M., "Detection and Analysis of Microcalcification Clusters in X-ray Mammograms using the h_{int} Representation," DPhil, Engineering Science, University of Oxford, 2001.

[130] Gurcan, M. N., Yardimci, Y., Cetin, A. E., and Ansari, R., "Detection of microcalcifications in mammograms using higher order statistics," *Signal Processing Letters, IEEE*, 4(8), (1997).

[131] Karssemeijer, N., "A stochastic model for automated detection of calcifications in digital mammograms," in *Information Processing in Medical Imaging*. vol. 511, ed: Springer Berlin / Heidelberg, 1991, p. 227.

[132] Harris, C. and Stephens, M., "A combined corner and edge detector," in *Alvey Vision Conference*, 1988, pp. 147-151.

[133] Chuang, Y.-Y. *Harris corner detector*. Accessed at: www.cyut.edu.tw/~yltang/course/image%20processing/harris.ppt.

[134] Werner, T. *Harris Corner Detector*. Accessed at: http://cmp.felk.cvut.cz/cmp/courses/PVR/2007/Labs/harris.pdf.

[135] Kadir, T., Zisserman, A., and Brady, M., "An Affine Invariant Salient Region Detector," in *European Conference on Computer Vision*, 2004, pp. 228-241.

[136] Kadir, T. and Brady, M., "Scale, Saliency and Image Description," *International Journal of Computer Vision*, 45(2), (2001).

[137] Electronics and Computer Science, University of Southampton. *Harris Corner Detector (Java Implementation)*. Accessed at: http://users.ecs.soton.ac.uk/msn/book/new_demo/corners/

[138] Ganoun, A. *Harris Corner Detector (Matlab Implementation)*. Accessed at: http://www.mathworks.com/matlabcentral/fileexchange/9272.

[139] Schmid, C., Mohr, R., and Bauckhage, C., "Evaluation of Interest Point Detectors," *International Journal of Computer Vision*, 2(37), (2000).

[140] Netsch, T. and Peitgen, H. O., "Scale-space signatures for the detection of clustered microcalcifications in digital mammograms," *Medical Imaging, IEEE Transactions on*, 18(9), (1999).

[141] Weickert, J., *Anisotropic Diffusion in Image Processing*: B. G. Teubner (Stuttgart), 1998.

[142] Perona, P. and Malik, J., "Scale-space and edge detection using anisotropic diffusion," *Pattern Analysis and Machine Intelligence, IEEE Transactions on*, 12(7), (1990).

[143] Linguraru, M. G., "Feature Detection in Mammographic Image Analysis," DPhil, Engineering Science, University of Oxford, 2002.

[144] Weickert, J., "A review of nonlinear diffusion filtering," in *Scale-Space Theory in Computer Vision*. vol. 1252, ed: Springer Berlin / Heidelberg, 1997, p. 1.

[145] Miranda, J. I. *Anisotropic Diffusion Model for Edge Detection: a Java Implementation*. Accessed at: http://www.scribd.com/doc/7909045/Anisotropic-Diffusion-Model-for-Edge-Detection-a-Java-implementation.

[146] Davies, D. H. and Dance, D. R., "Automatic computer detection of clustered calcifications in digital mammograms," *Phys. Med. Biol.*, 35(8), (1990).

[147] Alexandrov, A. Institute of Computer Science, Martin-Luther-Universitat Halle-Wittenberg. *Computer Vision 558: Corner Detection Overview and Comprison*. Accessed at: http://www2.informatik.uni-halle.de/agprbio/AG/Lehre/ABV_WS03/literatur/Corners.pdf

[148] Lihua, L., Yang, Z., Lei, Z., and Clark, R. A., "Anisotropic diffusion filtering of mammographic image for CAD in digital mammography," in *Signal Processing Proceedings, 2000. WCCC-ICSP 2000. 5th International Conference on*, 2000, p. 1159.

[149] Linguraru, M. G. and Michael, B., "An Anisotropic Diffusion Approach for Early Detection of Breast Cancer," *Technical Series*, XLIII((2001).

[150] JunJie, L., Jakas, A., Al-Obaidi, A., and Yonghuai, L., "A comparative study of different corner detection methods," in *Computational Intelligence in Robotics and Automation (CIRA), 2009 IEEE International Symposium on*, 2009, p. 509.

[151] Xinting, G., Zhuliang, Y., Sattar, F., and Venkateswarlu, R., "Multiscale corner detection for gray level images using Plessey method," in *Control, Automation, Robotics and Vision Conference, 2004. ICARCV 2004 8th*, 2004, p. 363.

[152] Bing, H., Jiyin, S., and Jing, L., "A fast approximate Harris corner detector," in *SPIE*, 2009, pp. 74952W-74952W-7.

[153] Felzenszwalb, P. and Huttenlocher, D., "Efficient Belief Propagation for Early Vision," *International Journal of Computer Vision*, 70(1), (2006).

[154] Bishop, C. M., *Pattern Recognition and Machine Learning*: Springer, 2006.

[155] Li, S. Z., *Markov Random Field Modeling in Image Analysis*: Springer, 2009.

[156] Heinrich, M. P., Jenkinson, M., Brady, M., and Schnabel, J., "Non-rigid Image Registration Through Efficient Discrete Optimization," in *Medical Image Analysis and Understanding*, 2011.

[157] German, S. and German, D., "Stochastic Relaxation, Gibbs Distributions, and the Bayesian Restoration of Images," *IeeE Transactions on Pattern Analysis and Machine Intelligence*, 6(6), (1984).

[158] Hammersley, J. M. and Clifford, P., "Markov field on finite graphs and lattices," 1971.

[159] Bourke, P. *Cross Correlation*. Accessed at: http://paulbourke.net/miscellaneous/correlate/.

[160] Yam, M., Brady, M., Highnam, R., Behrenbruch, C., English, R., and Kita, Y., "Three-Dimensional Reconstruction of Microcalcification Clusters from Two Mammographic Views," *IEEE Transactions on Medical Imaging*, 20(6), (2001).

[161] Yang, S.-C., Hsu, H.-H., Hsu, G.-C., Chung, P.-C., Guo, S.-M., Lo, C.-S., Yang, C.-W., Lee, S.-K., and Chang, C.-I., "3D localization of clustered microcalcifications using cranio-caudal and medio-lateral oblique views," *Computerized Medical Imaging and Graphics*, 29(7), (2005).

[162] Dobbins, J. T. and Godfrey, D. J., "Digital x-ray tomosynthesis: current state of the art and clinical potential," *Physics in medicine and biology*, 48(19), (2003).

[163] Kak, A. C. and Slaney, M., *Principles of Computerized Tomographic Imaging*: Society of Industrial and Applied Mathematics, 2001.

[164] Kinaham, P. E., Defrise, M., and Clackdoyle, R., *Emission Tomography: The Fundamentals of PET and SPECT*: Elsevier Academic Press, 2004.

[165] Smithuis, R. and Rijnappel, R. *Breast Calcifications - Differential diagnosis and BIRADS Classification*. Accessed at: http://www.radiologyassistant.nl/en/4793bfde0ed53. Cited on: 15 November 2008.

[166] Eric Fondrinier, M. D., Gerard Lorimier, M. D., Veronique Guerin-Boblet, M. D., Andree-Francoise Bertrand, M. D., Claude Mayras, M. D., and Nicolette Dauver, M. D., "Breast Microcalcifications: Multivariate Analysis of Radiologic and Clinical Factors for Carcinoma," *World Journal of Surgery*, 26((2002).

[167] Sun, Z., Liang, H.-w., and Xu, H.-m., "Classification of breast microcalcifications: radiological-pathological correlation," *Chinese Medical Journal*, 118(17), (2005).

[168] Lanyi, M., *Diagnosis and Differential Diagnosis Breast Calcifications*: Springer-Verlag, 1986.

[169] Margaret M. Eberl, C. H. F., Stephen B. Edge, Cathleen A. Carter, Martin C. Mahoney, "BI-RADS Classification for Management of Abnormal Mammograms," *American Board of Family Medicine*, 19((2006).

[170] Tse, G. M., Tan, P.-H., Pang, A. L. M., Tang, A. P. Y., and Cheung, H. S., "Calcification in breast lesions: pathologists' perspective," *J. Clin. Pathol*, 61((2008).

[171] Elyashiv, S. Breast Imaging Unit, Golda-Hasharon Hospital / Rbin Medical Center, Petach Tikva. *Calcifications in Mammography*. Accessed at: http://www.tau.ac.il/medicine/cme/radiology/radiology2006/elyashiv.pdf. Cited on: 15 November, 2008.

[172] Gromet, M., "Comparison of Computer-Aided Detection to Double Reading of Screening Mammograms: Review of 231,221 Mammograms," *Am. J. Roentgenol.*, 190(4), (2008).

[173] Kotsiantis, S. B., "Supervised Machine Learning: A Review of Classification Techniques," *Informatica*, 31((2007).

[174] Robert Gordon University. *The Back Propagation Algorithm*. Accessed at: http://www4.rgu.ac.uk/files/chapter3%20-%20bp.pdf.

[175] Hung, N., Hung, W. T., Thornton, B. S., Thornton, E., and Lee, W., "Classification of microcalcifications in mammograms using artificial neural networks," in *Engineering in Medicine and Biology Society, 1998. Proceedings of the 20th Annual International Conference of the IEEE*, 1998, p. 1006.

[176] Wouter, J. H. V., Nico, K., Johannes, D. M. O., and Jan, H. C. L. H., "Automated classification of clustered microcalcifications into malignant and benign types," *Medical Physics*, 27(11), (2000).

[177] Hamid, S.-Z., Siamak, P.-N., and Farshid Rafiee, R., "Shape-based and texture-based feature extraction for classification of microcalcifications in mammograms," 2001, pp. 301-310.

[178] Kramer, D. and Aghdasi, F., "Classification of microcalcifications in digitised mammograms using multiscale statistical texture analysis," in *Communications and Signal Processing, 1998. COMSIG '98. Proceedings of the 1998 South African Symposium on*, 1998, p. 121.

[179] Tromans, C. and Brady, M., "The Standard Attenuation Rate for Quantitative Mammography.," in *International Workshop on Digital Mammography (IWDM)*, Girona, Spain., 2010.

[180] Moshtagh, N. *Minimum Volume Enclosing Ellipsoid*. Accessed at: http://www.mathworks.com/matlabcentral/fileexchange/9542. Cited on: 5 January, 2010.

[181] Brady, J. M., "Keynote Presentation in IWDM 2010 by Prof. Michael Brady," 2010.